

59

DEVELOPMENT AND TEST OF A MICROFABRICATED BIPROPELLANT ROCKET ENGINE

by

ADAM POLLOK LONDON

S.B. Aeronautics and Astronautics, Massachusetts Institute of Technology, 1995
S.M. Aeronautics and Astronautics, Massachusetts Institute of Technology, 1996

Submitted to the Department of Aeronautics and Astronautics
in partial fulfillment of the requirements for the degree of

DOCTOR OF PHILOSOPHY

at the

MASSACHUSETTS INSTITUTE OF TECHNOLOGY

June 2000

© Massachusetts Institute of Technology 2000. All rights reserved.

Author

Department of Aeronautics and Astronautics
April 7, 2000

Certified by

Professor Jack L. Kerrebrock
Professor of Aeronautics and Astronautics, Emeritus, Committee Chairman

Certified by

Professor Alan H. Epstein
Richard C. MacLaurin Professor of Aeronautics and Astronautics

Certified by

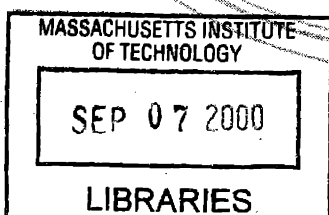
Professor Manuel Martinez-Sanchez
Professor of Aeronautics and Astronautics

Certified by

Professor S. Mark Spearing
Esther and Harold E. Edgerton Associate Professor of Aeronautics and Astronautics

Accepted by

Professor Nesbitt W. Hagood
Associate Professor of Aeronautics and Astronautics
Chairman, Department Graduate Committee



ARCHIVES

DEVELOPMENT AND TEST OF A MICROFABRICATED
BIPROPELLANT ROCKET ENGINE

by

ADAM POLLOK LONDON

Submitted to the Department of Aeronautics and Astronautics
on April 7, 2000, in partial fulfillment of the requirements for the degree of

DOCTOR OF PHILOSOPHY

ABSTRACT

The development of high aspect-ratio, high precision micromachining in silicon or silicon carbide suggests the feasibility of microfabricated, high chamber pressure chemical rocket engines. Such an engine, approximately 20x15x3 mm in size, would produce about three pounds of thrust using 300 sec I_{sp} propellants. As part of the present work, the feasibility of these engines has been investigated and a liquid-cooled, pressure-fed thrust chamber has been designed, fabricated, and tested to evaluate the feasibility of the concept.

The results of the tests to date using oxygen and methane as propellants support the feasibility of the concept, producing a maximum thrust of 1 N at a chamber pressure of 12 atm. Given the 1.2 gram mass of the thrust chamber, this corresponds to a thrust-to-weight ratio of 85:1. The characteristic exhaust velocity, c^* , a measure of combustion effectiveness, appears to be nearly independent of chamber pressure, indicating that chemical reaction rates are not limiting the combustion. Additionally, when effects of chamber heat loss are included, c^* appears to approach its predicted ideal value, indicating that the transport and mixing of propellants in the combustion chamber is of the right order to provide for complete combustion.

The thrust chamber was fabricated by etching the required patterns into each side of six 0.5 mm thick silicon wafers, and then diffusion bonding the six wafers together to create the one-piece thrust chamber. A packaging technique is presented to interface high pressure and high temperature fluids to the silicon rocket engine chip.

Additionally, initial modelling work has lead to the development of a methodology for mapping the feasible design space of microrocket engines, and for optimizing the performance of such systems given current limitations in microfabrication technology.

Thesis Supervisor: Professor Jack L. Kerrebrock
Title: Professor of Aeronautics and Astronautics, Emeritus

ACKNOWLEDGMENTS

It is hard to believe that the time has come to write the acknowledgments for my Ph.D. thesis. To quote myself a few years ago on a similar page, “Though it is my name on the title page, this thesis would not have been possible without the advice, friendship and help of many people.” That is even more true today than it was four years ago, and I’d like to take a moment to specifically thank some of these people.

I would like to thank my committee for their support and encouragement over the past few years, and in particular Prof. Jack Kerrebrock and Prof. Alan Epstein who essentially served as co-advisors to me in this endeavor. It has been a great pleasure to work with them both. I appreciated Prof. Kerrebrock’s frequent words of encouragement and his willingness to come run the vacuum pump or serve as the checklist checker. Also, I often found his ability to listen to a problem I have one day, and then arrive the following day with three potential solutions—complete with a Mathematica printout or two—rather useful. I know that I and many others have learned much from the example that Prof. Epstein, inventor of the microrocket engine, sets in terms of his dedication to the Lab and to his research, and in his insistence that when in doubt, one often should just sit down and “do the numbers.”

Herb Feinstein and James Letendre deserve a huge amount of credit for their work in building and assembling the the thrust stand and experimental apparatus that was used to test the rocket engines. I have nightmares imagining where I’d be if not for their help and dedication.

Speaking of “where would I be if it weren’t for . . . ,” I’d like to thank Prof. Mark Spearing and Todd Harrison, as well as Paul Bissonette and Paul Charpentier at Olin Aegis for their efforts in making the packaging of the microrocket a reality.

Thanks to Viktor Dubrowski for machining a whole host of bizarre pieces, and for his ability to fix most everything; to Bill Ames for dealing with lots of the little details in getting the rig together; to Diana Park for teaching me Illustrator, one command at a time, and for translating the weird Matlab mask plots into usable graphics; and to Lori Martinez, for keeping all of us sane and well fed!

Thanks to Dr. Robert Bayt for always showing me the way, and for figuring out all the hard parts of microfabrication first. A señor Arturo Ayón, el buen doctor, muchísimas gracias por tu ayuda, tu amistad, y por esa larga noche . . . I would also like to thank the staff of MTL, and in particular Kurt Broderick, for their assistance and words of advice during the fabrication phase of this work. I’d like to thank Dr. Yoav Peles for his efforts in the

fabrication of the second and especially third builds of the rocket.

I've had the privilege of working with a number of masters students over the years, and would like to thank them for their contributions to the successes of the project: Omar, Jake, Chris, Adriane, Rick, Antoine, and Sumita, thank you! I'd particularly like to thank Chris Protz for his help and good humor while running the tests, and wish him good luck and higher pressures in the months and years to come as he takes over this effort.

My time at the Gas Turbine Lab has been greatly enhanced by the friends I have made here who have helped me to keep the right perspective on life, and were always available to help with issues, technical or otherwise. Thanks to everyone in the GTL, but especially to Amit, Luc, Rory, Zolti, and Spad. Also, thanks to my officemates who put up with my ever-expanding desk over the years. Outside of the GTL, I'd like to thank Erik and Lee for their friendship, wise council, and fine taste in both walks and beverages, as well as for introducing me to swing. To Tom, Christie, Kathy, Norris, and the rest of the Park Street gang, thanks for being so welcoming, and for all of the good vibes over the past few months.

Brooks and Katherine: thanks for coming back to Boston and hanging out. I'm sorry to be deserting you here, but promise to visit as frequently as I can. Thanks to amok for keeping me eternally amused, and to Ashwin, ODK, Jeff, Jason, Shilpa, and Nidhi for not forgetting about me while I've been buried here in rocket-stuff.

Almost finally, I'd like to thank my parents and sister for their never-ending love, support, and encouragement. I could never have made it to this point without them always right behind me. Finally, I thank God for His good grace and for blessing me with such wonderful friends and family, and for providing me with many more amazing opportunities than I deserve.

One of the last things my grandfather said to me before he passed away was a question that resonated with me: "What are you building?" "Spaceships and airplanes," I told him. It has been great fun building these rocket engines for future (small) spaceships, and though I am off for now to try my hand at some other things, something tells me that my love for creating and building cool stuff will lead me at some point to get back to work on building my spaceships. I'm looking forward to the adventure!

This work was primarily supported by NASA/Glenn, Steven Schneider, technical monitor. Additional support was provided by NASA/Goddard through a Graduate Student Researcher Program fellowship administered by Dr. Jerry Soffen with David Skillman as technical advisor. Further support has been provided by the US Army Research Office, Dr T. Doligalski, technical manager; by DARPA, Dr. R. Rosenfeld, program manager; and by the MIT Lincoln Laboratory Advanced Concepts Committee. The support of all of these institutions and individuals is gratefully acknowledged.

CONTENTS

List of Figures	8
List of Tables	10
Nomenclature	13
1 Introduction	17
1.1 Background and Motivation	17
1.2 Potential of Microrocket Engines	20
1.2.1 Performance and Thrust to Weight Ratio	20
1.2.2 Cost	21
1.2.3 Modularity	22
1.3 Previous Work	22
1.4 Organization of Thesis	23
2 System Definition and Modeling	25
2.1 Introduction	25
2.2 Description of a Microrocket Engine System	25
2.3 Layout of thrust chamber	27
2.4 Introduction to Overall System Model	29
2.4.1 Model Inputs	30
2.4.2 Model Outputs	31
2.5 Description of Sub-Models	32
2.5.1 Parameterized rocket engine geometry	32
2.5.2 Rocket Performance and Mass Flow	34
2.5.3 Combustion Residence Time and Chamber Length	37
2.5.4 Wall Heat load	37

2.5.5	Final Coolant Temperature	40
2.5.6	Wall Thicknesses	40
2.5.7	Dimensions and Mass of Rocket Engine	41
2.5.8	Rockets Per Wafer Set and Number of Wafers	42
2.5.9	Side Cooling Passage Width	42
2.6	Model Results	45
2.6.1	Chamber Pressure Dependence	45
2.6.2	Geometry Dependence	48
2.7	Summary	54
3	Feasibility and Technology Limits	57
3.1	Introduction	57
3.2	Performance Metrics	58
3.3	Physical Constraints on Design	58
3.3.1	Maximum Heat Flux	59
3.3.2	Total Heat Load	61
3.3.3	Residence Time	62
3.3.4	Maximum Pump Pressure	63
3.4	Feasible Specific Impulse Envelope	63
3.4.1	Dependence on throat aspect ratio	64
3.4.2	Throat Area	66
3.4.3	Residence Time	69
3.4.4	Material of Construction	72
3.5	Baseline Design	74
3.6	Summary of Feasibility Limitations	77
3.7	Application of model results to other propellants	79
3.8	Summary	80
4	Design of Thrust Chamber	83
4.1	Introduction	83
4.2	Propellant Selection and Thrust Chamber Size	83
4.3	Heat Transfer Design	84
4.3.1	Design Methodology	84

4.3.2	Heat load	85
4.3.3	Coolant Path	86
4.3.4	Coolant Passage Design General Considerations	89
4.3.5	Choice of Design Heat Transfer Coefficient Correlation	90
4.3.6	Top Cooling Passage Design	92
4.3.7	Side Cooling Passage Design	98
4.4	Thermo-Structural Design and Modeling	100
4.4.1	Structural Design Choices	100
4.4.2	Cooling Passage Wall Thickness	102
4.4.3	Chamber wall thickness	104
4.4.4	Thermal modelling	104
4.5	Injector Design	107
4.5.1	Injector Spacing	107
4.5.2	Injector Diameter	109
4.6	Ignition	112
4.7	Conclusion	112
5	Fabrication and Packaging	113
5.1	Introduction	113
5.2	Microfabrication Concepts	113
5.2.1	Photolithography	114
5.2.2	Nested Masks	114
5.2.3	Deep Etching	116
5.3	Nozzle Etch Process Development	117
5.4	Mask Creation	120
5.5	Fabrication	126
5.5.1	Wafer preparation	126
5.5.2	Cap Plates	127
5.5.3	Wall Plates	129
5.5.4	Nozzle Plates	131
5.6	Wafer Bonding	133
5.7	Cross Sections	135

5.8	Packaging	138
5.9	Process Development	141
5.10	Further investigations and areas for improvement	144
5.10.1	Overall process yield	144
5.10.2	Quality of the glass seals	144
5.11	Summary	145
6	Experimental Setup	147
6.1	Overview of Experimental Apparatus	147
6.2	Thrust stand and mounting plate	148
6.3	Propellant flow system	150
6.3.1	Propellant measurement and control	152
6.3.2	Oxygen pressurization system	152
6.4	Coolant flow system	154
6.5	Ignition	156
6.6	Data acquisition and control	156
6.7	Video monitoring and recording	157
6.8	System calibration	158
6.8.1	Pressure transducers	158
6.8.2	Load cell	159
6.8.3	Control Regulators	159
6.9	Experimental Uncertainty	159
6.10	Experiment procedure overview	162
6.11	Summary	163
7	Experimental Results	165
7.1	Introduction	165
7.2	Testing Overview	165
7.3	Cold Flow Results	167
7.3.1	Static Pressure Test	167
7.3.2	Injector and Throat Area Characterization	168
7.3.3	Coolant Flow Characterization	171
7.4	Ignition Results	173

7.5	Initial Tests: Low Pressure	174
7.6	Water-cooled tests	176
7.6.1	Chamber Pressure and Thrust	180
7.6.2	Propellant Flow Rate	180
7.6.3	Coolant Pressures, Flow Rate, and Temperature	182
7.7	Summary	188
8	Analysis and Discussion of Results	189
8.1	Introduction	189
8.2	Specific Impulse	189
8.3	Heat Load	190
8.4	Characteristic Exhaust Velocity, c^*	196
8.5	Thrust Coefficient	198
8.6	Specific Impulse	201
8.7	Summary	201
9	Conclusions and Recommendations	205
9.1	Summary	205
9.2	Contributions	206
9.3	Recommendations for Future Work	207
A	Uncertainty Analysis	209
A.1	Introduction	209
A.2	Uncertainty of the Independent Measurements	209
A.2.1	Pressure	209
A.2.2	Thrust	210
A.2.3	Mass Flow	214
A.2.4	Temperature	216
A.3	Uncertainty of the Derived Quantities	216
A.3.1	Specific Impulse	217
A.3.2	Injector Diameter	217
A.3.3	Throat Area	217
A.3.4	Characteristic Exhaust Velocity, c^*	218

A.3.5	Thrust Coefficient	219
A.3.6	Heat Load	219
B	Fabrication Details	221
B.1	Process Steps	221
B.2	Recipes used in the STS Etcher	221
C	Example CEA Input and Output Files	227
C.1	LOX/Ethanol Combustion	227
C.1.1	Input File	227
C.1.2	Output File	228
C.2	Oxygen/Methane Combustion	232
C.2.1	Input File	232
C.2.2	Output File	233
D	Cold-side Heat Transfer Correlations	237
D.1	Nomenclature	237
D.2	Correlations	237
E	Experimental Checklists	241
	Bibliography	245

LIST OF FIGURES

2-1	Overall System Layout	26
2-2	Extruded Chamber and Nozzle Shape	27
2-3	Possible Wafer Layouts	28
2-4	Design wafer layout and terminology	28
2-5	Overall Model Flowchart	30
2-6	Parameters defining chamber and nozzle shape	33
2-7	Examples of scaled rocket shapes	34
2-8	Lines of constant flow parameters	36
2-9	Vacuum I_{sp} as function of P_c and O/F	36
2-10	Hot-side heat transfer correlations	39
2-11	A simple model of the thrust chamber and cooling passage walls.	41
2-12	Two cross-sections with bond lines	43
2-13	Dependence of T:Won chamber pressure	46
2-14	Heat load vs chamber pressure	47
2-15	Throat Cooling Parameters vs. Chamber Pressure	48
2-16	Thrust to weight ratio vs throat aspect ratio	49
2-17	Size Parameters vs. Throat Aspect Ratio	50
2-18	Fabrication Parameters vs. Throat Aspect Ratio	51
2-19	Heat Load vs. Throat aspect ratio	52
2-20	Throat heat flux vs Throat area ratio	53
2-21	Throat Cooling Parameters vs. Throat Aspect Ratio	53
3-1	Cold-side wall temperature vs. chamber pressure	60
3-2	Cooling passage width vs. chamber pressure	61
3-3	Final coolant temp vs. mixture ratio	62
3-4	Achievable vs required Pressure Rise	64
3-5	Contours of output parameters illustrating feasible operating space.	65

3-6 Feasible I_{sp} Envelope	66
3-7 Feasible I_{sp} for various throat aspect ratios	67
3-8 Performance and Fabrication Parameters	68
3-9 I_{sp} envelope for various throat areas	70
3-10 Performance and Fabrication Parameters	71
3-11 I_{sp} envelope for different residence times	73
3-12 I_{sp} envelope for SiC vs Si	75
3-13 Baseline Design Selection	76
3-14 Factors affecting heat load as O/F increases	80
4-1 Estimated local heat flux to the wall	86
4-2 Coolant Temperature Rise	87
4-3 Coolant Path Selection	88
4-4 Design Heat Transfer Correlation Selection	91
4-5 Top side cooling mask	93
4-6 Typical cross sections of top cooling passages	94
4-7 Top side cooling design	95
4-8 Nomenclature and Pin layout of top cooling passages.	96
4-9 Pin effective heat transfer	97
4-10 Top side cooling mask	98
4-11 Side Cooling Passage Design	101
4-12 Wall Fillet FEM Calculation	103
4-13 Wall thickness and fillet radius	103
4-14 Tensile Stress in Chamber wall	105
4-15 Thermal calculation at throat cross-section	105
4-16 Thermal calculation of chamber cross-section	106
4-17 Cross Section of Injector Layout	108
4-18 Location of Injectors	109
4-19 Specific Heat Ratio of Propellants	110
4-20 Injector design charts	111
5-1 Masking and etching process	114
5-2 Nested mask process	115

5-3	TMDE process	116
5-4	Scalloping of sidewall during etching	117
5-5	Feature size dependence of nozzle etch	117
5-6	MIT-37 Nozzle Etch	118
5-7	Nozzle Etch surface roughness	118
5-8	Nozzle Etch	119
5-9	Mask 1: Top Holes	121
5-10	Mask 2: Top Shallow	121
5-11	Mask 3: Top Deep	122
5-12	Mask 4: Injectors	122
5-13	Mask 5: Wall Cooling	123
5-14	Mask 6: Wall Interconnect	123
5-15	Mask 7: Nozzle Nested	124
5-16	Mask 8: Centerline	124
5-17	Mask 9: Bottom Holes	125
5-18	All masks superimposed	125
5-19	Cap Plate (Note: the bottom cap plate would have a different front side without the 11 fluid ports)	128
5-20	Top and Bottom Plate process	128
5-21	Wall Plate	129
5-22	Wall Plate process	130
5-23	Footing effect leads to depredation of the sidewalls.	131
5-24	Wall Plate damage during over-etch	132
5-25	Wall Plate damage reduced	133
5-26	Nozzle Plate	134
5-27	Nozzle Plate process	134
5-28	Build 1 Bonding	135
5-29	Cross sections of completed die	136
5-30	Cross section of completed die in flow direction	137
5-31	Schematic of rocket package	138
5-32	Steps in glass sealing of rocket chip	139
5-33	Kovar tubes glass sealed to rocket chip	140

5-34 Fully packaged thrust chamber die	140
5-35 Wafer of packaging test dies	141
5-36 Packaging Process Development	142
5-37 Pressure testing of glass bead packaging	143
5-38 Cross section of glass beads after sealing showing voids	145
5-39 Cross section of glass beads after sealing showing local silicon fracture	146
6-1 Overview of experimental apparatus	148
6-2 Views of thrust stand	149
6-3 Mounting plate on thrust stand	150
6-4 Schematics of the oxygen and methane flow systems	151
6-5 Propellant supply system components	153
6-6 Oxygen gas booster pump	153
6-7 Schematic of the cooling flow system	155
6-8 Cooling flow system components	155
6-9 Control signal for propellant supply	157
6-10 Pressure transducer calibration setup	158
6-11 Pressure transducer calibration	160
6-12 Example of load cell calibration for thrust measurement	161
6-13 Propellant supply pressure as a function of command signal.	161
7-1 Engine locations and die labels	166
7-2 Static pressure test failure	168
7-3 Example cold flow results	169
7-4 Injector Diameter for Die C3	170
7-5 Throat area calculation for Die C3.	171
7-6 Coolant flow characterization	172
7-7 Ignition results	174
7-8 Images from Tests 1 and 2	175
7-9 Ignitor wires after first test	175
7-10 Coolant flow and recorded thrust during first low pressure tests	177
7-11 Thrust produced by thermal expansion of supply tubes	178
7-12 Modifications to thrust stand to improve thrust measurement	178

7-13	Images from water cooled tests, run 72	179
7-14	Images from water cooled tests, run 73	179
7-15	Images from water cooled tests, run 87	180
7-16	Chamber Pressure and Thrust for the water-cooled tests	181
7-17	Propellant flow rates for the water-cooled tests	182
7-18	Coolant flow, outlet pressure, and outlet temperature	183
7-19	Coolant flow, outlet pressure, and outlet temperature	184
7-20	Closeup of coolant pressure and temperature, run 72	186
7-21	Closeup of coolant pressure and temperature, run 73	187
8-1	Comparison of inferred and predicted total heat load.	192
8-2	Difference between coolant outlet temperature and saturation temperature .	192
8-3	Predicted heat load for top and side passages if 30% of coolant flows through top passages	194
8-4	Predicted heat load for top and side passages if 45% of coolant flows through top passages	195
8-5	Comparison of experimental c^* with calculations	197
8-6	Measured Thrust coefficient	199
8-7	Ideal C_F as a function of nozzle area ratio	200
8-8	Comparison of experimental and predicted I_{sp}	202
A-1	Pressure Transducer Calibration 1	211
A-2	Pressure Transducer Calibration 2	212
A-3	Pressure Transducer Calibration 3	213
A-4	Thrust Stand Calibration	215

LIST OF TABLES

2.1	Material Properties of Silicon and Silicon Carbide	31
2.2	Chamber and Nozzle parameters and baseline values	34
2.3	Parameters used in chamber pressure study	45
2.4	Parameters for geometry study	48
3.1	Input Parameters for Baseline Design	74
3.2	Output Parameters for Baseline Design	78
4.1	Nominal Heat Transfer Parameters	89
5.1	Masks used in Fabrication	120
6.1	Summary of Experimental Uncertainty	162
7.1	Water-cooled Test Summary	166
7.2	Coolant parameters for hot tests	167
7.3	Effective Injector Diameters	170
A.1	Example uncertainties in pressure measurements	210
A.2	Example uncertainties in injector diameters	218
A.3	Example uncertainties in throat area	218
B.1	Process steps for fabricating thrust chamber	222
B.2	Recipe RKT-04	223
B.3	Recipe MIT-37	223
B.4	Recipe MIT-59	223
B.5	Recipe TM-02	224
B.6	Recipe MIT-56	224
B.7	Recipe MIT-51	224
B.8	Recipe SF6-4	225

E.1	Test Cell Preparation Checklist	242
E.2	Gas Pressurization Checklist	243
E.3	Hot or Cold Flow Run Checklist	244

NOMENCLATURE

Roman

A	Area, usually a cross-sectional flow area
A_t	Throat area
D	Diameter
D_h	Hydraulic diameter
I_{sp}	Specific impulse
L	Length
L_c	Chamber length
L_e	Expansion nozzle length
L^*	Characteristic chamber length
F	Thrust
M	Mach number
P	Pressure, also perimeter
\dot{Q}	Total heat load (heat per unit time)
R	Gas constant
S	Fractional uncertainty, also spacing between pins
T	Temperature
T_{aw}	Adiabatic wall temperature
T_b	Bulk fluid temperature
T_{bf}	Final bulk fluid temperature
T_w	Hot-side wall temperature
T_{wc}	Cold-side wall temperature
U	Jet velocity
V	Volume

c	Effective exhaust velocity, F/\dot{m}
c^*	Characteristic exhaust velocity, $P_c A_t / \dot{m}$
c_p	Specific heat at constant pressure
c_v	Specific heat at constant volume
g	Acceleration of gravity at Earth's surface.
h	Heat transfer coefficient, also height and specific enthalpy
h_c	cold-side heat transfer coefficient
h_g	Hot-side heat transfer coefficient
h_t	Throat height
h_t/w_t	Throat aspect ratio
l_w	Length or span of a wall
m_{eng}	Mass of one engine
\dot{m}	Mass flow
n_{sp}	Number of side cooling passage layers
\dot{q}	Heat flux (heat per unit area per unit time)
r_{cc}	Corner radius of chamber
r_{tc}	Converging radius of throat
r_{td}	Diverging radius of throat
t_w	Wall thickness
u	Velocity
w	Width
w_c	Chamber width
w_e	Nozzle exit width
w_{sp}	Side passage width, usually minimum required
w_t	Throat width

Non-dimensional groups

C_F	Thrust coefficient, $F/(P_c A_t)$
Nu	Nusselt number, hL/κ
O/F	Oxidizer to fuel ratio, by mass, $\dot{m}_{ox}/\dot{m}_{fuel}$
Pr	Prantl number, $\mu c_p/\kappa$
Re	Reynolds number, $\rho u L / \mu$
T:W	Thrust-to-weight ratio, $F/m_{eng}g$

Greek

α	Thermal expansion coefficient
α^*	Passage aspect ratio
γ	Specific heat ratio (gas constant), c_p/c_v
Δ	Change in a quantity
ϵ	Nozzle expansion ratio, A_e/A_t
κ	Thermal conductivity
μ	Viscosity
θ_c	Throat convergence angle
θ_d	Throat divergence angle
ρ	Density
σ	Stress
σ_{max}	Maximum allowable stress
τ_{res}	Chamber residence time

Subscripts

<i>c</i>	Chamber
<i>e</i>	Exit
<i>max</i>	Maximum
<i>min</i>	Minimum
<i>ref</i>	Reference condition
<i>t</i>	Throat, or total

Superscripts

*	Characteristic
---	----------------

Acronyms

BOE	Buffered Oxide Etch (or Etchant)
CVD	Chemical Vapor Deposition
MEMS	Micro-Electro-Mechanical Systems
RIE	Reactive Ion Etching
STS	Surface Technology Systems
TMDE	Time-Multiplexed Deep Etching

CHAPTER 1

INTRODUCTION

1.1 Background and Motivation

In 1994, Epstein [12] initiated an effort at MIT to develop micro-fabricated gas turbine engines for propulsion and electric power applications. These engines are expected to be approximately 20 mm square by 4 mm deep, and produce useful power in the range of 10-50 W. Silicon carbide and silicon were identified as promising materials of construction for such a system for two main reasons. First, gas turbine engines require high speed rotating turbomachinery. The primary figure of merit used in selecting a material for such systems is the strength to density ratio, which is larger for both silicon and silicon carbide than it is for the high temperature super-alloys typically used in large scale gas turbine engines.* Second, high precision fabrication techniques exist to make the necessary parts from these materials, particularly in the case of silicon, which is used in most MEMS (Micro Electro Mechanical Systems) devices.

The potential existence of high speed rotating gas turbines and compressors at the millimeter scale implies the application of this technology to another kind of turbomachinery: turbopumps for very small liquid propellant rocket engines. Current rocket thrusters of this scale are blow-down or regulated systems that rely on pressurized propellant tanks to drive the propellants into the combustion chamber and provide the pressure there. This leads to a requirement for thick-walled tanks, which are much heavier per unit mass of propellant being stored than tanks of a typical liquid-fueled launch vehicle whose engines employ turbopumps to pressurize the propellant prior to its injection into the chamber.

*At 800 K, The specific yield stress is near $5 \cdot 10^4 \text{ m}^2/\text{s}^2$ for Hastelloy X and Inconel 600, but is about $1.5 \cdot 10^5 \text{ m}^2/\text{s}^2$ for silicon carbide, and $3.5 \cdot 10^5 \text{ m}^2/\text{s}^2$ for silicon. [31]

If turbopumps could be added to the small rocket engines used on satellites, tank walls could be made thinner, resulting in a significant weight savings that could translate into a larger mass budget for payloads or additional fuel for a longer lifetime.[†] Additionally, because pumps allow for higher chamber pressures, the engines can be made smaller for the same thrust level, leading to additional weight savings. However, this weight savings is less significant, as the mass of the engines themselves tends to be a relatively small fraction of the total propulsion system weight.

This small size for a given thrust level implies another potential application of microfabricated rocket engines, namely small launch vehicles. Their small size and high thrust to weight ratio could enable very small launch vehicles,[‡] by providing the high performance and low mass necessary for orbital insertion at this small scale.

On traditional liquid-fueled launch vehicles, the engines themselves tend to weigh about twice as much as the payload being delivered to orbit. At launch, they are required to produce a thrust slightly larger than the total weight of the vehicle. If they could produce this same thrust while weighing much less, this weight savings could be used to increase the size of the payload. There are two ways that the thrust-to-weight ratio can be increased for a given propellant combination. As was already mentioned, a higher chamber pressure will lead to a smaller engine for a given thrust level. Additionally, by simply making the engine smaller at a constant chamber pressure, the thrust to weight ratio will increase, everything else being equal. This is because the thrust produced is proportional to the throat area, while the weight of the engine is proportional to its volume. For perfect scaling the ratio of the throat area to the overall volume will increase as the rocket is made smaller. If one takes a traditional engine and makes four copies of it, each exactly half the size (one eighth the volume and one quarter the exit area) of the original, the four engines together would produce the same thrust as the larger original engine, but weigh only half as much. One could then do the same with the half-size engine, and make a total of 16 quarter-size engines, which when ganged together would still produce the same thrust as the original, but together only weigh a quarter of the original engine. In theory, this process could be

[†]If one assumes that 30% of the satellite mass is fuel and that high pressure tanks weigh 10% of the fuel they contain, one would expect a total weight savings of around 2% of the satellite mass, or about a 6.5% increase in lifetime.

[‡]Payloads to orbit of 0.1 to 5 kg. See Francis [14] for a more detailed discussion of this concept.

continued indefinitely, leading to a massively-parallel thrust system with a very high thrust to weight ratio.

As is often the case, reality and practicality get in the way of theory. This approach was used to varying degrees in both the US and Soviet moon programs. The first stage of the Saturn V was powered by five F-1 engines, saving about half the weight of an equivalent single engine according to the above argument. The Soviet launcher was to be powered by about 25 engines. By the arguments above, one would have expected that together they weighed about a fifth of an equivalent single engine. The rocket never had a successful flight as there were a number of single engine failures that led to failure of the launch system. A system with a large number of engines has the capability to provide redundancy in that the loss of thrust from one could have a small effect on total thrust level. However, if the failure of one engine can not be contained, additional engines will multiply the number of single point failure modes for the launch system, leading to a significantly reduced overall system reliability.

Other practical issues arise as well. One must justify the additional complexity required in the plumbing and control of many versus fewer engines. Additionally, the traditional view is that there is a minimum chamber residence time required for complete combustion in rocket engines, which does not scale with size.[§] This means that one can not perform an exact scaling of engines without sacrificing efficiency, something launch vehicle designers are quite loathe to do.

Cost is another concern. Using traditional manufacturing methods, the cost of producing one half-size engine is probably not much less than the cost of producing a full-size engine, as in a perfect scaling each of the pieces would have to be reproduced at half-scale. The cost of a smaller engine might even exceed that of a larger one as it becomes harder to reproduce the detail of the original pieces at smaller and smaller scales. Eventually, limits in fabrication technology would prevent one from successfully making the smaller engine. In any case, the cost per unit thrust of an engine would certainly increase.

It is quite clear that the reduction in scale of rocket engines is not a so-called “silver-bullet,”

[§]This residence time is usually defined by L^* , the ratio of chamber volume to throat area, which is typically between 80 and 300 cm for large-scale rocket engines. [38]. The value of L^* for the thrust chamber tested in the present work is 6.5 cm.

automatically leading to better system performance. As is usually the case, a high-level system tradeoff is required in choosing the appropriate number and size of engines for a given propulsion system.

Nevertheless, the concept of the microrocket engine has the potential to overcome a number of these drawbacks inherent in the reduction in scale of large liquid-fueled rocket engines. These issues will be discussed in the next section.

1.2 Potential of Microrocket Engines

1.2.1 Performance and Thrust to Weight Ratio

The above argument would imply that scaling down a large-scale rocket engine, such as the RD-120,[¶] with a throat diameter of 185 mm to an engine with a characteristic throat dimension of 1 mm would imply a increase in the thrust-to-weight ratio, T:W, of 185 times, from about 75:1 to nearly 14,000:1. In fact, it is unlikely that such a direct scaling could be done, but the thrust chamber presented in this work should have a thrust to weight ratio of about 1250:1 at design. Operating at 10% of design chamber pressure, it has already demonstrated a T:W of 85:1.

A larger question is that of combustion, as it is the complete combustion of the propellants that allows rocket engine performance to approach ideal levels of specific impulse, a measure of fuel efficiency. As was mentioned in the previous chapter, the traditional view is that combustion processes do not scale to smaller sizes well. Essentially, this becomes an issue of residence time. If the time required for combustion to occur is smaller than the time any given quantity of propellant resides in the chamber, the combustion will be incomplete, and the engine will suffer a performance penalty. The characteristic chamber length, L^* , is a measure of this residence time, so experience has shown that the required residence time in a rocket engine combustion chamber must be constant.

If this were universally true, it would clearly indicate the infeasibility of microrocket engines. To further understand this effect, it is necessary to separate the combustion process

[¶]An engine developed in Russia that develops approximately 850,000 N of thrust with kerosene and oxygen as propellants. Data on the engine is taken from ref. [38].

into two parts. The first is the actual chemical reactions that convert the propellants into their reaction products, releasing the energy that increases their temperature and is then converted into directed kinetic energy by the expansion nozzle, producing thrust. The rates of these reaction are independent of scale, so if they are the limiting phase of the combustion process that set the minimum residence time, it would not be possible to effectively scale chemical rocket engines to the small scale. However, there is another factor to consider. In order for these reactions to take place, the fuel and oxidizer reactants must be in close proximity, and this is accomplished through injection and mixing in the chamber. In fact, this process typically occupies the majority of time a propellant element spends in a combustion chamber. This is a primarily fluid dynamic process, and it does scale. To first order, one may consider the mixing of two reactants as a diffusion process, which will take a shorter time to accomplish if the distance that each must diffuse is smaller. One would expect that this mixing length scale is on the order of the diameter or spacing of the propellant injectors. The use of microfabrication allows for very small injectors and injector spacings,^{||} which may imply that it is possible to reduce the injection and mixing time enough to allow for effective scaling of rocket engines to the millimeter scale.

It is difficult to analytically predict either the reaction rates or mixing times in rocket engine chambers. For this reason, an experimental approach has been taken in this work to explore the feasibility of scaling an engine to this scale. The initial results are quite promising, in that they imply that the reaction rate are not limiting the reaction, and that the mixing times are of the correct order to provide for complete combustion.

1.2.2 Cost

Another potential disadvantage for scaling rocket engines to mm-size is the cost of manufacturing them. It is likely that manufacturing a liquid cooled chemical rocket engine with a throat area on the order of 1 mm^2 using traditional materials and techniques would be at least as costly as manufacturing an equivalently complex large scale one, though it is not clear this would even be possible. The introduction of silicon-based microfabrication techniques addresses this issue in two ways. First, it provides a technique that allows for

^{||}The injector diameters of the thrust chamber tested in this work are $10\text{-}20 \mu\text{m}$, and their spacing is $150 \mu\text{m}$.

the very small ($10 \mu\text{m}$) features required, and second, it does this in a way that allows for batch fabrication of these devices. Since the engines are manufactured many at a time from a set of wafers, the unit costs can be greatly reduced, particularly in large scale production. Though it is still very early to be certain, initial estimates of the manufacturing costs of such devices range from hundreds to thousands of dollars, which is of the same order per unit thrust as the cost of large-scale engines.

1.2.3 Modularity

Finally, microrocket engines present the potential advantage of modularity. If they are mass-produced and an effective way to package them is found, one could imagine a number of them combined into a “thrust pack” that produced a given quantity of thrust. If a design called for more or less thrust, these units could be removed or added to change the total thrust level. It is likely that this could add flexibility to the design process, as vehicles select the desired quantity of thrust, rather than having to design a vehicle around an already existing engine with a given amount of thrust.

1.3 Previous Work

It is believed that this work is the first example of a continuously operating, liquid-cooled, bipropellant rocket engine thrust chamber with a throat area that is less than 1 mm^2 . Traditional engines in this thrust class typically decompose a hydrazine monopropellant, or use solid propellants, and have nozzles that are radiatively cooled. There is, however, a reasonable amount of related work, both in terms of “micropulsion,” often using silicon microfabrication techniques, and in terms of chemical combustion at these scales.

Janson [22] was one of the first to apply silicon batch fabrication techniques to micropulsion, using wet chemical etching techniques similar to those used in making ink-jet printer heads to create cold-gas thrusters.

Bayt [8] used the anisotropic deep reactive ion etching techniques reported by Ayon [3] (and also used in this work) to make smoothly-contoured nozzles, and demonstrated improved performance of cold gas thrusters. He also demonstrated an electrically augmented version

where the gas was heated prior to expansion.

Lewis [26] has proposed “digital micropropulsion,” and demonstrated a number of single shot solid propellant rocket motors, batch manufactured from silicon, each of millimeter-scale.

As part of the MIT Microengine Project, Tzeng [41] demonstrated hydrogen combustion at the millimeter scale in a traditionally fabricated steel and quartz test rig, and then Mehra [31] demonstrated both hydrogen and hydrocarbon combustion in air at low pressure (up to 3 bar) at the millimeter scale inside microfabricated silicon combustors.

Finally, as part of the current research effort on microrocket engines at MIT, some additional work has been performed. Al-Midani [1] investigated the feasibility of using electrically powered pumps to pressurize the propellants, and performed some studies of the fluid dynamics of the expansion nozzle design used in this work. He also investigated the kinetics of the oxygen-ethanol combustion, and simulated the start-up transient of a liquid oxygen-ethanol microrocket. Lopata [29] performed an experimental investigation of the cooling properties of supercritical ethanol at these scales by measuring the heat transfer capabilities of ethanol flowing through an electrically heated stainless steel capillary tube with an internal diameter of about $100 \mu\text{m}$. More recently, Faust [13] improved Lopata’s data reduction technique and extended the experiments to supercritical water. Most recently, Protz [35] has extended some of the work presented here and by Al-Midani to other storable non-cryogenic propellant combinations.

1.4 Organization of Thesis

This chapter has introduced the concept of a microrocket engine, and provided a preliminary indication of the potential benefits of such a system.

Chapter Two presents an overview of a conceptual microrocket engine system, and describes the set of models used to simulate the eventual performance of such a system.

In Chapter Three, these models are applied to engines using the oxygen/ethanol propellant combination in a study of their design space. The primary physical constraints on design

are identified, and the concept of a feasible specific impulse envelope is introduced, which quantifies the maximum specific impulse that can be expected from an engine as a function of chamber pressure. The effects on the size and shape of this geometry are explored as engine geometry and material properties are varied. Finally, the baseline design for an oxygen/ethanol rocket engine is presented.

Chapter Four discusses the detailed design of a cooled thrust chamber conceived to demonstrate experimentally the viability of microrocket engines. Specifically, it is to be used to evaluate the feasibility of injection, mixing, and combustion of propellants in rocket engines of this scale manufactured from silicon. It is a liquid-cooled thrust chamber that runs on gaseous oxygen and methane. Its size and design mass flow are taken from the baseline design of Chapter Three, but the cooling system is specifically designed for the heat loads expected from this particular propellant combination.

Chapter Five presents the fabrication and packaging of this demonstration thrust chamber. Using silicon microfabrication techniques, it is manufactured, sixteen at a time, from six single-crystal wafers 100 mm in diameter. A fluidic packaging technique is developed to provide a connection for liquids and gases to the silicon device capable of operating at high pressure and temperature.

Chapter Six describes the experimental apparatus that was used to test the thrust chambers.

Chapter Seven presents the results of the experiments that have been performed with the fabricated thrust chambers. To date, there have been six successful ignitions, with a maximum recorded thrust of about 1 N at a chamber pressure of 12.3 bar. This corresponds to 10% of the design chamber pressure, and a thrust to weight ratio of approximately 85:1.

Chapter Eight provides additional analysis and discussion of the results. The experimental data suggest that combustion is not being limited by incomplete reaction, as the combustion efficiency appears to be independent of pressure. Additionally, it suggests that when corrected for chamber heat loss, and nozzle separation effects, the measured performance is within 5-15% of what would be expected from an ideal rocket engine.

Finally, Chapter Nine presents a summary of the research and presents recommendations for further work in this area.

CHAPTER 2

SYSTEM DEFINITION AND MODELING

2.1 Introduction

The simple scaling arguments presented in the previous chapter suggest some significant advantages of microrocket engine technology. This chapter provides a definition of the microrocket system and its subsystems and describes the set of models that has been employed to simulate the eventual performance of microrocket systems. In the following chapter, this model will first be used to illustrate the feasible design space for microrocket engines, and then to choose a baseline design within this feasible space.

2.2 Description of a Microrocket Engine System

This section will provide an overview of a microrocket engine system. The complete system is illustrated conceptually in Figure 2-1. The three primary components of a microrocket system are the valves, the turbopumps, and the cooled thrust chamber. One could imagine combining these components in a number of different ways to create different rocket engine cycles, though the only cycle considered in this work is termed an expander cycle. In this type of cycle, the propellants would enter the chip through the valves at low pressure, and would then be pressurized by the turbopumps to the pressure required at the inlet to the cooling passages. The propellants next pass through the cooling jacket surrounding the chamber and nozzle to cool the thrust chamber walls to an allowable structural temperature, absorbing heat in the process. Some of this energy is then used to provide the original pressurization as the propellants pass through the turbopump turbines. Finally, the propellants are injected into the chamber where they mix and react to produce high

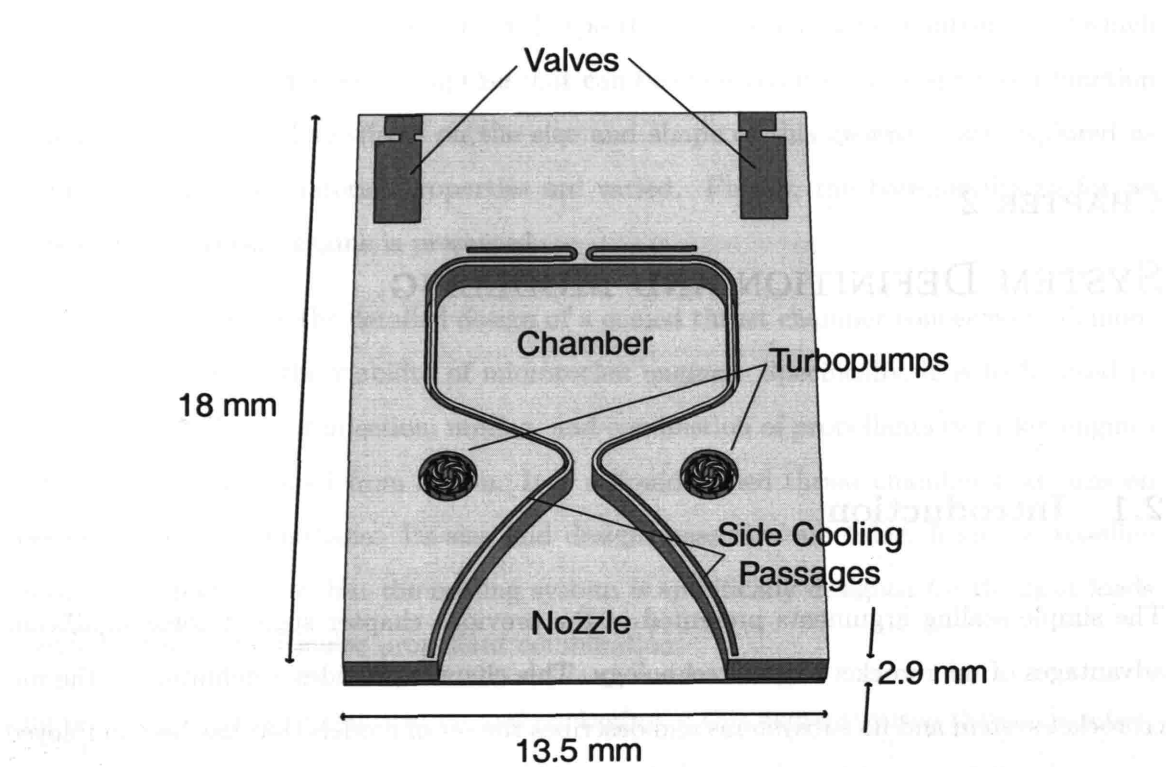


Figure 2-1: This figure illustrates a conceptual view of the location of the various system components. Illustration courtesy of Diana Park

temperature combustion products, which are expanded through the throat and exhaust nozzle to produce thrust.

The focus of this thesis is the cooled thrust chamber, and therefore is the primary basis of the model described in this chapter. The turbopumps are considered as well, but as it is determined that more than sufficient energy is available to drive them, only a very simplistic modeling effort is made. The valves are not discussed at all in this work, though an initial design study has been completed and a fabrication demonstration is in progress by Hölke [21].

As was discussed in the previous chapter, the engine system will be constructed using silicon microfabrication techniques.* Current silicon fabrication technology requires that all features be two dimensional shapes that are formed in a wafer surface using deep reactive ion etching. This leads to a chamber and nozzle shape similar to that illustrated in

*Later versions may use silicon carbide as the material of construction

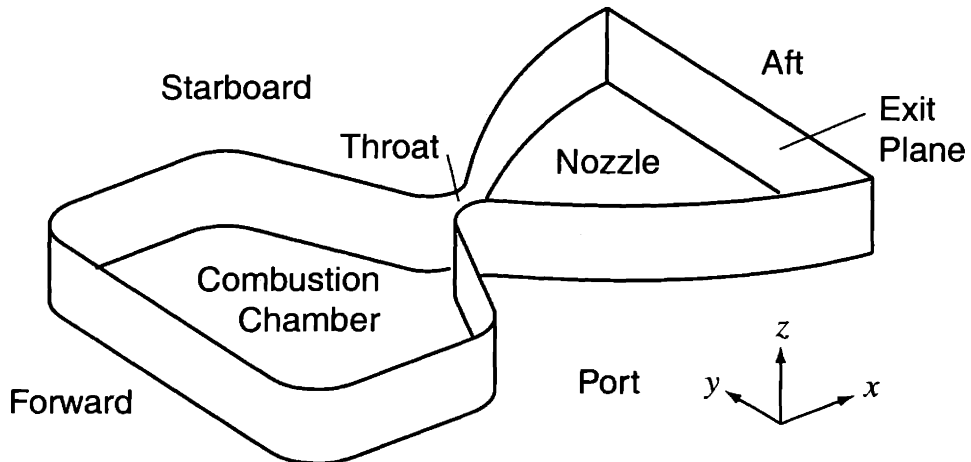


Figure 2-2: Extruded Chamber and Nozzle Shape. The annotations show locations discussed in the thesis, as well as the nautical terms used to identify locations, defined relative to the throat location.

Figure 2-2, which is quite different from the axisymmetric chamber and nozzle shape used in most traditional rocket engines. This figure also illustrates the coordinate system and nomenclature used throughout this thesis to identify locations. The origin of the coordinate system is taken as the center of the throat, with the x -axis extending in the flow direction towards the aft end of the thrust chamber, and the y -axis extending towards the starboard side. The throat area, A_t , is defined by its height in the z -direction, h_t , and by its width in the y -direction, w_t , rather than being defined by a diameter.

2.3 Layout of thrust chamber

The modelling effort assumes an overall layout for the thrust chamber, so it is instructive to briefly explore why this layout was selected. In order to do this, one must consider how it is constructed from a number of wafer layers. Figure 2-3 illustrates a number of potential cross sections of a microrocket thrust chamber. Though the diagrams are schematics and not to scale, each view could be considered a section parallel to the y -axis through the combustion chamber near its forward end.

The simplest way to create the chamber and nozzle would be to etch the shape shown in Figure 2-2 into a wafer, and then cap it with another wafer, as shown in (a). This presents

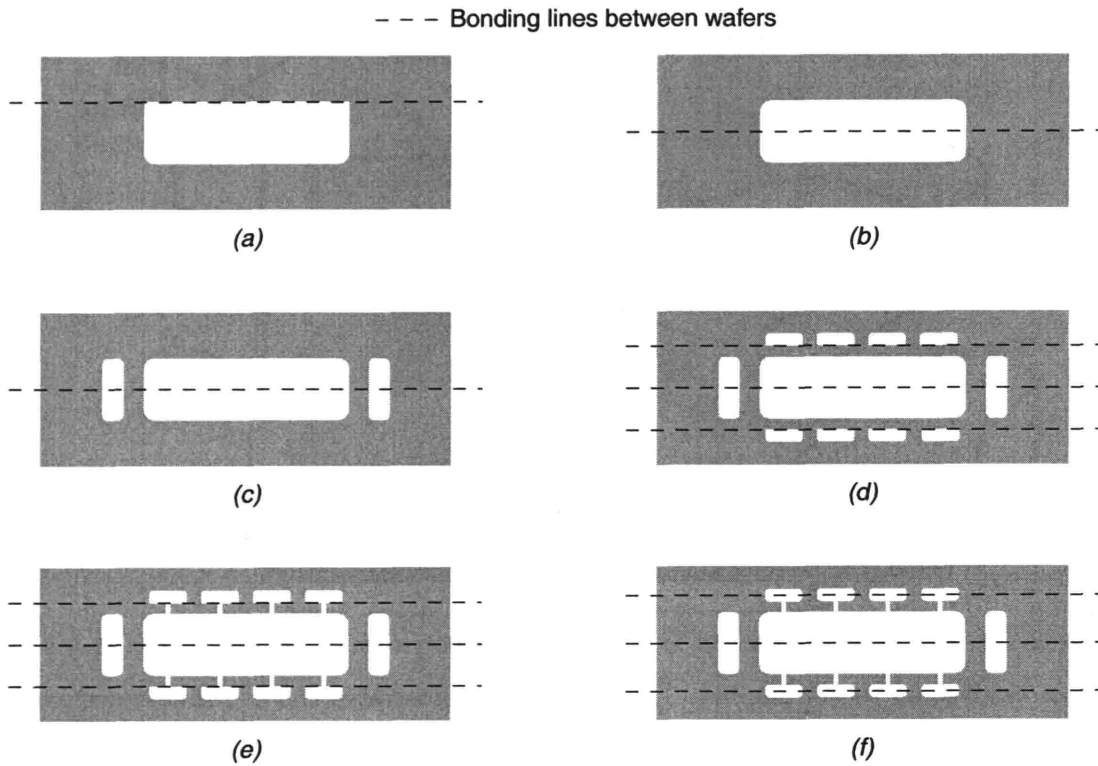


Figure 2-3: A sequence of cross sections (not to scale) illustrating the reasoning behind the generic wafer layout used in this work as shown in (f). The driving considerations are the need for cooling passages in close proximity to the chamber and nozzle, and the requirement that sharp corners be avoided at bond lines to prevent the high stress concentrations that would result at the corners from causing brittle failure in the silicon.

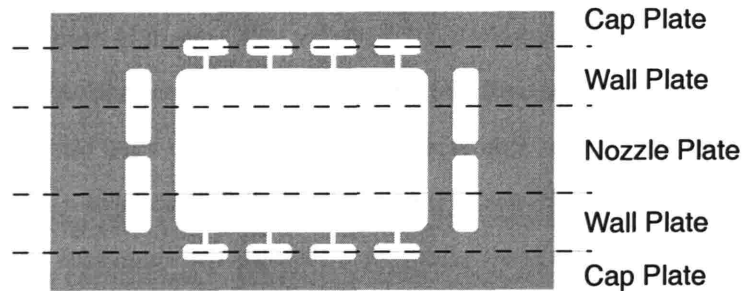


Figure 2-4: Adding one or more nozzle plates to the wafer set increases the layers of side cooling passages, and can be used to increase the height of the chamber and nozzle. The labels show the terminology used to refer to the three kinds of wafers used in this work.

a problem in that it results in sharp corners where the top wafer is bonded to the lower wafer. This would lead to very high stress concentrations when the chamber is pressurized, and lead to fracture of the brittle silicon. A better design is to etch half of the nozzle into two identical wafers, and bond these to each other, as in (b). Cooling passages around the chamber and nozzle will be required to keep the walls from melting, and side cooling passages are easily added as part of the same nozzle etch, shown in (c). However, having cooling passages on the top and bottom surfaces of the chamber and nozzle requires adding wafers. The two wafers defining the chamber and nozzle could be made thinner, and top and bottom cooling passages then etched into two additional wafers, as shown in (d). This also allows injectors or pressure taps or ignitor ports to be etched into the chamber from the opposite side of the wafers that contain the nozzle etch, as in (e). However, it has the same problem as in (a), that of sharp corners in locations of high stress, though this time, in the cooling channel walls. The solution is to use a technique called nested masking that allows etches of different depths from the same side of the wafer, and make the top and bottom cooling passages span the bond line between the capping and nozzle wafers, as in (f).

This is the general layout used throughout this thesis. Notice that the height of the cooling passages and the thickness of the top and bottom chamber walls can not vary across the wafer,[†] but that the thickness of the side walls of the nozzle can vary. The top and bottom wafers are termed cap plates, and the two wafers in the middle of Figure 2-3 are termed wall plates as they contain the top and bottom walls of the chamber and nozzle. Additionally, one could add one or more nozzle plates, as in Figure 2-4 to increase the number of layers of side cooling passages. The demonstration thrust chamber fabricated as part of this work has two of each kind of plate, or a total of six wafers.

2.4 Introduction to Overall System Model

This section will describe the overall model developed for a liquid oxygen/ethanol rocket engine system. The model takes a number of parameters describing an eventual engine,

[†]This is not entirely true in the case of the top cooling passages, since the upper half of the etch can be eliminated, leaving passages approximately half as high. Though this leads to unwanted sharp corners, it is acceptable on the side of the passage away from the nozzle for areas of the passage with small widths.

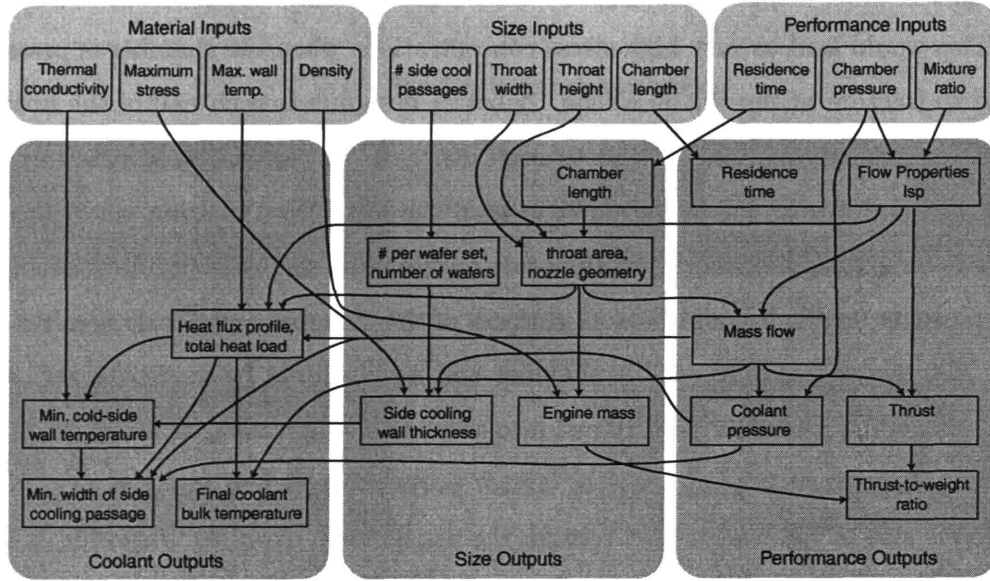


Figure 2-5: Flowchart of system model showing relationships between inputs and outputs.

and yields the important characteristics for determining the feasibility of that system. In addition to evaluating feasibility, it provides a number of performance and size related characteristics of the idealized system.

Figure 2-5 provides an illustration of the model's inputs and primary outputs, and traces the dependencies of those outputs. The next topics of this section discuss the inputs and outputs in more detail, and the following section discusses the sub-models that are used to calculate the various outputs of the model.

The model is implemented via a number of MATLAB routines, with essentially one routine per sub-model. A “master” routine distributes the inputs and coordinates the information flow between the various sub-models.

2.4.1 Model Inputs

The inputs to the model are selected to be those that one would need to choose in designing a microrocket engine. They can be divided into three categories: those related to the size and layout of the engine, those related to its performance, and those related to the material of construction.

Size Inputs: The two main size inputs are the width and height of the throat, w_t and h_t . They determine the overall scale of the engine, and together with the pressure, effectively determine the mass flow and thrust. An optional size input is the length of the chamber, L_c . Either this or the residence time (see below) can be specified, and one determines the other. The number of side cooling passages, n_{sp} , a layout parameter, is also an input to the model. However, it can also be calculated from h_t by assuming an average wafer thickness.

Performance Inputs: The primary performance inputs are the chamber pressure, P_c , and the oxidizer to fuel mixture ratio, O/F. The expansion ratio of the nozzle, ϵ , can be specified as well, though it is held constant at 15 for the current study. Finally, as mentioned above, the residence time may be specified. As this affects performance, it is included here, but it is used primarily to determine the required length of the chamber.

Material Inputs: The parameters of the model that depend on the material of construction are the maximum allowable wall temperature, T_w , as well as the thermal conductivity, κ , the maximum allowable stress, σ_{max} , and the density, ρ . The properties for the two materials considered are shown in Table 2.1.

Table 2.1: Material Properties of Silicon and Silicon Carbide. Based on information from [10, 28, 11].

Property	Silicon	Silicon Carbide
T_w	900 K	1400 K
κ	40 W/mK [800K]	63 W/mK [1000K]
ρ	2330 kg/m ³	3200 kg/m ³
σ_{max}	1000 MPa	600 MPa

2.4.2 Model Outputs

The model outputs are those that a designer would consider in evaluating the usefulness of a given rocket system. They can be divided into categories similar to the inputs: size, performance, and cooling.

Size Outputs: The primary size outputs are the length, width, and height or thickness of the engine (L , W , and H). Additionally, the mass of the engine, m_{eng} is returned, as well as the length of the chamber calculated from the desired residence time. Fabrication parameters such as the number of devices per wafer set, and number of wafers required are also considered size outputs. Critical wall thicknesses, such as that of the side cooling passage walls at the throat, and the required thickness of the chamber capping walls are also outputs.

Performance Outputs: The performance outputs are the thrust, F , the mass flow, \dot{m} , the specific impulse, I_{sp} (in vacuum), the residence time, τ_{res} , the thrust-to-weight ratio, and the characteristic exhaust velocity, c^* .[†] Additionally, the physical properties of the nozzle flow are available.

Cooling Outputs: The outputs relating to the cooling system include the heat flux profile to the wall, the integrated total heat load, and the maximum bulk temperature reached by the propellants while absorbing this load, T_{bf} . At the throat, the minimum required width of the side cooling passages, w_{sp} , is estimated, and the coolant-side wall temperature, T_{wc} , at this location is calculated. As the actual functional dependence of the hot-side heat flux is not well known for the very high heat fluxes expected in microrockets, all of these parameters are calculated using both the nominal heat flux correlation used in the design of the demonstration thrust chamber and a correlation that results in a higher predicted heat load.

2.5 Description of Sub-Models

2.5.1 Parameterized rocket engine geometry

In order to simulate an eventual rocket engine system, it is necessary to have a parameterized geometry that can be scaled to consider engines of different size. Based on current micro-fabrication etching techniques, the engines are constrained to have a geometry produced

[†]The characteristic exhaust velocity, c^* , is a measure of combustion temperature, and is defined as $P_c A_t / \dot{m}$.

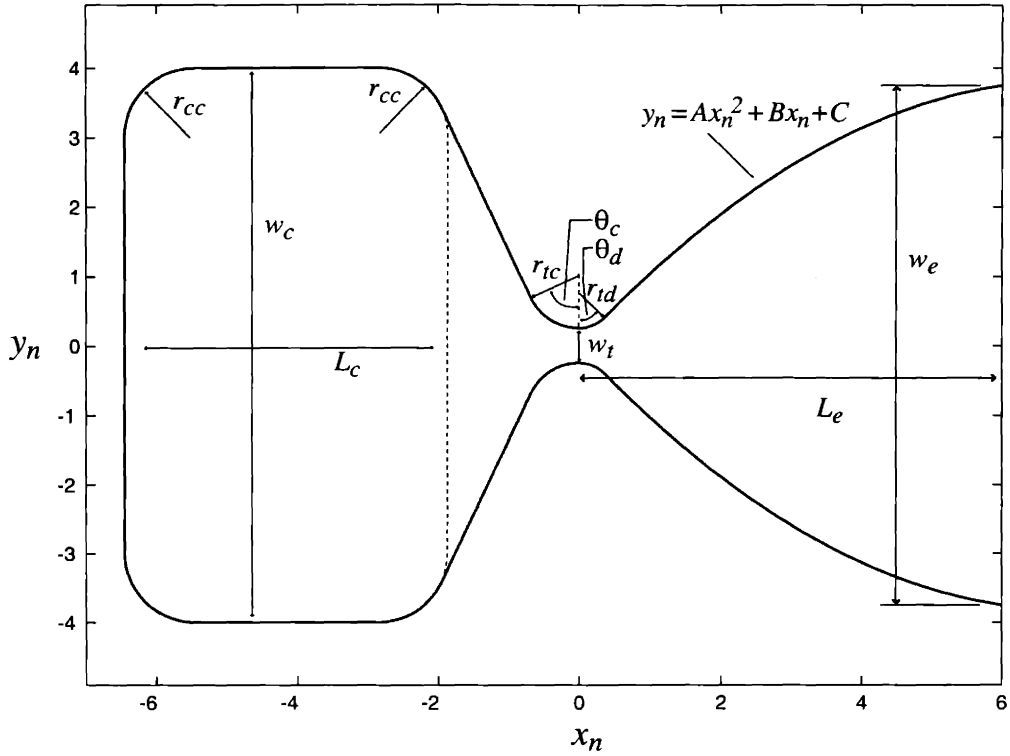


Figure 2-6: The parameters used to define the chamber and nozzle geometry. The baseline shape is pictured, with scale in mm.

by etching of two-dimensional features into wafer surfaces. An example of this is shown in Figure 2-2, an illustration of the chamber and nozzle section of the eventual demonstration microrocket. This shape is then parameterized to provide for a variety of rocket sizes.

The primary parameters of importance are the throat width and height which control the mass flow for a given chamber pressure; the chamber length which controls the combustion residence time; and the expansion ratio of the nozzle which impacts specific impulse and surface area of the expansion section of the nozzle. The full parameterization of the two dimensional rocket shape is presented in Figure 2-6. This shape is then extruded upwards by the throat height.

Table 2.2 presents the values of each parameter for the baseline geometry of the demonstration thrust chamber.

In the scaling study presented later in this chapter, the independent geometrical parameters are w_t , h_t , L_c . The other lengths and nozzle expansion profile are all scaled proportionally

Table 2.2: Chamber and Nozzle parameters and baseline values

Symbol	Description	Value	Symbol	Description	Value
w_t	Throat width	0.5 mm	r_{tc}	Converging throat radius	0.75 mm
h_t	Throat height	1.5 mm	r_{td}	Diverging throat radius	0.5 mm
w_c	Chamber width	8 mm	r_{cc}	Chamber corner radius	1 mm
w_e	Exit width	7.5 mm	θ_c	Chamber convergence angle	65 deg
L_c	Chamber length	4.5 mm	θ_d	Throat divergence angle	45 deg
L_e	Expansion length	6 mm			

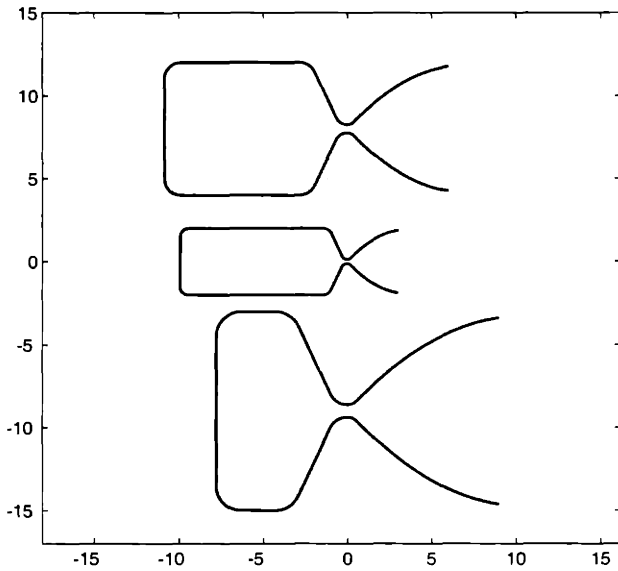


Figure 2-7: Examples of scaled nozzle shapes. Scale in mm. Top: $w_t = 0.5$ mm, $L_c = 9$ mm; Middle: $w_t = 0.25$ mm, $L_c = 9$ mm; Bottom: $w_t = 0.75$ mm, $L_c = 5$ mm.

to w_t , and the two angles are held constant. This allows the different nozzle flows to have the same Mach number in equivalent locations. Three examples of a scaled geometry are presented in Figure 2-7.

2.5.2 Rocket Performance and Mass Flow

The primary measure of performance for a rocket engine is its specific impulse, or I_{sp} . In this chapter and in Chapter 3, the specific impulse in vacuum is used in comparisons between different engine systems. The other performance metric considered is the thrust-to-weight ratio. Again, the vacuum thrust is used in this ratio. For a given chamber pressure and

propellant mixture ratio, the I_{sp} and other flow properties are determined using CEA, a NASA code developed by Gordon and McBride [16]. It has a rocket performance module that allows for adiabatic equilibrium and frozen calculations of rocket flow properties as a function of chamber pressure, propellant mixture ratio, and area ratio.

Rather than perform a new CEA run for each chamber pressure and mixture ratio considered, a large matrix of these runs are pre-computed and combined into a rocket performance database. For the ethanol/oxygen scaling study presented here, the chamber pressures considered are 10, 20, 30, ..., 200 bar, and the oxidizer to fuel mass ratios are 0.8, 0.9, ..., 3.0. The total number of runs in this performance database is then 460. From this matrix, a two-dimension linear interpolation predicts the performance parameters for any intermediate pressures or mixture ratios required by the model.

All of the calculations performed assume equilibrium chemistry up to the throat, and frozen chemistry in the expansion nozzle. Flow conditions are calculated at subsonic area ratios of 16 (the chamber), 13, 10, 5, and 2. Downstream of the throat, conditions are calculated at area ratios of 1 (the throat), 2, 3, 4, 6, 8, 10, 12, and 15 (the nominal exit plane). The flow properties at these discrete area ratios are then interpolated onto locations in the nozzle corresponding to locations of equivalent effective area ratio. This effective area ratio is based on an effective through-flow width, illustrated by the dashed lines perpendicular to the flow direction in Figure 2-8. Examples of the input and output files for a CEA run are presented in Appendix C. Figure 2-9 shows the vacuum I_{sp} for the full range of mixture ratios considered for a number of chamber pressures between 10 and 200 bar.

The results of these calculations are idealized in the sense that they are adiabatic, assume the combustion reactions proceed completely to equilibrium, and do not account for friction effects on the chamber and nozzle walls. The variation in I_{sp} with pressure is therefore due only to the effect of pressure on the equilibrium composition, and not due to its potential impact on the kinetic rates of the combustion reactions. For these reasons, one would expect the eventual performance of a microrocket engine to be lower than the values presented here. Nevertheless, this idealized model will prove valuable in identifying the feasible design space and upper performance limits of micro rocket engines.

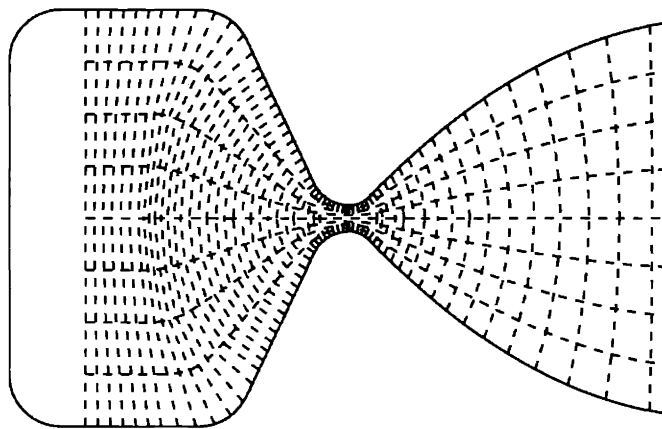


Figure 2-8: The dotted lines perpendicular to the flow direction show the surfaces of constant flow conditions used in the model.

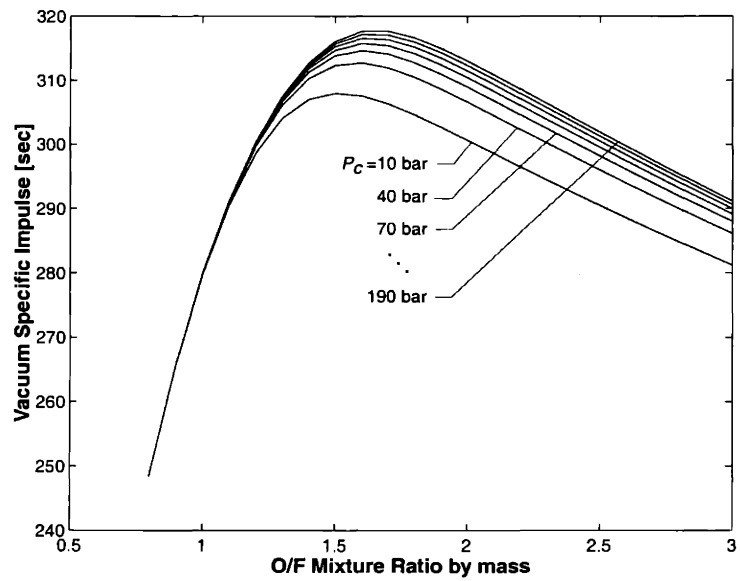


Figure 2-9: Vacuum I_{sp} for oxygen/ethanol combustion as a function of mixture ratio for a number of different chamber pressures.

2.5.3 Combustion Residence Time and Chamber Length

The chamber residence time is an important parameter considered in the design of micro rocket engines. It is defined as:

$$\tau_{res} = \frac{\rho_c V_c}{\dot{m}} \quad (2.1)$$

and corresponds to the average time a particle spends in the combustion chamber. It is worth noting that for a choked nozzle flow, both ρ_c and \dot{m} are directly proportional to P_c , so the residence time is independent of pressure. When calculating the chamber volume, V_c , the chamber is considered that area of the rocket forward (towards negative y -direction) of the dotted line in Figure 2-6. Thus, if the chamber density is known from the flow properties output by the CEA performance simulation discussed above, the chamber length can be written as a function of residence time:

$$L_c = \frac{1}{w_c} \left(\frac{\dot{m}\tau_{res}}{\rho_c h_t} + (4 - \pi)r_{cc}^2 \right) \quad (2.2)$$

This allows for either the chamber length or residence time to be considered the independent variable in the sizing model.

2.5.4 Wall Heat load

The heat load to the wall is estimated by utilizing a heat transfer coefficient, where the heat flux to the wall, \dot{q} , is considered proportional to the difference between the adiabatic wall temperature, T_{aw} , and the actual wall temperature, T_w .

$$\dot{q} = h_g (T_{aw} - T_w) \quad (2.3)$$

The hot side gas heat transfer coefficient, h_g , is generally obtained from empirical correlations. Hill and Peterson[20] suggest three correlations for rocket engine nozzles that are used in this work. These correlations are generally given in terms of non-dimensional parameters, with the Nusselt number, Nu, being the parameter that describes the heat transfer

coefficient:

$$\text{Nu} = \frac{h_g L}{\kappa} \quad (2.4)$$

The first of these correlations, originally based on fully developed turbulent pipe flow, is:

$$\text{Nu}_D = 0.023 \text{Re}_D^{0.8} \text{Pr}^{0.3} \quad (2.5)$$

where for the case of the rectangular cross section of the MicroRocket Thrust Chamber, both Nu and Re are based on D_l , a so-called “laminar” diameter, proposed in [23] to improve the accuracy of turbulent heat transfer correlations in rectangular channels.

$$D_l \approx D_h \left(\frac{2}{3} + \frac{11}{24} \alpha^* (2 - \alpha^*) \right) \quad (2.6)$$

where D_h is the hydraulic diameter, $4A/P$, and α^* is the aspect ratio of the channel.

The second correlation is suggested for use in the supersonic part of the nozzle and is quite similar to that presented above. In this case, Nu and Re are based on L , the “axial” distance downstream from the throat. Here,

$$\text{Nu}_L = a \text{Re}_L^{0.8} \text{Pr}^{0.33} \quad (2.7)$$

where a has a value of approximately 0.025 to 0.028.

For both of these correlations, a decision must be made as to what temperature is used for determining the fluid properties used in the non-dimensional parameters. One option is to use the local static, or bulk temperature, but the traditional choice is to use a film temperature, T_f . Hill and Peterson [20] suggest defining this as $T_f = T_w + 0.23(T_g - T_w) + 0.19(T_{aw} - T_w)$ for the supersonic portion of the nozzle, and as $T_f = (T_w + T_g)/2$ for the chamber and subsonic portion of the nozzle. Both T_f and T were considered, but as can be seen in Figure 2-10, T_f predicts a significantly lower heat flux. Though this would be desirable, the bulk temperature is used to evaluate properties in this work, as it provides a more conservative estimate, given the large uncertainties in predicting rocket heat fluxes.

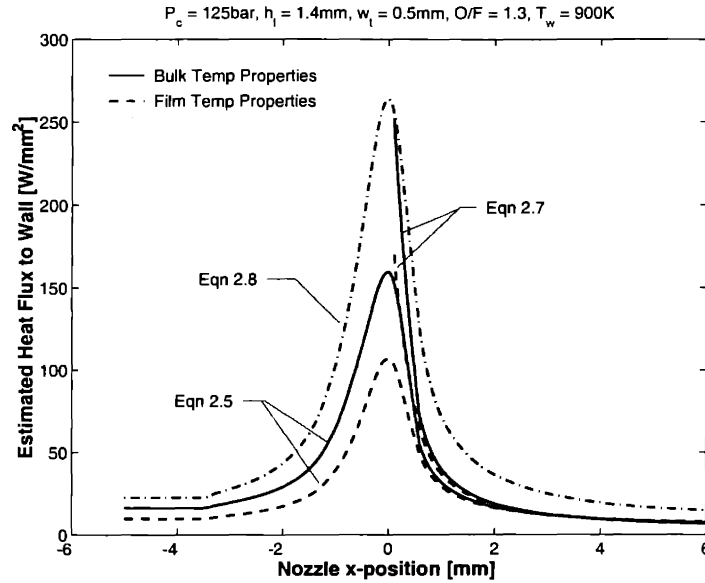


Figure 2-10: The various correlations considered for hot-side heat transfer estimation. The two used in the design are Equation 2.5 with properties evaluated at the bulk temperature (called the nominal heat flux case), and Equation 2.8 (called the high heat flux case).

The third correlation is originally due to Bartz[9], and can be written as:

$$h_g = \left[\frac{0.026}{(D_t)^{0.2}} \left(\frac{\mu^{0.2} c_p}{\text{Pr}^{0.6}} \right)_c \left(\frac{p_c}{c^*} \right)^{0.8} \left(\frac{D_t}{r_t} \right)^{0.1} \right] \left(\frac{A_t}{A} \right)^{0.9} \sigma \quad (2.8)$$

where the subscript c refers to chamber or stagnation conditions, and t to throat conditions. r_t is the radius of curvature of the nozzle wall at the throat, and σ is defined as

$$\sigma = \frac{1}{\left[\frac{1}{2} \frac{T_w}{T_c} \left(1 + \frac{\gamma-1}{2} M^2 \right) + \frac{1}{2} \right]^{0.8-0.2\omega} \left(1 + \frac{\gamma-1}{2} M^2 \right)^{0.2\omega}} \quad (2.9)$$

where ω is the exponent in a power-law viscosity-temperature relationship. ($\mu \propto T^\omega$)

The flow properties provided by the CEA calculation are used to evaluate the local Re and Pr required by the above correlations to produce the estimated h_g . This along with the flow temperature and the input wall temperature determine the heat flux profile, shown in Figure 2-10. Given the large variation in predicted heat fluxes, two cases are considered in the model: a “nominal” case predicted using Equation 2.5 with bulk temperature properties, and a “high” heat flux case, predicted using Equation 2.8.

The heat flux profiles are then integrated over the surface area of the scaled rocket shape being considered to determine the total heat load to the propellants serving as coolant.

2.5.5 Final Coolant Temperature

The final coolant bulk temperature, T_{bf} , is calculated by determining at what temperature the increase in total enthalpy of the fuel and oxidizer equals the total heat load:

$$\dot{m}_{ox}(h_{ox}(T_{bf}) - h_{ox}(T_{bi_{ox}})) + \dot{m}_{fuel}(h_{fuel}(T_{bf}) - h_{fuel}(T_{bi_{fuel}})) = \dot{Q}_{tot} \quad (2.10)$$

where T_{bi} is the initial coolant temperature, which could be different for each propellant. T_{bf} will depend primarily on \dot{Q}_{tot} , but will also depend on mixture ratio. The assumption is made that the propellants are routed in such a way that both absorb the correct fraction of the total heat to have an equal final temperature, as this maximizes the total quantity of heat that can be absorbed into the coolants.

2.5.6 Wall Thicknesses

There are two wall thicknesses that are important in the rocket scaling presented here. The first is that of the chamber capping walls, which contain a pressure of P_c . The second is the thickness of the side cooling channel wall, which must contain the pressure of the coolant.

To first order, the walls of the microrocket can be considered beams (really plates) that are clamped on each side, and subjected to a uniform pressure, as is illustrated in Figure 2-11. The maximum stress for this case is the bending stress at the roots, which can be shown to be:

$$\sigma_{max} = \frac{p}{2} \left(\frac{l_w}{t_w} \right)^2 \quad (2.11)$$

This suggests that the required thickness of the wall will scale as the square root of the pressure it contains, and will be proportional to the span. The wall thicknesses are therefore scaled from reference wall thicknesses determined from a more detailed analysis discussed

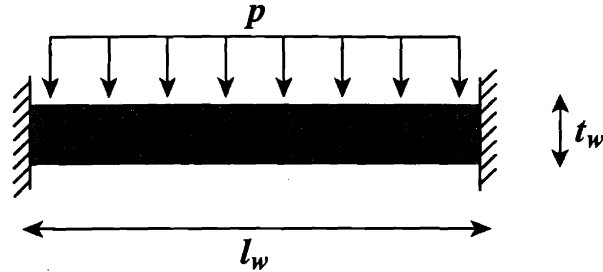


Figure 2-11: A simple model of the thrust chamber and cooling passage walls.

in Chapter 4 as follows:

$$t_w = l_w \left(\frac{t_w}{l_w} \right)_{ref} \sqrt{\frac{P}{f P_{ref}}} \quad (2.12)$$

where in this case, f represents the relative strength of the material and is either 1 for silicon or 0.6 for silicon carbide. The other reference values are presented in the following table:

Reference Quantity	Chamber Wall	Cooling Wall
$t_{w_{ref}}$	650 μm	80 μm
$l_{w_{ref}}$	6 mm	400 μm
P_{ref}	125 bar	300 bar

2.5.7 Dimensions and Mass of Rocket Engine

Based on the chosen inputs for a given rocket engine system, the overall dimensions of the rocket chip are determined. The thickness of the chip is determined by adding the thickness of the chamber wall caps to the height of the extruded nozzle shape. The width of the chip is found by adding a constant extra width to the width of the chamber, and the length of the chip is determined by adding a constant extra length to the overall length of the chamber and nozzle. The extra length and width are to account for plumbing, valves, turbopumps, etc., and therefore the mass determined from this calculation can be considered to be representative of an eventual microfabricated rocket engine in service, less any mass

for interconnects.[§] For this study, the extra width and length are both 5.5 mm.

The net volume of the rocket is determined by taking the volume of the chip as defined by its overall length, width, and height, and subtracting the volume of the chamber and nozzle. This volume is then multiplied by the density of the material of construction (2330 kg/m³ for silicon or 3200 kg/m³ for silicon carbide) to determine the overall rocket mass. This is then used to calculate the thrust to weight ratio.

2.5.8 Rockets Per Wafer Set and Number of Wafers

To provide a sense of the number of rockets that would be produced in a given wafer set, 100 mm wafers are considered. It is assumed that no feature may be closer than 5 mm from the edge of the wafer, and thus a rectangle inscribed in a 90 mm-diameter circle is considered the maximum extent of rocket die. The width of this rectangle is 54 mm, and its length is 72 mm. The number of engines that will fit inside this rectangle is then easily determined. This represents an estimate of the number of devices that can be produced in a given wafer set, though a more careful layout of rockets onto the wafer would likely be performed once a final choice of size has been made to further increase this number.

As was discussed earlier in this chapter, there are three types of wafers in a microrocket engine wafer set: the top and bottom plates, the two wall plates, and the nozzle plates. The number of nozzle plates, and thus the total number of wafers required per wafer set is determined from the number of layers of side cooling channels, n_{sp} . Specifically, the number of nozzle plates is one less than n_{sp} , meaning the total number of wafers is $n_{sp} + 3$. This is illustrated in Figure 2-12 for a n_{sp} of 1 and 3.

2.5.9 Side Cooling Passage Width

The side cooling passages at the throat are one of the critical design locations, and can limit the feasibility of a given design. To address this, the model provides the coolant-side wall

[§]In looking at the pictures of the packaged engines tested in this work shown later in Chapter 5, one might expect that the mass of the interconnects and packaging would dominate the mass of the engine. It is unlikely that this will be the case, as eventual engines should require two low pressure fluid connections, rather than the eleven high pressure ones seen here, and it is likely that a number of engines could share the same set of feed lines.

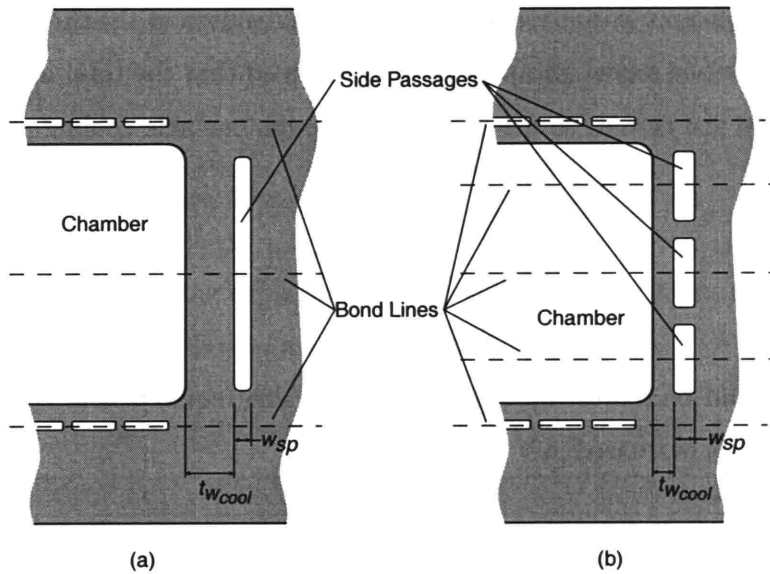


Figure 2-12: Two cross sections with bondlines. The number of wafers required depends on the number of side cooling passages. In (a), there is one side cooling passage, and four wafers are required: two cap plates (top and bottom), and two wall plates. In (b), there are three side passages, and six wafers are required: the four from (a), plus an additional two nozzle plates. Notice that fewer side passages leads to a longer span and therefore a thicker side wall for a given coolant pressure.

temperature and the required cooling passage width at the throat.

The coolant-side wall temperature, T_{wc} is determined simply from the hot-side wall temperature, the cooling passage wall thickness, and the heat flux:

$$T_{wc} = T_w - \dot{q} \frac{t_{w_{cool}}}{\kappa} \quad (2.13)$$

The width of the side cooling passages, w_{sp} , must be tailored to produce a heat flux into the passage equal to the throat heat flux. Without doing a detailed design of the entire cooling system, it is difficult to say what this will be precisely. However, the following approach provides a reasonable approximation of the w_{sp} that is required at the throat, and illustrates its dependence on other model parameters. It is assumed that the total mass flow is evenly distributed around the throat, so the mass flow through one side cooling passage will then be:

$$\dot{m}_{sp} = \dot{m} \frac{h_t}{2(h_t + w_t)} \frac{1}{n_{sp}} \quad (2.14)$$

This mass flow could be either the oxidizer or fuel. The required heat transfer coefficient for each propellant is evaluated as

$$h_{req} = \frac{\dot{q}}{T_{wc} - T_b} \quad (2.15)$$

where T_b is a representative coolant bulk temperature depending on the propellant being considered. In this case, T_b for oxygen is 200 K, and for ethanol is 350 K. The height of the passage is simply $h_{sp} = h_t/n_{sp} - h_{sep}$, where h_{sep} is the distance separating passages, taken to be a constant 0.1 mm in this model. Given the height of the passage, the width of the passage, w_{sp} required to produce h_{req} for each propellant is estimated using the nominal coolant-side heat transfer design correlation discussed in the next chapter:

$$\frac{h_{req} D_h}{\kappa} = 0.025 \text{Re}^{0.8} \text{Pr}^{0.4} \quad (2.16)$$

where w_{sp} influences D_h and Re , and the fluid properties are evaluated at the expected bulk temperature near the throat for the propellant being considered. This leads to a w_{sp}

required for each propellant, both of which are returned by the model.

2.6 Model Results

This section will present the results of the model for two cases considered. The first is an engine of constant size, with a throat area of 0.7 mm^2 and a throat aspect ratio (h_t/w_t) of 3. In this case, the chamber pressure is varied from 15 to 195 bar, illustrating the dependence of the various outputs on chamber pressure. The second case is for a set of engines where the chamber pressure and throat area are held fixed at 125 bar and 0.70 mm^2 , respectively, but the throat aspect ratio is varied from 0.5 to 20. This illustrates the geometrical dependences of the model.

2.6.1 Chamber Pressure Dependence

In the first case considered, the chamber pressure is varied from 15 to 195 bar. The other parameters are held at the fixed values presented in Table 2.3:

Table 2.3: Parameters used in chamber pressure study

Symbol	Description	Value
h_t	Throat height	1.45 mm
w_t	Throat width	0.48 mm
τ_{res}	Chamber residence time	0.1 msec
O/F	Oxidizer to fuel ratio	1.3
T_w	Hot-side wall temperature	900 K
n_{sp}	Number of side cooling passages	3

Performance

As was seen previously in Figure 2-9, there is a relatively small variation of I_{sp} with chamber pressure. It increases from 304.4 sec at $P_c = 15 \text{ bar}$ to 307.2 sec at $P_c = 195 \text{ bar}$. As I_{sp} changes only slightly and A_t is constant, the thrust increases essentially linearly from 1.9 to 24.4 N over the range of P_c considered. The thrust to weight ratio is plotted in Figure 2-13(a), and is seen to increase with pressure as expected. Since the scale is constant, the

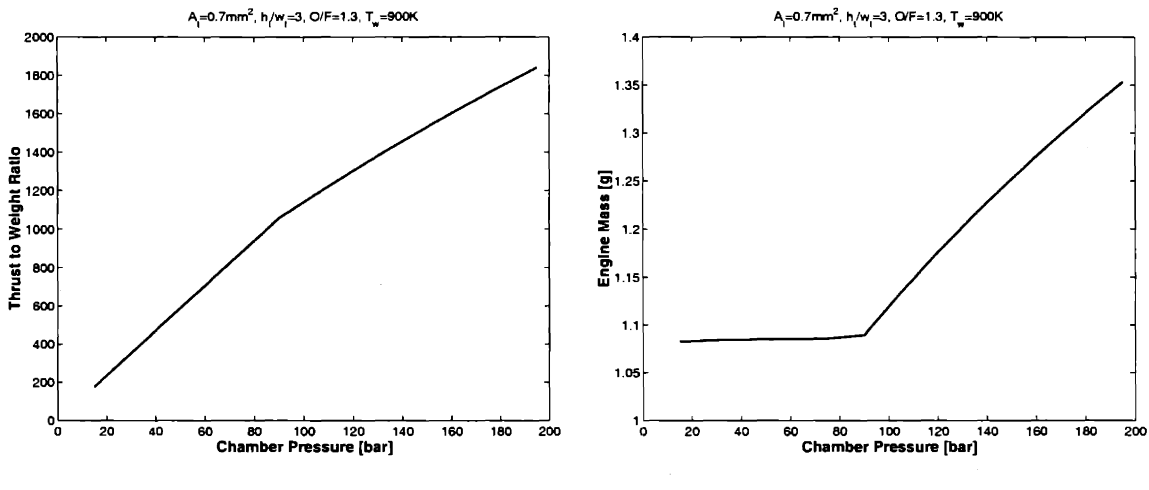


Figure 2-13: Plots of thrust to weight ratio and engine mass as functions of P_c . The engine mass begins to increase once the chamber wall thickness required to contain the pressure exceeds its minimum value, leading to a lower slope in the T:W plot.

mass of the engine is essentially constant, though at high pressure it begins to increase as the chamber wall thickness required to support the chamber pressure begins to exceed the minimum thickness of $500 \mu\text{m}$. As can be seen in Figure 2-13(b), this occurs at $P_c \sim 90 \text{ bar}$, and leads to the lower slope in the T:W vs. P_c curve of Figure 2-13(a).

Size

The length of the engine at this scale is about 17.7 mm, and its width is 13.2 mm. The height is 2.45 mm at low pressure, but increases for pressures above 90 bar to 2.94 mm at 195 bar. As there are three side cooling passages, it requires six wafer layers to manufacture the device, and will yield a total of 16 devices per wafer stack, assuming 100 mm diameter wafers.

⁴Due to the small variation in chamber temperature, a 2% increase in chamber length, from 4.39 to 4.48 mm, is required to maintain $\tau_{res} = 0.1$ msec. This leads to a 0.5% change in length over the pressure range considered.

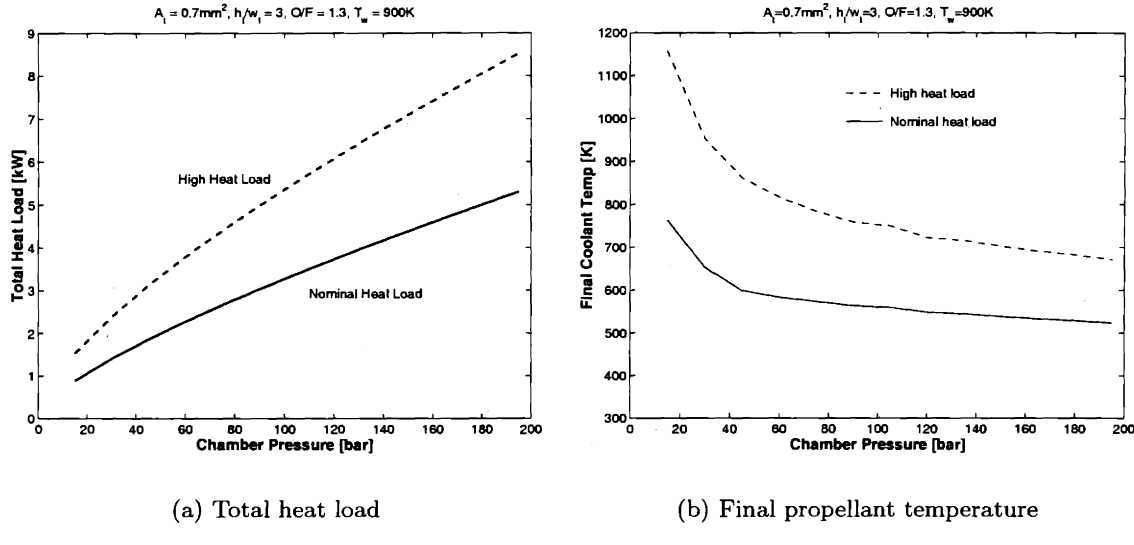


Figure 2-14: Total heat load to walls and final temperature reached by propellants in absorbing it. T_{bf} decreases with increasing P_c because the mass flow rises more quickly than the heat load.

Cooling

The total heat load and corresponding final propellant temperature are shown as functions of P_c in Figure 2-14. The total heat load increases with chamber pressure, but the total mass flow increases more rapidly, leading to a final coolant temperature that decreases with increasing pressure. One can see that for the high heat load case, the calculated T_{bf} exceeds the design wall temperature for pressures below 50 bar, which violates the assumption of a constant hot-side wall temperature, and implies that if the high heat load correlation is accurate, an engine of this size could not operate below that chamber pressure. This is one of the fundamental limitations that is discussed in the next chapter.

The cooling at the throat is another critical factor. The local heat flux here increases from 38 to 221 W/mm² over the range of P_c for the nominal heat load case, and from 66 to 360 W/mm² for the high heat load case. As the hot-side wall temperature remains constant, the cold-side wall temperature decreases with pressure, as is seen in Figure 2-15(a). For the nominal heat load case, the required width for the side cooling passages at the throat is shown in Figure 2-15(b). At some pressure, this width will become too small to be successfully fabricated, and at a slightly higher pressure, the cold-side wall temperature

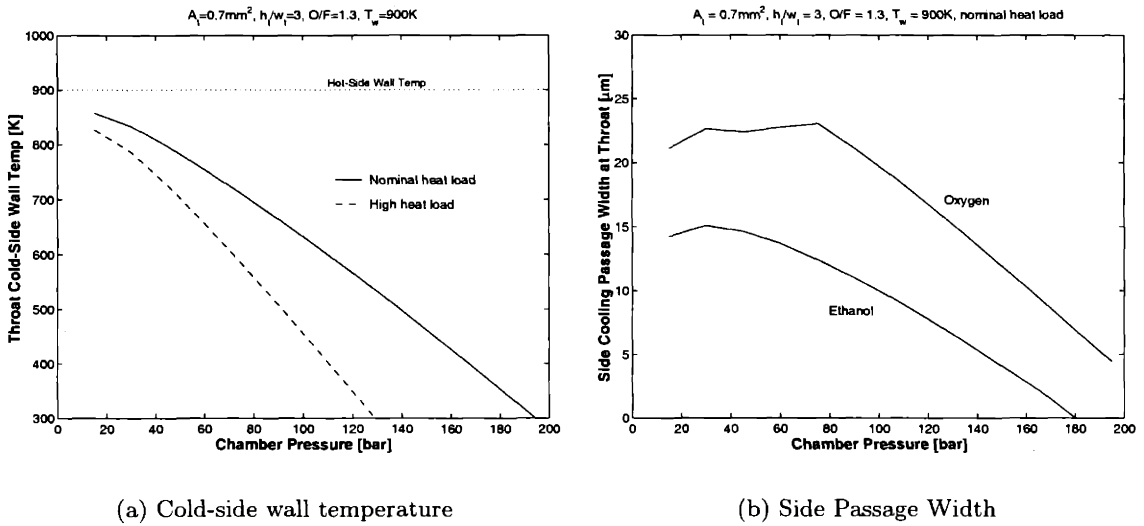


Figure 2-15: Cold-side wall temperature and width of the side cooling passage required to absorb the maximum heat flux at the throat. The side passage width is only plotted for the nominal heat flux.

will be as low as the propellant temperature making cooling the throat impossible. This is another limitation discussed in the following chapter.

2.6.2 Geometry Dependence

In the second case considered, all parameters are held fixed except for the throat height and width which are varied in such a way as to provide the same throat area as in the previous case, but at a variable throat aspect ratio. The aspect ratios considered range from 0.5 to 20. The fixed parameters are presented in Table 2.4.

Table 2.4: Parameters for geometry study

Symbol	Description	Value
P_c	Chamber pressure	125 bar
w_t	Throat area	0.70 mm ²
τ_{res}	Chamber residence time	0.1 msec
O/F	Oxidizer to fuel ratio	1.3
T_w	Hot-side wall temperature	900 K
	Average wafer thickness (used to calculate n_{sp})	500 μ m

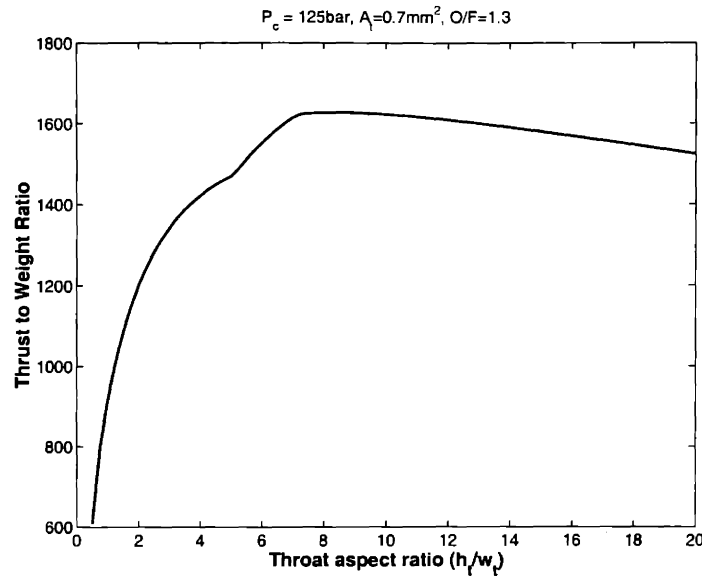


Figure 2-16: Thrust to weight ratio as function of throat aspect ratio. The thrust is constant, so the maximum corresponds to a minimum mass at $h_t/w_t \sim 8$.

Performance

Because the chamber pressure, throat area, and O/F ratio are all constant, the mass flow, I_{sp} , and thrust are also constant. For these parameters, the thrust is 15.7 N at a mass flow of 5.2 g/sec and I_{sp} of 306.9 sec. The mass of the engine varies considerably, leading to a thrust to weight ratio which has a maximum value at $h_t/w_t \sim 8$ for this case, as can be seen in Figure 2-16. The next section will discuss the reasons for this mass dependence.

Size

The throat height and width are shown in Figure 2-17(a). Since the nozzle width and length scale with the throat width, the overall chip length and width also decrease as the throat aspect ratio, h_t/w_t , increases, as seen in Figure 2-17(b). The chip height is the (increasing) throat height plus twice the (relatively constant) chamber top wall thickness, leading to a shallow minimum in mass of approximately 1 g, as seen in Figure 2-17(c). The changes in chamber capping wall thickness seen in Figure 2-17(d) are due to a changing span length

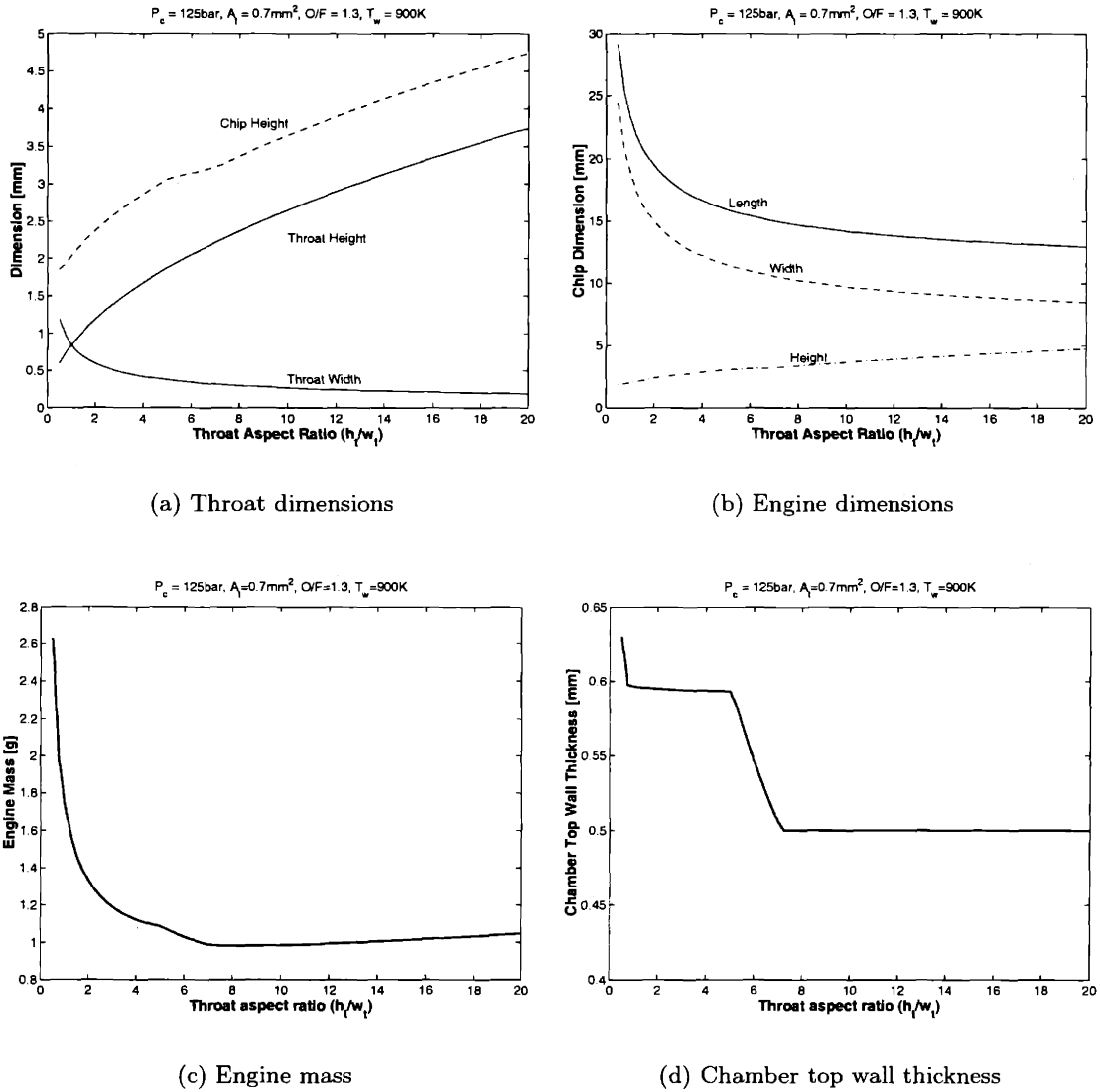


Figure 2-17: Size parameters as a function of throat aspect ratio. The throat dimensions in (a) lead to the scaling of the overall width and length and height in (b), which in turn determine the total mass in (c). The variations in chip height beyond the increase from h_t are from the chamber top wall thickness, shown in (d).

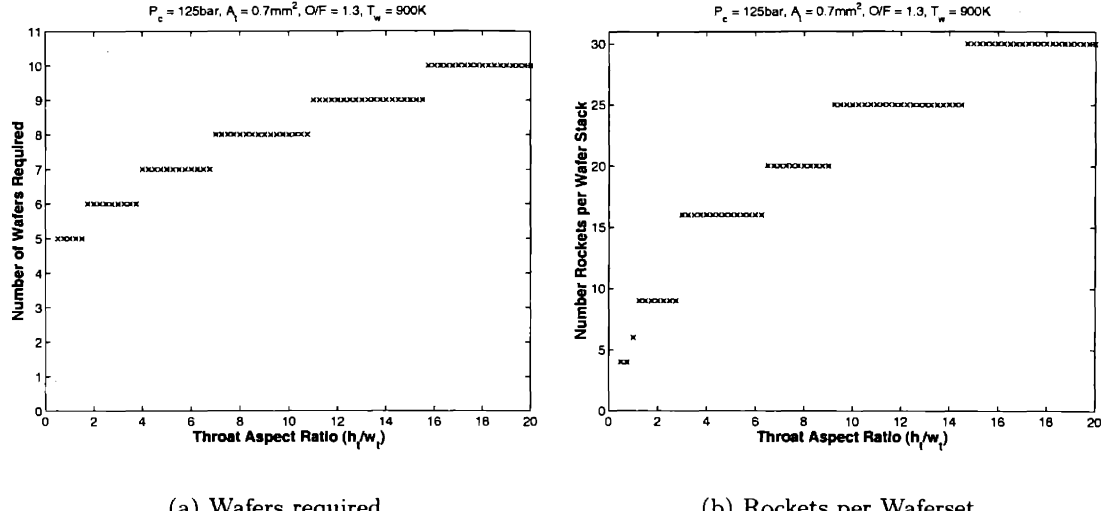


Figure 2-18: As an average wafer thickness is set at $500\text{ }\mu\text{m}$, the number of wafers required increases as h_t increases (a). Since the total area required per engine is greatly reduced as w_t is reduced, the number of rockets per wafer set increases (b).

for the wall. Initially, the minimum chamber length is longer than is needed^{||} to produce a $\tau_{res} = 0.1$ msec, so the chamber span decreases as w_t decreases until L_c reaches the value needed to produce this design residence time. At this point, L_c is less than w_c and remains the controlling span length while w_c continues to decrease with w_t . Eventually, w_c becomes small enough to become the controlling span length, and the chamber wall thickness decreases until it reaches its minimum value of $500\text{ }\mu\text{m}$.

As the total height increases from 2 to 4.5 mm, the number of wafers required to fabricate these rockets increases from 5 to 10 (Figure 2-18(a)). However, the yield per wafer stack increases from 4 to 30, as the lateral extent of the rockets decreases (Figure 2-18(b)). In this case, the number of wafers required was calculated based on an average wafer thickness. If that thickness was allowed to increase, the number of required wafers would decrease as well, but this would lead to a longer span for the side cooling passage walls, making them thicker, which in turn would cause problems for the throat cooling discussed below.

^{||}Based on the model for the nozzle geometry (see Figure 2-6), $L_c \geq 2r_{cc}$, and $r_{cc} \propto w_t$, so if w_t is large enough, the minimum chamber volume may be larger than that required to produce the desired τ_{res} .

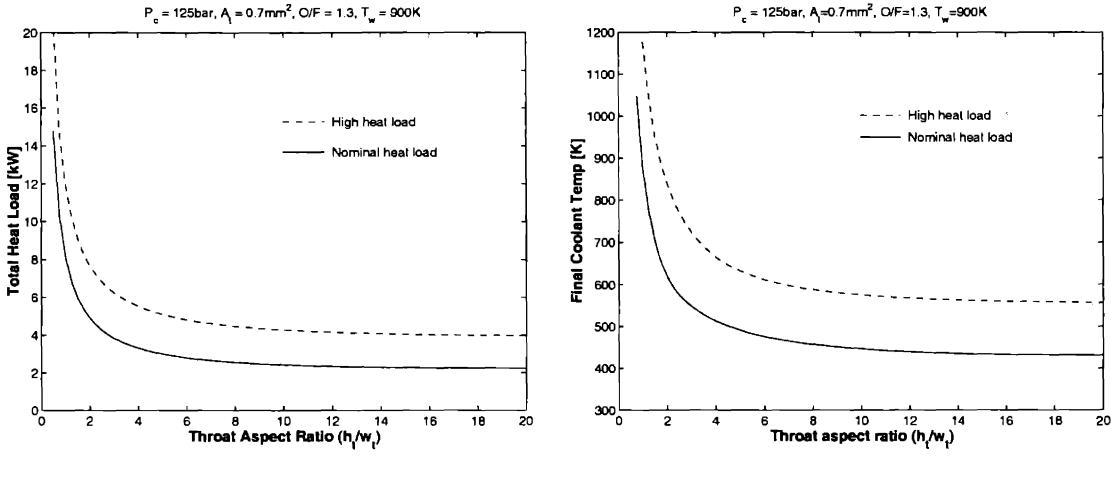


Figure 2-19: Because the top and bottom internal surface area scales with w_t^2 , the total heat load decreases with increasing h_t/w_t . Since the mass flow is constant, T_{bf} decreases as well.

Cooling

The total heat load and corresponding final propellant temperature are shown as functions of throat aspect ratio in Figure 2-19. The total heat load decreases rapidly as the total internal surface area is decreased, since the top and bottom areas scale as w_t^2 . Since the mass flow is constant, the final propellant temperature shows a corresponding decrease. One can see that for h_t/w_t below 1 or 2, the calculated T_{bf} exceeds the limiting wall temperature of 900 K, violating the design assumption. This means that an engine operating at these conditions would not function, and implies that for a given thrust level, there will be a minimum feasible h_t/w_t .

The local heat flux at the throat is shown in Figure 2-20 as a function of h_t/w_t . It has a minimum at $h_t/w_t = 1$, where the equivalent diameter of the throat cross-section is maximized. As the aspect ratio increases and w_t gets smaller, the equivalent diameter decreases as well, leading to a predicted nominal throat heat flux that increases from 150 to nearly 200 W/mm² over the range of h_t/w_t considered.

This higher heat flux leads to a lower cold-side wall temperature and makes cooling the throat more difficult. This is illustrated in Figure 2-21, which shows both the cold-side

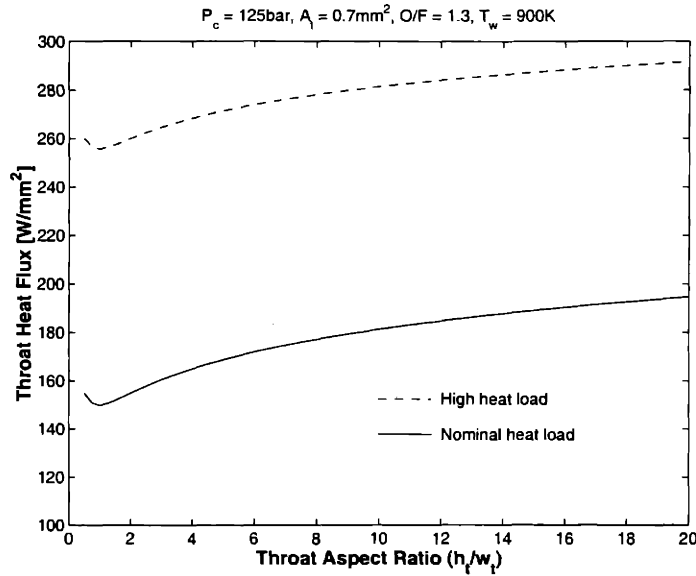


Figure 2-20: Throat heat flux as a function of throat area ratio. As the throat area ratio increases, the effective diameter decreases, leading to an increase in local heat flux.

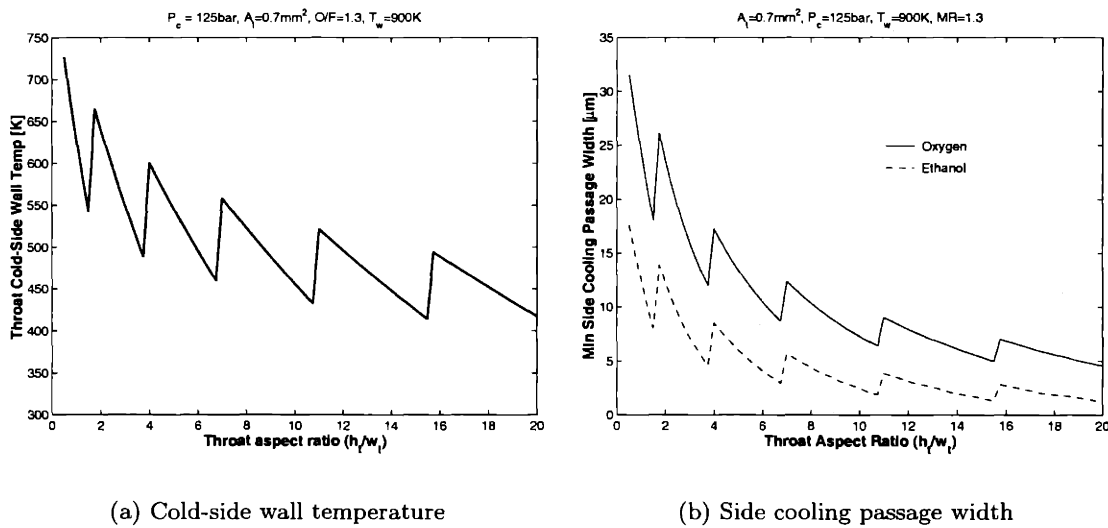


Figure 2-21: Plots of cold-side wall temperature and required width of side cooling passages at the throat. Both are for the nominal heat flux case. The jumps correspond to steps in the number of wafers, which then decrease the span of the cooling walls, allowing them to be thinner and decreasing the temperature drop across them.

wall temperature and the required width of the side cooling passages as functions of the throat aspect ratio. The jumps in the plot correspond to when the number of wafers is incremented, increasing the number of layers of side cooling passages by one. This allows the cooling channel walls to have a shorter span, which means they can be thinner, and leads to a reduction in the temperature drop across them. This explains the importance of using relatively thin wafers, mentioned previously. Though it would be possible to construct a rocket using fewer wafers, the fabrication limitation of etch width and trench aspect ratio would be encountered at a much lower h_t/w_t . This can be seen extrapolating one of the early segments of the curve in Figure 2-21(b) to higher h_t/w_t , without allowing it to jump to the curves corresponding to increasing numbers of wafer layers.

2.7 Summary

This chapter has presented the components of a model developed to predict the performance and physical size of microrocket engines, given a set of inputs that a designer would have to choose from. It then presented the results generated by this model for two case studies. In the first case, the dependence of microrocket performance on chamber pressure was investigated by varying the chamber pressure while the geometry of the device was held essentially constant. In the second case, the dependence on geometrical parameters was investigated by holding the pressure, thrust, and mass flow constant, while varying the throat aspect ratio.

For a constant geometry, as the chamber pressure increases, the following was noted:

1. Mass flow, thrust, and thrust-to-weight ratio all increase nearly linearly.
2. Total heat load increases, but at a smaller rate than mass flow, leading to a decrease in final propellant temperature.
3. The cold-side wall temperature at the throat decreases rapidly, leading to an decrease in the required width of the side cooling passages at the throat.

For a constant chamber pressure and throat area, the following was noted as the throat aspect ratio is increased:

1. Initially the engine mass falls quickly, but then reaches a shallow minimum, corresponding to a maximum in thrust-to-weight ratio.
2. Initially, the total heat load and final propellant temperature both decrease rapidly as the top and bottom surface area are reduced through scaling, but they appear to level out as h_t/w_t is increased further.
3. The heat flux at the throat increases due to the decrease in the effective diameter of the throat cross section. This leads the cold-side wall temperature at the throat to decrease, with a corresponding decrease in the required width of the side cooling passages at the throat.

In the next chapter, the model presented here will be used to make a more explicit definition of the constraints and limitations of microrocket design. The feasible design space of such engines will be explored, and a baseline design will be chosen for further development.

CHAPTER 3

FEASIBILITY AND TECHNOLOGY LIMITS

3.1 Introduction

In the previous chapter, a model for the performance of microrocket engines was developed. In this chapter, this model is used to explore the feasible design space of these engines. Again, the propellant combination considered is liquid oxygen and ethanol. A number of potential constraints on the design are identified, and then combined to form the concept of a feasible specific impulse envelope. This is a plot of how the achievable specific impulse, or I_{sp} , varies as a function of chamber pressure for a given engine geometry. For most geometries, there appears to be a pressure at which the achievable I_{sp} is maximized. It is worth noting that this is an idealized I_{sp} that it is calculated assuming equilibrium combustion in the chamber.* At low pressure, the I_{sp} is limited by the final propellant temperature, and at high pressures it is limited by the width of the side cooling passages that can be etched. The I_{sp} envelope is seen to expand and contract as the parameters that define the geometry are varied, which leads to a decision as to the baseline design parameters for the present study. Finally, it is shown that once the technology exists to manufacture a microrocket from silicon carbide, the feasible I_{sp} envelope will expand significantly, even reaching its ideal maximum extent in a number of cases.

*This means that there would be an additional dependence of I_{sp} on pressure if the residence time is too short for the reaction to come to equilibrium, since reaction rates increase with pressure. One of the primary goals of the experimental section of this work is to evaluate the importance of this effect.

3.2 Performance Metrics

The two performance metrics considered in the evaluation of possible rocket systems are the vacuum specific impulse (a measure of the fuel efficiency of the rocket engine), and the thrust to weight ratio. At a mission level, the I_{sp} determines how much propellant is required to perform a given mission, and the thrust-to-weight ratio, or T:W, determines how much mass must be allocated to the propulsion system to produce the necessary thrust levels.

In this case of this study, the I_{sp} is chosen as the more important parameter, and much of this chapter presents how it can be maximized. In most cases, a tradeoff exists, and the T:W can be increased at the expense of I_{sp} . However, at the pressures being considered, the T:W is almost always more than an order of magnitude larger than current high-performance large-scale rocket engines, which is sufficient in most applications to gain most of the advantages that come from high T:W engines.[†]

3.3 Physical Constraints on Design

There are at least four physical constraints on the design of the rocket system that will be discussed in the rest of this section:

1. Residence Time Limit: There is a minimum time required for combustion to take place to completion, releasing the propellants stored chemical energy. There are two parts to this process: the mixing of the propellants and the actual chemical reactions between fuel and oxidizer that release the energy, both of which must occur to completion to maximize potential performance. This means the propellants must spend a certain quantity of time in the combustion chamber, and leads to a minimum required chamber volume.
2. Maximum Heat Flux Limit: Since the design goal is to have the hot-side wall temperature remain constant, and the temperature drop through the wall is proportional to

[†]If one assumes that a current engine has a T:W of 60, 90% of the engine mass can be saved by increasing the T:W to 600, but only an additional 7% is saved by increasing it further to 1800.

the heat flux, the cold-side wall temperature will be lower in areas with large local heat flux. If the heat flux is high enough, the cold-side wall temperature corresponding to the design hot-side wall temperature will drop below the coolant bulk temperature, making cooling impossible. This implies a maximum allowable heat flux.

3. Total Heat Load Limit: In keeping the walls below their structural failure temperature, there is a limit to the temperature the propellants, acting as coolants, can be heated. This temperature must be less than the design wall temperature, and sets the total allowable heat load to the walls.
4. Maximum Pump Pressure Limit: In an expander cycle, the power used to drive the pumps that pressurize the propellants comes from the energy deposited in the propellants while they are cooling the walls. This energy, equivalent to the total heat load, sets a maximum feasible pump exit pressure.

3.3.1 Maximum Heat Flux

At high chamber pressures, the maximum heat flux limit becomes the primary constraint on system performance. As the chamber pressure increases, the total mass flow, and thus local heat flux, increases as well. At the same time, the pressure in the cooling jacket must also be rising to remain at the same multiple above the chamber pressure, necessitating a thicker cooling passage wall to contain this pressure. Either effect would lead to an increase in the temperature drop through the wall, but as both are occurring at once, an even larger temperature drop results. Figure 3-1 shows the cold-side wall temperature, T_{wc} , at the throat location, and how it decreases with increasing chamber pressure. It also shows how increasing O/F leads to a lower T_{wc} . If T_{wc} were to reach the bulk temperature of the coolant at the throat (about 250K for oxygen or 350K for ethanol) cooling would no longer be possible. In practice, this would never happen, as the hot-side wall temperature would increase enough so that the cold-side temperature was high enough to deliver the heat flux to the coolant. This increase in temperature of the hot-side wall would quickly lead to failure of the wall. As an example, if the design T_w is 900 K, and the coolant enters at 300 K, the maximum allowable temperature drop through the wall is about 500 K, which for a 100 μm thick wall with an average thermal conductivity of 40 W/mK, leads to a

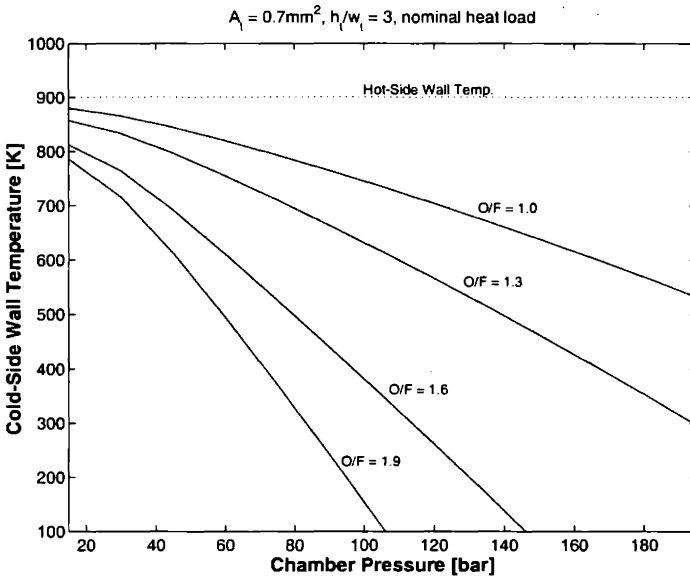


Figure 3-1: The cold-side wall temperature decreases as chamber pressure increases. Once the wall temperature reaches that of the coolant, cooling is no longer possible.

maximum allowable heat flux of 200 W/mm².

Choosing the limit as that point where T_{wc} equals the coolant bulk temperature, T_b , assumes that an infinite heat transfer coefficient can be generated. As this is clearly impossible, this constraint is perhaps better cast in terms of the width of the side cooling channel that is needed to produce a heat flux into the coolant equivalent to the throat heat flux at the wall to coolant temperature difference ($T_{wc} - T_b$) available. Figure 3-2 shows this width, assuming oxygen is cooling the sidewalls. Fabrication constraints on etching deep trenches limit this width to around 10 μm , meaning that in order to have a high chamber pressure, and thus high T:W, the mixture ratio will have to be lowered to yield a lower local throat heat flux.

It is worth noting that it may be possible to ease this fabrication constraint somewhat by increasing the local heat transfer coefficient, as is done in the current work for the demonstration thrust chamber using turbulators and pin-fins (This is discussed in Chapter 4). The cold-side wall temperature equaling the bulk coolant temperature remains a hard limit, however.

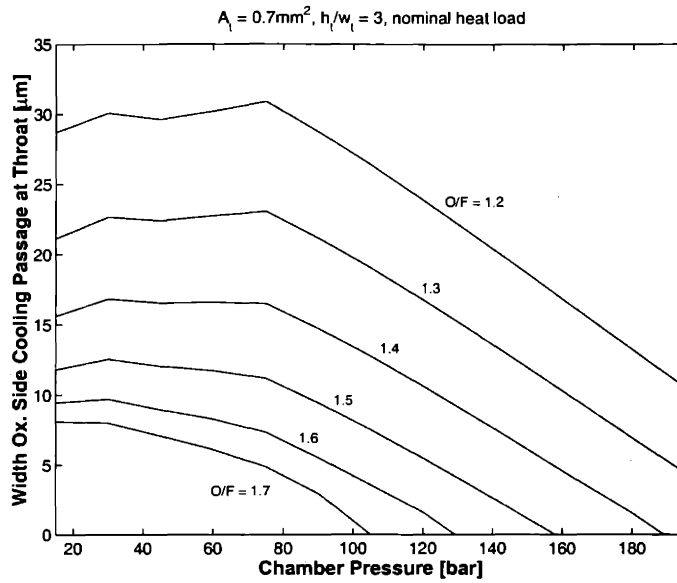


Figure 3-2: The required width of the side cooling passages decreases as chamber pressure increases. Fabrication abilities limit the minimum width of a passage that can be etched to approximately $10 \mu\text{m}$.

3.3.2 Total Heat Load

The total heat load is best represented by the final bulk temperature to which the propellants are heated while absorbing it, T_{bf} . Figure 3-3 plots this as a function of mixture ratio for a number of pressures. One can see that T_{bf} —and therefore the total heat load—depends strongly on mixture ratio. This effect appears to be due primarily to two factors. The first is an increasing thermal conductivity of the gas as the mixture ratio, and therefore the chamber temperature, is increased. The second is the increase in chamber temperature itself.[†] Also, one can see that as the pressure increases, T_{bf} decreases. This is because the heat flux scales as $P_c^{0.8}$, while the mass flow scales directly with P_c . Thus, at higher pressures, there is more mass flow available per unit of total heat load, and the propellants do not need to be heated as much to absorb it. For this reason, the limitation on total heat load will be more important at low pressures. One can see that if T_{bf} is limited to 700 K, the O/F ratio must be kept below about 1.3 for $P_c \approx 30$ bar, but can be as high as 1.6 for $P_c \approx 200$ bar.

[†]See Figure 3-14 and Section 3.6 at the end of this Chapter for a further discussion of this effect.

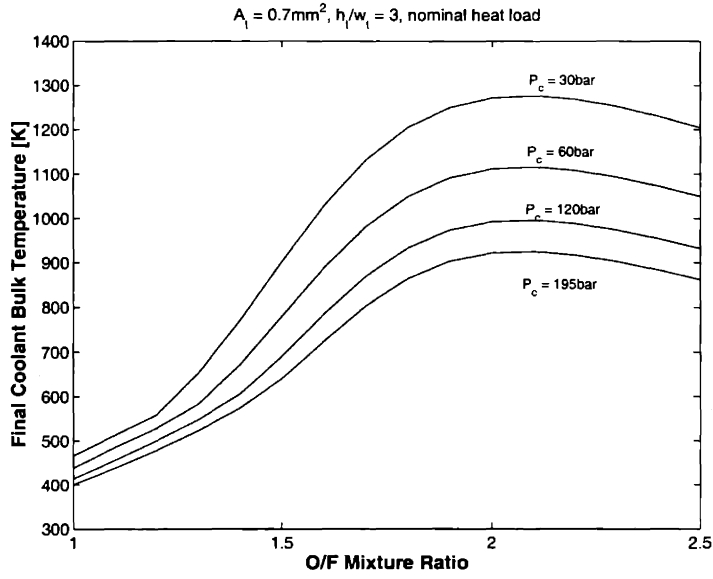


Figure 3-3: The total heat load (and thus final coolant temperature) depends strongly on mixture ratio, but decreases with increasing chamber pressure (or mass flow).

3.3.3 Residence Time

The chamber volume must be large enough to provide sufficient residence time for the propellants to react fully. It is difficult to accurately predict this time, and therefore it is not explicitly used as a constraint in the present model. Instead, the residence time is considered an input used to size the chamber, and the baseline value is chosen based on the work of Al-Midani [1]. It is nevertheless instructive to consider how a residence time constraint would interact with other limitations and parameters.

If one assumes that the chamber will always be made large enough to provide sufficient residence time, the physical mechanism that will limit the feasibility in this case is simply the total heat load constraint discussed above. This is because about half of the total heat load comes from the chamber, so increasing the residence time (and therefore the internal surface area of the chamber) will increase the total heat load as well. This implies that for a given pressure and mixture ratio, there is a maximum achievable residence time.

Al-Midani [1] performed a kinetic calculation for oxygen and ethanol combustion assuming a perfectly stirred reactor model, and estimated the kinetic time as approximately 5 μsec at $P_c \sim 100$ bar. To provide additional time for mixing and transport of the propellants, the

baseline chamber residence time was chosen to be approximately 100 μ sec. Although the estimation of reaction rates at these pressures and temperatures is notoriously inaccurate, this suggests that the residence time may not be a limiting factor in the feasibility of a microrocket system. The experimental results presented in Chapters 7 and 8 appear to support this conclusion.

3.3.4 Maximum Pump Pressure

The pump pressure limitation is not an important constraint on this system, as can be seen in Figure 3-4. In a manner similar to the final coolant temperature, the feasible pump delivery pressure decreases as chamber pressure increases. This would imply that there is some pressure above which the system is not feasible. In practice however, other limitations become important before this point is reached, specifically the limitation on maximum heat flux. Specifically, in the case of Figure 3-4(a), the maximum heat flux constraint limits the acceptable O/F to no more than about 1.2, and one can see that this leaves a large margin of available pressure rise. Figure 3-4(b) shows that this remains true even when the total available energy is reduced by increasing the throat aspect ratio to reduce the internal wall surface area of the rocket and thus the total heat load available for pumping.

3.4 Feasible Specific Impulse Envelope

In the two case studies presented in the previous chapter, the mixture ratio was assumed to be constant. In fact, for a given geometry, a designer is free to choose both chamber pressure and the mixture ratio. Figure 3-5 shows contours of specific impulse (I_{sp}), thrust to weight ratio (T:W), final coolant temperature (T_{bf}), and side cooling passage width (w_{sp}) for a geometry similar to the baseline case identified later. It is clear that to maximize I_{sp} , one would want a high chamber pressure and a mixture ratio near 1.65. The constraints mentioned above make this an impossibility, leaving only the shaded region as a feasible operating range.

As one moves along the boundary of this feasible operating range, the maximum achievable I_{sp} at each pressure can be determined. This is then plotted, as in Figure 3-6, to show the

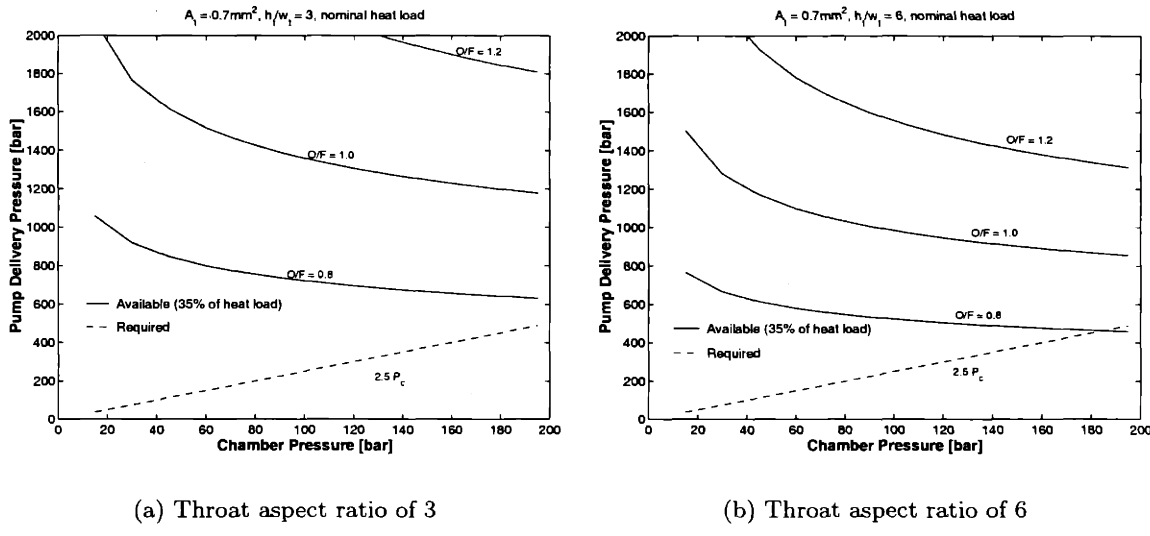


Figure 3-4: Plots of achievable pressure rise, assuming 35% of heating power is used to pressurize. O/F ratios expected in the device are almost always larger than 1.2, showing that the pump pressurization constraint will not be a large factor in these systems.

maximum achievable I_{sp} as a function of pressure. The final coolant temperature constraint limits I_{sp} at low pressures, and the minimum side cooling passage width constraint limits it at high pressures. The feasible I_{sp} envelope is simply the combination of these two constraints and the ideal I_{sp} . This envelope is illustrated in Figure 3-6 for the two constraints used throughout this chapter, namely that T_{bf} cannot exceed 700 K, and that w_{sp} must be larger than 10 μm .

For the rest of this section, the dependence of the feasible I_{sp} envelope on a number of variables will be discussed.

3.4.1 Dependence on throat aspect ratio

In the previous chapter, increasing the throat aspect ratio (h_t/w_t) reduced the total heat load, but increased the throat heat flux. This is seen in Figure 3-7 which shows the feasible I_{sp} envelopes for a number of throat aspect ratios. As h_t/w_t is increased, the I_{sp} boundary shifts to the left on the plot. The peaks of the feasible I_{sp} envelopes are relatively constant,[§]

[§]The I_{sp} at these peaks varies by about 3.5 sec for the range of h_t/w_t considered, with a largest value of 313.5 at $h_t/w_t = 3$ for the nominal heat load case and 304.5 at $h_t/w_t = 6$ for the high heat load case.

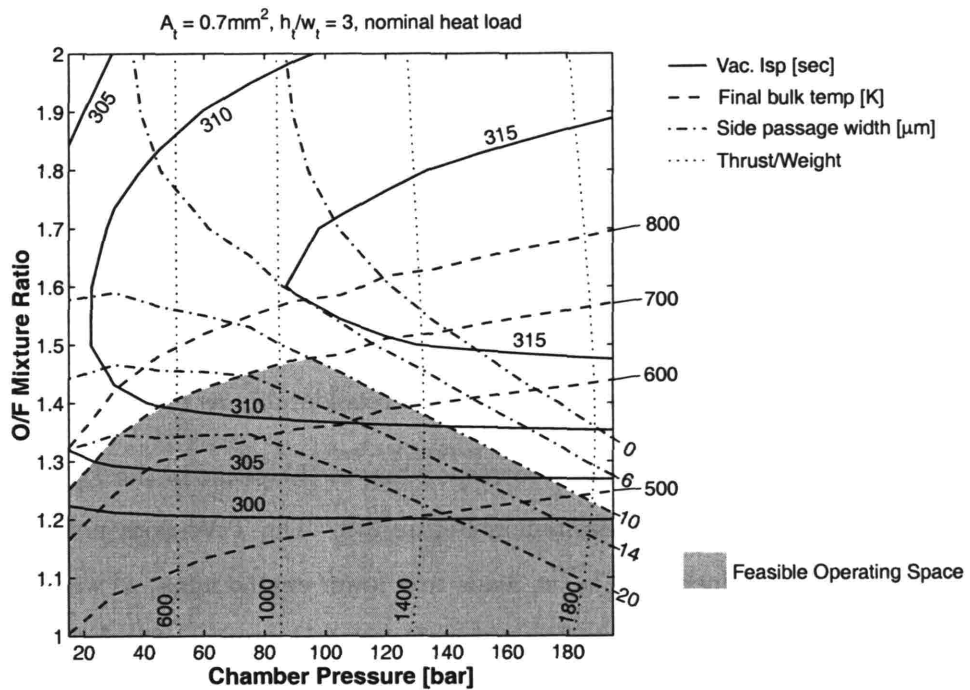


Figure 3-5: Contours of I_{sp} , T:W, T_{bf} , and required w_{sp} for an engine geometry similar to the baseline design. T_{bf} must be less than approximately 700K, and current fabrication technology limits w_{sp} to no less than 10 μm . This leaves a feasible operating space only in the shaded region of the plot, resulting in an achievable I_{sp} below the theoretical maximum. The maximum achievable I_{sp} is approximately 312 sec, at a chamber pressure near 100 bar. A w_{sp} of zero is the point where T_{wc} equals the local bulk temperature of the coolant.

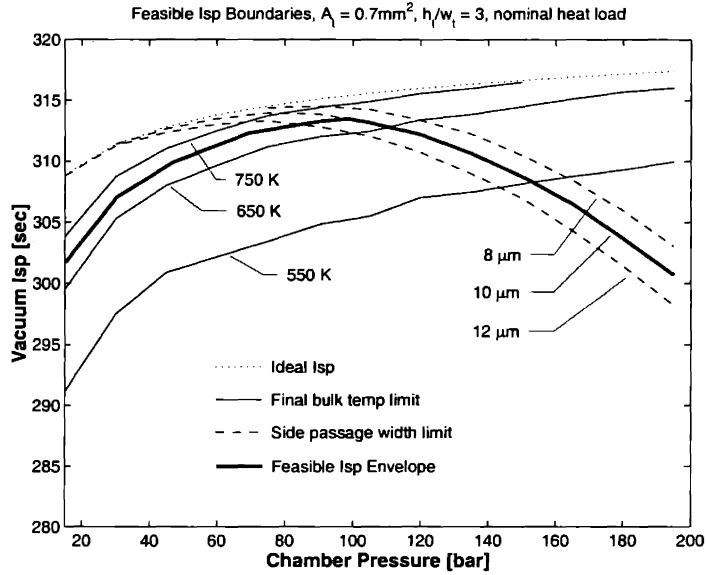


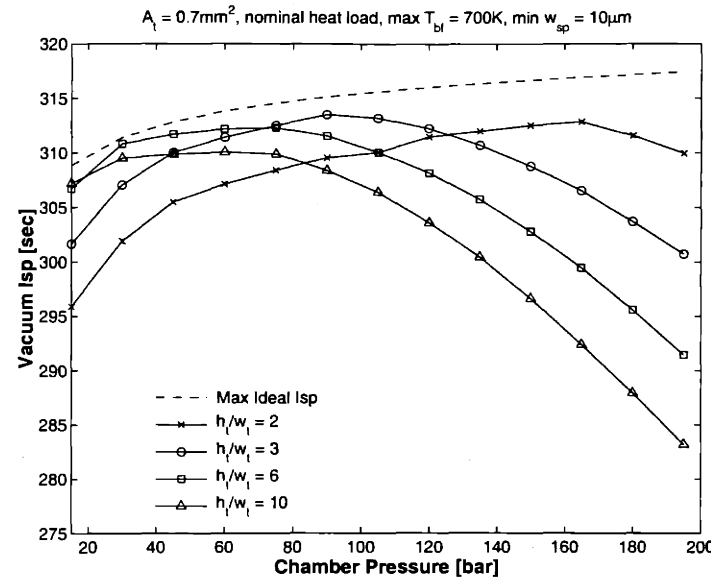
Figure 3-6: The two constraints are combined to define a feasible I_{sp} envelope as a function of chamber pressure for a given geometry.

though the P_c at which these peaks occur decreases considerably as h_t/w_t is increased.

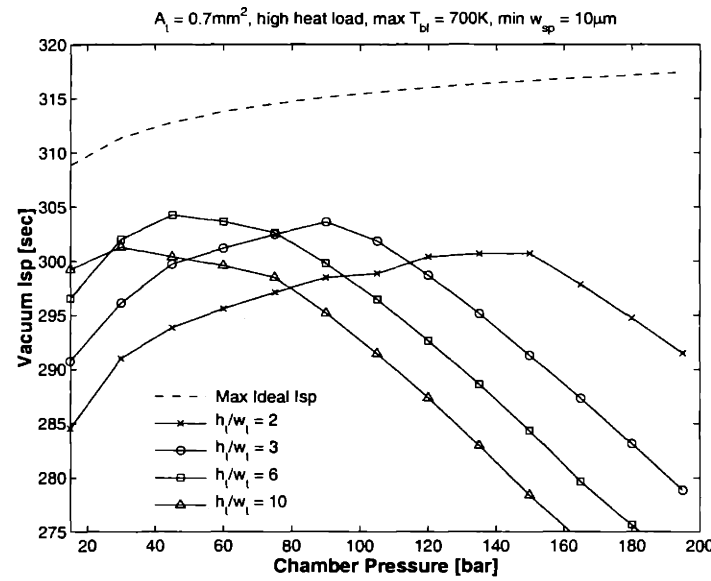
Performance and fabrication parameters corresponding to the peaks in the I_{sp} envelope for the nominal heat load case are presented in Figure 3-8. The T:W does not decrease as quickly as P_c because the increased h_t/w_t leads to a lower engine mass, as was seen in the previous chapter. As expected, the devices per wafer set and number of wafers required for fabrication both increase with h_t/w_t . It is likely that one would accept the 30% lower T:W that comes from moving from a h_t/w_t of 2 to 3 in order to nearly double the number of rockets that fit on a wafer set, from 9 to 16, particularly as this does not change the number of wafers required for fabrication.

3.4.2 Throat Area

In the previous chapter, the only geometry dependence considered was varying the throat aspect ratio. It is important also to consider the overall size of the engine, which is best characterized by the throat area, A_t . Figure 3-9 shows how the feasible I_{sp} envelope enlarges with increasing A_t for $h_t/w_t=3$. For the nominal heat load case, the chamber pressure at which the I_{sp} peaks is essentially constant until the envelope expands to reach the ideal



(a) Nominal Heat Load



(b) High Heat Load

Figure 3-7: The peak achievable I_{sp} occurs at decreasing pressures as the throat aspect ratio increases. For the nominal heat flux correlation, the maximum I_{sp} appears to occur near $h_t/w_t = 3$.

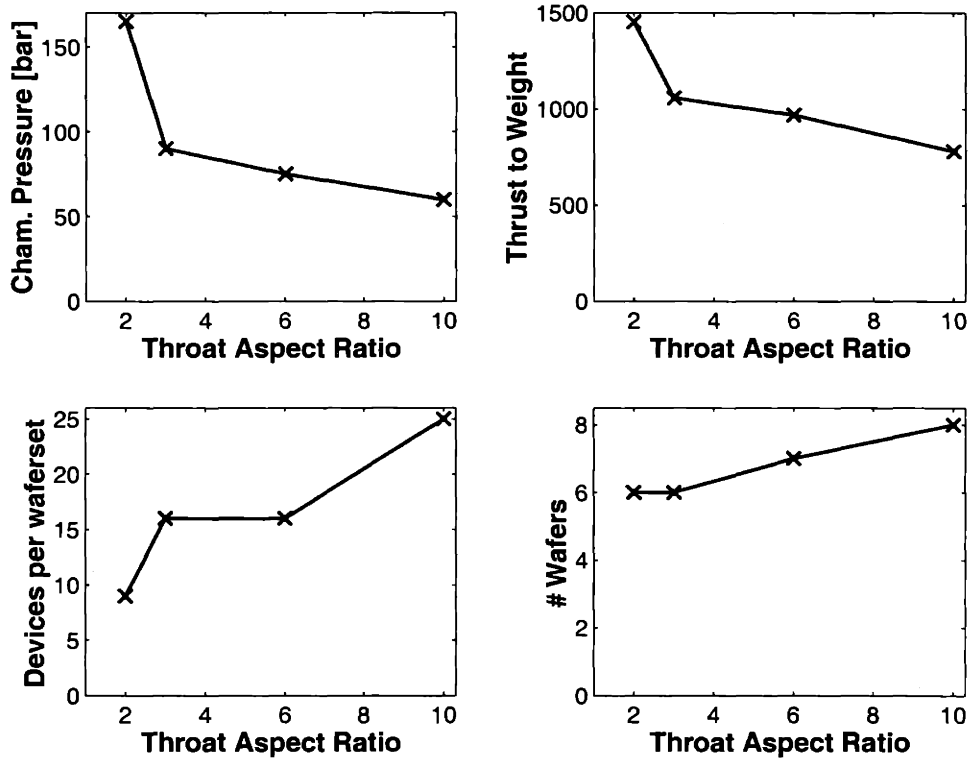


Figure 3-8: Values of model output parameters at the peaks in the four I_{sp} envelopes for $h_t/w_t = 2, 3, 6, 10$. The chamber pressure at which this peak occurs decreases as h_t/w_t increases. Since a larger h_t/w_t also leads to a lower engine mass, T:W decreases to a lesser degree than P_c . Moving from a h_t/w_t of 2 to 3 leads to a 30% reduction in T:W, but yields nearly double the number of devices per wafer set while maintaining the same number of wafers required for construction. All points are for the nominal heat load case.

limit. At this point, both the peak feasible I_{sp} and the chamber pressure at which it occurs will continue to increase with A_t , moving to the right on the ideal I_{sp} curve.

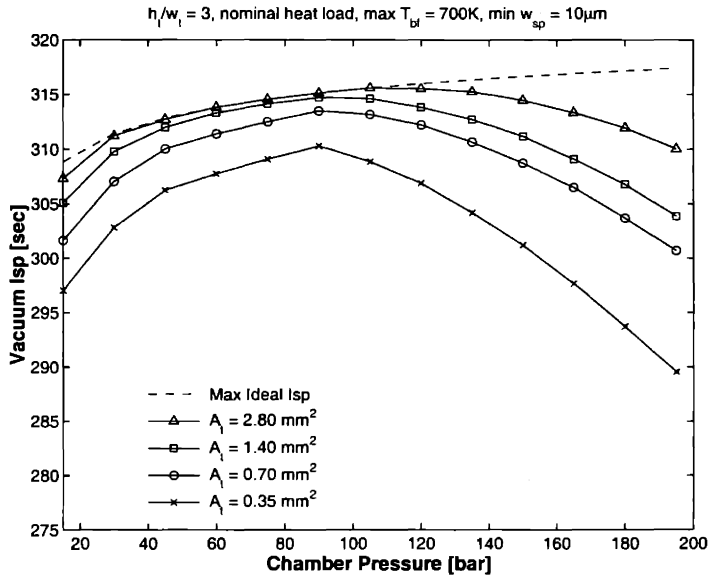
Figure 3-10 shows the performance and fabrication parameters as a function of A_t for the peak of each feasible I_{sp} envelope. Interestingly, though the chamber pressure at these peaks is essentially constant, T:W actually increases with increasing A_t , contrary to the basic scaling arguments presented in Chapter 1. The primary reason for this is that at the scales being considered, the engine mass does not scale as $A_t^{3/2}$ as one would expect, but instead increases nearly linearly with A_t . This is because the constant extra width and length added to the extent of the chamber and nozzle in modelling the overall mass of the engine tend to dominate the overall volume at small A_t . If both the thrust and mass were directly proportional to A_t , the T:W would be constant, but since the model predicts a non-zero mass at $A_t = 0$ (which corresponds to zero thrust), the thrust to weight ratio must increase from zero to this constant value, which is the increase seen here. A smaller effect is that as A_t increases, the maximum achievable I_{sp} (and P_c) are increasing also, leading to the thrust increasing at a rate slightly larger than the normal linear dependence on A_t .

As A_t continues to increase beyond the range considered here, the extra width held constant in the model would either become small compared to the actual device or would begin to scale as some representative length, and the engine mass would then begin to scale as expected, leading to an eventual decrease in T:W. Of course, extending A_t much beyond the range considered here quickly takes one out of scales traditionally associated with microfabrication.

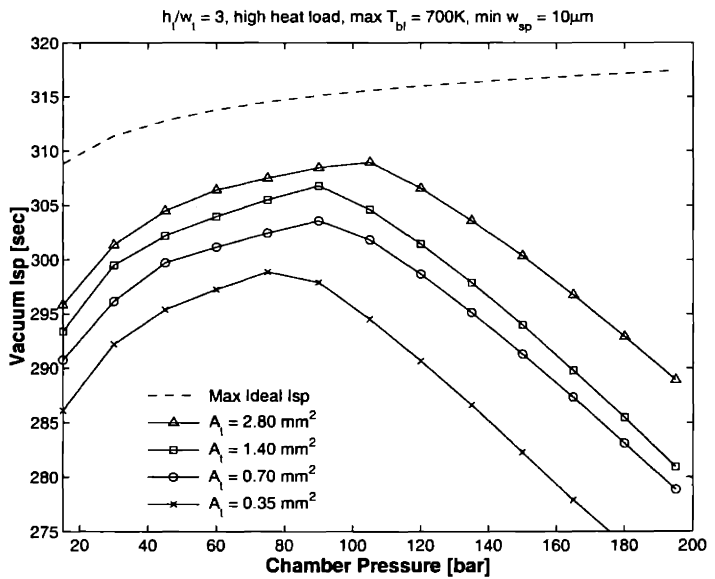
Though increasing A_t appears to enable both larger I_{sp} and higher T:W, this comes at the cost of some fabrication parameters. As can be seen in Figure 3-10, the number of devices produced per wafer set decreases from 16 to 4 as A_t increases from 0.7 to 2.8 mm². Over the same range, the number of wafers required per wafer set increases from 6 to 9.

3.4.3 Residence Time

All of the previous results have been based on a nominal residence time of 0.1 msec. As it is difficult to accurately predict the residence time required for complete combustion, it is instructive to see how changing the residence time impacts the feasible I_{sp} envelope.



(a) Nominal heat load



(b) High heat load

Figure 3-9: The feasible I_{sp} envelope enlarges as A_t is increased.

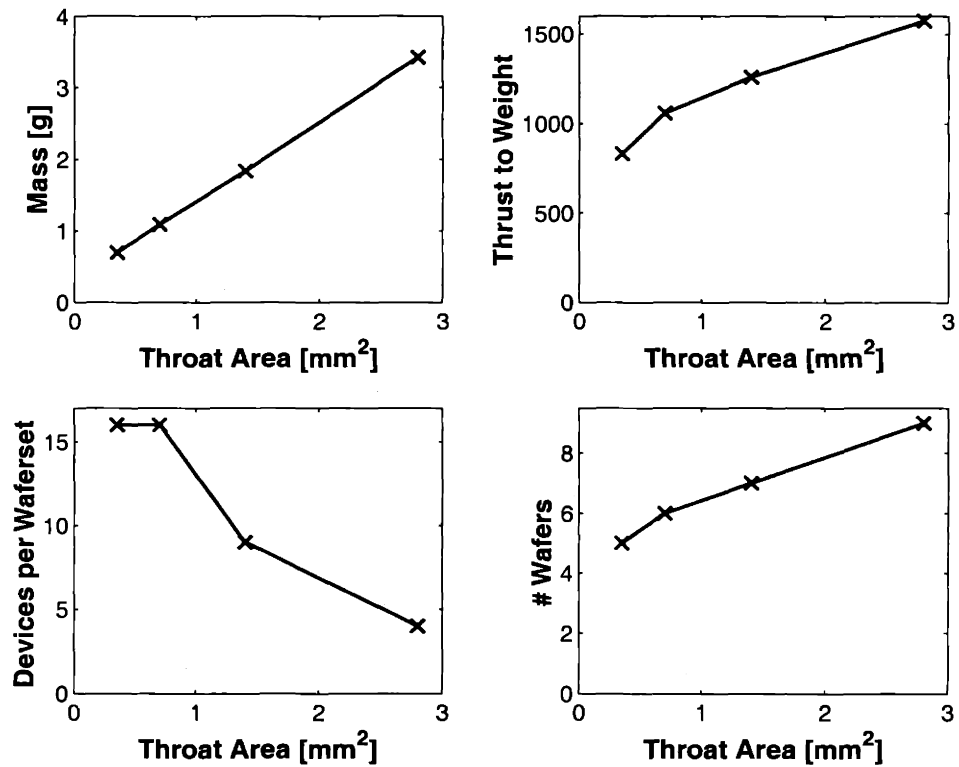


Figure 3-10: The mass of an engine increases nearly linearly with A_t at these small scales. Since the model predicts a non-zero mass at $A_t = 0$, the thrust to weight increases over this range of A_t , though it would eventually begin to decrease as the mass becomes proportional to $A_t^{1.5}$. However, moving to larger A_t yields fewer rockets per wafer set and requires more wafers. All points are for the nominal heat load case.

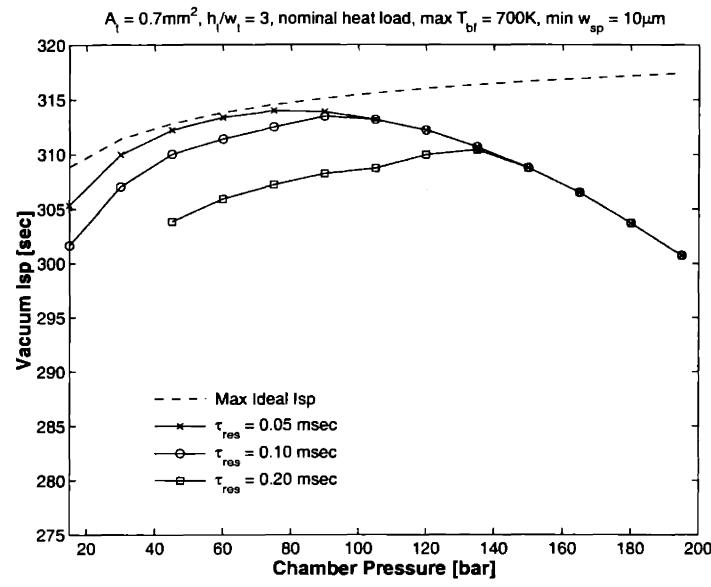
Figure 3-11 shows that changing the residence time is essentially the same as changing the value of the maximum T_{bf} constraint, so that lowering the residence time enlarges the I_{sp} envelope at low chamber pressure. Since the residence time required for complete combustion is not well known, the designers tendency is to be conservative, and provide a large residence time to ensure complete combustion and therefore high performance. However, the above implies that making the chamber too large can in fact have a negative impact on performance, as the increased surface area leads to a larger total heat load, and therefore a lower maximum feasible I_{sp} . This emphasizes the importance of determining the actual required residence time empirically.

3.4.4 Material of Construction

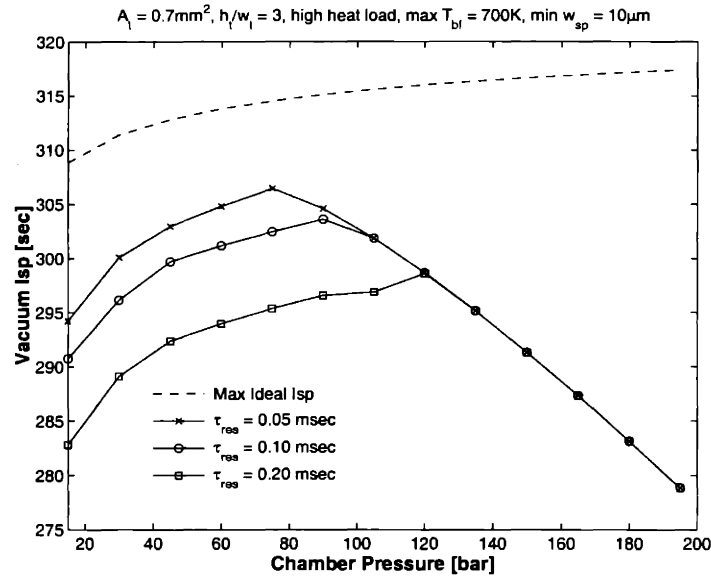
Current technology limits the selection of materials that can be used for microfabricated rocket engine systems to essentially silicon only, which is why that material has been the focus of this feasibility discussion. However, there is significant work being done at MIT to develop similar capabilities in materials that retain their strength at higher temperatures, with a specific focus on silicon carbide. [28, 10, 11]

To illustrate the benefits that higher temperature capable materials would bring, the model was run using the properties of silicon carbide, and assuming a hot-side wall temperature of 1400 K. Figure 3-12 compares the feasible I_{sp} envelope for a rocket made of silicon carbide with one made of silicon for $A_t = 0.7\text{mm}^2$ and $h_t/w_t = 3$. If T_{bf} is allowed to come to 1200 K, one can see that the envelope enlarges all the way to the ideal boundary, except in the high heat flux case, where the maximum throat heat flux constraint becomes important at the highest pressures.[¶] If one assumes that other factors such as thermal decomposition limit T_{bf} to 700 K as in the silicon case, one sees that the higher hot-side wall temperature reduces the heat load sufficiently to enlarge the envelope at low chamber pressures, and that having the temperature drop through the wall at the throat start at 1400 instead of 900 K greatly eases the maximum heat load constraint, allowing much higher P_c , and therefore a higher thrust to weight ratio as well as specific impulse.

[¶]If the plot of I_{sp} envelope were extended to higher chamber pressures, the heat flux constraint would eventually become important for all of these cases.



(a) Nominal heat load



(b) High heat load

Figure 3-11: Changing the required residence time is essentially equivalent to changing the allowable T_{bf} , as it only impacts the total heat load.

Table 3.1: Input Parameters for Baseline Design

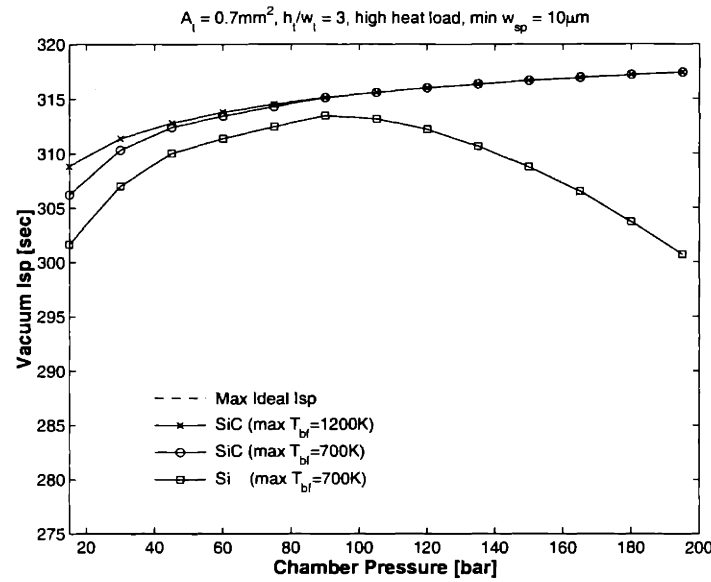
Symbol	Description	Value
P_c	Chamber pressure	125 bar
A_t	Throat area	0.70 mm ²
h_t	Throat height	1.40 mm
w_t	Throat width	0.50 mm
τ_{res}	Chamber residence time	0.1 msec
O/F	Oxidizer to fuel ratio	1.3
T_w	Hot-side wall temperature	900 K
n_{sp}	Number of side cooling passages	3

Once silicon carbide manufacturing technology is available, it will certainly enlarge high-pressure side of the feasible operating regime of microrocket engines, and would therefore lead to somewhat improved I_{sp} and larger T:W. However, as should be clear from the prior discussion, high performance microrocket engines are feasible given current silicon manufacturing techniques.

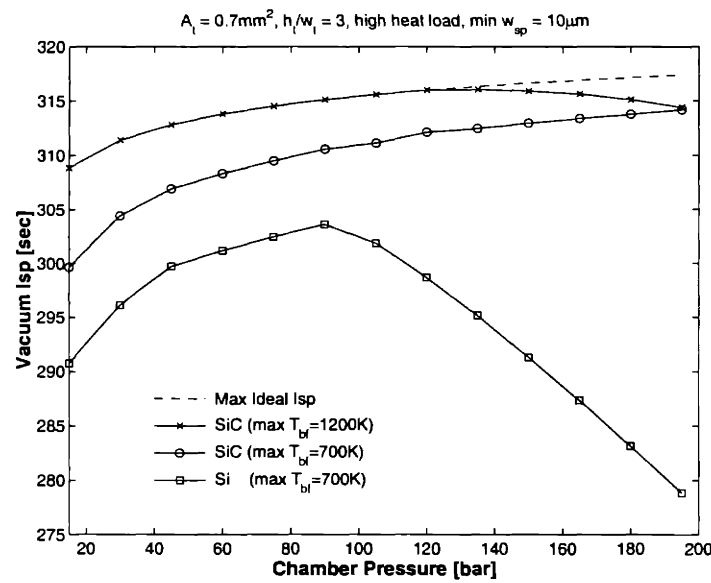
3.5 Baseline Design

The feasible I_{sp} envelope for the baseline design size is shown in Figure 3-13. The size of the baseline design was chosen prior to the completion of the full model, based on a preliminary study that held P_c and the O/F ratio fixed, in order to maintain the chamber temperature at a relatively arbitrary 3000 K. That study did apply the same feasibility constraints presented here in choosing the geometry, namely that T_{bf} should be below a fixed value and w_{sp} must be larger than a minimum allowable etched feature size. A T_{bf} near 550 K was chosen to provide a margin, and because ethanol physical property data were more readily available up to that temperature.

One can see that the baseline design falls in the area between the feasible boundaries based on the nominal and high heat load predictions. If the high heat load prediction ends up being more accurate, the design O/F and perhaps P_c would have to be reduced for a system of that size to be feasible. The input parameters for the baseline design are shown in Table 3.1, and the outputs from the model are shown in Table 3.2, clustered into performance, size, and cooling groups.



(a) Nominal heat load



(b) High heat load

Figure 3-12: If silicon carbide is used as the material of construction, the I_{sp} envelope expands to nearly the ideal limit for the range of pressures shown here. The hot-side wall temperature is taken as 1400 K for the silicon carbide cases, and 900 K for the silicon case.

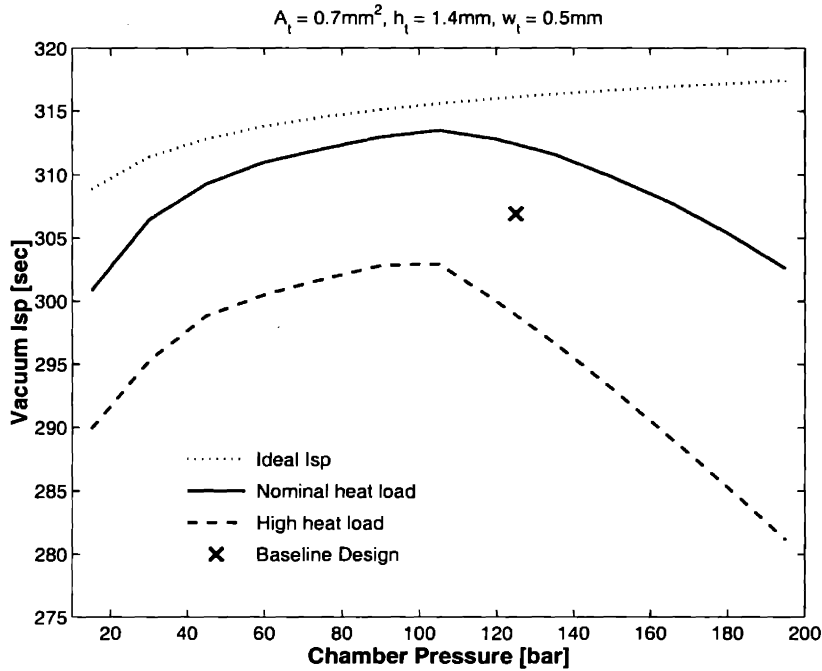


Figure 3-13: Location of baseline design and feasible I_{sp} envelope for the baseline geometry.

Based on the results presented earlier in this chapter as to the dependencies of performance and fabrication parameters on geometry when the feasible I_{sp} is maximized, the baseline design appears to be near the optimal size for a microrocket engine, particularly for the first one. A larger throat area would produce more thrust, a higher I_{sp} , and a higher T:W, as was shown in Section 3.4.2. However, this comes at the cost of a larger number of wafers required and a fewer number of rockets produced per wafer set, particularly in the case of the 100 mm diameter wafers used in this work. As the fabrication process for these devices was untested, this cost was deemed to be too large. The throat aspect ratio also appears to be near optimal, as it maximizes the feasible I_{sp} at a sufficiently high P_c to yield a large T:W without sacrificing the number of rockets per wafer set.

Unfortunately, the baseline design for a liquid oxygen and ethanol rocket engine is probably not implementable in practice, as was pointed out by Al-Midani [1]. The reason is due to the turbopumps, mostly ignored in the discussion above. The oxygen must remain in liquid state for it to be pumped effectively, but given the short dimensions and high thermal conductivity of silicon, it is not clear how the inlet to the pump could be thermally isolated from the rest of the engine. This suggests that the oxygen would tend to vaporize on the

way to the pump, leading to so-called “vapor lock,” and the system would never be able to start up. To overcome this limitation, non-cryogenic, or storable, liquid propellants are required. The application of the model to other propellants will be briefly discussed below.

3.6 Summary of Feasibility Limitations

There are two factors discussed above that limit the feasibility of microrocket engines: the throat heat flux and the total heat load. Both of these depend on chamber pressure and mixture ratio, but both also have strong dependencies on nozzle geometry. At low chamber pressures, the total heat load constraint is important, as for a constant engine size, the capacity to absorb heat increases with mass flow, which scales linearly with chamber pressure, while the total heat load scales as chamber pressure to some power slightly less than one. (usually assumed to be 0.8). This means that as the chamber pressure is reduced at constant mixture ratio, the heat load will go up faster than the ability to absorb it, which will lead to a low pressure feasibility limit.

At high chamber pressures, the throat heat flux is the constraint. As the chamber pressure increases, the pressure in the coolant passages will increase as well, leading to thicker side walls. The throat heat flux will increase also, and these two factors will add together increase the temperature drop through the wall. Eventually, if the hot-side wall temperature is held fixed, the cold-side wall temperature will drop to the point that it is impossible to generate the coolant heat transfer coefficient required to absorb this heat flux at the temperature difference between the cold-side wall and the local coolant bulk temperature. This leads to a high pressure feasibility limit.

In terms of the dependence on geometry, an increasing throat aspect ratio decreases total surface area, thus reducing the total heat load, and easing the first constraint, but at the same time it leads to a smaller effective throat diameter, increasing the magnitude of the the throat heat flux, and making the second constraint appear at lower pressure. Thus increasing the throat aspect ratio will cause the feasible pressure range to shift to lower pressures. On the other hand, increasing the throat aspect ratio eases both of the constraints. In the first case, a larger throat area leads to more mass flow, which, like increased chamber pressure, leads to the heat load becoming smaller relative to the propellant total

Table 3.2: Output Parameters for Baseline Design

Symbol	Description	Value
I_{sp}	Vacuum Specific Impulse	307 sec
T:W	Thrust to weight ratio	1320
F	Thrust	15.7 N
\dot{m}	Mass flow	5.2 g/sec
m_{eng}	Engine mass	1.2 g
l	Rocket length	18 mm
w	Rocket width	13.5 mm
h	Rocket height	2.6 mm
-	Rockets per wafer set	16
-	Wafer layers	6
T_{bf}	Final propellant temperature	556 K* 737 K†
w_{sp}	Side cooling passage width (oxygen)	17.2 μm^* 4.2 μm^\dagger
w_{sp}	Side cooling passage width (ethanol)	8.0 μm^* N/A †
\dot{Q}_{tot}	Total heat load	4.0 kW* 6.5 kW†
\dot{q}_{max}	Throat heat flux	160 W/mm ² * 260 W/mm ² †
$T_{wc_{min}}$	Throat cold-side wall temperature	566 K* 348 K†
	*nominal heat load correlation	
	†high heat load correlation	

heat capacity. In terms of the throat heat flux, the larger throat area leads to a larger effective throat diameter, which decreases the local heat flux for a constant mass flow per unit area.

Both of these limitations depend on the heat flux, and for a given pressure would be eased if the heat flux were lowered at the same mass flow. This is accomplished by lowering the mixture ratio, which in turn lowers the I_{sp} , leading to the dependence of feasible I_{sp} on chamber pressure as seen throughout this chapter. The components that are used to calculate the heat flux are shown as function of mixture ratio in Figure 3-14, where each is plotted as a ratio to its value at O/F=0.8. The curves are plotted for chamber conditions, but look nearly identical at the throat. One can see that over the range of mixture ratio considered, the heat flux increases by a factor of 7. Most of this effect is due to the increase in temperature difference between the adiabatic wall temperature and the wall temperature, which increases by more than a factor of 3. The heat transfer coefficient increases by a factor of slightly more than 2, due to the thermal conductivity increasing by a factor of 4 while the Nusselt number decreases by half. Thus, changing the mixture ratio has a dramatic effect on heat load, and can be reduced to allow the limitations above to be met, at a cost of I_{sp} .

3.7 Application of model results to other propellants

Though the model was specifically constructed for the oxygen and ethanol propellant combination, the mechanisms that limit the feasibility of these engines and the trends that can be drawn from this chapter are more general. The limitations that determine the feasibility of a future rocket engine system will be the same, and the trends with geometry will also be similar. The change in heat flux seen in the oxygen and ethanol combination may not be as dramatic, but the trends should be the same, leading to a similar construction of a feasible I_{sp} envelope. It is likely, in fact, that the throat heat flux limit will be more severe, as the limitations presented here were for the oxygen passage width, which assumed the oxygen doing the cooling was at 250 K. It is likely that the storables propellants would be about 100 K warmer than this, leading to a throat heat flux boundary that is shifted to lower pressures. The total heat load constraint may also be set at a lower T_{bf} as a number

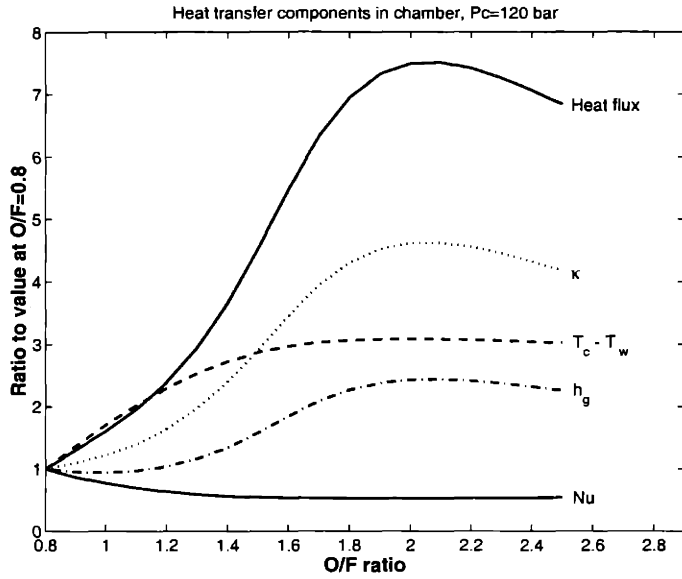


Figure 3-14: Change in heat flux, thermal conductivity (κ), temperature difference ($T_c - T_w$), heat transfer coefficient (h_g), and Nusselt number (Nu) relative to their respective values at O/F=0.8. The heat flux is $h_g(T_c - T_w)$, and $h_g \propto \kappa \text{Nu}$.

of the storable propellants tend to decompose thermally at temperatures below the 700 K considered here.

The methodology of the model may be easily adapted to other propellant combinations by inserting the thermochemistry results for those combinations, as well as providing the physical properties of the fluids that are needed to estimate coolant heat transfer coefficient and overall temperature rise. This work has been begun by Protz[35].

3.8 Summary

This chapter has described two major mechanisms that limit the feasibility of microrocket engines, and illustrated their dependence on chamber pressure, mixture ratio, and geometry. This was used to generate feasible I_{sp} envelopes which show that for a given geometry, there is a pressure where I_{sp} is maximized at a value that is usually below the maximum ideal I_{sp} for that pressure.

The next chapter will discuss the design of a rocket engine thrust chamber that has been constructed to demonstrate experimentally the feasibility of combustion and cooling at these

scales and chamber pressures.

CHAPTER 4

DESIGN OF THRUST CHAMBER

4.1 Introduction

This chapter discusses both the design process and the as-built design of the demonstration microrocket engine thrust chamber. The results of this phase of the work are critical dimensions, the choice of the path the coolant takes through the thrust chamber, and a detailed design of the local cross section of each cooling passage at each location. These results are then translated into mask drawings based on the fabrication process and requirements, discussed in the next chapter.

4.2 Propellant Selection and Thrust Chamber Size

Although the last two chapters considered liquid oxygen and ethanol as propellants, the thrust chamber that has been designed and built as part of this thesis uses gaseous oxygen and methane as propellants. This allows for gaseous injection of the propellants, and avoids the added experimental complexity of using liquid oxygen.

The thrust chamber size was chosen to be essentially the same as the baseline design for the oxygen/ethanol engine presented in the previous chapter. The shape of the chamber and nozzle is the same, specifically, the characteristic dimensions are a throat width of 0.5 mm, and a chamber length of 4.5 mm. To maintain the same mass flow of 5 g/sec, the throat height is increased to 1.5 mm. The oxygen/methane propellant combination tends to burn at a higher temperature than oxygen/ethanol, so a slightly more fuel-rich oxidizer to fuel mixture ratio (by mass) of 2.3 is chosen. The stoichiometric mixture ratio is approximately

4. At the design chamber pressure of 125 bar, this leads to a predicted chamber temperature of 3150 K, instead of the 3050 K predicted for the oxygen/ethanol combination.

4.3 Heat Transfer Design

Ethanol is selected as the design coolant for the chamber, as its critical pressure is 63 bar. This allows avoidance of two-phased flow in the cooling passages and greatly simplifies the design procedure.

4.3.1 Design Methodology

The methodology for the design of the cooling passages is as follows:

The design goal is to maintain the hot-side of the wall at a uniform temperature below silicon's softening temperature. Chen [10] suggests temperatures be limited to 950 K, and the design wall temperature is chosen to be 900 K to provide a design margin. Given this wall temperature, and the one-dimensional estimates of nozzle flow properties, the hot-side heat transfer coefficient is estimated. This coefficient and the difference between the adiabatic wall temperature and the desired wall temperature determine the local heat flux that the cooling passages must be designed to absorb. If this local heat flux is integrated over the internal surface area of the chamber and nozzle, the total heat load to the wall is found, which determines the total temperature increase of the coolants, an important parameter.

Once the spacial distribution of heat flux to the wall required to keep the wall at a uniform temperature is known, the cold-side cooling passages must be designed to adequately receive it. The heat flux that will be absorbed into the coolant can be estimated as a heat transfer coefficient based on the local coolant flow properties multiplied by the difference between the cold-side wall temperature and the local reference, or "bulk," temperature of the coolant. By assuming that in steady state all the heat goes into increasing the enthalpy of the coolant, one can determine the bulk coolant temperature as a function of position given the total coolant mass flow, and its direction of flow in the engine. As the desired local heat flux is known from the hot-side calculation, the cold-side wall temperature can be

calculated given the hot-side wall temperature, the thickness of the wall, and the thermal conductivity of silicon as a function of temperature. The local heat flux divided by the difference between the cold-side wall temperature and the local bulk temperature of the coolant gives the required local coolant heat transfer coefficient, or h_c . The cooling channel must then be designed so as to produce the correct h_c at each location. The primary means of accomplishing this is to vary the channel flow area, which changes ρu for a constant mass flow, yielding a changing heat transfer coefficient. In some areas, additional cold-side surface area is provided to reduce the required h_c while keeping the net heat flux to the coolant unchanged.

4.3.2 Heat load

The first step in the heat transfer design process is the evaluation of the heat load to the wall that must be absorbed by the coolant to keep the wall at an acceptable temperature. This heat load is estimated using the same correlations introduced in the previous chapters.

The three correlations are applied to the flow parameters available for the thrust chamber propellants, oxygen and methane, and the local heat flux (Equation 2.3) is plotted in Figure 4-1. One can quickly see that the results these correlations yield differ from one another by more than a factor of two. When integrated over the interior surface area, the total heat load to the walls predicted by the high heat load correlation is 7.5 kW, while that predicted by the nominal heat load correlation when the properties are evaluated at a film temperature is 3.3 kW. The middle case, using the nominal correlation and evaluating fluid properties at T_g , the local static temperature yields an integrated heat load to the walls of 4.7 kW. It is this later approach that was used as the nominal heat load correlation shown in previous chapters.

As the correlations produce estimates that vary from each other significantly, it is apparent that the actual heat load can only be determined empirically. Figure 4-2 shows the final coolant temperature that would be expected for both water and ethanol as a function of total coolant mass flow for steady state absorption of the three total heat loads mentioned earlier. It is apparent that even if the maximum coolant temperature is limited to 600K, the full range of estimated total heat load may be covered by varying the coolant flow rate

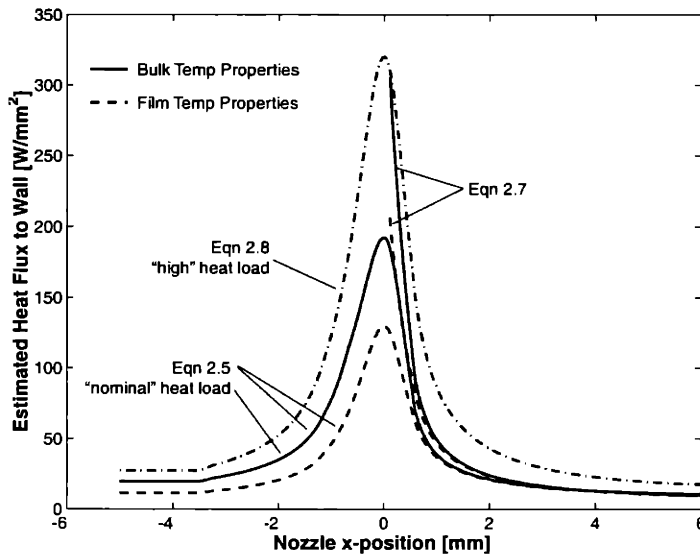


Figure 4-1: Estimated local heat flux to the thrust chamber walls for various heat transfer correlations considered. The hot side of the wall is kept at a constant temperature of 900K.

from approximately 2.5 to 6.5 g/s, which is well within the capabilities of the experimental apparatus.* (See Chapter 6 for a discussion of the apparatus.)

The total heat load predicted by the nominal heat load correlation falls in the middle of the range, and previous feasibility work with Ethanol and Oxygen as propellants showed that this form best predicted the rocket heat flux data available for those propellants as presented by [37]. For these reasons, this correlation is used in the design of the thrust chamber, and the total heat load of 4.7 kW is considered the design point.

4.3.3 Coolant Path

Given the heat flux, or \dot{q} , profile discussed above, the thickness of a cooling passage wall, t_w , and the thermal conductivity of silicon, κ , the local coolant-side wall temperature can

*Unfortunately, although the apparatus is capable of providing this range of flow rates, the pressure drop through the fabricated cooling passages was too large, and the packaging technique has limited the feasible inlet pressure, resulting in a maximum coolant flow rate achieved through the thrust chamber of approximately 1.5 grams/sec.

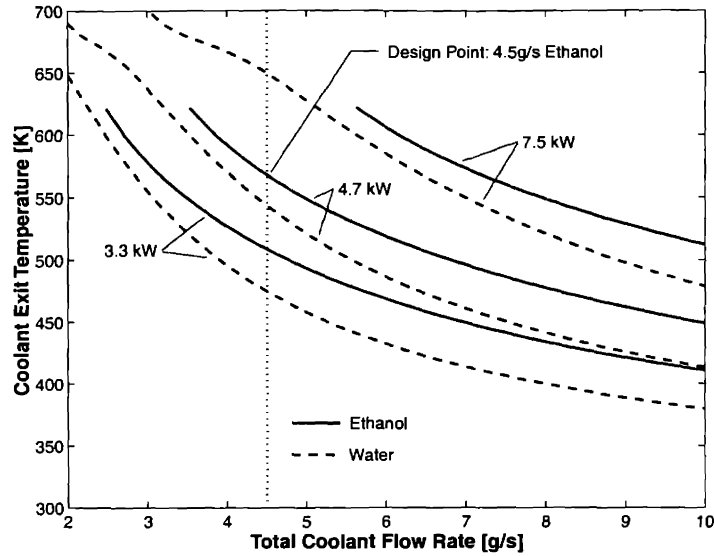


Figure 4-2: Temperature rise of coolants (water and ethanol) as a function of total coolant mass flow for various total heat loads. The enthalpy of both fluids is evaluated at a pressure of 300 atm. The enthalpy data for ethanol are only available to 350C.

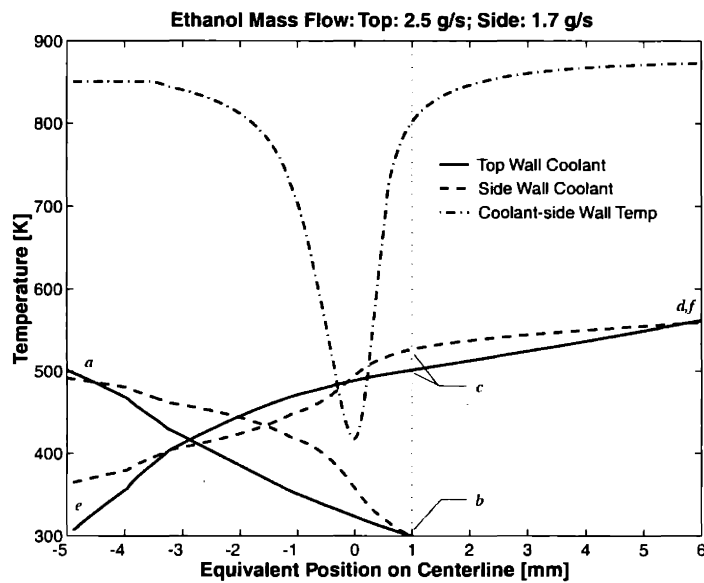
be written as

$$T_{wc} = T_w - \dot{q} \frac{t_w}{\kappa} \quad (4.1)$$

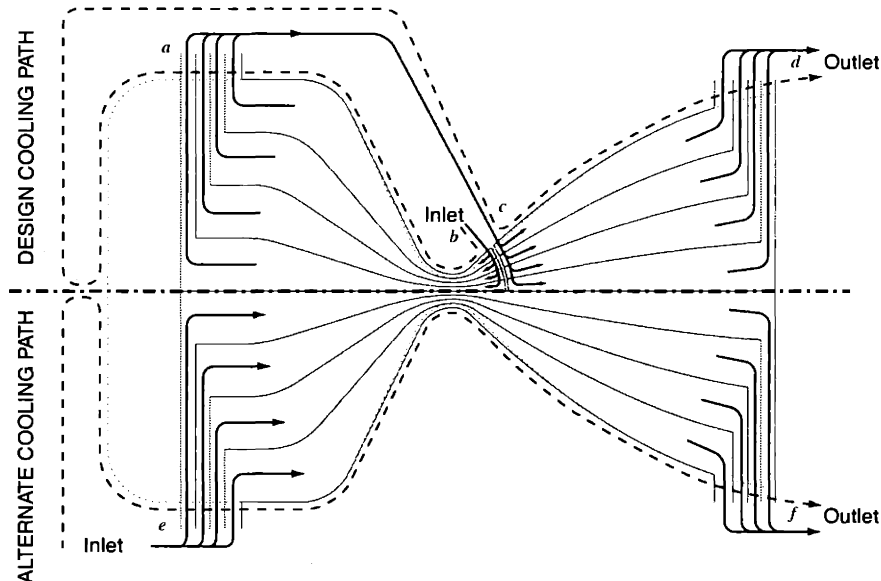
where the thermal conductivity is evaluated at an appropriate average wall temperature. For the design heat flux profile, this coolant side wall temperature is shown in Figure 4-3(a) for the top and bottom walls. The cold-side wall temperature is slightly different for the side walls as the side wall thickness varies along the length of the thrust chamber.

As the heat flux profile is considered known, the coolant bulk temperature at each position can be evaluated using an energy balance approach, given a coolant mass flow. The heat flux into the coolant in an elemental volume is equated with a rise in enthalpy, and from the local enthalpy per unit mass of the fluid, the bulk temperature, or T_b , is determined as a function of position in the rocket.

In order for heat to transfer into the coolant and still maintain the desired hot-side wall temperature, the coolant bulk temperature must everywhere be less than the design cold-side wall temperature shown in Figure 4-3(a). This provides a constraint in the coolant



(a) Temperatures of coolant and cold-side wall



(b) Flow path schematics

Figure 4-3: The design cooling path is shown in the upper half of the lower figure. It enters at location *b* near the throat and cools the chamber first. Once at location *a*, the coolant is piped around to reenter at *c* and then is used to cool the expansion nozzle, exiting at *d*. A more typical approach that will not work is shown on the lower half of figure (b). Here the coolant enters at *e* and flows all the way to exit at *f*. This is flawed because the coolant temperature will be too high near the throat.

path design, as is illustrated in Figure 4-3, which shows two possible coolant flow paths. In the path shown in the lower half of Figure 4-3(b), the coolant enters at the forward end of the chamber (*e* in Figure 4-3(a)) and flows all the way to the exit of the nozzle, *f*. This approach is flawed, as after absorbing all the heat necessary to cool the chamber, the calculated coolant bulk temperature in the region near the throat would exceed the required cold-side wall temperature.[†] A coolant path that cools the throat first is required so that the coolant bulk temperature will still be low enough to allow heat transfer. This approach is used in the coolant path chosen in the design, and which is depicted in the upper half of Figure 4-3(b). In Figure 4-3(a) this corresponds to the path where that begins at point *c*, continues to the left to cool the chamber, and then is piped around from *a* to *c*, where it re-enters the cooling passages to cool the expansion nozzle, exiting at *d*.

4.3.4 Coolant Passage Design General Considerations

Once the overall coolant path is determined, the cooling passages must be designed to create the correct cold-side heat transfer coefficient at each location. This is primarily an effort in tailoring the local mass flux (ρu) and cooling surface area.

It is instructive to begin by considering the cooling at three nominal locations: the chamber, the throat, and a representative location in the expansion nozzle. Table 4.1 shows the local heat flux, temperature drop in the wall, coolant bulk temperature, and required heat transfer coefficient at each of these locations.

Table 4.1: Nominal Heat Transfer Parameters

Location	Heat Flux [W/mm ²]	Wall ΔT [K]	Bulk Temp. [K]	Heat Transfer Coef. [W/m ² K]
Chamber	20	50	450	$5.0 \cdot 10^4$
Throat	200	500	320	$2.5 \cdot 10^6$
Expansion Nozzle	10	25	500	$3.1 \cdot 10^4$

The ratio of required h_c at the throat to that at the chamber is 50, while the ratio of chamber width to throat width is 16. To first order, one expects h_c to scale with ρu , and thus to

[†]In practice this would not really occur, as both the cold- and hot-side wall temperatures at the throat would rise to the levels needed to sustain the throat heat flux, causing a thermal failure of the wall.

scale inversely with the cross sectional area of the coolant flow channel. As the coolant must cool all of the exposed thrust chamber and nozzle walls, the simplest passage design for the top and bottom walls would be to have constant height passages whose widths were proportional to the local chamber flow width. In this case, the ratio of ρu in the cooling passages at the throat to that in those over the chamber would be 16, much less than the desired 50.[‡] Thus, if the coolant flow rate is selected to properly cool the throat, it will be approximately three times larger than is required to cool the chamber. Because the bulk of the total heat load is absorbed in the chamber, this would lead to a much higher coolant flow rate than Figure 4-2 requires.

Though there is no limitation on the coolant mass flow in the present work, as the thrust chamber's coolant flow rate is not tied to the propellant flow rate, it is desired to simulate an eventual regeneratively cooled system as closely as possible. For this reason, the design coolant flow rate is considered a given, set by the total heat load of the assumed heat flux profile, and the passages are designed within this constraint. This implies that additional measures need to be taken in the region of the throat to increase h_c beyond the "automatic" factor of 16 increase mentioned previously. The subsequent sections discuss these methods as well as the specific design of the cooling passages.

4.3.5 Choice of Design Heat Transfer Coefficient Correlation

A number of correlations for the cold-side heat transfer were considered in the design of the cooling passages. Lopata [29] performed an experimental characterization of supercritical ethanol as a coolant for the Re and heat fluxes of interest to the rocket. Subsequently Faust [13] performed a more detailed reduction of the original data set, and improved Lopata's estimates of the cold-side heat transfer coefficient. Faust's data are presented in Figure 4-4, along with the predicted h_c based on a number of correlations considered in the design of the cooling passages. The correlation selected for the design, referred to as "nominal" in the figures, is similar to the Dittus-Boelter Nu dependence:

$$Nu_b = 0.025Re_b^{0.8}Pr_b^{0.4} \quad (4.2)$$

[‡]In fact, the situation is probably even worse than this, since h_c goes like $(\rho u)^{0.8}$.

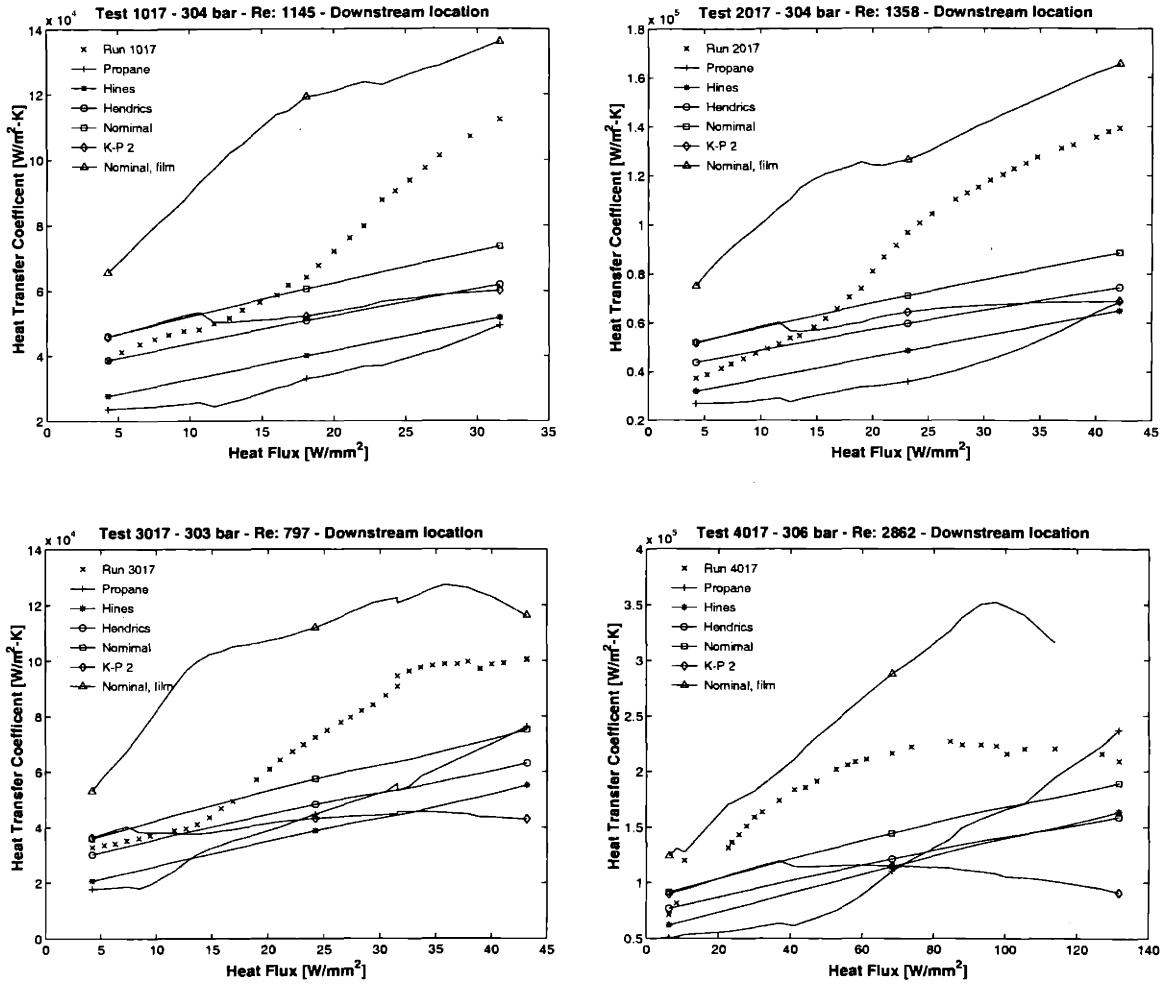


Figure 4-4: Comparison of experimentally-determined h_c [13] with the predictions from a number of correlations. Re is evaluated at tube entry conditions. The “nominal” correlation (Equation 4.2) is used as the design correlation.

and is chosen as the correlation closest to the data, without overestimating h_c in the heat flux regime expected in the thrust chamber ($20 \text{ W/mm}^2 < \dot{q} < 200 \text{ W/mm}^2$).[§] See Appendix D for a discussion of the other correlations considered for the design and shown in Figure 4-4.

[§]At the time of the selection of the design correlation, Faust [13] had not completed her work, and Lopata’s [29] estimates of h_c were approximately twice as large. In this case the design correlation was conservative over the entire range of heat flux, not just for heat fluxes greater than $\sim 20 \text{ W/mm}^2$

4.3.6 Top Cooling Passage Design

The coolant for the top and bottom walls is split into 16 parallel channels, eight each on top and bottom. Considering the symmetry about the centerline, only four must be explicitly designed. The final design of the cooling passages is pictured in Figure 4-5. The coolant enters approximately 1 mm downstream of the throat, and travels towards the throat. The coolant channel height for this region is $30 \mu\text{m}$. Near the throat, there are a number of pins to locally increase the effective heat transfer by an estimated 200%. After flowing past the throat, the pins end, and the channel height increases to $50 \mu\text{m}$. From this point to the forward end of the chamber, there are a number of fins in the flow direction, each $30 \mu\text{m}$ high. These increase the cooling surface area, and increase ρu by adding blockage. For much of the chamber area, each cooling passage is divided into two sub-passages which flow in parallel. This ensures that the wall between the cooling passages and the chamber does not span too wide a distance. The upper $20 \mu\text{m}$ of the $50 \mu\text{m}$ high separating wall is broken periodically to ensure pressure communication between the sub-passages.

Each passage exits the forward end of the chamber in a narrower passage $200 \mu\text{m}$ high. Once outboard past the edge of the chamber, the four channels are combined and are piped to the entry area of the expansion nozzle cooling jacket, just aft of their original entry location downstream of the throat. Because the heat load in the expansion nozzle is less severe than that of the chamber and throat, no additional surface area is required for cooling. However, the width of the passages becomes a concern structurally towards the exit of the nozzle, and elongated posts are inserted in the center of the passages to decrease the unsupported span of the coolant channel wall. At the aft end of the nozzle, the passages again exit towards the chip edges in narrower passages $200 \mu\text{m}$ high. Finally, they pass through metering holes on the way to the two exit ports for the top and bottom cooling passages.

Chamber Cooling and Fin Design

Much of the detailed tailoring of the cooling passages was done in the region of the chamber. Typical cross sections of the cooling passages are shown to scale in Figure 4-6, which also defines the nomenclature used below. The bumps extruding from the lower wall are the fins, which run along the length of the passage, as can be seen in Figure 4-5. The nominal design

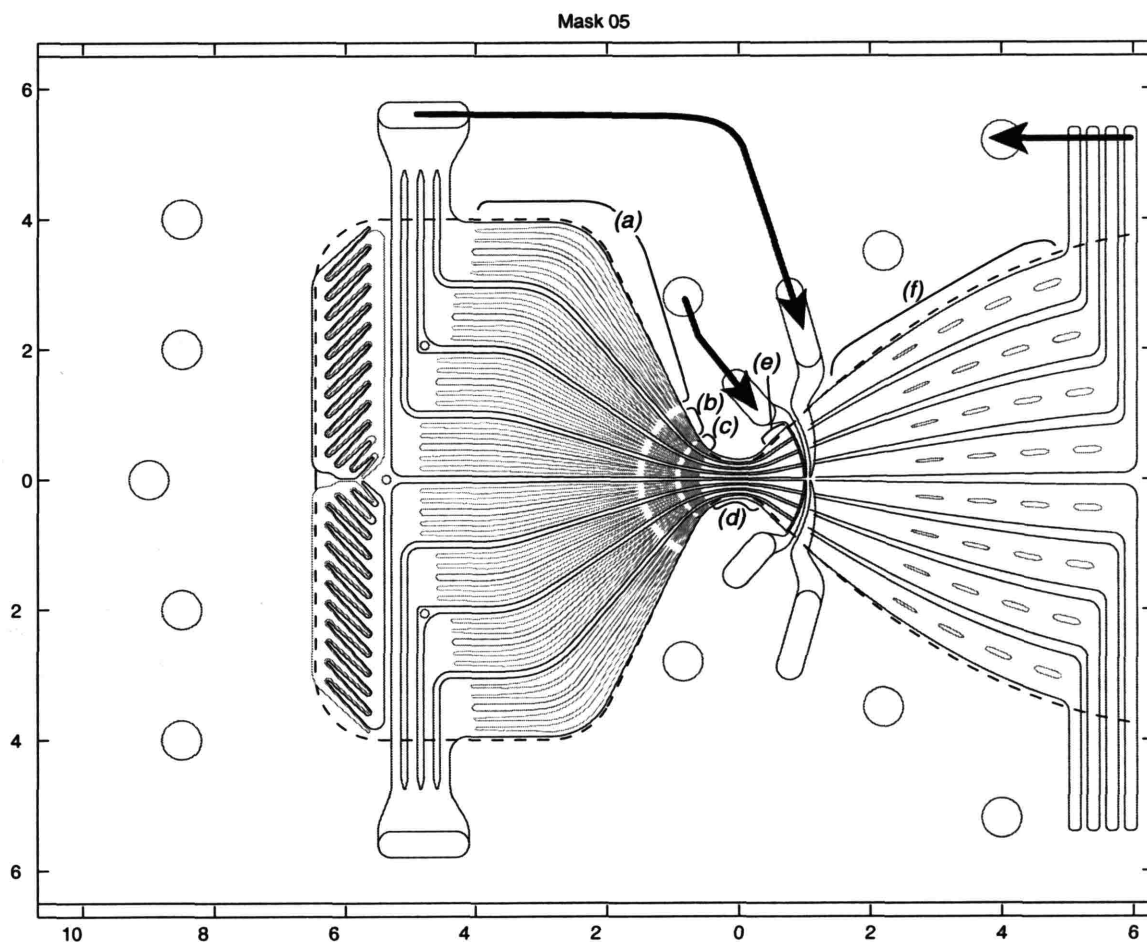


Figure 4-5: Illustration of the mask that defines the top and bottom cooling passages. The scale is in mm. The narrow features above the chamber are the fins referred to in the text.

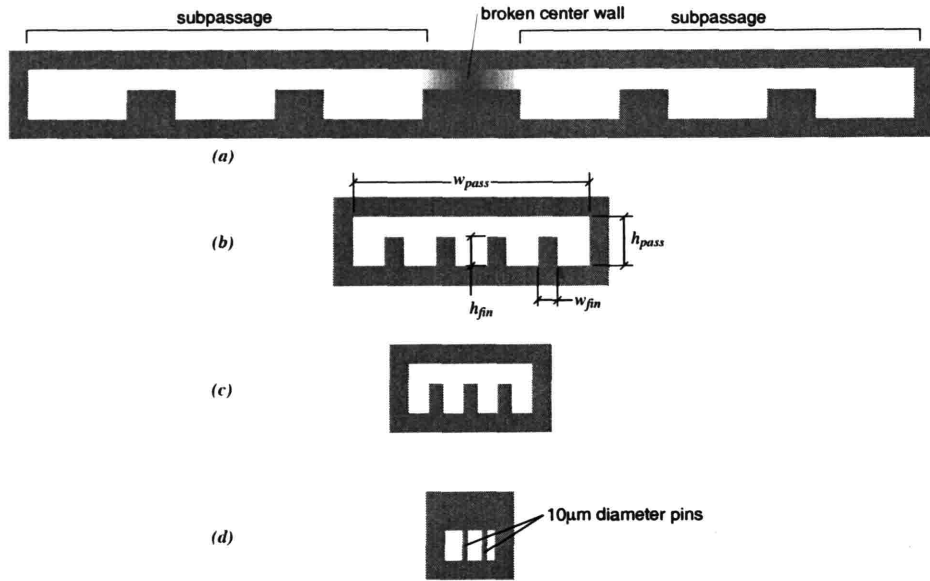
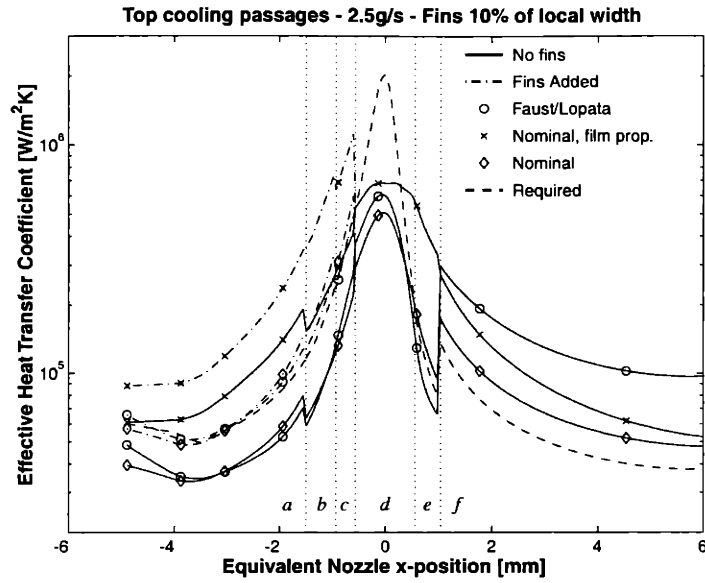


Figure 4-6: Typical cross sections of top side cooling passages in various regions. The labels correspond to the regions shown in Figure 4-7. They are drawn to scale where $h_{pass} = 50 \mu\text{m}$.

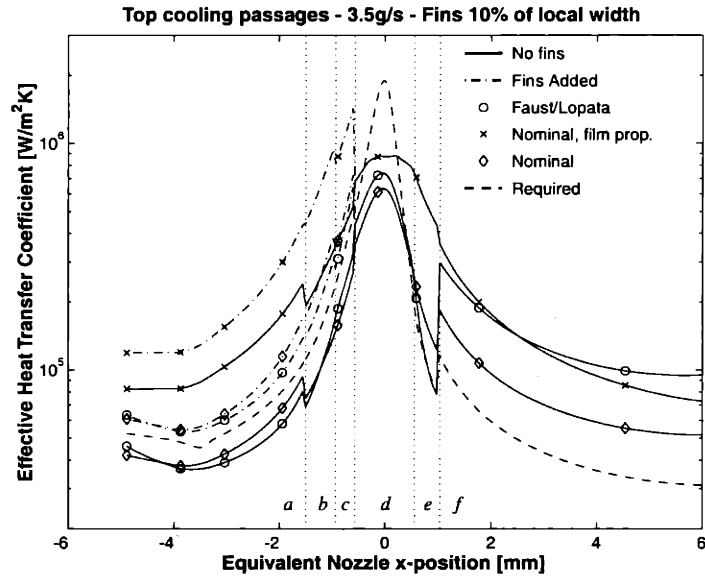
correlation was first applied to the top cooling passages assuming they had no fins and were simply rectangular with a width proportional to the local flow width of the nozzle. Figure 4-7 shows that this would provide insufficient cooling. By adding fins of varying width and number, the predicted heat transfer coefficient can be increased and tailored to meet the design condition. In Figure 4-7, the plots with fins are for fins with a width always 10% of the local passage width ($w_{fin} = 0.1w_{pass}$). There are two fins in each of the sub-passages in region (a), four in each passage in region (b), and three in each passage in region (c). Region (d) is above the throat where the passage height is reduced and pins rather than fins are used (see Pin Design below).

Once the number of fins in each location is set, the fin width is varied at each axial location from its nominal 10% of local passage width so that the predicted heat transfer coefficient will match that required in the design case. It is interesting to note that for a given mass flow, number of fins, and passage width, the local Re is independent of fin width, since the perimeter is constant and an increase in ρu will be canceled by a decrease in the hydraulic diameter:

$$\text{Re} = \frac{\rho u D_h}{\mu} = \frac{\frac{\dot{m}}{A} \frac{4A}{P}}{\mu} = \frac{4\dot{m}}{\mu P}$$

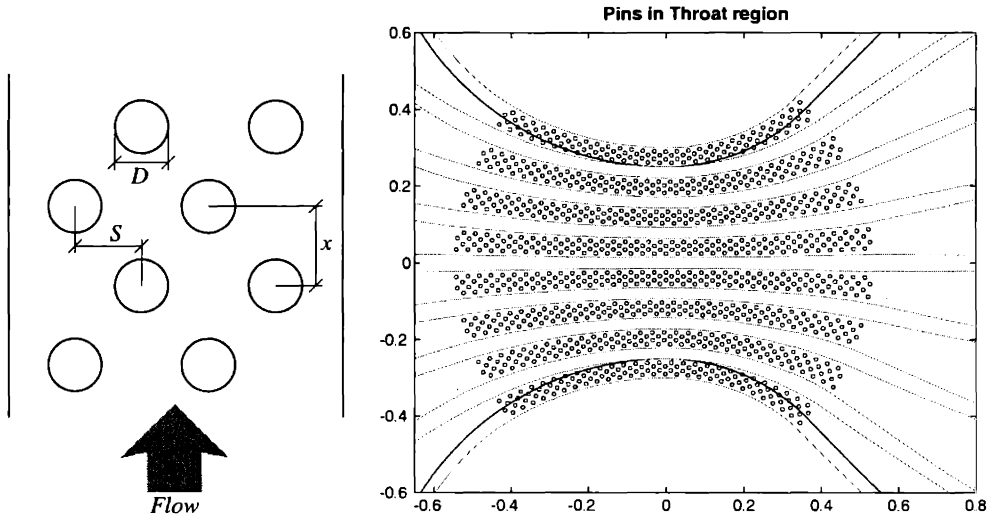


(a) Design case with 2.5 g/s of top coolant flow.



(b) Additional coolant case with 3.5 g/s of top coolant flow.

Figure 4-7: Top side cooling correlations. The Faust/Lopata curve is based on data from [13]. The Nominal correlation suggests the need for fins to increase the surface area in the chamber region. In the nozzle exit, no fins are required. At the throat, adding fins is not sufficient, and another approach is required. The vertical lines mark the regions also shown in Figures 4-5 and 4-6, which are locations where the number of fins changes, leading to the jumps in effective h_c for the regions forward of the throat. The larger jump downstream of the throat is the location where the coolant is first introduced, flowing forward towards the chamber, and then is re-introduced after cooling the chamber to cool the exit nozzle.



(a) Pin nomenclature. H is the height of the pin out of the plane of the page.

(b) Final pin layout in vicinity of throat. Dimensions are in mm. The solid line shows the location of the nozzle throat below the cooling passages.

Figure 4-8: Nomenclature and Pin layout of top cooling passages.

Because changing the width of the fin, w_{fin} does not impact the fluid properties at a given location, Nu is also independent of this width, as it depends only on Re and the local fluid properties. The heat transfer coefficient then scales inversely with D_h , so it increases as w_{fin} is increased.

Throat Cooling and Pin Design

Due to the very high heat load at the throat and the relatively small temperature difference between the coolant bulk temperature and the coolant-side wall temperature, adding fins is insufficient to generate a large enough heat transfer coefficient. Instead, the passage height is reduced to $30 \mu\text{m}$, and $10 \mu\text{m}$ diameter pins are placed in a staggered array inside the passages. The resulting features are quite similar to those used in combustor liners and turbine blade internal cooling geometries in modern gas turbine engines. Because of its μm -scale, and use of a liquid coolant, Re based on pin diameter for the present thrust chamber is in a range that has been previously investigated for applications to gas turbine engine cooling. Armstrong and Winstanley[2] provide a review of this work.

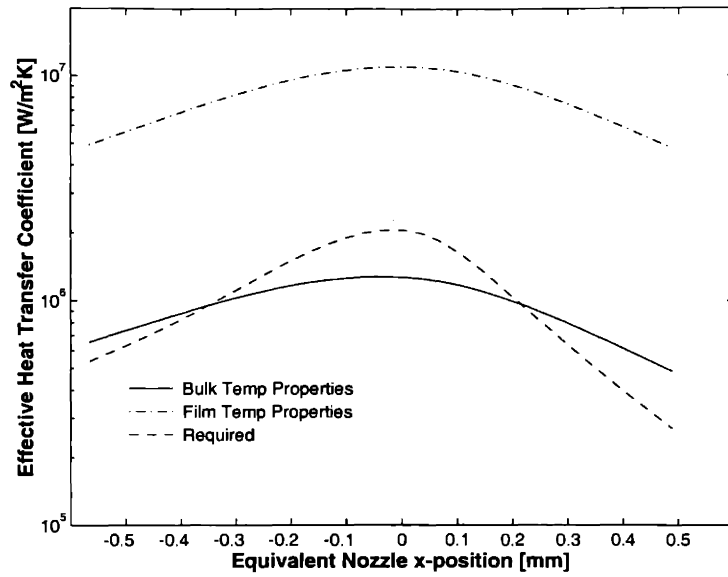


Figure 4-9: Plot of predicted heat transfer coefficient in region of pins above throat.

Metzger[32] suggests the following correlation for the array-averaged Nu:

$$\text{Nu}_D = 0.135 \text{ Re}_D^{0.69} \left(\frac{x}{D} \right)^{-0.34} \quad (4.3)$$

where Re_D ($= \dot{m}D/\mu A_{min}$) is based on the minimum cross-sectional flow area. The correlation is suggested for the parameter range of $1.5 < x/D < 5.0$, $0.5 < H/D < 3.0$, and $10^3 < \text{Re}_D < 10^5$. The geometric parameters are defined in Figure 4-8(a). For the thrust chamber, $D = 10 \mu\text{m}$ is chosen, with $x/D = 1.5$. Figure 4-8(b) shows the layout of the pins in the neighborhood of the throat. Figure 4-9 shows the predicted effective heat transfer coefficient for two different cases. One evaluates fluid properties at the bulk temperature, and the other at the film temperature. At the throat, the required effective h_c is between these two estimates, and it is likely that the actual heat transfer will also lie within this range. Because the precise location of the peak in heat flux is unknown, extra cooling is provided both upstream and downstream of the throat to provide additional cooling margin.

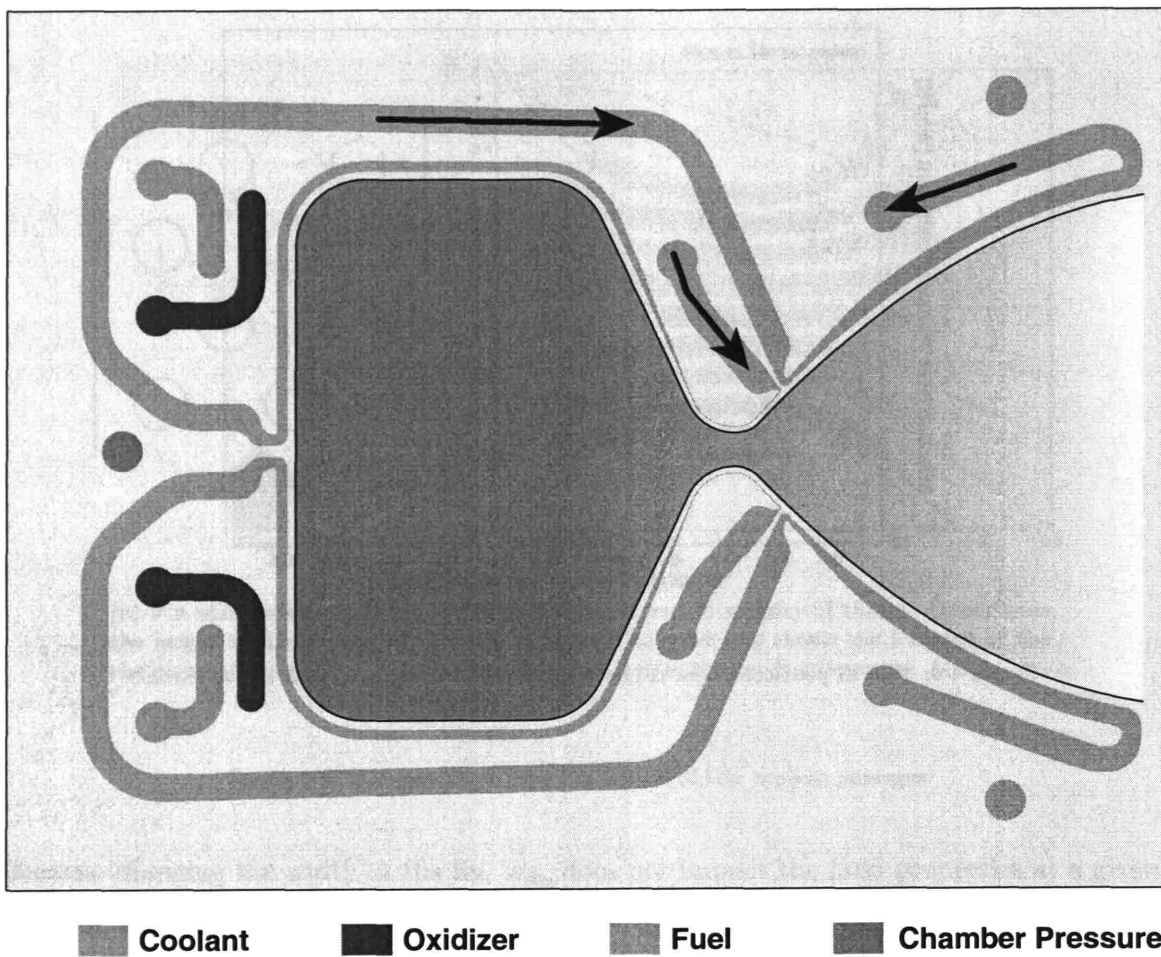


Figure 4-10: Illustration of the mask that defines the sidewall cooling passages.

4.3.7 Side Cooling Passage Design

The sidewall cooling flow enters the chip at the same location as the top and bottom cooling flow. There are six sidewall cooling passages, three each on each side of the chamber. The passages are each nominally a constant $400 \mu\text{m}$ high, but in practice the height is less in the vicinity of the throat where non-idealities in the etching process cause smaller features to be etched more slowly than larger features.[¶] The final design of the sidewall cooling channels is pictured in Figure 4-10. Because of symmetry, only one channel must be designed. The coolant begins to cool the wall approximately 1 mm downstream of the throat and flows

[¶]The etching conditions were highly customized to minimize this effect during the fabrication process. See Chapter 5 for a discussion of this effort.

towards the throat in a manner analogous to the top cooling channels. Near the throat, so-called “turbulators” are introduced on the side walls to locally increase the heat transfer into the coolant. For the chamber cooling, the heat load is lower, and the passage widens as necessary. The cooling passages wrap all the way around to the engine centerline at the forward end of the chamber. At this point, the three passages from one side are combined and piped around to just downstream of their entry point, where they cool the expansion nozzle sidewalls. Finally, they are recombined and the sidewall coolant exits the chip from the inboard pair of coolant exit ports.

Passage Width and Turbulator Design

The process for the design of the side cooling passages is quite similar to that of the top cooling passages, though the geometry limits the number of design parameters available. The thickness of the wall separating the coolant and the hot combustion gases is tailored as a function of position, something not available in the design of the top-wall cooling where the wall thickness is only a function of etch depths. The nominal side wall thickness is $120 \mu\text{m}$, but is decreased to $80 \mu\text{m}$ near the throat to reduce the temperature drop across the wall, thereby easing the requirement on the cold-side heat transfer coefficient, h_c .

The width of the cooling passage is chosen using the nominal design correlation to provide the required h_c at each axial location, except in the region near the throat. Near the throat, this design approach would require a passage width less than the minimum width deemed feasible for fabrication. Based on previous fabrication experience, this minimum width is set at $8 \mu\text{m}$ [7]. As can be seen in Figure 4-11, the nominal correlation predicts an h_c for the $8 \mu\text{m}$ wide passage at the throat that is approximately two times lower than required. To increase h_c locally, transverse ribs, or “turbulators,” are placed on the side walls. As was the case with the pins above the throat, the gas turbine cooling literature describes results for turbulators in channels whose Re are similar to those found in the present work.^{||}

The work of Han and colleagues [17] consistently suggested an h_c for the roughened passages at least a factor of two larger than a smooth passage over a large range of Re . Liou and

^{||}The Re of the side passage near the throat is 3000 if viscosity is evaluated at the bulk temperature, and 7000 if it is evaluated at the film temperature. By comparison, Liou and Hwang [27] investigated ribbed channels with Re 5000 and above.

Hwang [27] extended the investigations to lower Re and suggest a correlation of the form:

$$\frac{\text{Nu}}{\text{Nu}_s} = 10.721 \text{Re}^{-0.144} (p/H)^{-0.121} \quad (4.4)$$

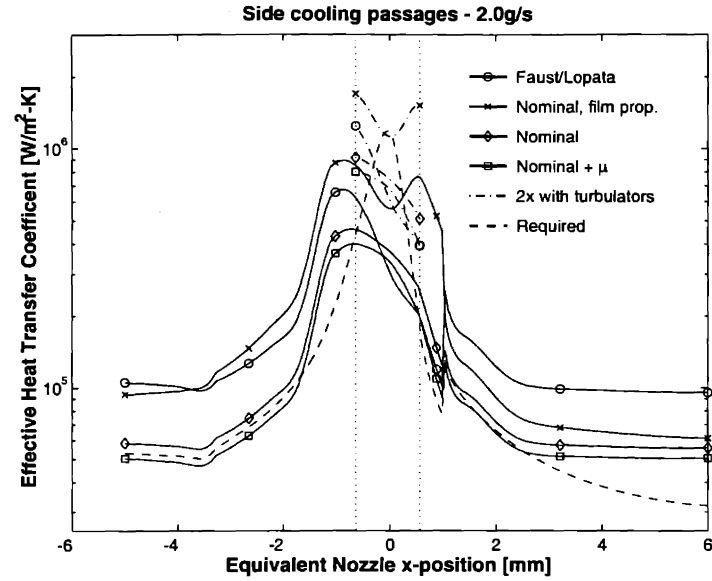
where Nu_s is the smooth duct Nu, and p/H is the pitch (distance between ribs in flow direction) to height ratio of the ribs. The above correlation is for a turbulator height to hydraulic diameter ratio of 0.063, which corresponds to a rib height of approximately 1 μm at the throat. A p/H of 15, meaning the ribs are placed every 15 μm in the flow direction, is selected for the design. Figure 4-11 shows the prediction of Equation 4.4 for the side cooling passages, as designed and with an additional 25% of the design cooling flow.

4.4 Thermo-Structural Design and Modeling

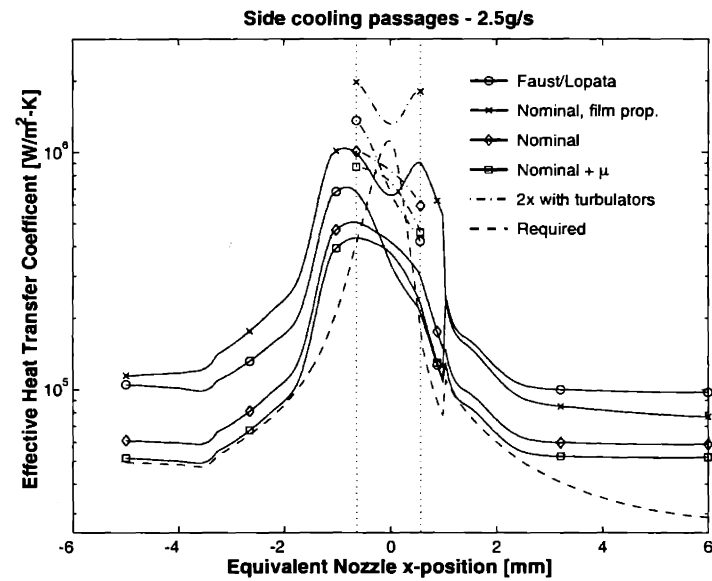
As part of the design process, decisions were made regarding the thickness of walls, the maximum allowable span of side and top cooling walls, thickness of the chamber wall, and minimum allowable fillet radii at the bottom of etched features. Additionally, the one-dimensional approach presented above for the cooling passage design was complemented by a number of two and three-dimensional simulations using the ABAQUS finite element structural modelling code. This section will describe these structural choices, and present some results of the numerical stress and heat transfer calculations.

4.4.1 Structural Design Choices

Single-crystal silicon is a relatively strong material. Chen [10] performed an extensive investigation of its properties for micro-heat engines. As it is a brittle material for temperatures below 800 K, the strength is highly dependent on the surface flaws created through processing techniques used in fabrication. He suggests a strength in excess of 1 GPa for the processing and etching techniques used in this work.



(a) Design case with 2.0 g/s of side coolant flow.



(b) Additional coolant case with 2.5 g/s of side coolant flow.

Figure 4-11: Predicted heat transfer coefficient for design geometry for two cooling flow rates. Nominal design point is (a). The Lopata/Faust curve is based on data from [13]. The design away from the throat is conservatively based on the nominal correlation using bulk fluid properties. The “film prop.” curve is the nominal correlation where properties are evaluated at a film temperature. The nominal + μ correlation is designed to account for viscosity variation in the flow. The vertical lines depict the region near the throat where the turbulators are added.

4.4.2 Cooling Passage Wall Thickness

Based on the model developed to scale the required wall thicknesses in Chapter 2, a first estimation of wall thicknesses may be made by considering the maximum length-to-thickness ratio:

$$\frac{l_w}{t_w} = \sqrt{\frac{2\sigma_{max}}{p}} \quad (4.5)$$

For a pressure of 300 bar, the maximum allowable l_w/t_w is 8 for a σ_{max} of 1 GPa and 4.5 for a σ_{max} of 300 MPa. For areas of the design where the wall thickness is not critical, a ratio of 4 is chosen as a default for the cooling passages to provide for a design margin.

Side Cooling Passages

Near the throat, the sidewall cooling passage wall thickness is critical, however, as it is one of the limiting factors of the design. As was mentioned previously, the wall thickness is reduced from 125 μm away from the throat to 80 μm near the throat. This smaller wall thickness requires additional calculations to verify its structural soundness. To this end, a calculation was performed on a two-dimensional slice of the coolant wall, pictured in Figure 4-12. At the throat, where both the the wall and cooling passage are narrowest, the wall is actually curved, with a radius of 750 μm to the hot-side of the wall. For this reason, both an axisymmetric and plain strain calculation are performed. The axisymmetric case simulates the curved wall, and the plain strain case simulates a straight and infinitely long wall. The fillet radius and wall thickness are varied, and maximum principal stress is shown in Figure 4-13 for the 80- and 100 μm thick wall cases. One can see that stress is much reduced in the curved wall as expected, and that a 100 μm thick straight wall is essentially equivalent to an 80 μm thick curved wall. Fillet radii above 7 μm are generally sufficient, though even at the throat where the maximum fillet radius will be about 5 μm , the predicted peak stress remains less than 1 GPa, at 850 MPa.**

**The mask width is 8 μm , but at least 1 μm of growth is expected on the trench sidewalls, leading to a baseline width of 10 μm . Thus the fillet radius will be $\leq 5 \mu\text{m}$. However, since the etch will tend to be shallower here, the wall span will be less than the baseline 400 μm , and the expected stress correspondingly less also.

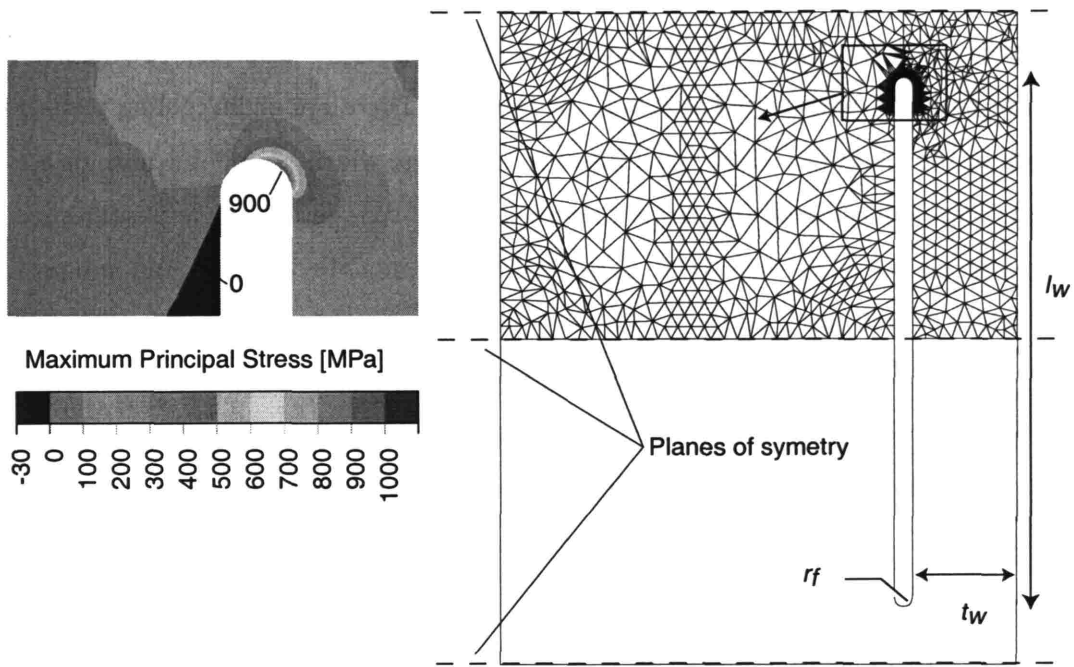


Figure 4-12: A sample calculation used in the cooling wall width and fillet radius study. The closeup shown is of the result of the $t_w = 80 \mu\text{m}$ and $r_f = 7 \mu\text{m}$ calculation.

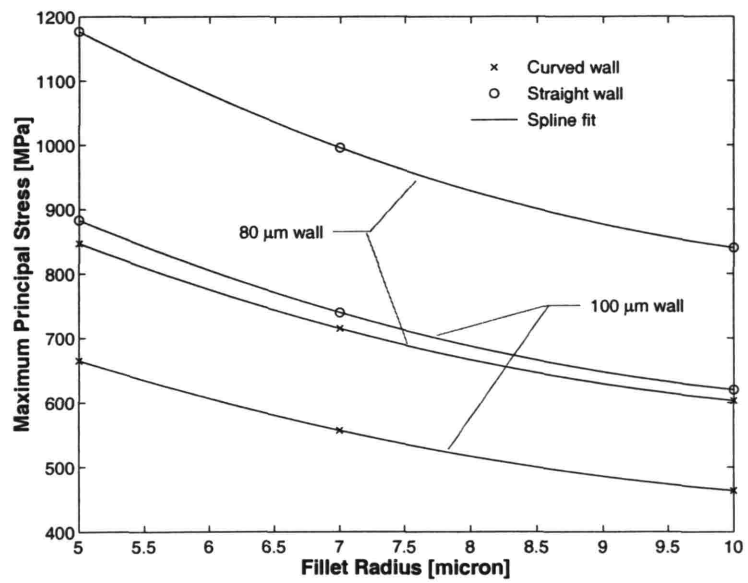


Figure 4-13: Results of Wall thickness and fillet radius study.

Top Cooling Passages

The above results for the straight walls are generally applicable to the top cooling passages, which are designed with a wall thickness of $100 \mu\text{m}$. There are eight cooling passages on each side of the chamber, which would lead to a passage width of about 1 mm, or a l_w/t_w of 10. As this is considered too large, the passages are split into two sub-passages, as was discussed in earlier in Section 4.3.6. The walls separating the passages and sub-passages have a width of $100 \mu\text{m}$, leaving a $400 \mu\text{m}$ span for the cooling walls, exactly analogous to the straight side cooling walls considered above. In the aft part of the cooling jacket above the expansion nozzle, the width of the cooling passage again becomes too large, and elongated posts are added to reduce the span to an acceptable level.

4.4.3 Chamber wall thickness

The design chamber pressure is 125 bar, and thus the simple model presented above suggests a maximum l_w/t_w of 9 for σ_{max} of 500 MPa. The chamber is 8 mm wide and approximately 5 mm in length. The selected wall thickness of $660 \mu\text{m}$ corresponds to a span of 5.9 mm, which is conservative as it is the shorter of the two spans that to first order controls the strength of the chamber wall. In addition, a three dimensional stress calculation was performed on the full chamber geometry, and is pictured in Figure 4-14. This calculation predicts that the peak stress is at the forward edge of the chamber, and is approximately 800 MPa.

4.4.4 Thermal modelling

In addition to the structural modelling discussed above, extensive two dimensional thermal models of the structure were developed. These were used to verify the one-dimensional cooling passage design process discussed earlier in this chapter. Two pertinent examples are presented in Figures 4-15 and 4-16. They show the expected temperature at cross sections through the throat and the chamber.

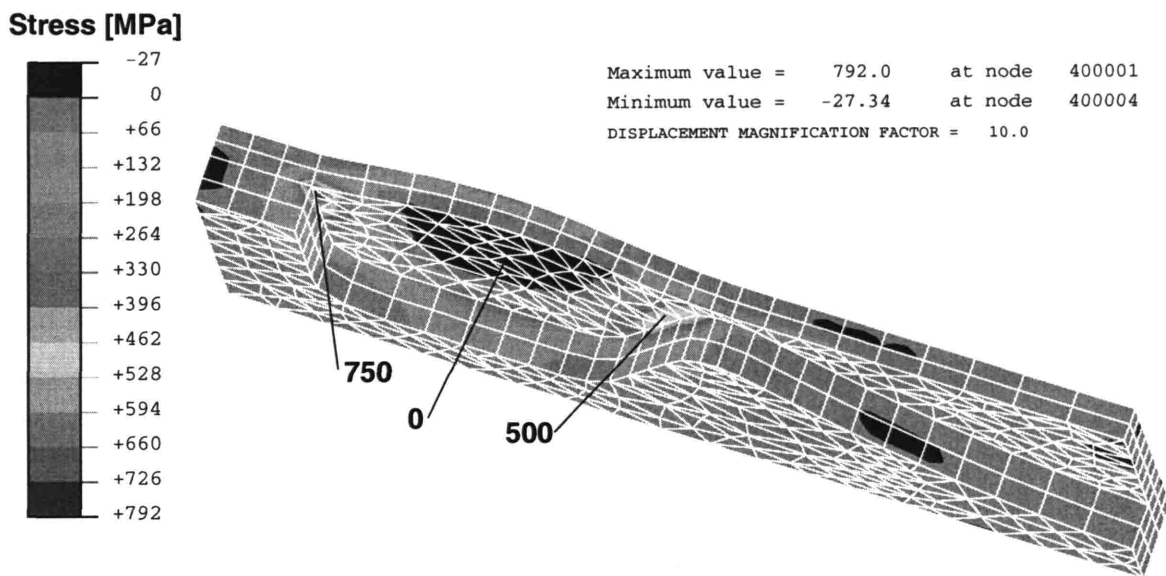


Figure 4-14: A simulation of the tensile stress levels in the chamber wall.

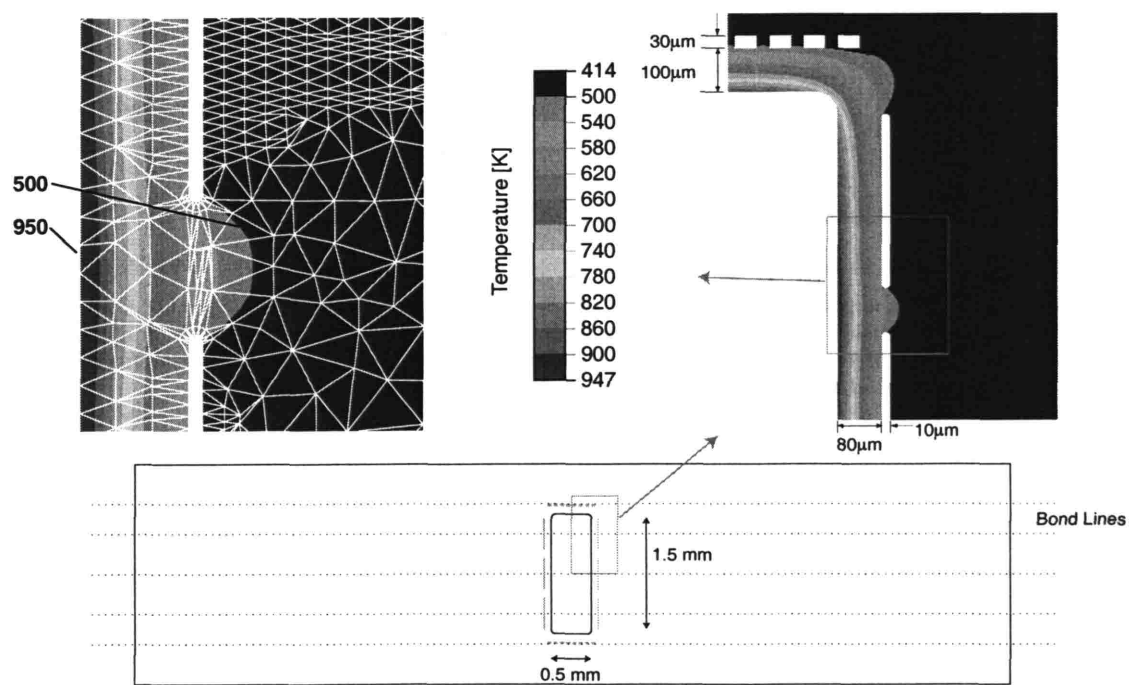


Figure 4-15: The throat cross-section, showing temperature profiles through the throat wall

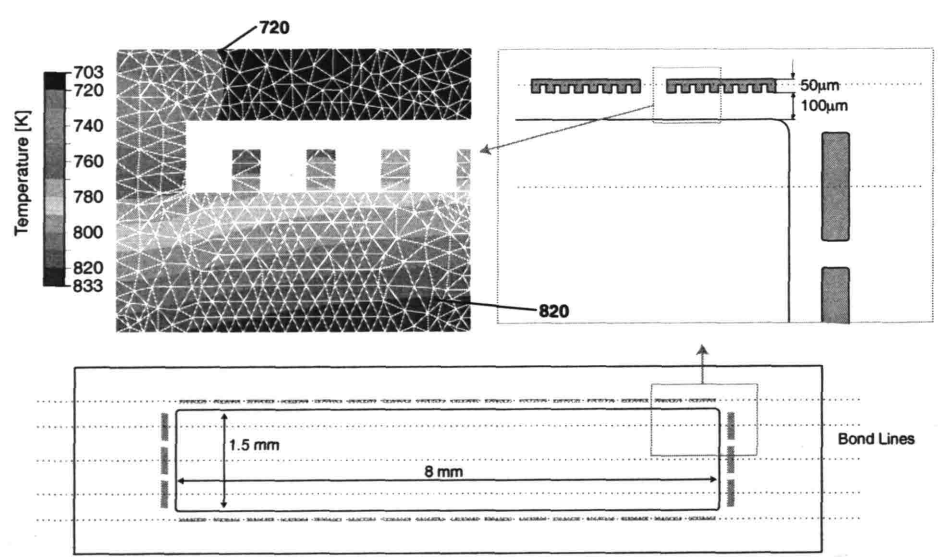


Figure 4-16: Chamber cross-section showing temperature profiles through the chamber wall. As the outside wall temperature is 70 K below the design temperature, it is apparent that there is more cooling area than is necessary. In the final design, the number is decreased to two per sub-passage, rather than the seven pictured here.

4.5 Injector Design

This section describes the design of the propellant injectors. As was discussed in Chapter 2, in the eventual engine system a near-sonic injection of the propellants is desired to minimize the potential for dynamic coupling between the pumping system and the combustion process. Due to fabrication constraints, the injectors are located on the upper and lower walls of the combustion chamber, and are placed on a square grid alternating between fuel and oxidizer. On the opposite wall, the pattern is reversed, so that each fuel jet shares a centerline axis with, and impinges on, an oxidizer jet from the opposite wall, and vice versa. Figure 4-5 shows the interdigitated fuel and oxidizer manifolds that feed this checkerboard pattern.

This design leads to the propellants being injected transverse to the main flow path. There is much literature available on transverse injection, but in this case, as the ratio between the momentum flux of an injector and that of the cross flow is approximately 800, the cross flow can effectively be ignored. In the design, the injectors are simply treated as jets emptying into a quiescent volume.

4.5.1 Injector Spacing

The first design choice was the spacing of the jets. LeFebvre [25] suggests that the velocity field of a jet as a function of radius from the jet centerline at a distance x downstream of the jet injection plane can be approximated as

$$\frac{U}{U_m} = e^{-K_u \left(\frac{r}{x}\right)^2} \quad (4.6)$$

If an effective jet width is defined as that radius where the velocity has fallen to some small fraction f of its centerline value, one can write

$$\frac{r_j}{x} = \sqrt{\frac{\ln f}{-K_u}} \quad (4.7)$$

According to LeFebvre, $K_u \sim 88$, so $r_j/x \sim 0.185$ for $f = 0.05$, and the jet spreading angle is approximately 10.5 degrees. It is desired to have two jets next to each other meet

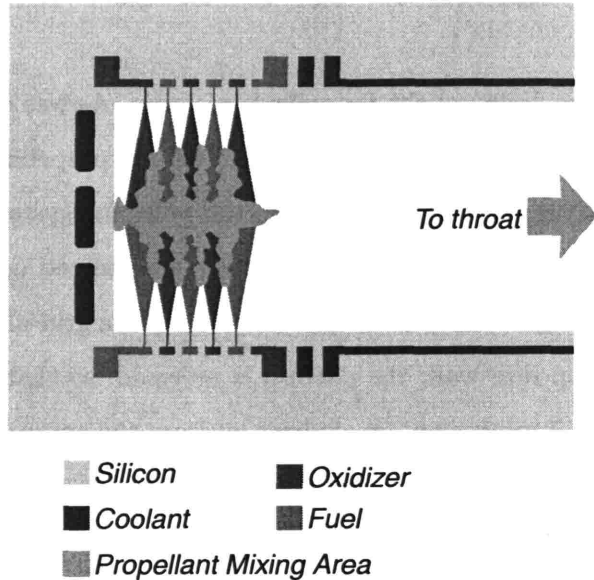


Figure 4-17: A cross section through the five rows of injectors. It is drawn to scale where the height of the chamber is 1.5 mm.

approximately halfway to the chamber centerplane, so that there is shear mixing on each side of the jet, as well as the mixing from the jets impinging on each other from opposite sides of the chamber. This distance is nominally one quarter of the chamber height, or $375 \mu\text{m}$. This would imply an injector spacing of $138 \mu\text{m}$. A round number of $150 \mu\text{m}$ is chosen as the design grid spacing distance as the injector diameter will be approximately 10 to $15 \mu\text{m}$. A cross section through the injectors is shown in Figure 4-17.

LeFebvre suggests

$$\frac{U_o}{U_m} = 0.16 \frac{x}{D_j} - 1.5 \quad (4.8)$$

as the ratio of jet entrance velocity to jet centerline velocity. If $15 \mu\text{m}$ is taken as a representative jet diameter, the distance to the centerplane of the chamber is 50 diameters, and one would expect the centerline velocity to be about 15% of the jet injection velocity.

Given the spacing of injectors, the number of injectors can be determined. It is desirable to have the injectors mostly confined to the forward end of the chamber so that there is time and distance for the propellants to continue to react and mix as they proceed toward the throat. Based on this reason, and the results of the injector sizing discussed below,

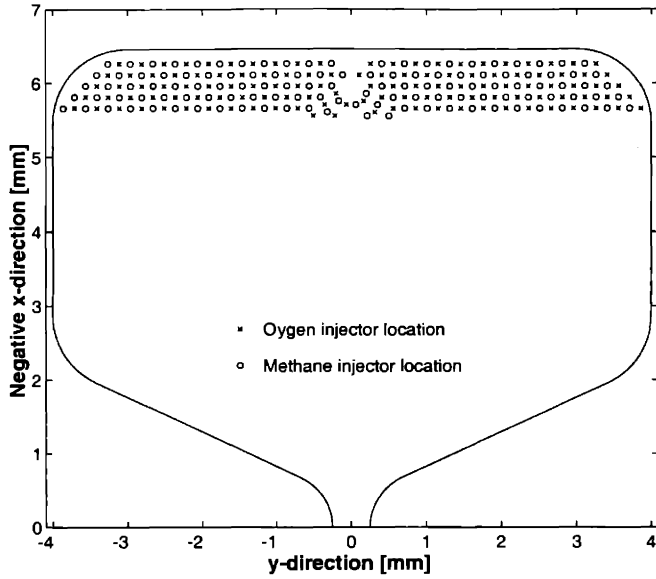


Figure 4-18: Locations of the oxidizer and fuel injectors, looking down on the chamber with the throat at the lower edge of the plot.

five rows of injectors are used, occupying most of the forward 1 mm of the chamber. This spacing and number of rows leads to a total of 484 injectors, 242 each for the oxygen and methane. The injector locations are pictured in Figure 4-18.

4.5.2 Injector Diameter

Ideally, the injectors should be made as small as possible. For a given total injector area, a larger number of injectors of smaller size will lead to a larger jet perimeter, and thus larger surface area at the interface between oxidizer and fuel. This in turn will lead to improved mixing. As these injectors must be etched through the $100\ \mu\text{m}$ wall separating the main flow path from the injection manifolds, there is a minimum feature size that can be successfully resolved and etched. This minimum feature size is approximately $10\ \mu\text{m}$.

For the purposes of calculating a design injector diameter, both methane and oxygen are considered ideal gases.^{††} Given that the eventual flow rate and mixture ratio will be controlled by the supply pressure in the propellant supply system, the precise fabrication of

^{††}This is an excellent approximation for oxygen at the design injection condition of 150 bar and 350 K, but less so for methane, as its compressibility factor, $Z = P/\rho RT$, at these conditions is 0.92.

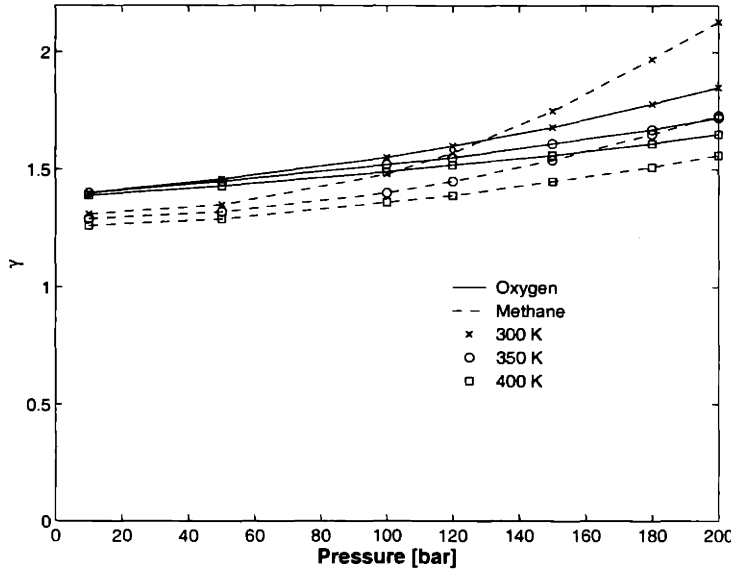


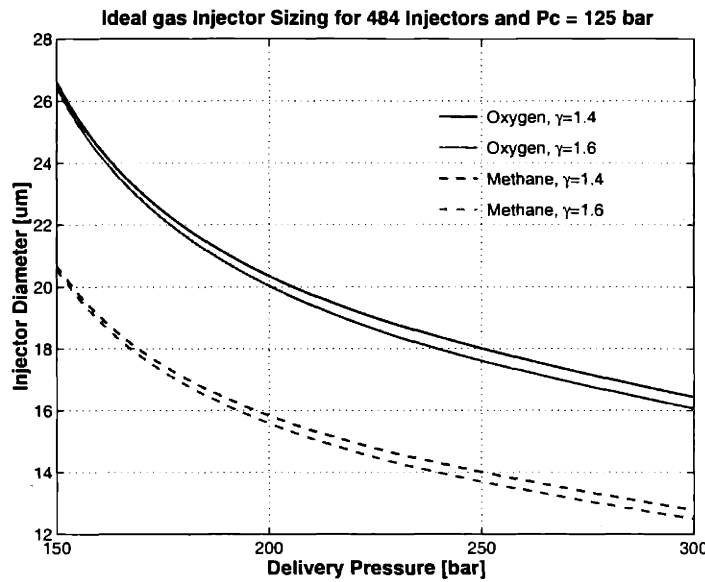
Figure 4-19: Specific heat ratio, γ , of oxygen and methane for different temperatures and pressures. The data are taken from refs. [39, 40].

the injector to a specific diameter is not very critical, so variations of γ , the specific heat ratio, with pressure and temperature (see Figure 4-19) are considered only to bound the calculation.

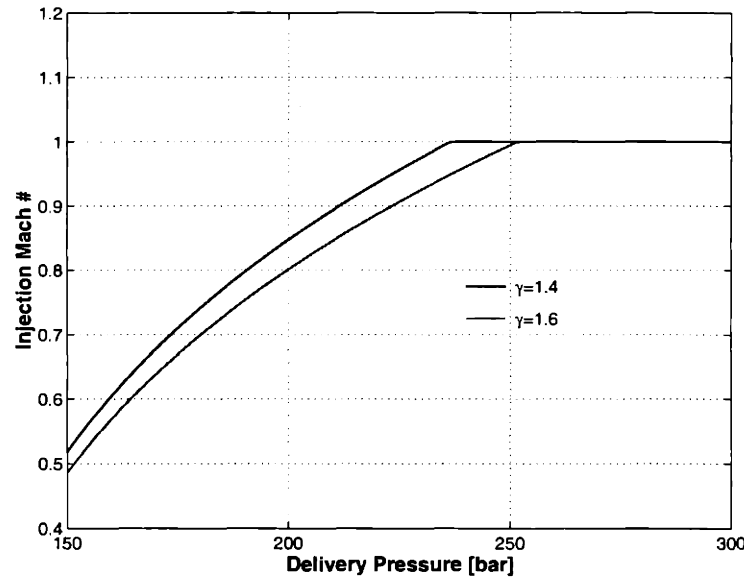
Given an average γ , the design chamber pressure, and a range of supply pressures upstream of the injectors, the pressure ratio, and thus injection Mach number, can be calculated, as is pictured in Figure 4-20(b). Given the Mach number, and total temperature, the flow per unit injector area,

$$\frac{\dot{m}}{A_j} = \frac{P_j}{\sqrt{RT_t}} \frac{\sqrt{\gamma M^2}}{(1 + \frac{\gamma-1}{2} M^2)^{\frac{\gamma+1}{2(\gamma-1)}}} \quad (4.9)$$

is calculated, and used to determine the injector diameter, plotted in Figure 4-20(a). For choked injectors, the supply pressure must be approximately 250 bar, which corresponds to diameters of 18 and 14 μm for the oxygen and methane injectors, respectively. Given the expected enlargement through the fabrication process, the circles on the injector mask are made 13 and 10 μm , respectively.



(a) Calculated injector diameter for design mass flow of 5 g/s



(b) Injector Mach number

Figure 4-20: Ideal gas design charts for injectors: a) Diameter of injector at various supply pressures; b) corresponding injector Mach number.

4.6 Ignition

In the initial design, three holes from each of the top and bottom surfaces are provided with access to the chamber. The design intent was to have these used for the insertion of electrodes which would be used to draw a spark across the short dimension of the chamber, igniting the propellant mixture. In the first build of the thrust chamber, these six holes each had a diameter of $130\ \mu\text{m}$. It was not possible to locate electrodes of that diameter that had sufficient insulation to prevent electrical contact through the silicon structure from shorting out the pair of electrodes prior to them reaching a high enough voltage differential to produce a spark. Prior to the second build, a supplier of glass-coated tungsten wire with an outside diameter of 0.009 inch ($230\ \mu\text{m}$) was located, and the center pair of ignitor holes was enlarged to a diameter of $240\ \mu\text{m}$, while the other two pairs of ignitor holes was eliminated.

For all the tests reported in this thesis, the ignition was performed by a small spark gap inserted into the chamber through the throat, and the ignitor holes were sealed as part of the packaging procedure discussed in the next chapter.

4.7 Conclusion

This chapter has presented the design approach and final design of the demonstration thrust chamber. Based on the decisions presented here, the masks required for fabrication can be generated. This process as well as the fabrication and packaging of the thrust chamber are discussed in the next chapter.

CHAPTER 5

FABRICATION AND PACKAGING

5.1 Introduction

This chapter discusses the fabrication and packaging of the microrocket thrust chamber. Using the design decisions discussed in the previous chapter, a fabrication plan was created and a mask set was generated. Three builds of the thrust chamber have been completed, and the fabrication section will discuss how the lessons learned during the first fabrication translated into small changes in the fabrication process for the following builds.

The other focus of this chapter is the packaging of the finished device. As turbopumps are not yet in existence at these scales to provide high pressure fluids to the thrust chamber, a method was devised to transport high pressure liquid and gases from the laboratory bench-top setting to the internal passages of the thrust chamber.

5.2 Microfabrication Concepts

The rocket thrust chamber was fabricated using bulk micromachining techniques. These involve the selective removal of material from silicon wafer substrates through chemical etching. A number of etched wafers are then bonded together to form a laminated stack of finished devices. A more complete discussion of bulk micromachining can be found in many texts, such as that by Madou [?], but three aspects will be discussed briefly here. These are photolithography, used to define features on the wafers; nested masks, used to allow for two different etch depths on a given side of a wafer; and deep reactive ion etching (DRIE), the specific process used to do the etching for this work.

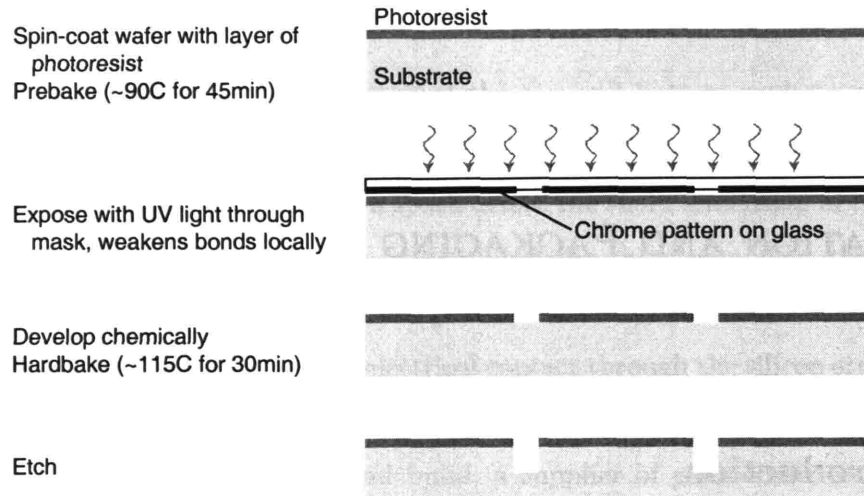


Figure 5-1: Masking and etching process

5.2.1 Photolithography

The fundamental unit process used in microfabrication is photolithography, illustrated in Figure 5-1. This is the process by which a pattern defined in chrome on a glass plate (called a mask) is transferred to the wafer where it can be etched. In this work, it is performed using contact exposure, where the mask pattern is a one-to-one image of the shape to be transferred to the wafer. A photo-sensitive polymer, termed photoresist (or simply “resist”), is spin-coated onto the wafer. It is then brought into contact with the mask, where the resist visible though the clear areas of the mask is exposed to UV light, causing a local weakening of the polymer’s bonds. It is then developed, essentially washing away the areas of resist that had been exposed to the light, and hard-baked. At this point, the resist can be used as a mask for a chemical etch of the substrate on to which it was coated. In this work, this substrate is either a silicon wafer itself, or a thin layer of silicon dioxide on top of a silicon wafer. In the case of the oxide layer, once it is patterned and etched, it can then serve as an etching mask for the silicon substrate below.

5.2.2 Nested Masks

One limitation of the basic photolithography process discussed above is that all features will be etched to essentially the same depth. There are a number of cases where two different

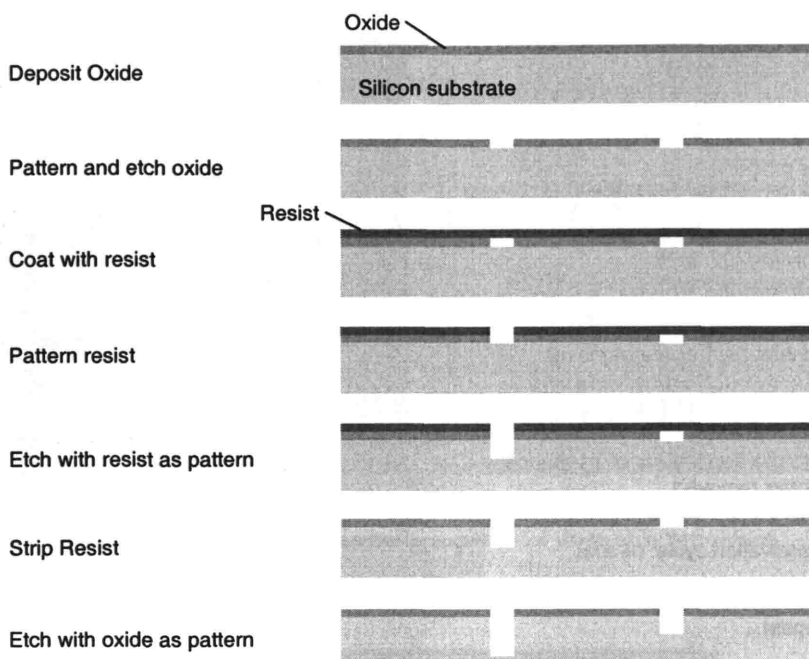


Figure 5-2: Nested mask process

etch depths may be required, leading to the introduction of a nested mask. Both oxide and photoresist can serve as a mask to the deep silicon etching process discussed in the next section. The nested mask process takes advantage of this to create a two-depth etch in one side of a wafer. The process is illustrated in Figure 5-2. It begins with the deposition of an oxide layer, which is patterned with the features for both the deep and shallow etches. The top of this mask is coated with photoresist, which is patterned with only the deep etch features. The etching begins with the photoresist mask, to a depth approximately equal to the difference in depths between the deep and shallow features. Next, the resist is removed, and the etch continues, using the oxide mask, until the shallow features reach their desired depth.*

*As etch rates are dependent on feature size and vary somewhat with feature depth, the actual time for each etch must be empirically determined for each nested-mask.

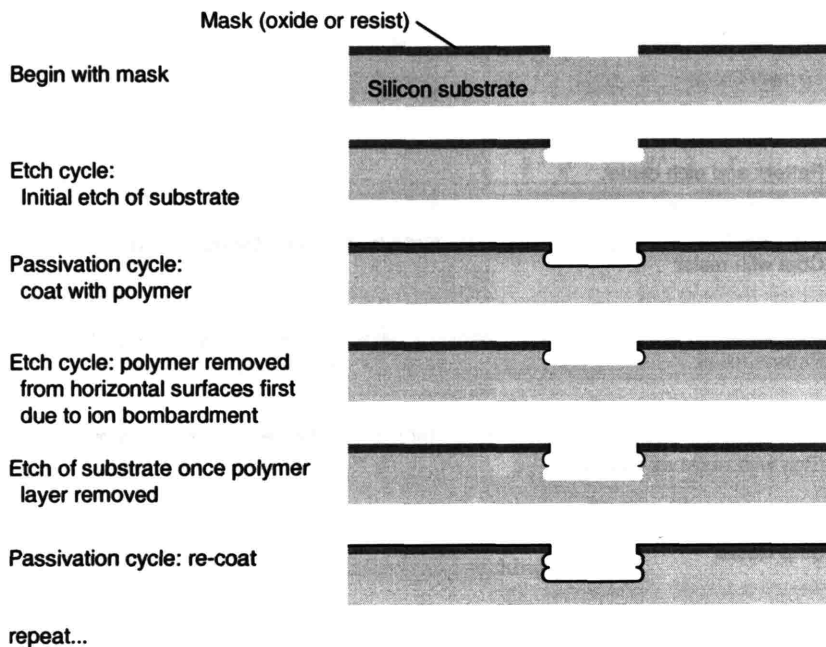


Figure 5-3: Time-multiplexed deep etching (TMDE) process steps

5.2.3 Deep Etching

The etching technique used in this work is time-multiplexed deep etching, or TMDE. The concept is illustrated in Figure 5-3, and is based on a process developed by Robert Bosch GmbH [?]. The etching tool used at MIT was manufactured by Surface Technology Systems, and has been extensively characterized by Ayon, et. al. [3, 4, 5].

The etching process proceeds with alternating etch and passivation cycles. The ion-assisted etch cycle produces a shallow, nearly isotropic etch into the substrate using a fluorine chemistry, with SF_6 as the feed gas. This shallow etch is then coated by a thin polymer layer in the passivation cycle, derived from C_4F_8 . During the etch cycle, the polymer is primarily removed by ion-bombardment, meaning the layer at the bottom of the feature is removed first, exposing this lower surface to the etchant, while leaving the sidewalls protected. The lower surface is etched, and passivation begins again, re-covering the side walls. The cycles of etching and passivation repeat until the desired feature depth is reached, and leads to a characteristic scalloping pattern on the side walls. This pattern is illustrated in Figure 5-4, a micrograph showing the interface between side wall and bottom of a test

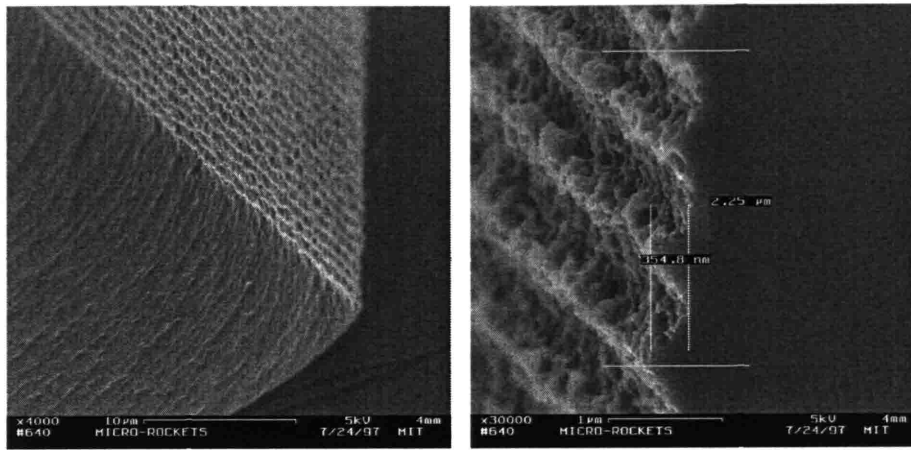


Figure 5-4: Scalloping of side walls as result of deep etch procedure.

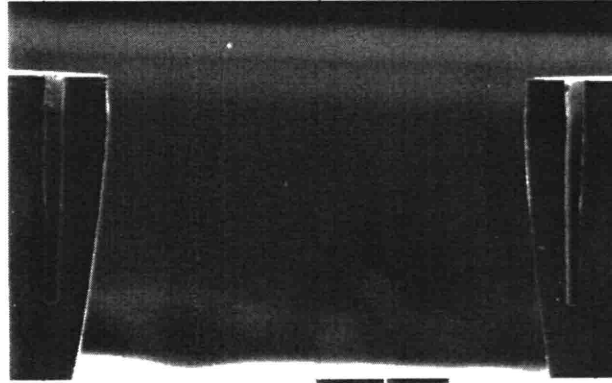


Figure 5-5: Micrograph of wafer cross-section at throat. This early test etch through a $450 \mu\text{m}$ wafer illustrates the dependence of etch rate on feature size.

etch near the exit of the microrocket nozzle. The size of this scalloping is small compared to the dimensions of interest in the microrocket and many other microdevices, meaning this etching technique can be used to produce deep features with straight walls.

5.3 Nozzle Etch Process Development

One of the primary fabrication challenges of the microrocket design is the need to etch the large chamber and nozzle features at the same time as the side cooling passages are etched. This etch, which occurs on six different surfaces in the process, is called the nozzle etch.

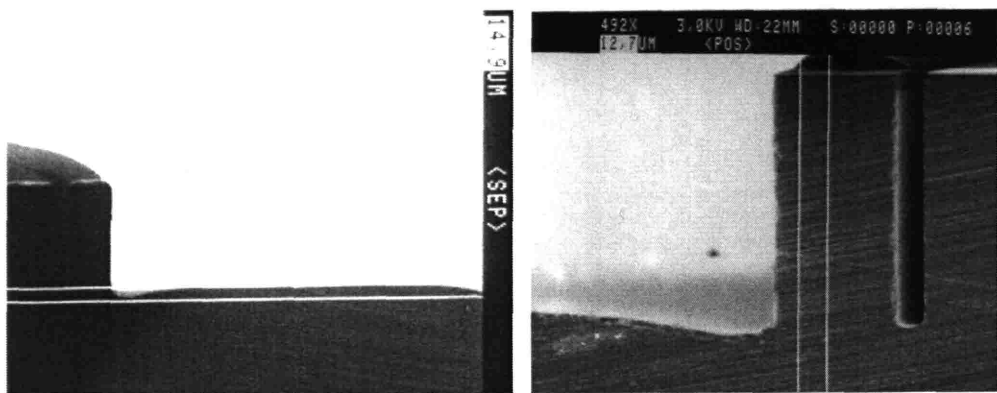
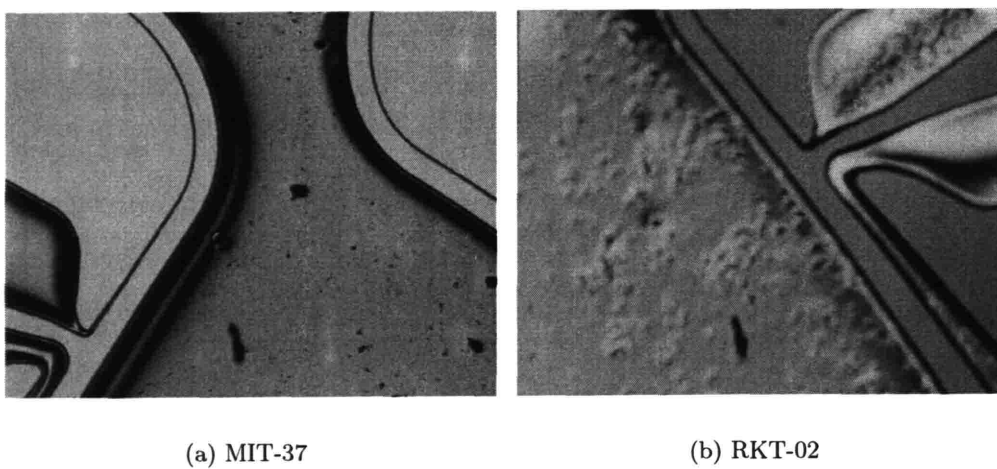


Figure 5-6: Example of Nozzle Etch using recipe MIT-37. Note convex bottom surface, but similar etch depth for cooling passage ($\sim 15\mu\text{m}$ wide) and nozzle throat (500 μm wide)



(a) MIT-37

(b) RKT-02

Figure 5-7: Example of surface roughness for two nozzle etches.

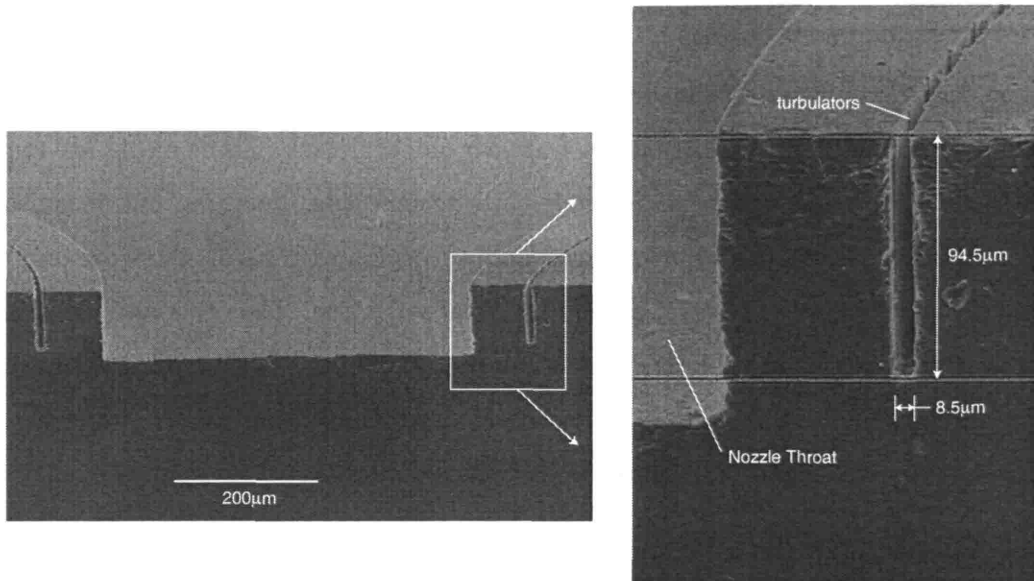


Figure 5-8: Example of Nozzle Etch using recipe RKT-04

For most etching conditions, small features etch more slowly than large features, as can be seen in Figure 5-5, a micrograph of the nozzle throat cross section after an early test etch of the rocket nozzle. In his work characterizing the etcher, Ayon reported an etch recipe that yielded an etch rate that was nearly independent of feature size, termed MIT-37 [3]. This recipe served as the basis for the development of the nozzle etch used in this work. The initial test etch performed using MIT-37 is shown in Figure 5-6. The lower surface is convex, which is not desired, and the high passivation flow leads to a rough bottom surface, seen in Figure 5-7. A series of etch recipes were tried, varying passivation cycle time, etch platen power, and APC angle[†]. The one termed RKT-04 was deemed the best compromise between surface roughness, bottom surface profile, and dependence of etch rate on feature size. The cross section of a test etch using this recipe is shown in Figure 5-8. The changes from MIT-37 are a decrease in APC angle and in passivation cycle time. The detailed parameters of this and other etch recipes used in this work are listed in Appendix B.

[†]Automatic Pressure Controller. The angle refers to the angle of a butterfly valve used to control the pressure in the etching chamber.

5.4 Mask Creation

Based on the overall layout of the device, and the decisions made during the design phase, it is possible to define the features that must appear on each mask. Three masks are required for each wafer, as each wafer has a single etch on one side, requiring one mask, and a nested etch on its other side, requiring two. However, symmetry means there are only three different types of wafers, so a total of nine masks are required. The otherwise identical top and bottom wafers require different masks for their top sides so that the fluid inlets are only on the top wafer, which implies the need for a tenth mask, but this is compensated by the fact that the wall plates and nozzle plates share one mask.

The detailed point-by-point geometry of the masks is generated using a number of MATLAB routines. Another set of MATLAB routines converts these shapes into small straight line segments, and writes a file containing a full description of the mask geometry in an industry-standard CIF format. This file is imported into a commercial mask design program called L-EDIT, where it is slightly edited, and output in the more compact, binary GDS format. This is the preferred format of the mask vendor, who uses this final file to produce the actual masks.

Table 5.1 identifies the nine masks, and the features that each one contains.

Figures 5-9 to 5-17 show the nine masks individually, and Figure 5-18 shows all the masks superimposed.

Table 5.1: Masks used in Fabrication

Mask	Name	Description
1	Top Holes	Fluid Inlet holes, die labels, ignitor ports
2	Top Shallow	Upper top cooling, propellant manifolds
3	Top Deep	Deep top cooling, propellant distribution
4	Injectors	Injectors, wall plate through holes, metering holes
5	Wall Cooling	Top cooling, propellant manifolds
6	Wall Interconn	Nozzle, side cooling, top cooling interconnect
7	Nozzle Nested	Nozzle, nozzle plate through holes
8	Centerline	Nozzle, side cooling, side cooling interconnect
9	Bottom Holes	Ignitor ports, die labels

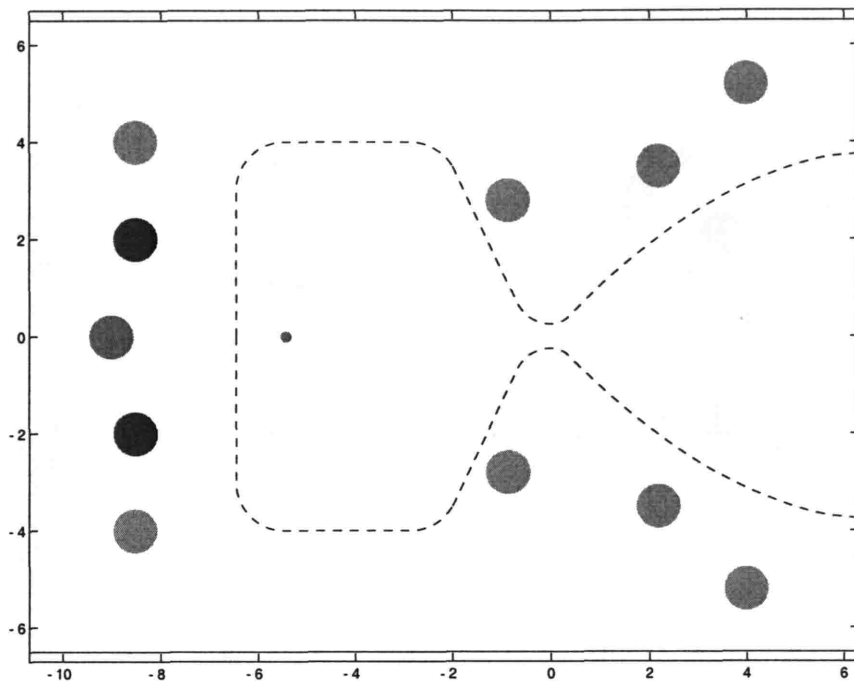


Figure 5-9: Mask 1. Top Holes. Defines inlet holes, injectors, and vents (not shown). Other features not shown identify individual die and show location for diesawing. Used for etch on front side of top plate. The dashed outline of the nozzle is not on the mask.

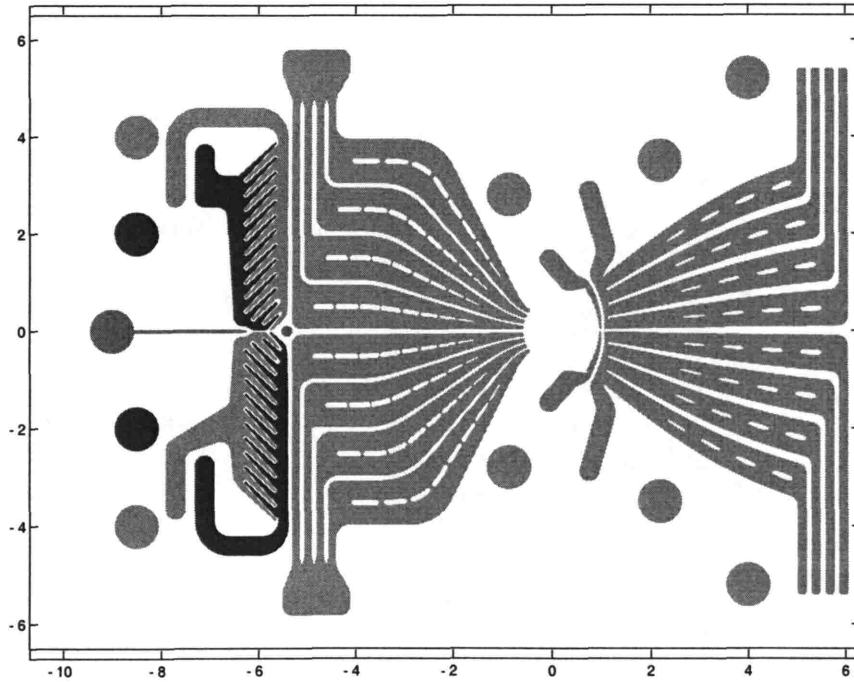


Figure 5-10: Mask 2: Top Shallow. Defines the upper half of the top cooling passages, and the propellant manifolds. Used for a shallow etch on the back side of top and bottom plates.

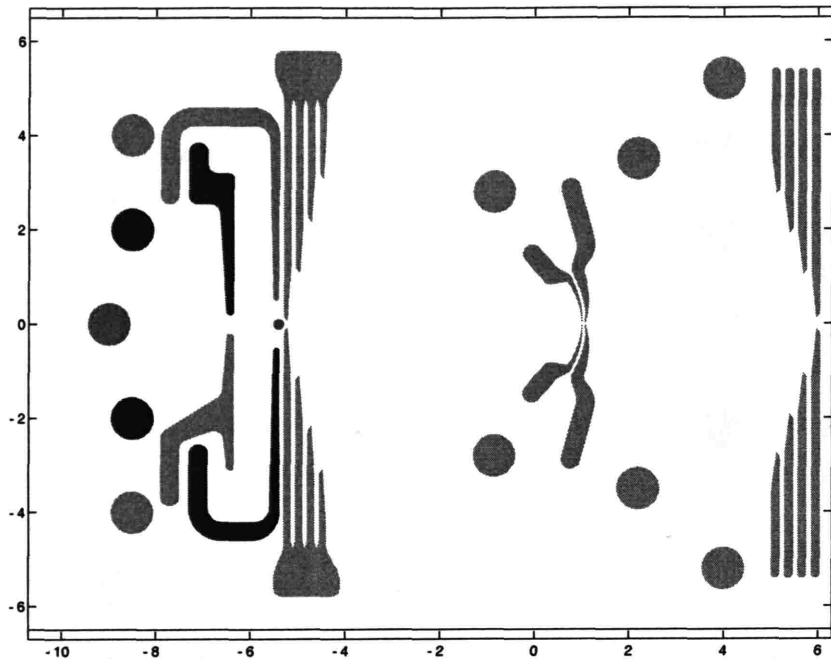


Figure 5-11: Mask 3: Top Deep. Defines passages that feed and collect coolant from top wall cooling, as well as direct propellants to the correct manifold. Used for 200 μm deep etch on the back side of top and bottom plates.

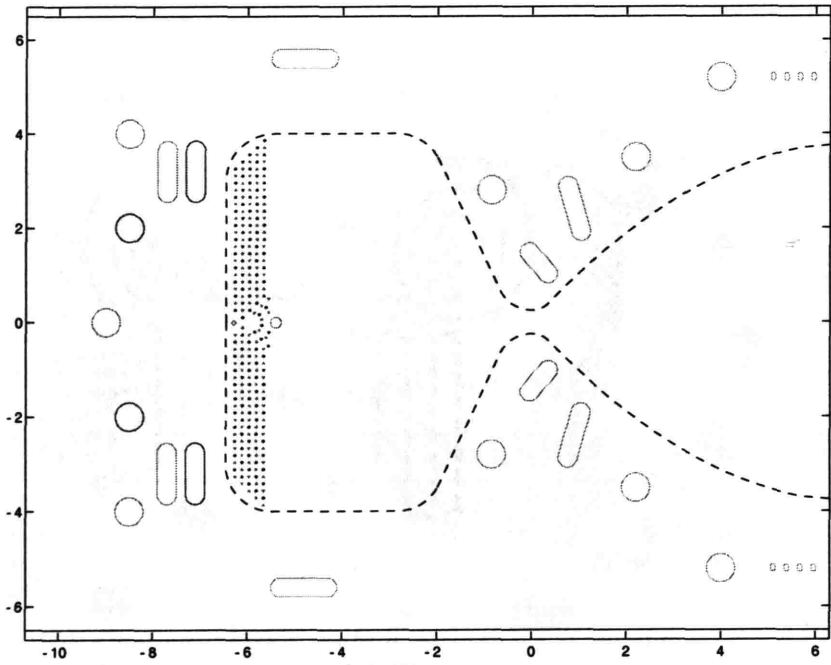


Figure 5-12: Mask 4: Injectors. Defines injectors, ignitor ports, coolant metering holes, and other features that must be etched through the wall plates. Outlines, termed "halos" (see section 5.5.3) define most features. Used in deep etch from front side of wall plates. Nozzle outline for reference only.

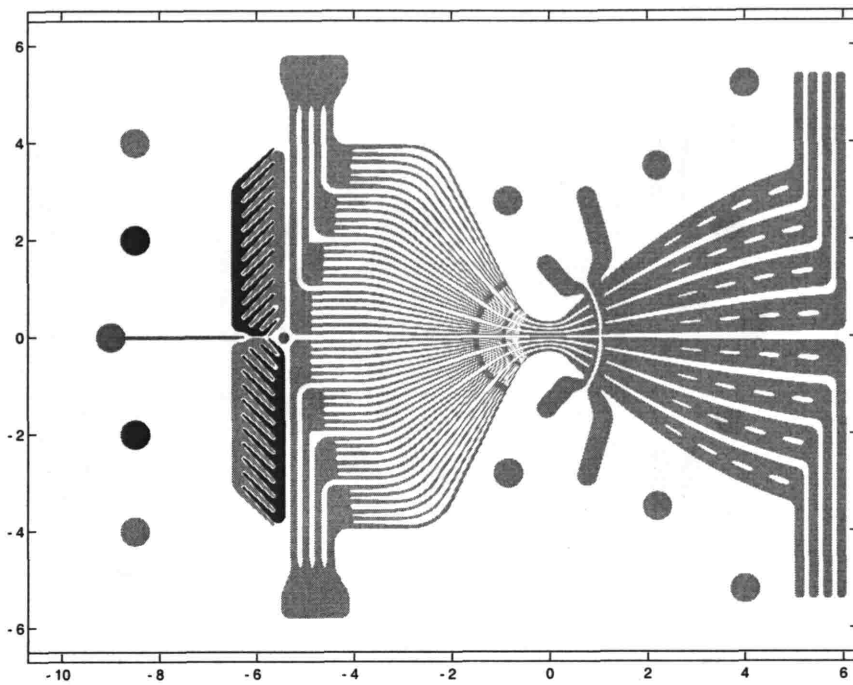


Figure 5-13: Mask 5: Wall Cooling. Defines the lower half of the top cooling passages, as well as the propellant manifolds. Used in shallow etch from front side of wall plates.

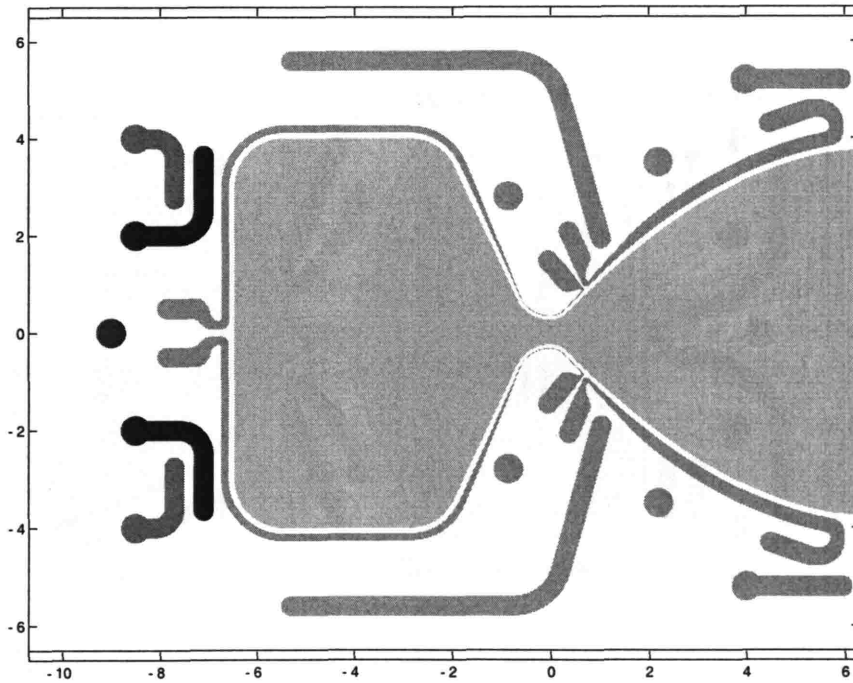


Figure 5-14: Mask 6: Wall Interconnect. Defines the main flow path, side cooling passages, and the passage than transports the top wall coolants from chamber to exit nozzle. Etched into the back side of the wall plates, and the front side of the nozzle plates.

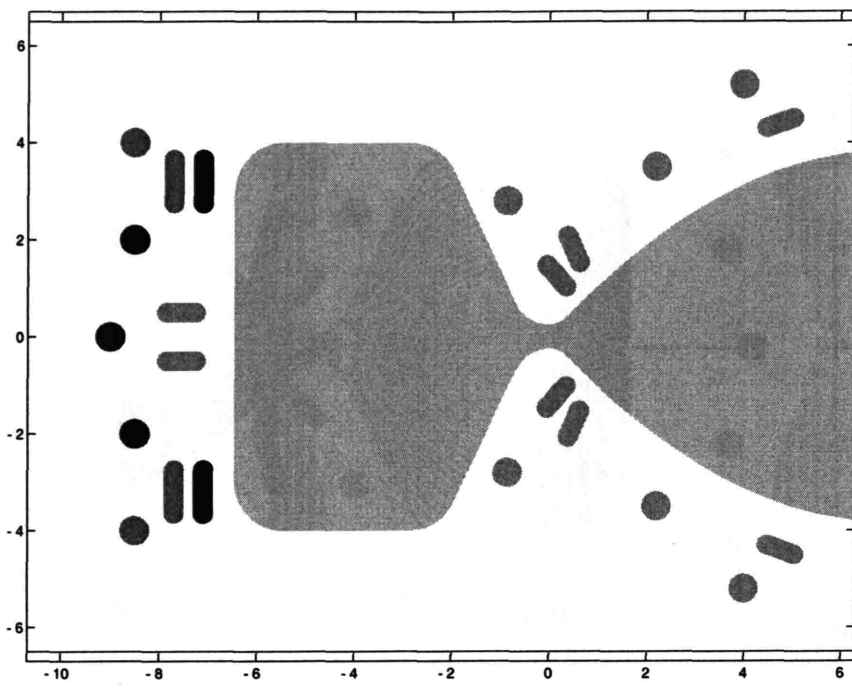


Figure 5-15: Mask 7: Nozzle Nested. Defines those features that must be etched all the way through the nozzle plates, particularly the nozzle. Used for a 150 μm "head start" etch on the front side of the nozzle plates prior to etching using Mask 6.

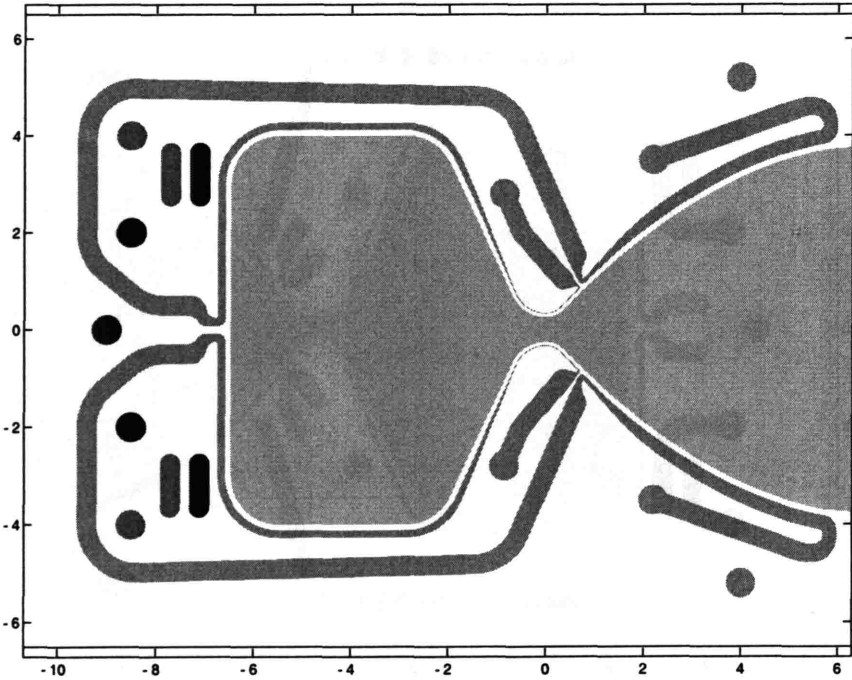


Figure 5-16: Mask 8: Centerline. Defines the main flow path, side cooling passages, and the passage that transports the side coolant from chamber to exit nozzle. Etched into the back side of the nozzle plates that forms the center plane of the thrust chamber.

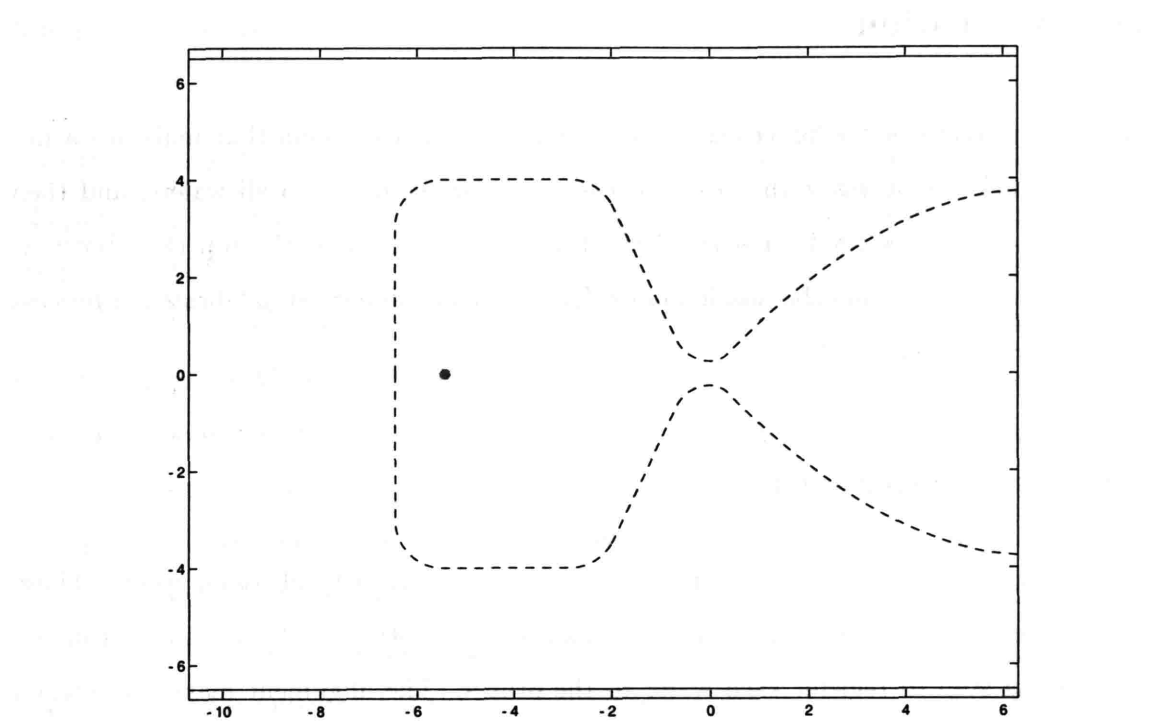


Figure 5-17: Mask 9: Bottom Holes. Defines the ignitor port and is used on the front side of the bottom plate instead of Mask 1, so that the inlet holes are not present. Also contains the die identification and diesaw marks. Nozzle outline shown for reference only.

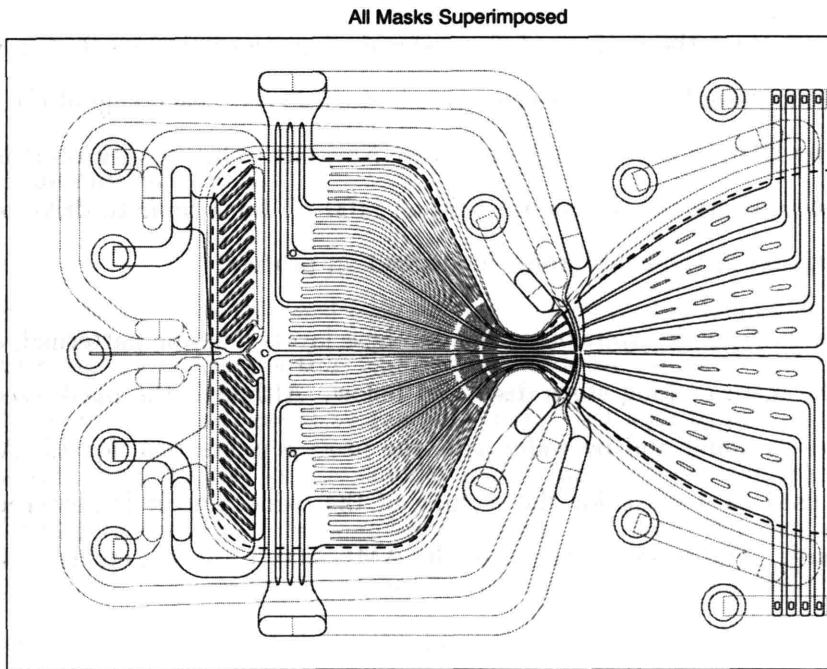


Figure 5-18: All masks superimposed. Shows the alignment of features from mask to mask. Only the outlines of features are shown, for clarity.

5.5 Fabrication

This section describes the processes used to fabricate the six wafers that make up a microrocket stack. It begins with those processes that are common to all wafers, and then discusses the steps required for each of the three types of wafers, the top (and bottom) plates, the wall plates, and the nozzle plates. The complete step-by-step fabrication process is presented in Appendix B.

5.5.1 Wafer preparation

The process begins with the definition of alignment marks on each side of all wafers. These alignment marks are used to register each mask to one another, and are also used in the final bonding step to register each wafer to the others. The alignment marks are etched approximately $1.5 \mu\text{m}$ deep, and the back-to-front alignment is performed using an infrared alignment system to see through the wafer.

Once all the wafers have alignment marks, the next step is the deposition of the silicon dioxide (usually termed simply “oxide” in this chapter) layer used both as a mask for etching and to protect the surface of the wafer during processing so that it will be more likely to bond successfully. $2 \mu\text{m}$ of this oxide is deposited on each side of the wafers using the ConceptOne CVD system manufactured by Novellus. This deposition is followed by a densification step where the wafers are held at 1100°C for 1 hour to drive off the excess hydrogen remaining in the oxide from the deposition process.

Once the wafers have oxide layers on each side, these layers must be patterned, as they serve as masks to the main etching steps discussed below. Although the mask used to pattern the oxide varies by wafer and by wafer side, the process is identical for all. A $2 \mu\text{m}$ thick photoresist is used as a mask for the etching of the oxide, and it is patterned using the appropriate mask. The oxide is etched in the AME5000, a plasma-etcher, using CHF_3 as the etchant.

Once the oxide on both sides of the wafers has been patterned, the primary fabrication steps that involve deep silicon etching can begin. These steps are described in more detail in the following sections for each of the three types of wafers.

5.5.2 Cap Plates

Like the rest of the wafers in the microrocket stack, three etches are used to define the 525 μm thick top and bottom plates. Processing begins on the front side, where first etch is approximately 350 μm deep and defines the top half of the inlet holes and ignitor ports. In the case of the bottom wafer, there are no inlet holes, so only the ignitor ports are etched. For the top plate, Mask 1 is used for this step, and for the bottom plate, Mask 9 is used. The back side of the wafer is then processed. Here the first etch is 200 μm deep using the first stage of the nested mask, defined in photoresist using Mask 2. This etch finishes the through etch of the inlet holes and ignitor ports and creates the deep parts of the top-side cooling passages used for coolant distribution and collection. The photoresist is stripped, and the previously defined oxide mask (#3) remains. A 20 μm etch is performed using this mask, defining the upper half of the top and bottom cooling passages. Figure ?? shows the front and back of one die from the finished plate, and Figure 5-20 shows the process for this wafer.

Process Enhancements

The first build of the microrocket used only an oxide mask on the front side of this wafer. It was discovered during processing that the 2 μm of oxide would be eroded during etching, limiting the feasible depth that could be reached in the first etch to about 300 μm for the large features and about 250 μm for the smaller ignitor ports. Since the ignitor ports pass all the way through this wafer to the chamber, the deep etch from the back side had to be made 50% deeper than was designed (About 300 μm deep rather than 200 μm). This was fixed for the second and following builds by providing an additional photoresist mask on top of the oxide (patterned with the same mask) that allows the first etch to proceed past its design of 350 μm depth. This in turn allows the back side deep etch to stop once its design depth of 200 μm is reached.

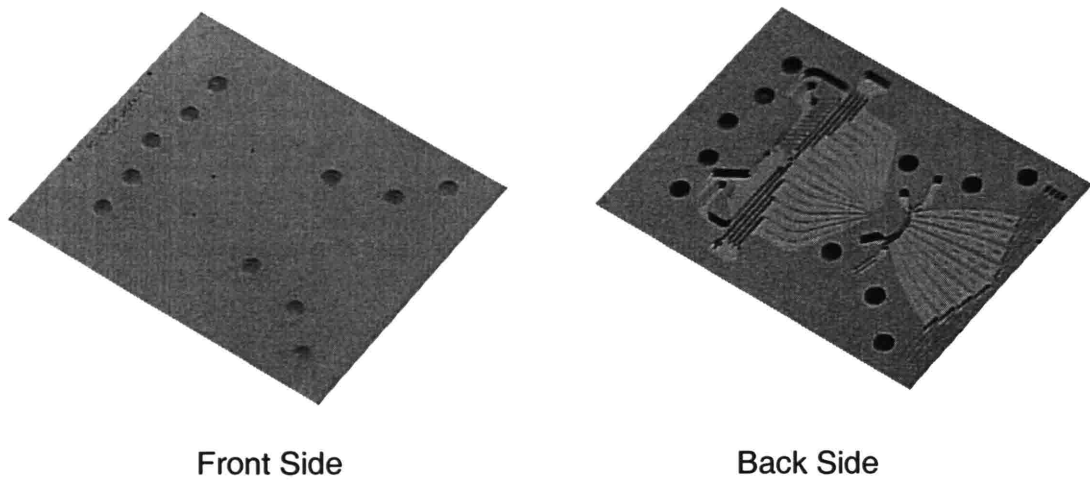


Figure 5-19: Cap Plate (Note: the bottom cap plate would have a different front side without the 11 fluid ports)

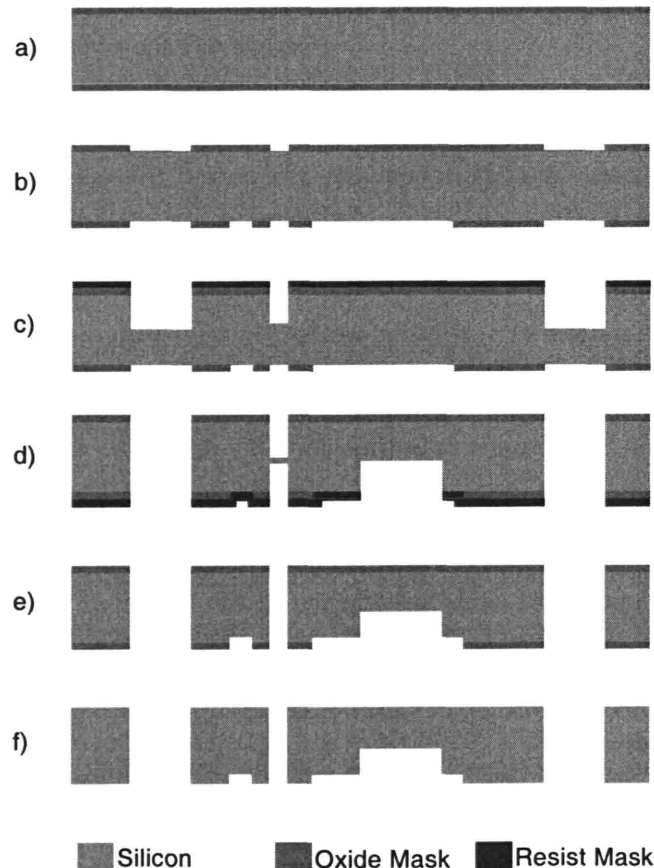


Figure 5-20: Top and Bottom Plate process

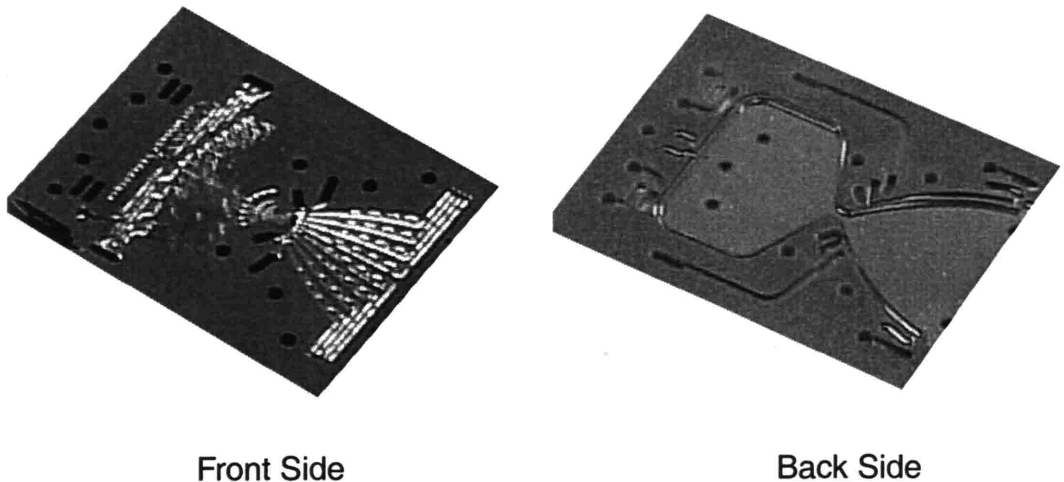


Figure 5-21: Wall Plate

5.5.3 Wall Plates

The $400\text{ }\mu\text{m}$ thick wall plates are the most challenging wafers to fabricate. They begin with a $250\text{ }\mu\text{m}$ etch using the nozzle etch recipe into their back side, with Mask 6 as the oxide mask. This is followed by a coating of thick photoresist on the front side, which is patterned using Mask 4 to define the injector holes and other features that must pass through this wafer. Since the injector holes are so small (10 and $13\text{ }\mu\text{m}$ on the mask), their etch rate is low ($\sim 1.2\text{ }\mu\text{m/min}$), and it takes a relatively long time to etch them through the $150\text{ }\mu\text{m}$ wall. Once this etch is complete and all the injector ports are through the chamber wall, the thick resist is removed, and the lower half of the top and bottom cooling passages are etched $30\text{ }\mu\text{m}$ deep using Mask 5, previously defined in the oxide layer. Figure 5-21 shows the front and back of one die from the finished plate, and Figure 5-22 shows the process for this wafer.

Process Enhancements

The etch that defines the injectors is performed with the wafer mounted to a quartz handle wafer. This allows it to be visually inspected to determine when the injector etch is complete. As was discussed earlier, large features etch more quickly than small features, which means that the large features defining through-wafer holes for propellant and coolant piping cleared

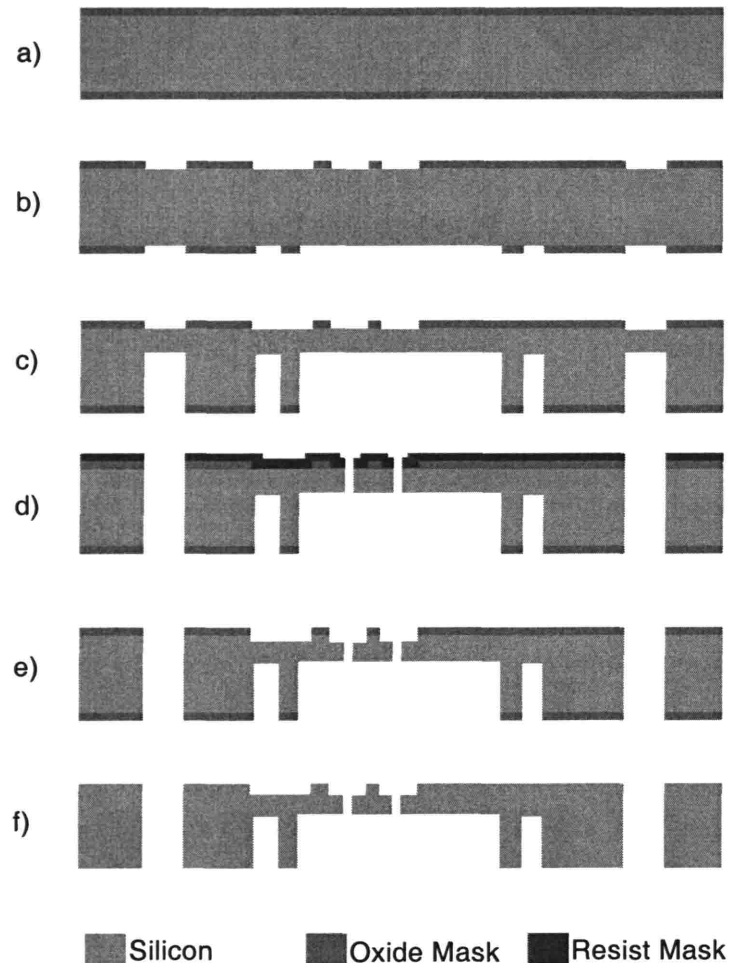


Figure 5-22: Wall Plate process

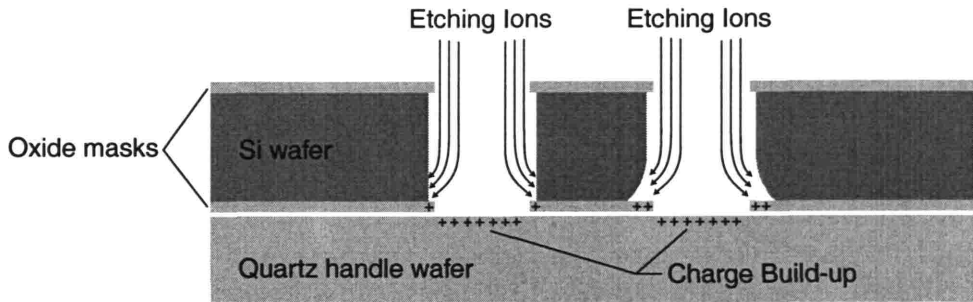


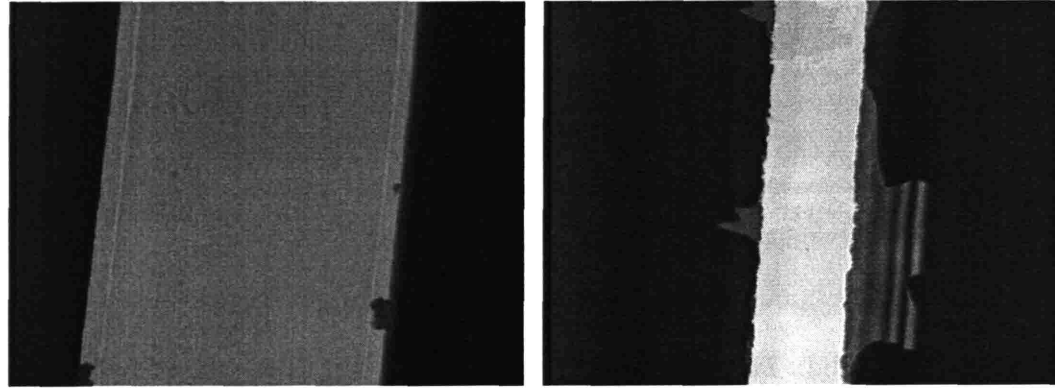
Figure 5-23: The trench at the left shows the initial charge build-up in the quartz handle wafer and in the oxide mask on the lower wafer surface that occurs once the feature being etched through the wafer has cleared. As the etching ions are deflected by the repulsion from these like-charges, they tend to impinge on the sidewalls and lead to significant depreciation, as shown in the right trench. See Ayon [6] for additional discussion of this “footing” effect.

before the injectors did. This meant that these features had to be over-etched, leading to significant side-wall damage (see Figure 5-24) from the so-called “footing” effect described by Ayon [6], where a charge build-up at the bottom of a trench leads to a deflection of the etching ions into the lower part of the sidewalls. This occurs when there is an insulated material such as oxide at the bottom of an etch, and is illustrated in Figure 5-23.

The solution to this issue is to introduce a halo mask for the injector etch step. A halo mask, as shown in Figure 5-12, is one where only a small ribbon around the periphery of a feature, or halo, is defined on the mask. The halo is etched through the wafer, causing the rest of the large feature to fall out. The halo etch allows for large features to be etched at similar etch rates as small features, without the need for a specially tailored etch recipe. A $15 \mu\text{m}$ wide halo was implemented on a new mask 4, and was used for the second and all following builds. The results are seen in Figure 5-25. Though some overetching is still required as long $15 \mu\text{m}$ -wide trenches will etch faster than injector holes with a diameter of $15 \mu\text{m}$, the sidewall damage is greatly reduced.

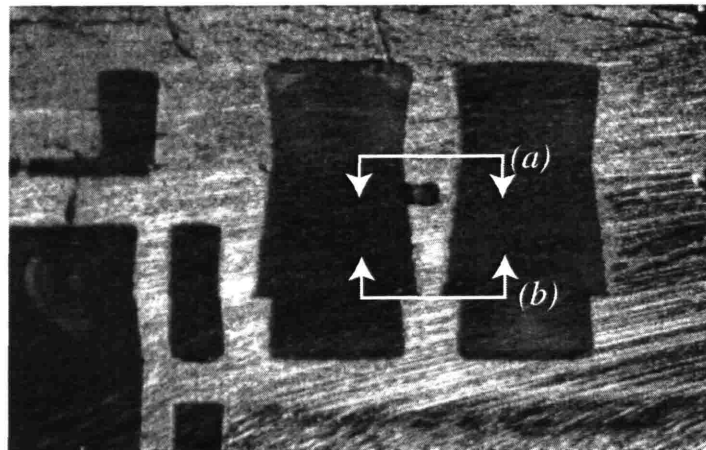
5.5.4 Nozzle Plates

The 500 or $525 \mu\text{m}$ thick nozzle plates have very similar patterns in each side of their oxide coating, defined by Masks 6 and 8. The first step is to add a photoresist mask to one side (usually the back side, which forms the centerplane of the rocket). This is defined by



(a) Front side of wafer

(b) Back side of wafer



(c) Cross-section, wall plate is center wafer

Figure 5-24: Wall Plate damage from footing effect. Both (a) and (b) are of same wall at same magnification (nominal width of $200 \mu\text{m}$). The bonding surface at the back side is reduced to less than a third of its previous width, seen in the bonded cross-section in (c).

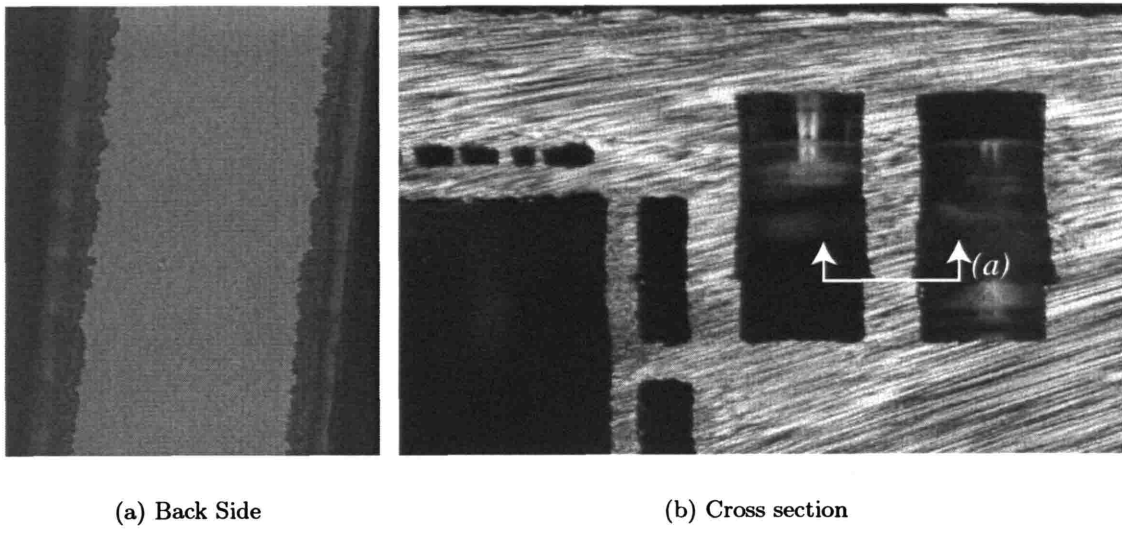


Figure 5-25: Wall Plate damage from footing effect is reduced. Image in (a) is of same wall in second build at same magnification (nominal width of 200 μm) shown previously. The use of a halo significantly reduces the over-etch damage seen in Figure 5-24(b).

Mask 7, which allows etching only in areas where the nozzle plate will be etched all the way through, primarily the chamber and nozzle itself. A 175 μm etch is performed using this mask, providing a head start for those areas that need to be etched through the wafer. This resist mask is then removed, and each side of the wafer is etched using the side cooling passage etch recipe to a depth of 200 μm . Figure 5-26 shows the front and back of one die from the finished plate, and Figure 5-27 depicts the process for this wafer.

5.6 Wafer Bonding

Once the 18 etching steps are completed, the six wafers are ready for bonding. The oxide masks, also serving as protection for the surfaces to be bonded, are stripped using BOE,[‡] and the wafers undergo a final cleaning procedure. They are then aligned and pressed together in an aligner-bonder manufactured by Electric Visions. The final step is a 1 hour anneal at 1100 °C to create the diffusion bond. Figure 5-28 shows an infrared image of the bonded first build of the microrocket, before and after the final anneal step. The fringes at

[‡] Buffered Oxide Etchant, a hydrofluoric acid solution

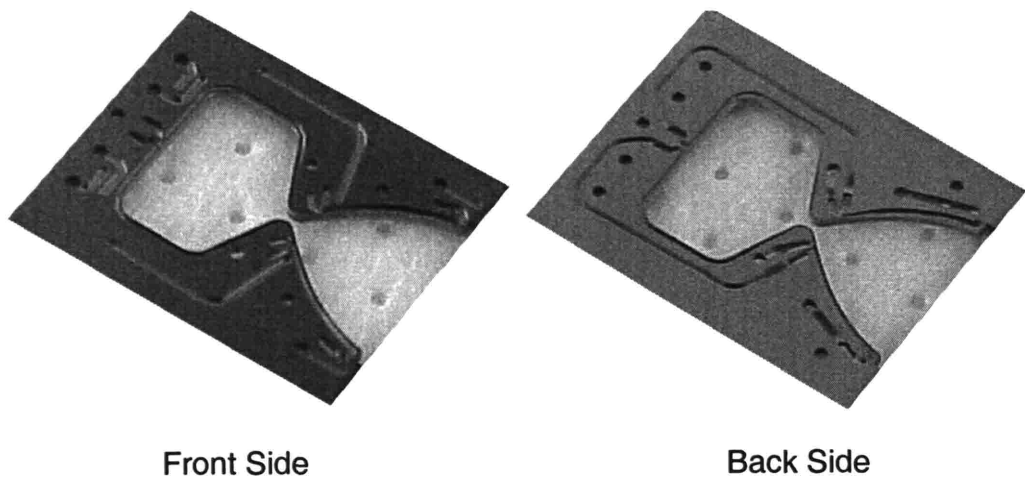


Figure 5-26: Nozzle Plate (Note: the texture and dots in the nozzle area are the surface the wafer is resting on when the pictures were taken)

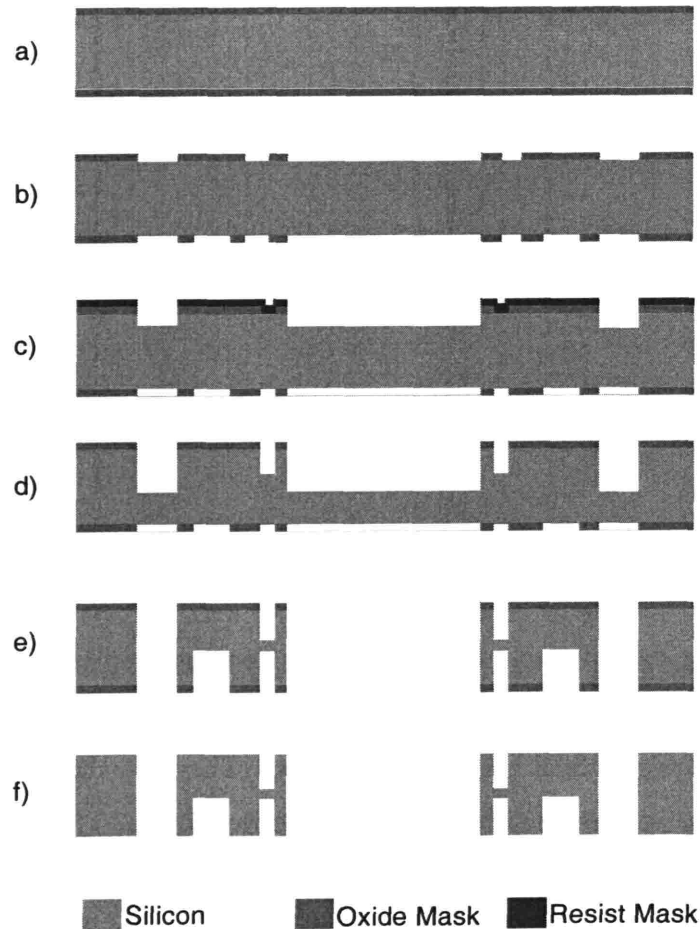


Figure 5-27: Nozzle Plate process

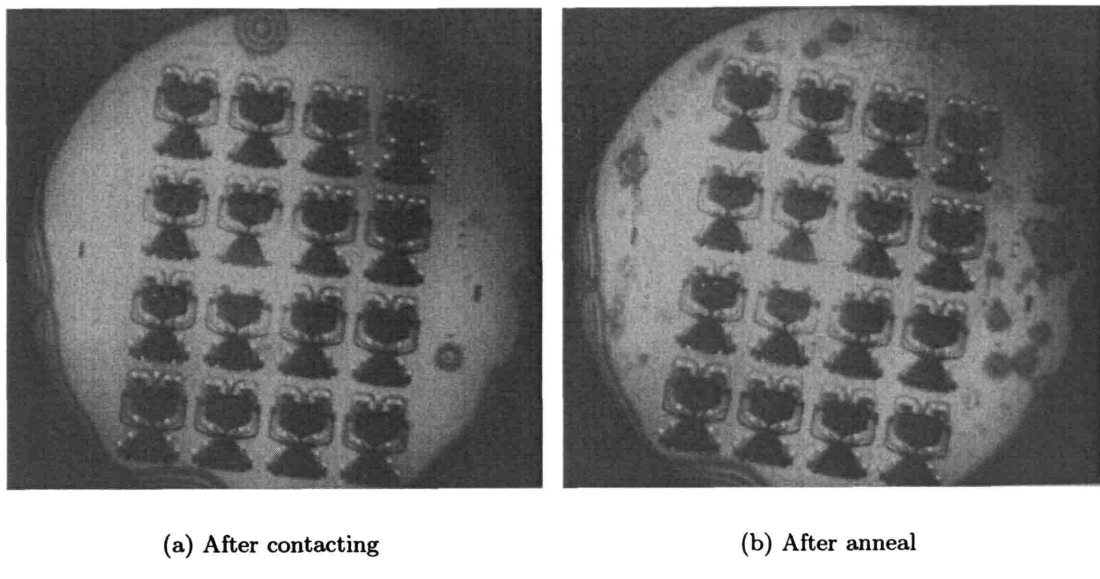
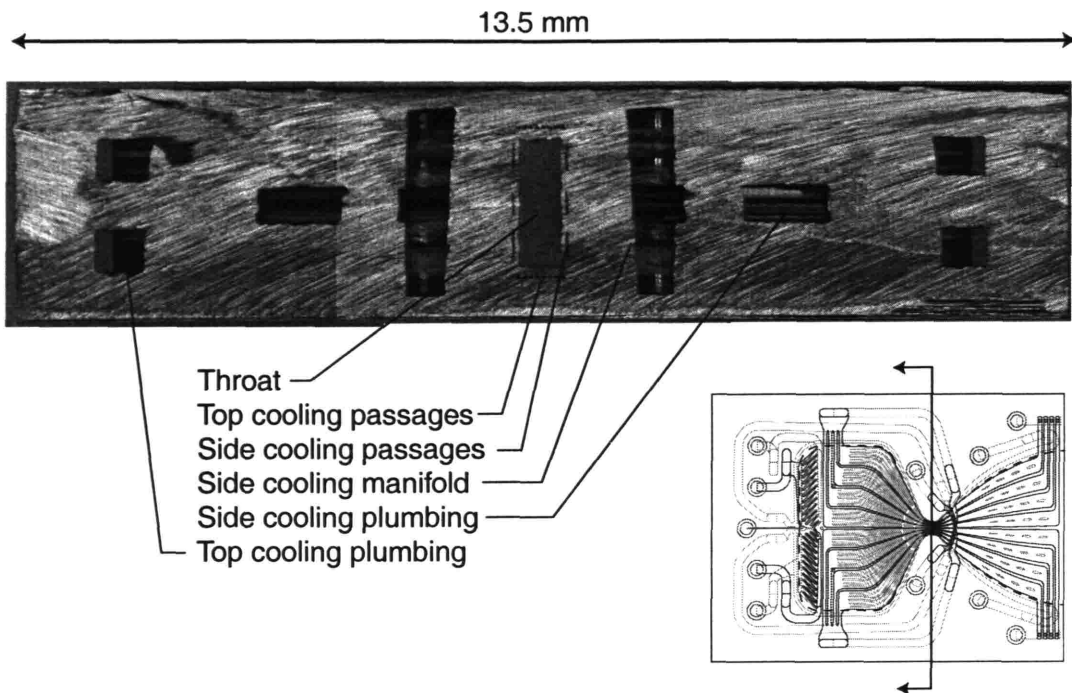


Figure 5-28: Infrared pictures of first build after initial contacting (a), and after one hour anneal at 1100 °C (b). Fringes show areas of poor bond quality.

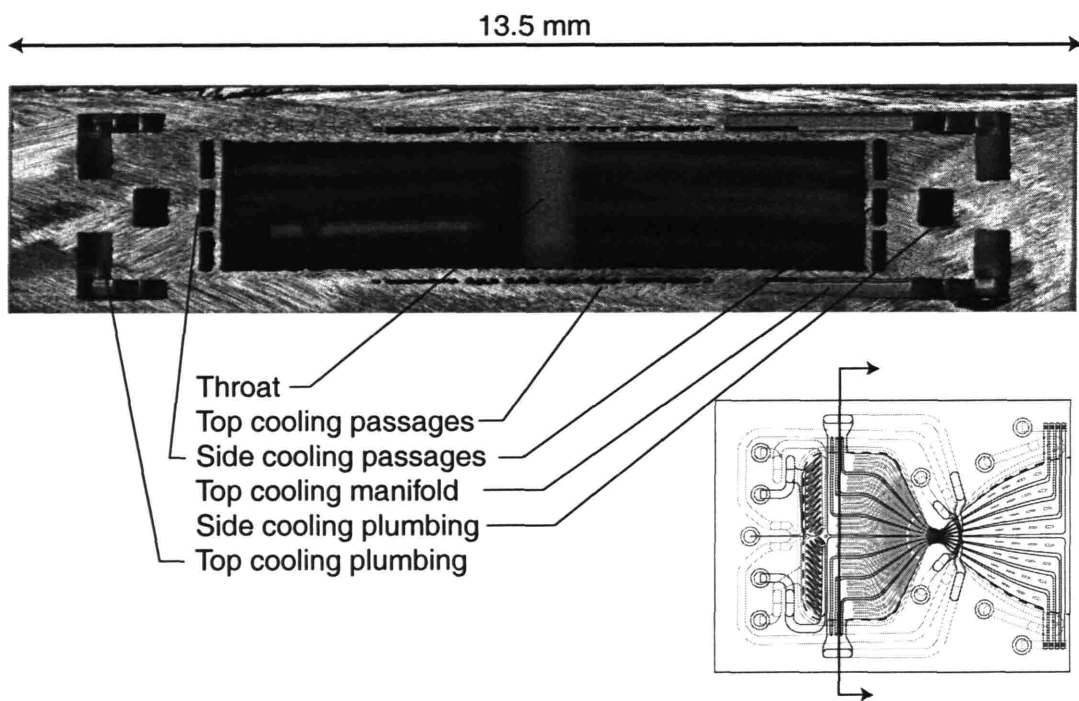
the left of the wafer indicate poor bond quality in those small areas, but the lack of these fringes over the rest of the wafer indicates an excellent bond.

5.7 Cross Sections

Figures 5-29 and 5-30 show three cross sections of a completed die from build 2.



(a) Throat cross section



(b) Chamber cross section

Figure 5-29: These cross sections are from Build 2, and illustrate the various features of the completed thrust chamber.

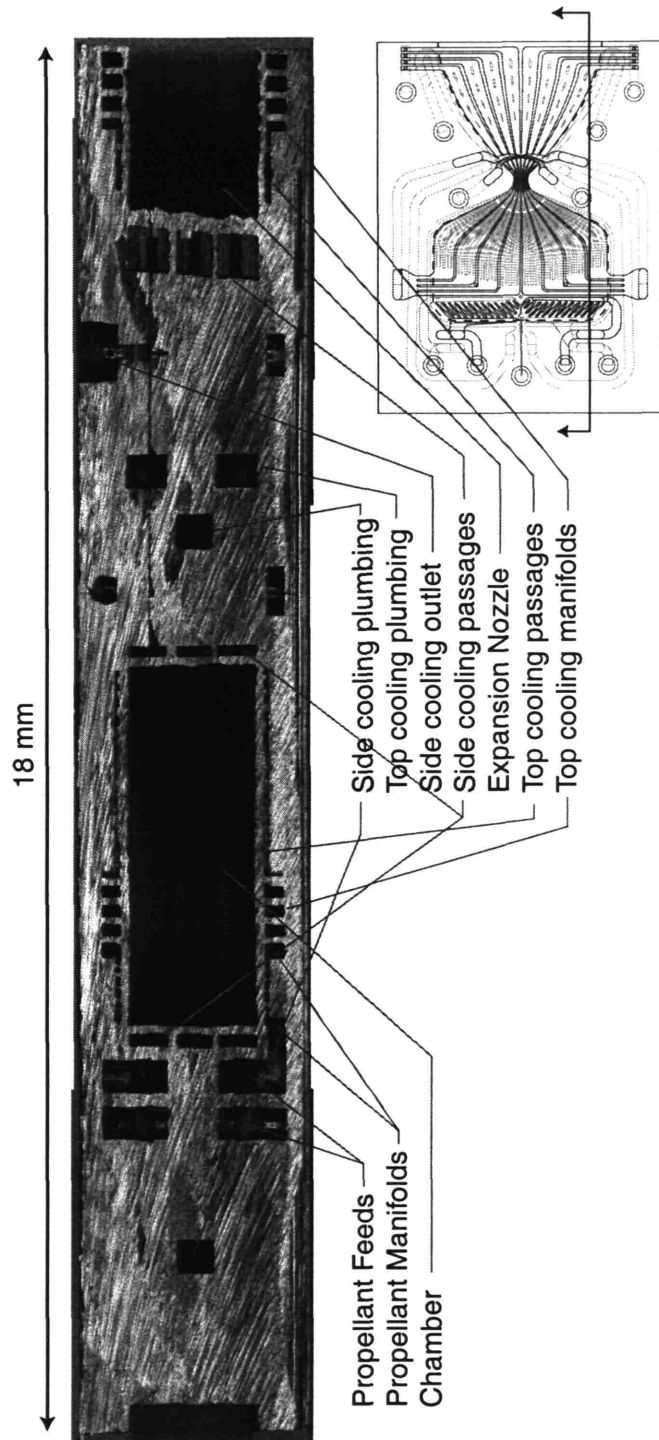


Figure 5-30: This is a cross sections through a Build 2 die in the flow direction, and illustrate the various features of the completed thrust chamber.

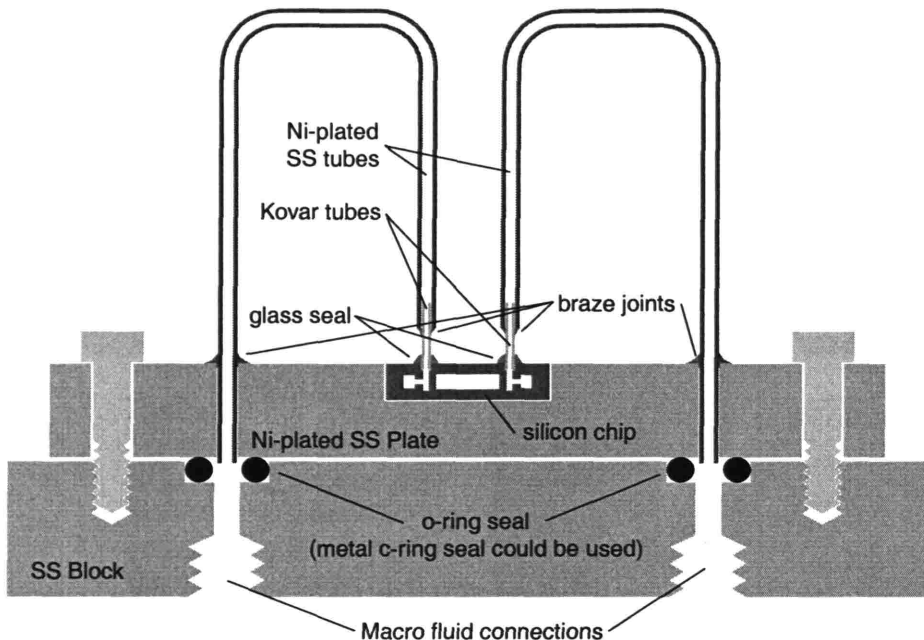


Figure 5-31: Schematic of rocket package.

5.8 Packaging

The demonstration microrocket is designed to operate with propellant and coolant inlet pressures near 250 bar, and coolant outlet temperatures around 700 K. This is beyond the capabilities of traditional adhesives or elastomer o-ring seals. Therefore, a new interconnect technique has been developed to provide fluid connections to silicon devices capable of operating at high pressure and high temperature.

The general concept is pictured in Figure 5-31. The silicon chip is placed into a recess in a nickel-plated stainless steel plate. Short (1 cm long) Kovar[§] tubes are sealed to the silicon by melting a glass bead around them. Larger nickel-plated stainless steel u-tubes are inserted over these tubes and into the plate, and brazed into place using a copper-silver eutectic braze. This creates a packaged die that can then be bolted to a larger block which is in turn connected to the macro fluid connections of the laboratory.

The process for creating this is illustrated in Figure 5-32. The first step is to glass seal the

[§]Kovar is Carpenter Technology's registered trademark for Alloy 29-17, nominally 29% Nickel, 17% copper, and balance Iron. It is selected for its low thermal expansion coefficient and because it is used in glass to metal seals.

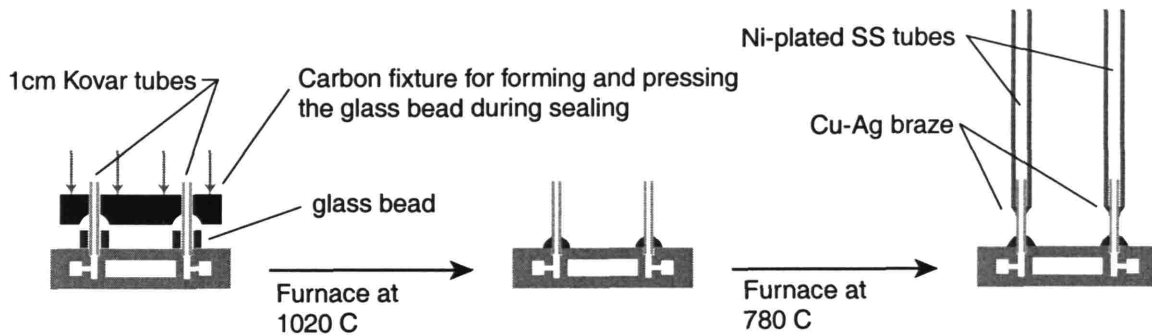


Figure 5-32: The first step in the packaging process involves sealing the 1 cm Kovar tubes to the silicon engine. The glass is pressed into shape using a carbon fixture. After this, a second pass through a lower temperature furnace attaches the longer u-shaped tubes via a brazing process.

Kovar tubes to the silicon. The tubes fit into the inlet ports of the silicon, and glass beads of the appropriate composition are placed around them. A carbon fixture with a hole pattern matching that of the die, and containing countersunk recesses on its lower side to guide the shape of the glass as it melts, is placed above. Some additional weight is added to this fixture to provide the force necessary to form the beads, and the assembly is sent through a glass sealing furnace at approximately 1020 °C. The result is pictured in Figure 5-33.

Continuing with the flow of Figure 5-32, the chip with its Kovar tubes is placed into the recess of the stainless steel plate. Stainless steel tubes are inserted over the Kovar tubes and into the corresponding hole in the plate, and preforms of the copper-silver braze are placed at the braze locations. Both the plate and these tubes have been previously plated with a thin (tens of microinches) layer of nickel to enhance the wetting of the braze and to protect the steel from oxidation. The entire assembly makes a second pass through the furnace at approximately 780 °C, yielding the completed package shown in Figure 5-34. There are two reasons for using a two-step process with both Kovar and stainless steel tubes. First, using short tubes allows the carbon fixture to be removed (and reused) after the initial glass sealing step. Second, the stainless tubes have the same thermal expansion as the main block during the brazing process, reducing thermal stresses.

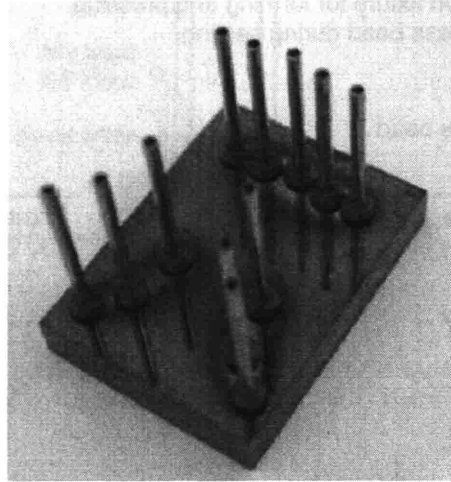
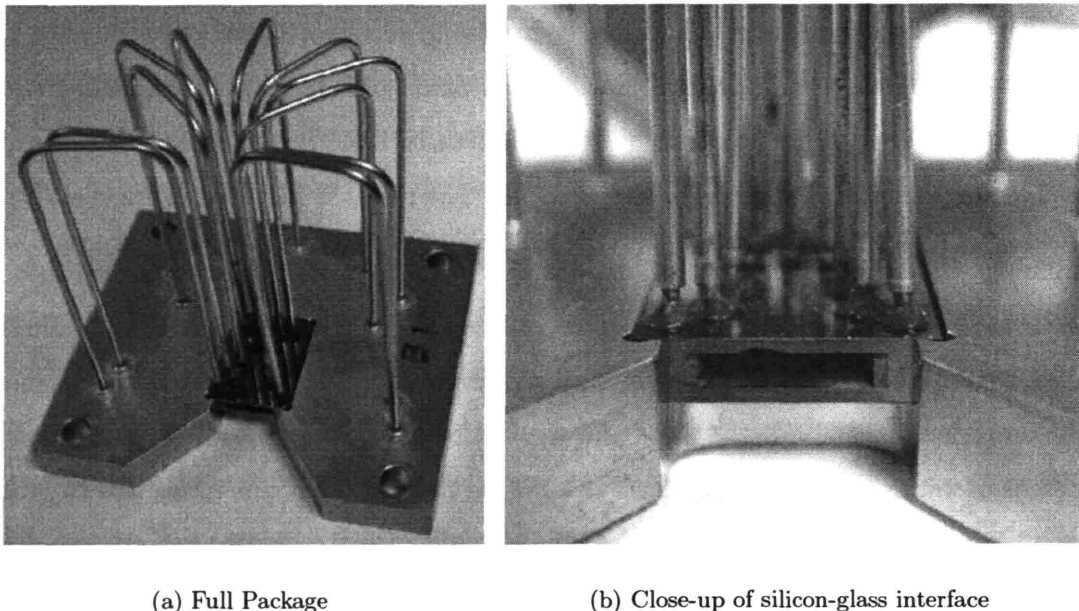


Figure 5-33: First stage of packaging involves sealing short (1 cm) kovar tubes to rocket chip. This is shown for a blank test die with only inlet holes defined.



(a) Full Package

(b) Close-up of silicon-glass interface

Figure 5-34: Fully packaged thrust chamber die. The die shown, B1 of the first build, was the first rocket thrust chamber to operate successfully.

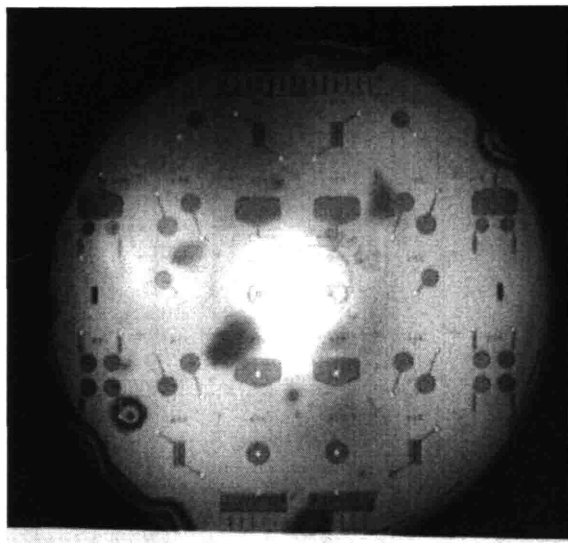


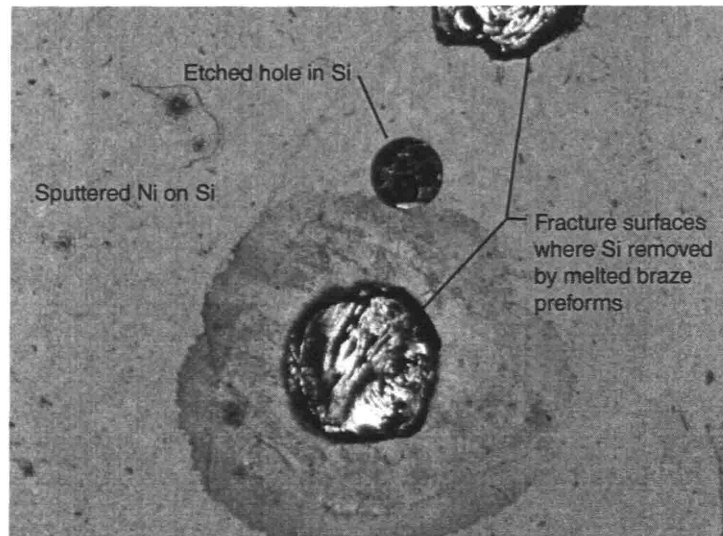
Figure 5-35: This infrared image shows a bonded wafer set containing the test structures used to develop and evaluate the packaging process.

5.9 Process Development[¶]

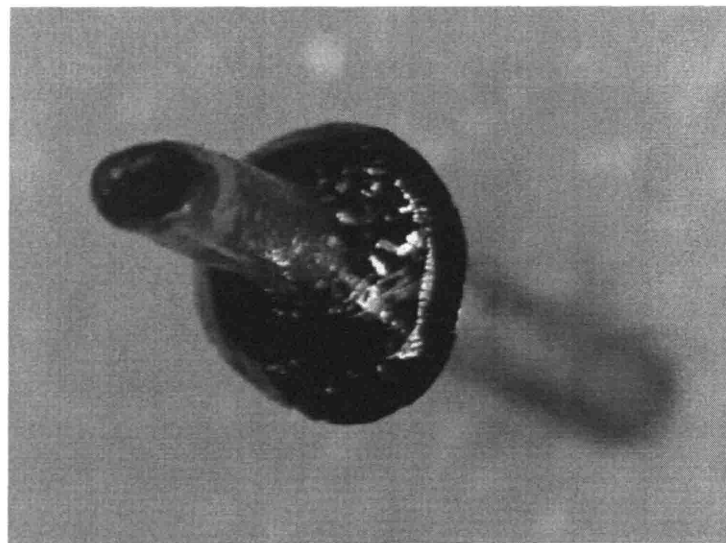
As high pressure and high temperature capable connections to silicon have not previously been demonstrated, a significant effort was required to get to the finished package shown in Figure 5-34. To this end, a set of test structures was fabricated using two silicon wafers, as shown in Figure 5-35. These test structures are cavities that can be pressurized in order to verify the strength of the seals made during packaging. Initial efforts focused on metalizing the surface of the silicon pieces with nickel, and then brazing a tube to those surfaces. Though it was possible to sputter deposit a coat of nickel onto the silicon dies, the thermal mismatch between the braze material and the silicon was large enough to cause spalling of the silicon as the braze cooled, as shown in Figure 5-36(a).

This lead to the decision to use glass sealing techniques, as there are types of glass that have similar thermal expansion characteristics to silicon. Glass beads manufactured from Corning 7052-type glass were selected due to its low thermal expansion coefficient.

[¶]The packaging development work was performed at Olin Aegis Corporation in New Bedford, Massachusetts, primarily by Paul Bissonette under the guidance of Paul Charpentier and Steven Tower. It was their suggestion that led to the use of the glass bead as the sealing technology, and it was their support and expertise in this area that made the packaging effort successful.



(a) Spalling of the silicon



(b) Silicon remains bonded to glass after failure

Figure 5-36: In (a) pits can be seen where the silicon has been removed by braze preforms after they were melted and then cooled. In (b), Silicon fracture surfaces can be seen still attached to the bottom of a glass bead once the joint had failed in handling.

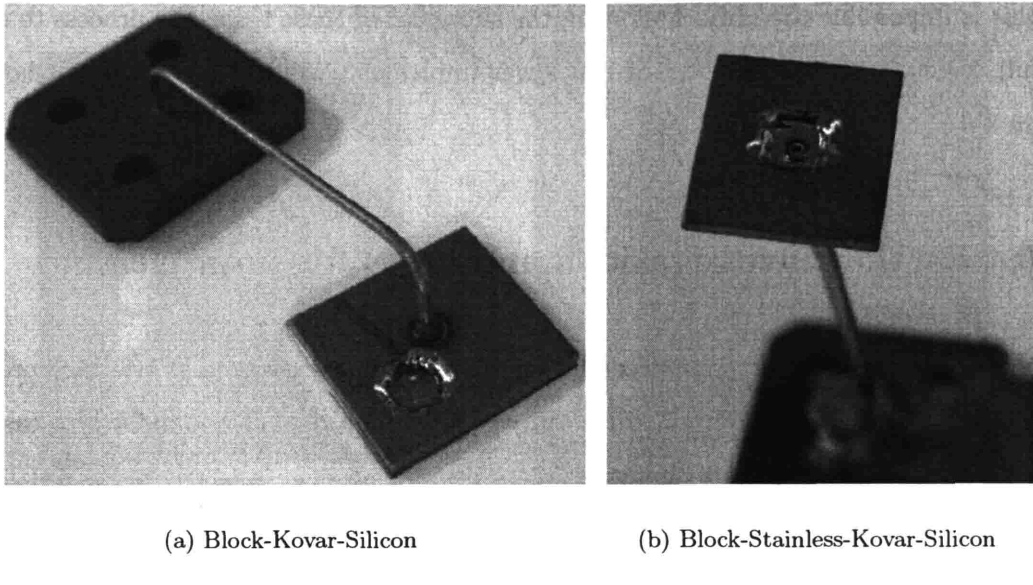


Figure 5-37: Two examples of silicon failure prior to glass bead failure. The pressure at failure in (a) was not recorded; failure in (b) occurred at 1320 psi (90 bar).

Initial test pieces were fabricated using dies from the wafer set shown earlier, a small stainless steel block, and single piece of Kovar tubing, as seen in Figure 5-37(a). In these tests, the Kovar tube was first brazed to the stainless block using a copper braze at approximately 1100 °C. It was then assembled with the silicon piece, the glass bead, and a removable carbon fixture and passed through the furnace to perform the glass seal. As can be seen in that figure, during pressurization tests, failure of the silicon die occurred prior to failure of the glass bead. Also encouraging is the fact that when kovar tubes would break off the silicon due to rough handling, the fracture would occur in the silicon, pulling silicon off the chip surface with the glass bead, rather than at the silicon-glass interface. This is shown in Figure 5-36(b). This implies that the glass is adhering well to the silicon.

Based on the results from the single kovar tube process, the stainless-kovar-silicon process was tried. This involves a second pass through the furnace for the glass seal joint once it is formed, as the copper-silver braze forms at a lower temperature than the glass seal. Two test pieces, one of which is pictured in Figure 5-37(b) were made and tested. The one shown in that figure failed at approximately 90 bar (1320 psi), when the lower silicon cap burst, but the glass seal and braze joints remained intact. The other test piece failed at 175 bar (2543 psi), due to a failure of the glass bead. None of the glass bead remained on

the Kovar tube, which may imply that the failure occurred at the kovar-silicon interface, but this is impossible to verify. Following the successes of these tests, the process to create the full package using eleven sets of tubes was implemented, with the results as shown in Figure 5-34.

5.10 Further investigations and areas for improvement

Though the packaging effort was successful, in that it provided a way to deliver high pressure fluids from the laboratory setting to the silicon chip, there remain a number of areas with room for improvement of the technique.

5.10.1 Overall process yield

Of the ten die from the first build that were to be packaged, five were completed successfully. Two die were lost during the initial glass sealing of the Kovar tubes, and three die developed clogged stainless steel tubes during the brazing step as the braze flowed too much and entered the tubes.^{||} Of the five die that made it through the packaging process, one had a glass bead failure during the cooling flow characterization, rendering it untestable. Though a fifty percent yield is rather encouraging for the first live batch through a new packaging process, there is clearly room for improvement, particularly in ensuring that the braze does not flow into the tubes.

5.10.2 Quality of the glass seals

A second area where there is room for improvement is in the strength and quality of the glass seals themselves. Of the six die that made it to characterization and testing, all had small leaks through the glass seals, and two devices failed because of failed seals. A complete investigation of the strength and quality of glass seals used for this silicon sealing has not been performed as part of this work, though there is now an ongoing effort by Harrison [18] to better understand and characterize the process. Two of his findings are

^{||}One of these three die was eventually salvaged by drilling out the plugs formed by the braze. The drilling process caused failure of the glass seals in the other two.

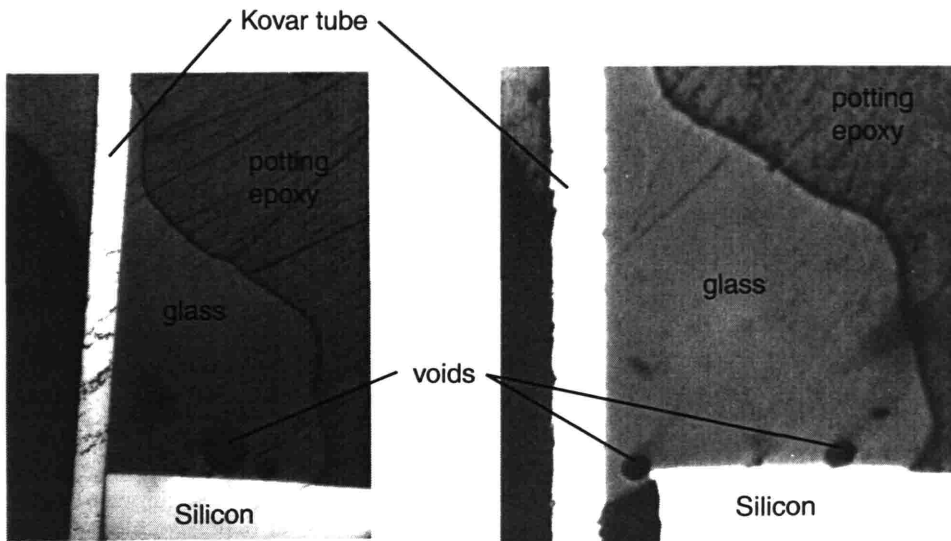


Figure 5-38: Two examples of cross-sections showing the kovar/bead/silicon interface. It is apparent that the glass does not readily wet the silicon, and that voids are present in the glass. (Photos courtesy of Todd Harrison [18])

worth briefly discussing here. In investigating the glass beads as formed by this process, he noticed large voids forming inside the glass, often at the silicon-glass interface, as can be seen in Figure 5-38. These appear to be due to the fact that the glass is not fully compacted when pressed into the initial bead form, and therefore the void space coalesces while in the furnace into larger voids. These certainly have a negative impact on the strength of the seal, and may also provide part of the leak path that has been observed. Secondly, he noticed that in a number of cases the silicon had fractured locally underneath the glass seal, as in Figure 5-39. Such a fracture would produce a weaker seal as the pressure load would have to be carried by a smaller fraction of the glass-silicon contact surface. In addition, it would provide a leak path through much of the glass bead, and may partially account for the leaks that have been seen in the packaged devices.

5.11 Summary

This chapter has discussed the fabrication and packaging of the microrocket thrust chamber. It presented the mask designs, and then discussed the fabrication process steps to produce a wafer set of engines. Process enhancements that were incorporated into future builds

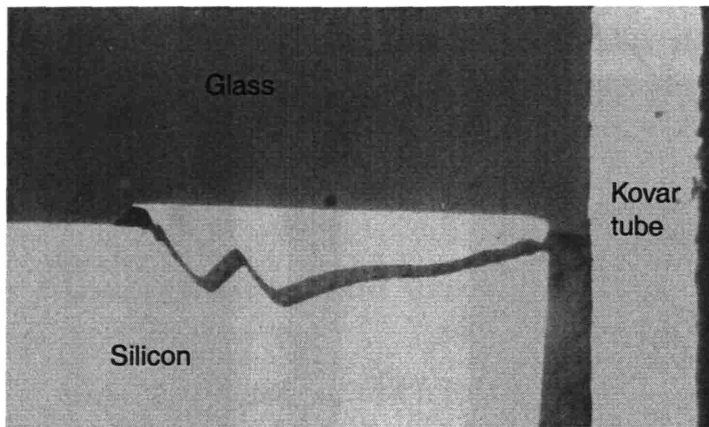


Figure 5-39: A close-up of a cross-section of the kovar/bead/silicon interface that illustrates a local fracture of the silicon surface. The crack provides a leak path through much of the bead, and similar effects could explain the slow leaks that have been experienced. (Photo courtesy of Todd Harrison [18])

were reviewed. Additionally, the packaging technique that was developed to provide high pressure fluids to the silicon chip was presented.

The next chapter will present the experimental apparatus that the completed package is bolted to in order to perform a test. It has been designed to feed the propellants and coolant into the chip, and to record the operating parameters of the rocket engine, such as thrust, mass flow, chamber pressure, and coolant temperature rise.

CHAPTER 6

EXPERIMENTAL SETUP

6.1 Overview of Experimental Apparatus*

This chapter will describe the experimental apparatus constructed to deliver the propellants and coolant to the thrust chamber and to provide engineering data used in analyzing the performance of the system. There are three primary subsystems of the apparatus:

1. The thrust stand and package mounting plate. This provides the interface to the packaged thrust chamber, and is the location where the thrust, pressure, and temperature measurements are taken.
2. The propellant supply. This provides a supply of both methane and oxygen to the thrust stand at individually computer-controlled pressures. The mass flow of each propellant is measured. Additionally, this system includes the gas booster pump needed to charge a run cylinder with high pressure oxygen prior to each run.
3. The coolant supply. This provides a supply of high-pressure coolant (water or ethanol) from the upstream run tanks to the thrust stand, and then receives the two coolant outflows from the thrust stand, where they either pass through metering valves to ambient conditions, or are received into two pressurized dump tanks used to explicitly set the coolant outlet pressure. The total coolant mass flow is measured upstream of the thrust stand.

*The detailed design of the thrust stand, mounting plates, various mounting brackets, and the propellant and coolant flow systems was performed at Lincoln Laboratory by Herbert Feinstein. The fabrication of the various mounting brackets, and the primary plumbing and assembly of the apparatus were completed there under his supervision. The support of the Lincoln Laboratory Advanced Concepts Committee, and the dedication exhibited by Mr. Feinstein to this effort are gratefully acknowledged.

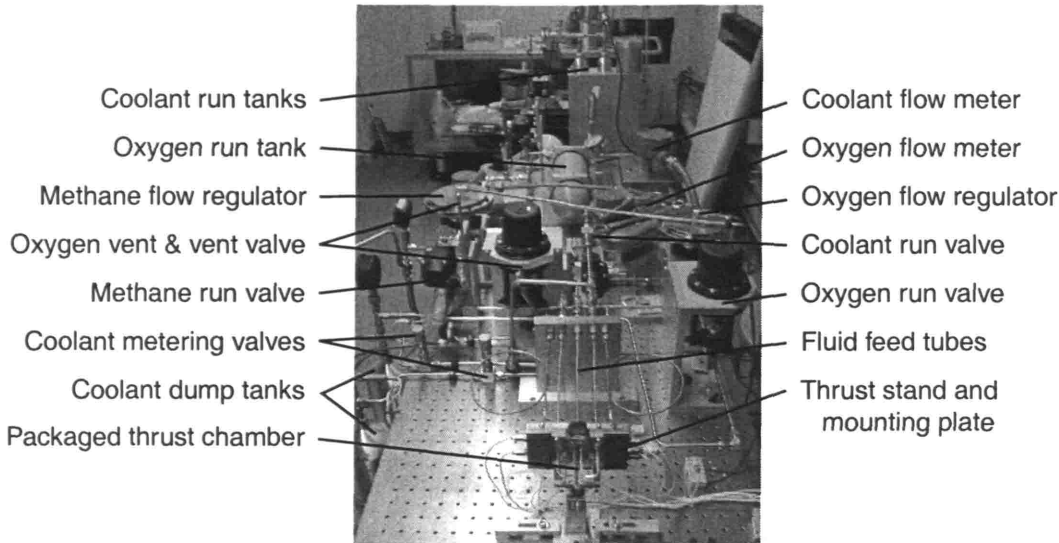


Figure 6-1: View of experimental apparatus, with most components labeled.

A high voltage spark-gap ignitor inserted into the chamber through the throat has been used to supply the ignition energy for the runs. A computer-based data acquisition system is used to acquire the 21 channels of data that are recorded during a firing at a sample rate of 500 or 1000 Hz.

Figure 6-1 shows a photograph of the experimental apparatus. The primary systems are mounted on a table in a test cell, and the data acquisition, control, gas handling, and monitoring equipment are located in an adjacent control room. The following sections will discuss the four primary subsystems, the ignition system, the data acquisition and control system, the sensor calibration, and the sequence for performing a test.

6.2 Thrust stand and mounting plate

Photographs of the thrust stand and mounting plate are shown in Figure 6-2. The packaged thrust chamber is removed in Figure 6-3, illustrating the elastomer o-rings that provide the seal for each fluid. The six pressure transducers are visible around the perimeter of the plate, with five measuring the pressure of one of the fluids, and the sixth used to measure chamber pressure. The transducers used are manufactured by Kulite Semiconductor (model XTME-190) for high temperature operation (continuous use at up to 500 K), and have a

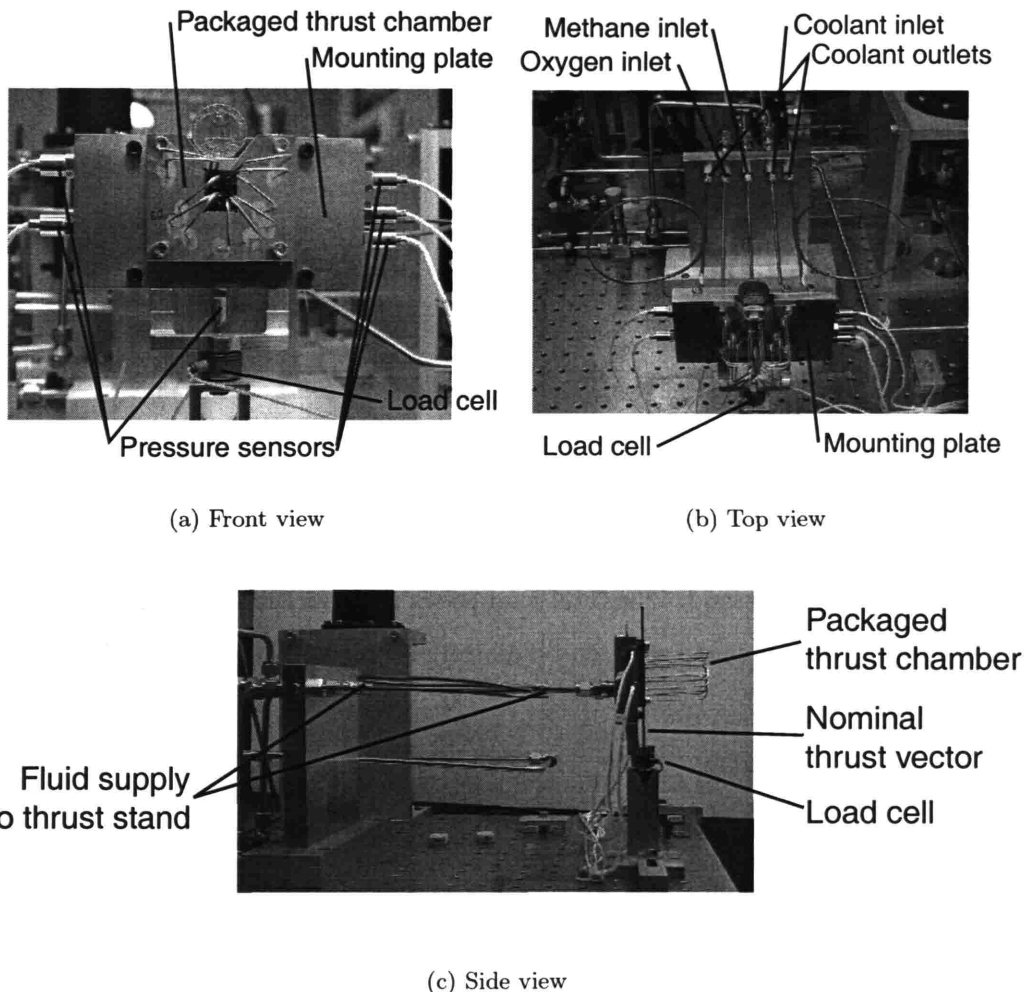


Figure 6-2: Front, top and side view of the thrust stand with a packaged thrust chamber attached.

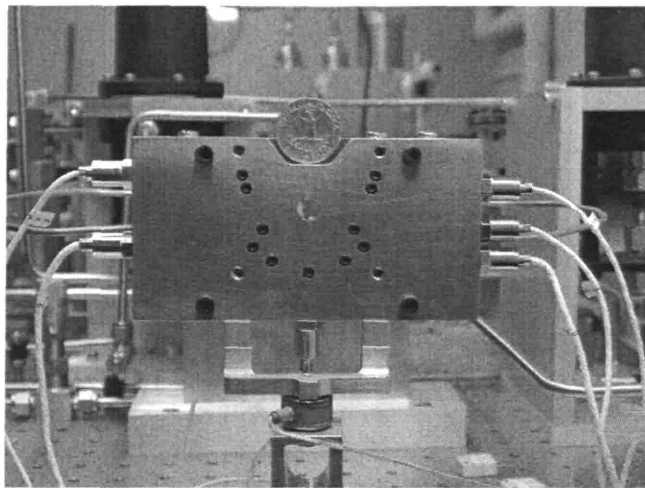


Figure 6-3: View of mounting plate with packaged thrust chamber removed, showing the o-rings that seal the 11 fluid connections

range of 0-5000 psi (0-340 bar).

This mounting plate is supported above a load cell that is used to measure the thrust. The five fluid connections (oxygen in, methane in, coolant in, top coolant out, and side coolant out) are made to the back side of the mounting plate through small tubes which serve as the flexure for the thrust stand. The 5 lbf load cell is manufactured by Omega Engineering, model LCF-5, and is positioned so as to be directly in line with the expected thrust vector, as seen in Figure 6-2(c).

Using a high temperature ceramic adhesive,[†] K-type thermocouples are attached to the coolant inlet and outlet tubes on the packaged engine to measure the coolant temperature. The 0.010 in diameter thermocouples are manufactured by Omega Engineering, model KMQIN-010G-12.

6.3 Propellant flow system

A schematic for each of the propellant flow systems is shown in Figure 6-4. The primary difference between the two systems is the the oxygen is not stored external to the apparatus at high pressure, but instead a pump is used to charge a high pressure cylinder with oxygen

[†]Aremco Ceramabond 865, chosen for its high thermal conductivity ($\sim 200 \text{ W/m K}$)

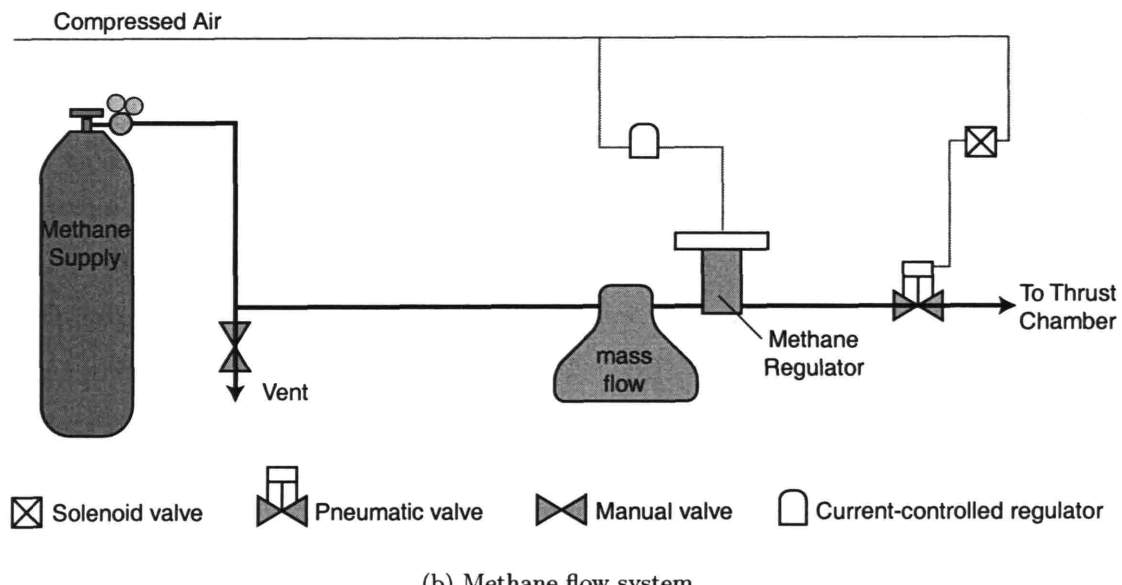
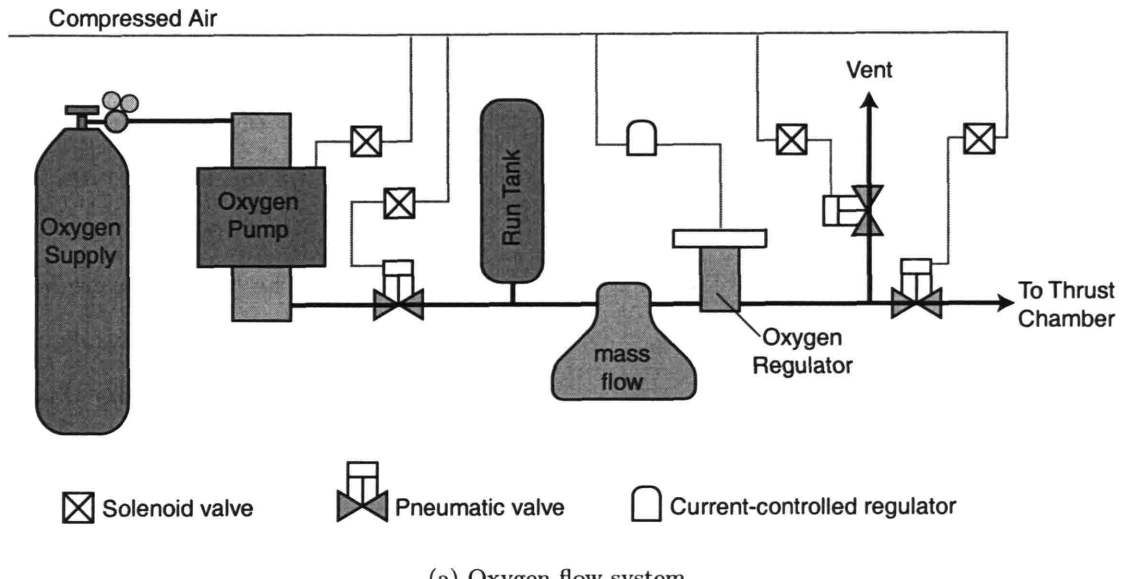


Figure 6-4: Schematics of the oxygen and methane flow systems.

prior to each run. Once this high pressure gas is produced, the two systems are essentially identical, so the propellant measurement and control will be discussed first, as it applies to both propellants, followed by a description of the oxygen pressurization.

6.3.1 Propellant measurement and control

The propellant mass flows are controlled indirectly by using a set of computer-controlled regulators to define how their supply pressure varies with time. As the injectors inside the thrust chamber are choked, the mass flow will be essentially proportional to this supply pressure. Controlling this supply pressure is a two step process. The regulators are loaded via a diaphragm using pressurized air in such a way that the outlet pressure of the regulator is maintained at approximately 75 times the loading air pressure. This means that the loading air pressure would vary between 0 and 50 psi to produce a propellant supply pressure between the 0 to 250 bar (3700 psi) range desired in the experiment. The loading air pressure is controlled by another regulator that sets its downstream pressure between 0 and 100 psi based on an input current between 4 and 20 mA, which in turn is supplied via the control computer. The air-loaded propellant regulators are manufactured by Tescom, model 24-2012, and the current controlled regulators used to set the loading air pressure are manufactured by ProportionAir, model QB1TFIE100.

Upstream of the main regulators, a mass flow meter is placed in each propellant line to measure the flow rate. They are manufactured by MicroMotion, a division of Fisher-Rosemount, model CMF010P, and are designed for a maximum operating pressure of 6000 psi. Downstream of each regulator there is a pneumatically operated valve which is used to provide a positive shutoff between the propellant supply system and the thrust stand. Figure 6-5 shows a photograph of the propellant supply system, with the various components labeled.

6.3.2 Oxygen pressurization system

As eventual tests will call for oxygen supply pressures in excess of 3500 psi, and commercial oxygen bottles are only available with pressures up to about 2500 psi, a method was needed for pressurizing oxygen. A commercial air-driven oxygen gas booster pump is used to pressurize a tank on the test stand, which is then used as the supply of high pressure

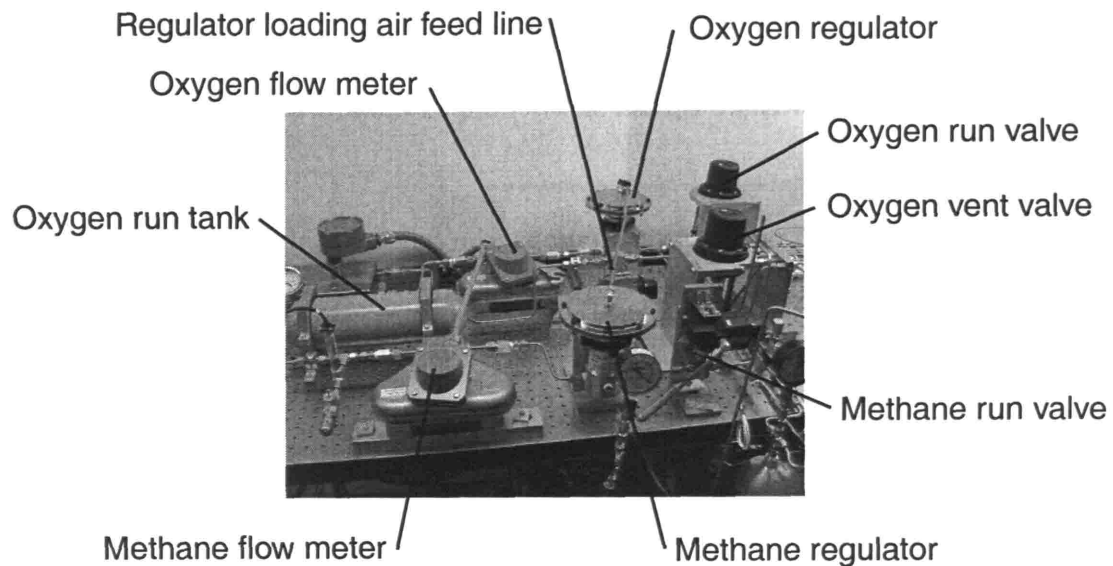


Figure 6-5: The components of the propellant supply system

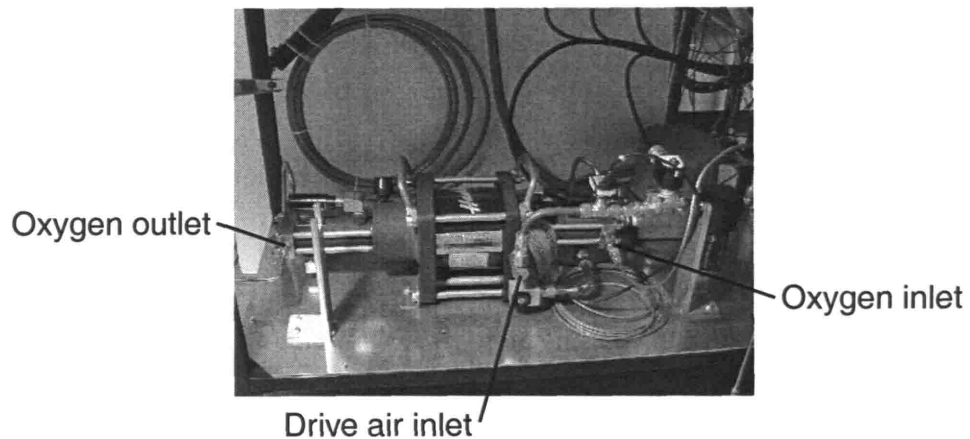


Figure 6-6: Oxygen gas booster pump

oxygen for a given run. The gas booster is manufactured by Haskell, model 28007, and the air used to drive it is provided by an in-house oil-free air compressor.

The oxygen system has an additional valve downstream of its main regulator which is used to perform a remote venting of the oxygen run tank. In this case, the valve is opened, and the regulator outlet pressure is then slowly ramped upward to ensure a slow release of oxygen into the test cell.

Figure 6-6 is a photograph of the oxygen pump. The run tank can be seen in Figure 6-5.

6.4 Coolant flow system

A schematic of the cooling flow system is shown in Figure 6-7. The coolant is stored upstream of the thrust chamber in a pair of 500 cc high pressure cylinders. Prior to a run, these cylinders are filled, and then isolated from the fill tube. Helium is then used to pressurize the coolant to the desired upstream pressure. Between the supply tanks and the thrust chamber is a mass flow meter, also manufactured by MicroMotion, model DH6, and a pneumatic isolation valve.

After flowing through the thrust chamber cooling passages to cool the walls, the coolant is collected and passes through a set of metering valves that can be adjusted to help regulate the flow of coolant. For most of the tests presented in this thesis, the outlet of the metering valves was vented to the atmosphere, but more recently a modification has been made, and the metering valves empty into two one gallon tanks which can be independently pressurized to set the coolant exit pressure explicitly. In this later case, the metering valves are left fully open.

Figure 6-8 shows images of the various components of the cooling system, including the fill tube and run cylinders, the metering valves, and the outlet dump tanks.

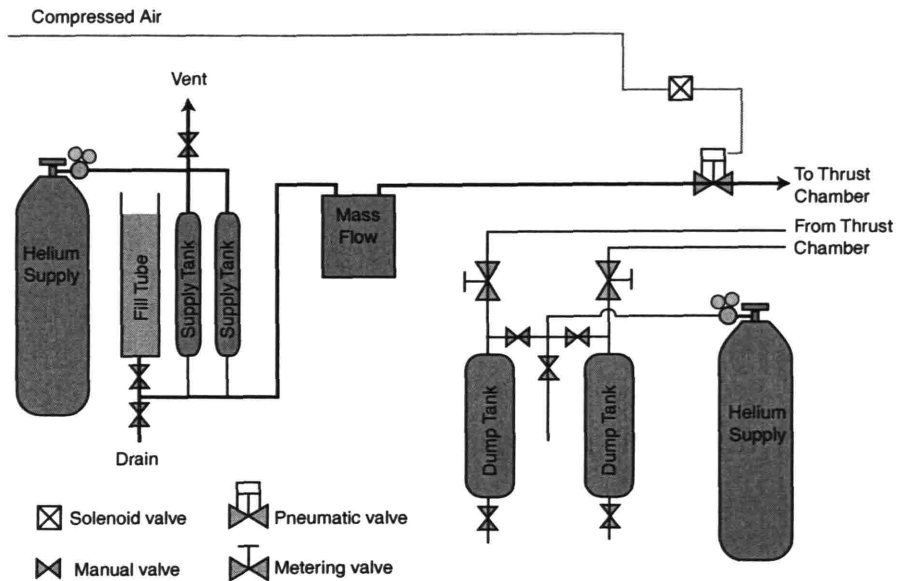


Figure 6-7: Schematic of the cooling flow system

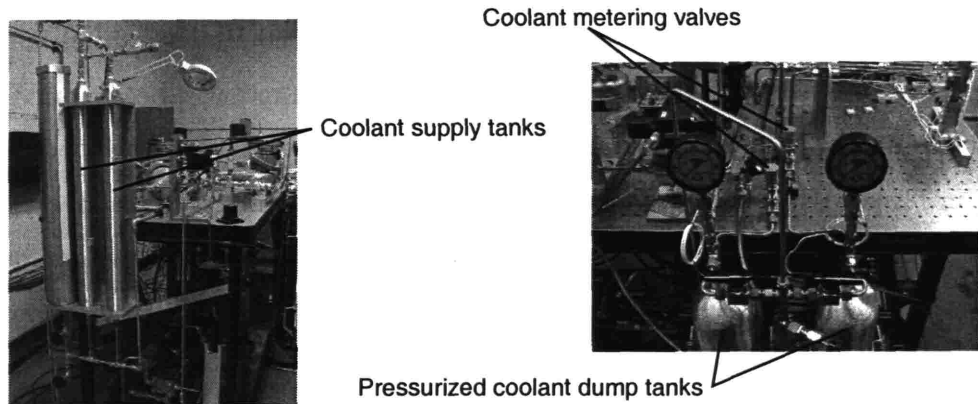


Figure 6-8: Photographs of the cooling flow system components

6.5 Ignition

The ignitor is a pair of #32 magnet wires that are twisted together, leaving a gap of approximately 0.5 mm between the ends. Once the thrust chamber is mounted to the thrust stand, the ignitor is inserted into the chamber from above, and its height is set such that its end is approximately in the center of the combustion chamber. Once propellant flow begins, a high voltage is delivered to the wires, generating a spark, which in turn ignites the mixture. Once the mixture ignites and the test transitions to higher flow rates, the ignitor is ejected through the throat.

6.6 Data acquisition and control

The data acquisition system records the voltage and current signals from the pressure transducers, mass flow meters, and thermocouples. The raw signal is sent through an appropriate signal conditioning and amplifier module in the 5B series, manufactured by Analog Devices, where it is converted to a 0-5 V signal which is then captured using a A/D capture board manufactured by National Instruments, model AT-MIO-64E-3. This board also has two analog output channels which are used to control the propellant supply regulators. LabView software running on a Dell Optiplex Pentium II computer is used to acquire the data and generate the control outputs.

The LabView software is used to acquire data at 500 or 1000 Hz into a first-in-first-out memory buffer of fixed size, which always contains the most recent set of data. A typical buffer of this high speed data would be about 5 seconds longer than the planned run time. After a run, it is written to disk for post processing. Additionally, the most recent 0.2 sec worth of data is continually averaged, and displayed in real time on the computer for monitoring of the experiment. This 5 Hz data is also saved in memory, but into a buffer without a fixed length so that no part is overwritten. This means that the full history of the preparation and pressurization steps prior to a run is available at a low sampling rate, while the details of the run itself are available at a higher sampling rate.

The control of the propellant flow regulators is also done via the LabView software. It is an open loop control, where a pressure profile is determined prior to the beginning of a run,

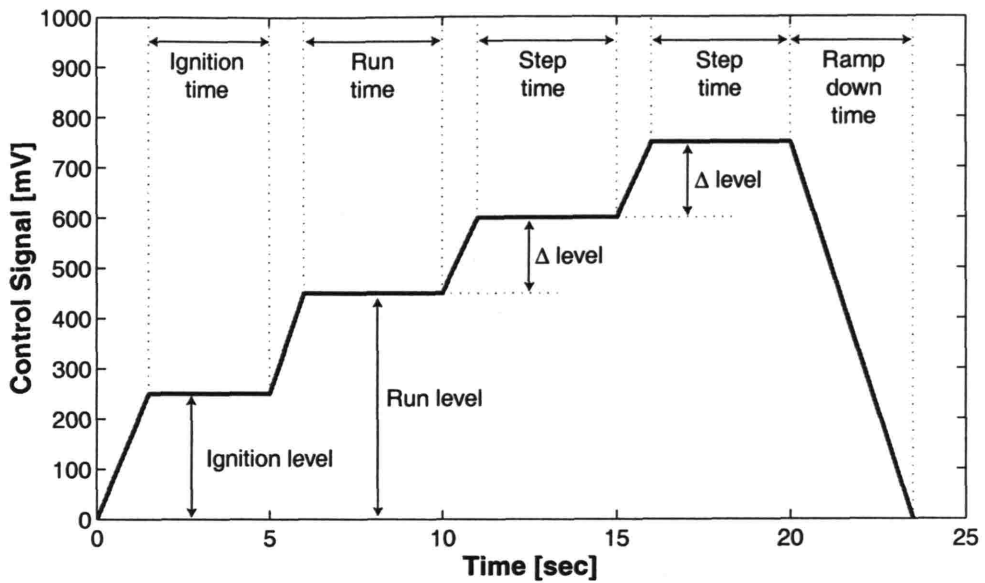


Figure 6-9: Example of control signal, which is then converted into a supply pressure profile for the propellants. The primary parameters that control the profile are labeled. In addition, the number of extra steps can be set (2 are shown here), and the various ramp up times can also be set.

and it then written to the two analog output channels once the firing button is pressed. The output of the board is a 0-5V signal, which is converted to the 0 to 20 mA current signal required by the 0-100 psi regulator by a signal conditioning module.

The output levels are defined in the software via the control signal level, expressed in mV, as this corresponds approximately to the eventual propellant supply pressure in psi. An example of a control signal profile is shown in Figure 6-9, illustrating the various parameters that can be set prior to a run.

The pneumatic valves are also controlled using LabView, but via a separate digital I/O board, model PC-DIO-24PNP, which is used to control a set of solenoid valves, which in turn supply shop air to the pneumatic valve actuators.

6.7 Video monitoring and recording

Four cameras are used to monitor and record the run. One provides a wide angle overview of the whole apparatus, and the other three focus on the thrust chamber itself. Of these

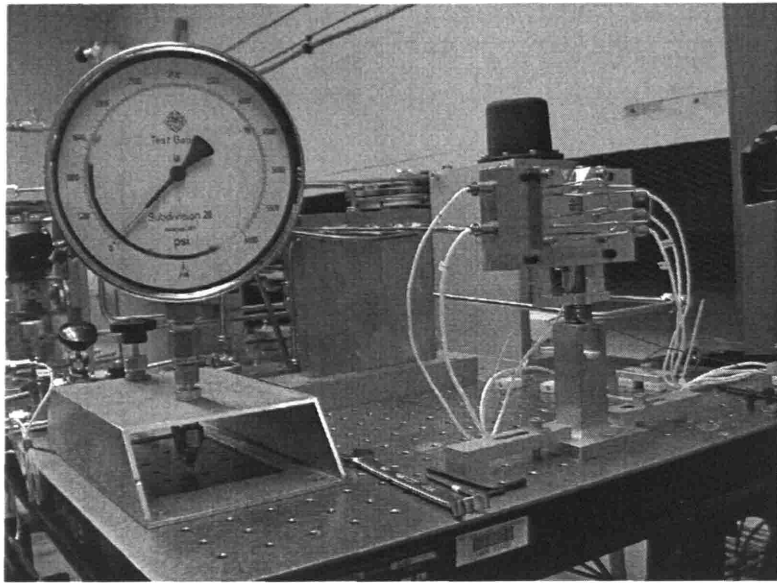


Figure 6-10: Pressure transducer calibration setup

three, one is an infrared camera to record thermal information, one is a digital video recorder with a microphone, and the third is a standard video-only CCD camera.

6.8 System calibration

This section will discuss the calibration procedure for the pressure transducers and load cell. The mass flow meters were pre-calibrated at the factory.

6.8.1 Pressure transducers

To calibrate the pressure transducers, a block used for thrust chamber packaging was modified to shunt all six of the transducers together. A 6000 psi test gauge with a stated accuracy of 0.25% was connected to the coolant outlet port, and helium was used in the fuel flow system to pressurize the system. The setup is shown in Figure 6-10. The helium pressure was increased in approximately 200 psi increments, and the pressure as measured by the test gauge was recorded at each point. The regulator was closed, and a coolant outlet valve was opened and closed repeatedly to relieve the pressure and provide a second set of calibration data as the pressure decreased to see if there were any hysteresis effects. The

results of the calibration are shown in Figure 6-11. A linear fit to the data yields a slope, in psi per volt of input signal. When reducing the raw data from each test run, this same slope is used, but the zero offset is recomputed based on the conditions immediately prior to the test. This calibration procedure was repeated after three and a half months, and the values for the slopes had changed by 1% or less for three of the transducers, and between 1.2 and 1.6% for the other three.

6.8.2 Load cell

The load cell used to measure thrust was calibrated in a manner similar to the pressure sensors. A known set of weights were placed on top of the thrust stand to increase and then decrease the load seen by the cell. From this data, a linear slope was deduced, and used to convert the load cell voltage output to thrust measurements. Again, prior to each run, a zero thrust condition is used to set the zero value for that run. Figure 6-12 shows an example of one of these calibrations. This calibration was repeated after six months, and the value of the slope or scale factor changed by approximately 0.8%.

6.8.3 Control Regulators

The final pressure output of the control regulators was characterized to provide the necessary information to choose the correct control setting for a desired propellant pressure. This was done during cold flow tests, by using various control settings and measuring the resulting propellant supply pressure. A linear fit was performed, and the results are shown in Figure 6-13.

6.9 Experimental Uncertainty

Appendix A presents an analysis of the uncertainty in the measured and derived quantities, which is summarized in Table 6.1 for typical values of the measured parameters discussed in this chapter.

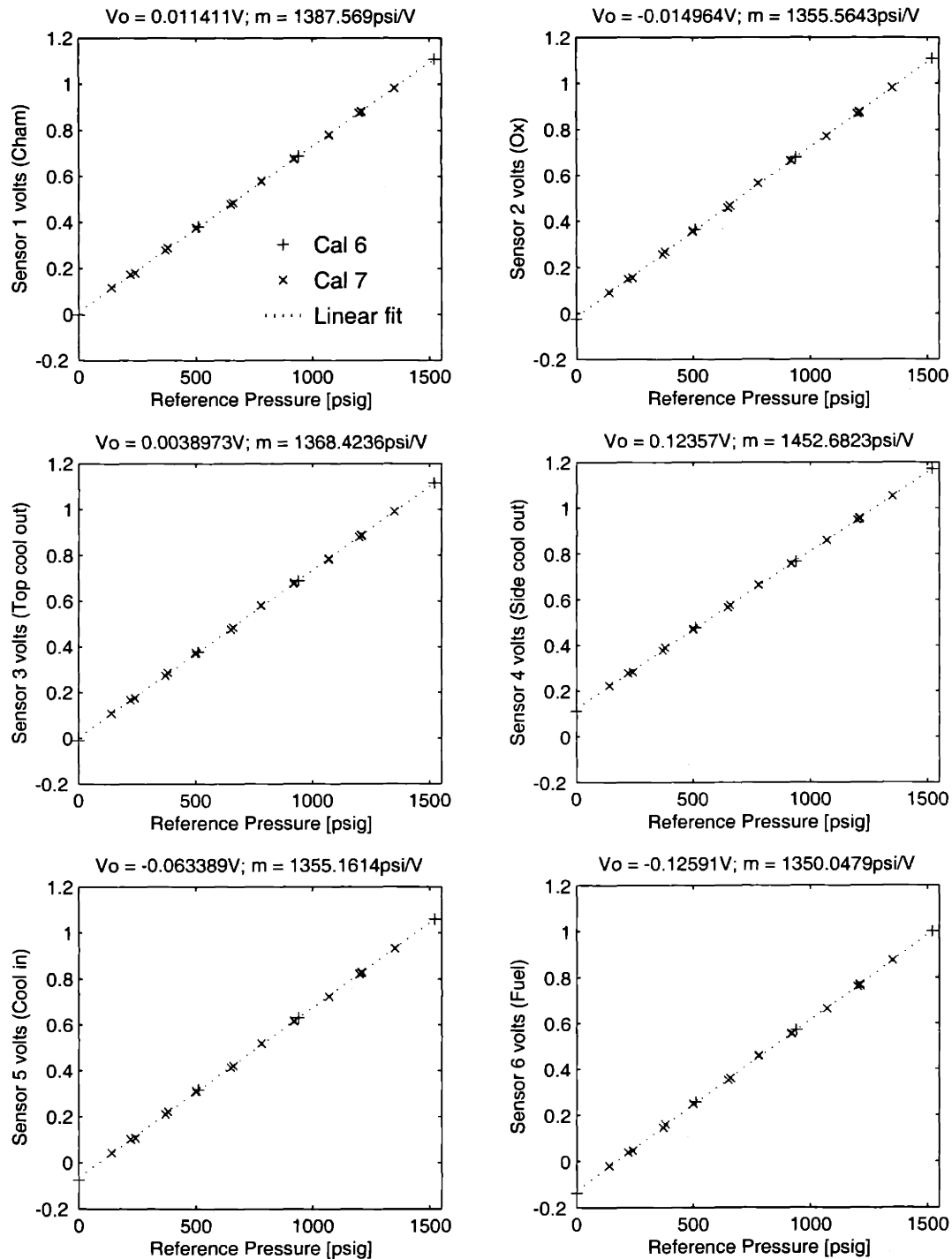


Figure 6-11: Pressure transducer calibration

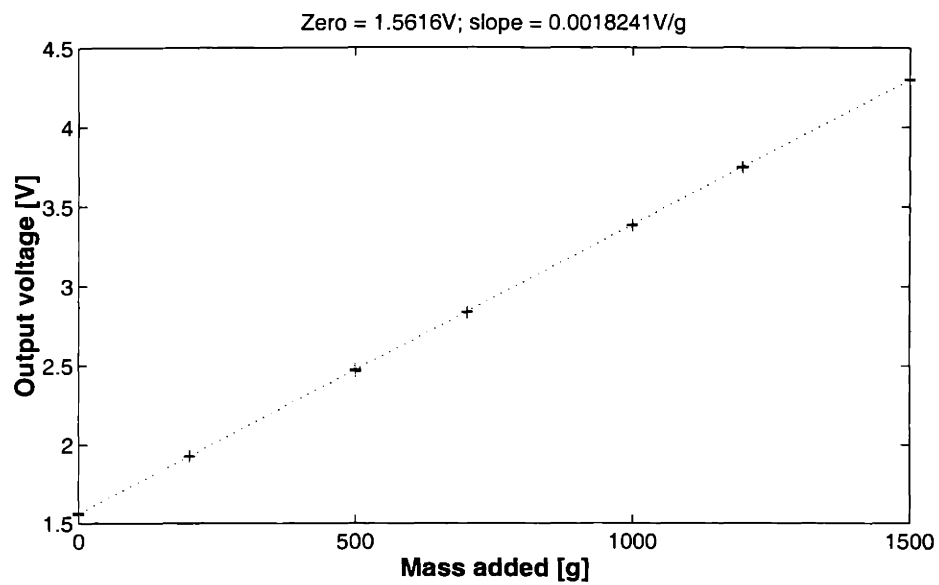


Figure 6-12: Example of load cell calibration for thrust measurement

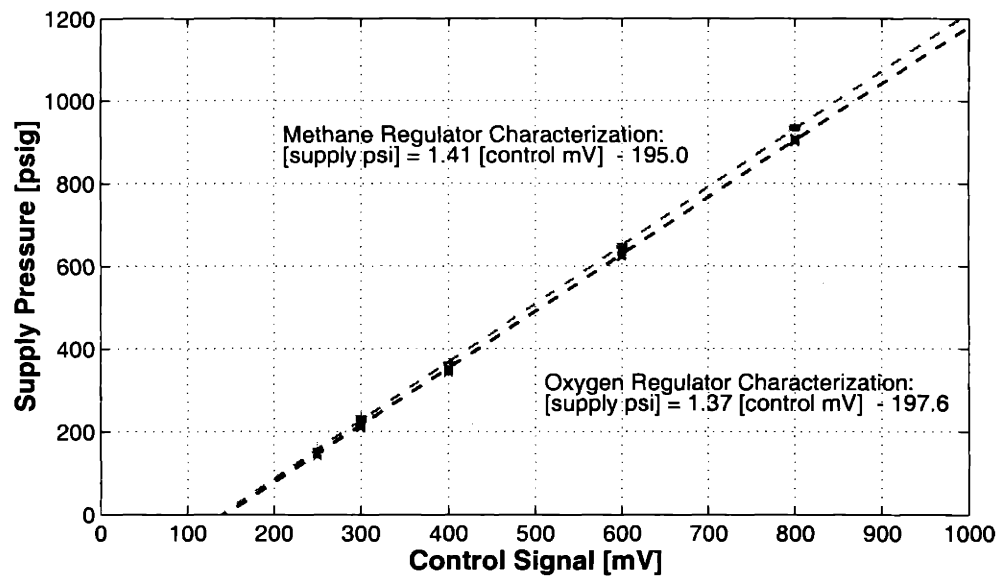


Figure 6-13: Propellant supply pressure as a function of command signal.

Table 6.1: Summary of Experimental Uncertainty

Parameter	Typical Value		Uncertainty	% Uncertainty
Chamber pressure	10	bar	0.53 bar	5.3
Supply pressure	100	bar	3.0 bar	3.0
Thrust	1	N	0.09 N	9.0
Propellant mass flow	0.4	g/s	0.003 g/s	0.8
Coolant mass flow	1	g/s	0.005 g/s	0.5
Temperature	450	K	12 K	2.7

6.10 Experiment procedure overview

This section will briefly describe the procedure following in performing a run. An example of the detailed checklist that is actually used is shown in Appendix E.

The first step is to fill the thrust chamber cooling passages with coolant. To avoid the possibility of trapped air bubbles, this is done by drawing a vacuum between the coolant flow isolation valve upstream of the chamber and the coolant outlet downstream. Once at vacuum, the isolation valve is manually opened, allowing coolant to flow into the chip and through the cooling passages. Next, the test area is prepared for the run, by verifying that the video equipment is running, and that the coolant outlet metering valves are set to their proper position (or fully open if the pressurized dump tanks are being used to set the coolant outlet conditions.) Finally, the ignitor is prepared, and inserted into the chamber through the nozzle. At this point all personnel leave the test cell until the completion of the test.

The next step is to pressurize the oxygen run tank. The oxygen supply bottle is open, and its regulator set to fill the oxygen side of the system up to the flow regulator with oxygen at about 150 psi. The air drive valve for the oxygen pump is opened, and the pump pressurizes the run cylinder with oxygen.

At this point, the methane supply bottle is opened, pressurizing the methane system up to the regulator. The propellants are now ready for a test.

Next, the coolant isolation valve is opened, and the inlet pressure (and possibly outlet pressures) adjusted until the desired coolant pressures and flow rate is achieved. Once the

coolant is flowing at the correct rate, the test begins.

The video recorders are set to begin recording, and the propellant isolation valves are opened. Finally, the command is given to fire, and the computer commands the propellant pressure profiles to begin. Once the propellants begin flowing, the ignition button is pressed, and (hopefully!) ignition occurs.

After the test is complete, the helium is vented to depressurize the coolant and stop its flow, the methane is vented outside of the test room, and finally, the oxygen run tank is vented into the test cell. Once the test cell fan has run for a few minutes, the test cell can be re-occupied.

6.11 Summary

This chapter has described the experimental apparatus and procedure used in testing of the microrocket thrust chamber. The next chapter will discuss the results of the tests that have been conducted, and the following chapter will discuss the implications of these results.

CHAPTER 7

EXPERIMENTAL RESULTS

7.1 Introduction

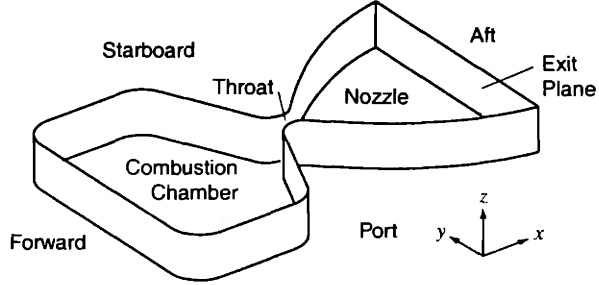
This chapter will present the results from the experimental phase of this work. The five tests where ignition occurred will be reviewed, as will a number of the tests where it did not. Further, the results from the cold flow characterization of the devices will be presented. The highest chamber pressure that has been achieved is 12.3 bar, during the fourth test. At this chamber pressure, the thrust was approximately 1 N.

Figure 7-1 presents a reminder of the terminology used to describe locations in the rocket nozzle, and provides a key to the locations of the various die on the overall wafer. Die identifiers are of the form B4, which signifies the fourth column in the second row of dies. All the tests presented in this thesis are from the first build of devices.

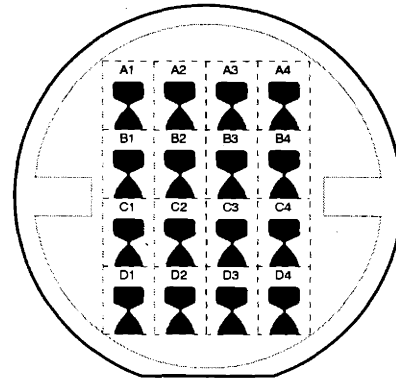
7.2 Testing Overview

Of the twelve attempts to fire the thrust chamber, five had successful ignitions. At least six of the remaining seven appear to have failed to ignite due to an insufficient characterization of the relative area of oxygen and methane injectors, leading to an overly fuel rich mixture. The twelve tests presented here were conducted using water as the coolant,* using the downstream metering valves to control the pressure at the outlet. Future tests will be conducted with ethanol as a coolant, and use the pressurized tanks at the coolant outlets to

*The thrust chamber was designed to be cooled by ethanol, but it was decided to use water as the coolant for the initial tests of the engine as it is not flammable.



(a) Nomenclature



(b) Die identification

Figure 7-1: Nomenclature used to describe locations in and around the thrust chamber, and key to the labels used to identify die. Letters signify the row and numbers the column on the wafer.

Table 7.1: Water-cooled Test Summary

Run	Die	Ignite?	Fail?	O ₂ /CH ₄ control setting [mV]	Start	Run	Δ + steps	max P _c [bar]	max Thrust [N]
35	B1	y	n	200/200	-	-	-	1.5	-
36	B1	y	n	250/250	-	-	-	2.5	0.2
63	A2	n	n	225/225	350/400	-	-	-	-
64	A2	n	n	225/225	350/400	-	-	-	-
65	A2	n	n	225/225	350/400	-	-	-	-
66	A2	n	n	225/225	350/400	-	-	-	-
67	A2	n	n	225/225	350/400	-	-	-	-
68	A2	n	n	225/225	350/400	-	-	-	-
71	A2	n	n	250/225	400/400	-	-	-	-
72	A2	y	n	250/225	400/400	-	-	7.0	0.55
73	A2	y	y	250/225	600/600	-	-	12.3	1.0
87	C4	y	y	250/225	400/400	200/200 + 1	-	10	0.8

explicitly set the coolant pressure drop. Table 7.1 presents a summary of the water-cooled tests.

Table 7.2 shows the cooling parameters for each of the runs with a successful ignition.

Table 7.2: Coolant parameters for hot tests

Run	Die	Coolant	Pressure [bar]			Mass flow [g/s]
			Inlet	Top Outlet	Side Outlet	
35	B1	water	40	1	1	1.2
36	B1	water	35	1	1	1.0
72	A2	water	40	4	3.2	0.95
73	A2	water	54	4.5	4.5	1.2
87	C4	water	82	2.5	4.2	1.3

In addition to these twelve tests, there have been a large number of cold flow tests performed to trouble-shoot the experimental system and to characterize the as-built die. The next sections will discuss the cold flow results, describe the two initial low chamber pressure firings, and finally present the results of the three higher chamber pressure water-cooled tests.

7.3 Cold Flow Results

7.3.1 Static Pressure Test

The first test performed was a static pressure test of the cooling passages. The port side cooling passages of die D3 were pressurized to failure using helium. The helium was fed in through the coolant inlet port; the pressure sensor was placed on the side cooling outlet port; and the top and bottom coolant outlet port was capped. Failure occurred at approximately 85 bar. Images of the failed die are shown in Figure 7-2. Some of the fractures propagated across the centerline into the starboard side cooling passages, so those passages could not be independently tested. Most of the damage appears to be of the top cooling passages, particularly at the aft end of the nozzle where the four passages turn to run perpendicular to the flow direction, which could imply that this was the original source of the failure. However, there is a ‘v’-shaped hole in the upper port side cooling passage approximately

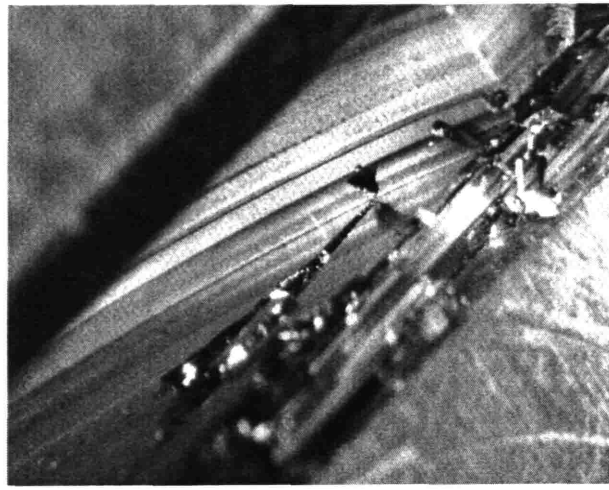


Figure 7-2: Image of die D2 after static pressure test to failure. Most of the failed area is near aft end of nozzle, though localized damage is apparent on sidewall.

half way down the nozzle, so, as is often the case in brittle fracture, it is not possible to state the origin of the failure conclusively. Though 85 bar is much lower than the design condition of 300 bar, it is still above the critical pressure of ethanol, which is necessary to avoid local boiling in the passages.

7.3.2 Injector and Throat Area Characterization

Prior to each test, the injector sizes must be characterized in order to determine the relative supply pressures required for the methane and oxygen to have the desired mixture ratio. Also, the throat area needs to be characterized. This is done by flowing the propellants through the rocket at various supply pressures and measuring the respective mass flow rates and chamber pressures. The supply pressures and mass flows for an example run are shown in Figure 7-3. The transient peaks in mass flow following a ramp in pressure appear to be due to mass storage in the feed lines between the control regulators and the thrust chamber. Given the steady-state mass flow at each run condition, the supply pressure upstream of the injectors, and the total temperature,[†] the total effective injector area, A_{eff} , can be

[†]This temperature is assumed to be the temperature of the room, as the gas has passed through 10-20 feet of tubing at room temperature prior to entering the chip. Even if this is not the case, the important parameter for setting the propellant mixture ratio is the ratio of the total injector area for each propellant, which would depend on the ratio of the temperature of each propellant, assumed to be one.

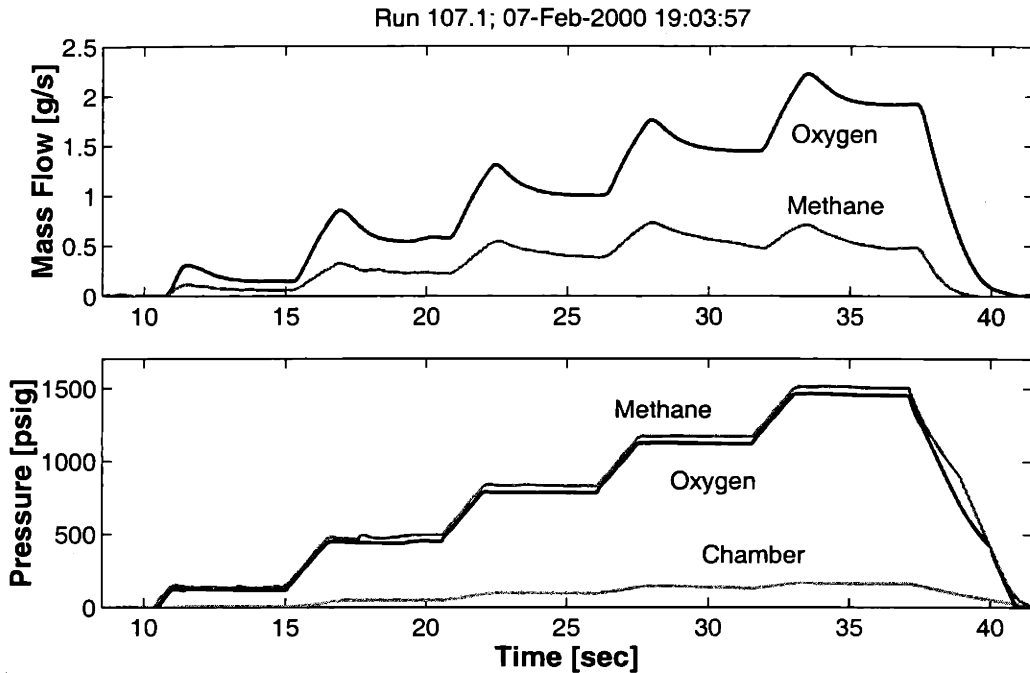


Figure 7-3: Time traces of cold flow test from Run 107 (Die C3), showing the oxygen and methane supply pressures and mass flows.

determined from the ideal choked flow relation:

$$\frac{\dot{m}}{A_{\text{eff}}} = \frac{P}{\sqrt{R T_t}} \left(\frac{2}{\gamma + 1} \right)^{\frac{\gamma+1}{2(\gamma-1)}} \quad (7.1)$$

and can then be used to calculate the effective injector diameter, given the number of injectors. The same equation is used to calculate the effective throat area, where P is in this case the chamber pressure, and the specific heat ratio, γ , and gas constant, R , must be for the mixture of gasses, rather than for a single propellant. These are calculated by taking a mole fraction-weighted average of the respective properties of each propellant.

The injector diameter as calculated for Die C3 is shown in Figure 7-4. The throat area for the same die is shown in Figure 7-5. Table 7.3 shows the averaged effective injector diameter and throat area for each of the die that have been tested.

The design throat area is 0.75 mm^2 , so the measured throat areas are 10 to 20% larger than design. Some of this can be accounted for by the fact that the nozzle plates used in the builds were $525 \mu\text{m}$ thick, rather than the $500 \mu\text{m}$ thick of the design, which would directly

Table 7.3: Effective injector diameters, area ratio, and throat area

Die	Oxygen Injector Diameter [μm]	Methane Injector Diameter [μm]	Injector Area Ratio A_{ox}/A_{fuel}	Throat Area [mm 2]
A2	18.6	14.7	1.60	0.87
B1	18.0	12.9	1.95	0.80
C3	19.7	14.1	1.95	0.93
C4	19.7	15.4	1.64	0.92

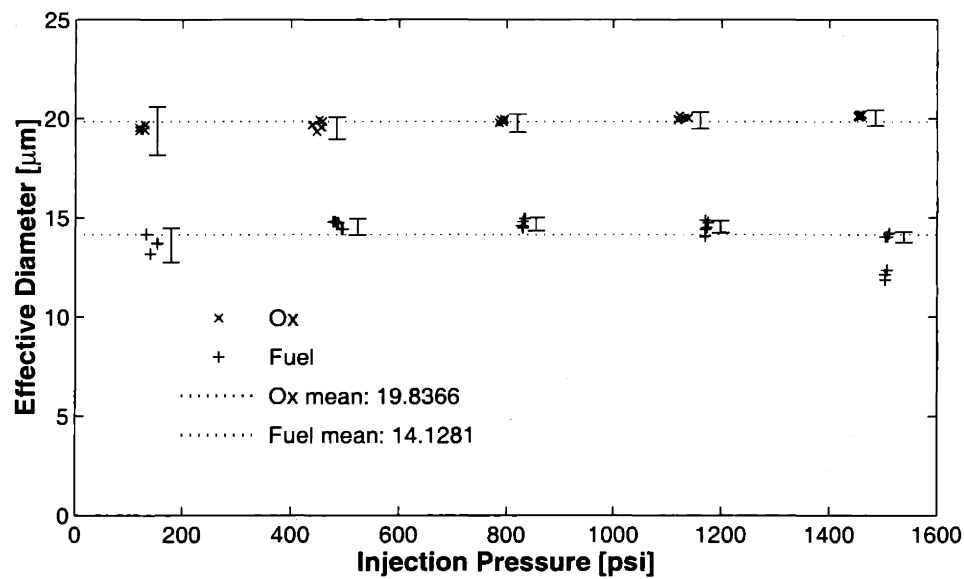


Figure 7-4: Injector diameter for die C3 as calculated for a number of points in steady state from data shown in Figure 7-3 above, and mean of these values.

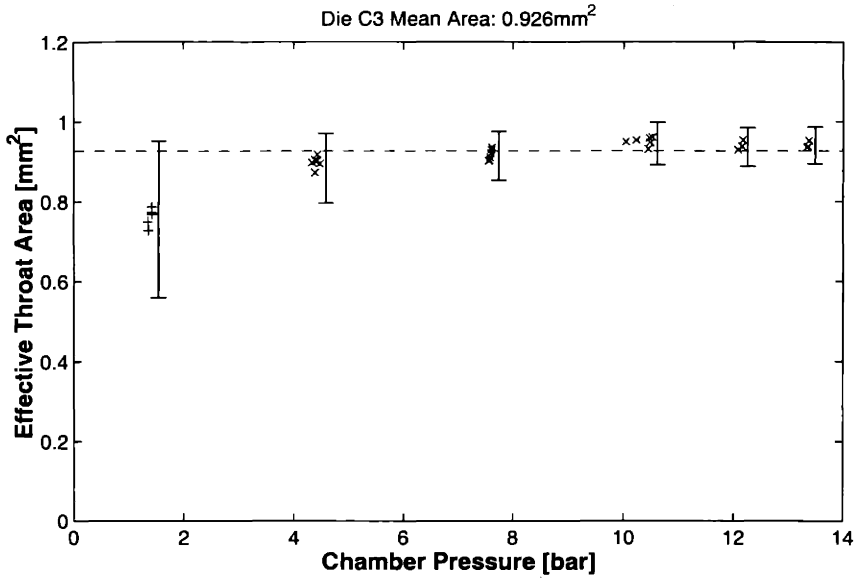


Figure 7-5: Throat area calculation for Die C3.

lead to a 3.3% increase in throat area. The rest of the area increase would have to be due to the wall plate nozzle etch leading to a throat that is deeper and/or wider than the design condition. Given the throat perimeter of 4 mm, an additional 6.5% area increase would be equivalent to the the perimeter moving outward by an average of 12 μm , which given the uncertainties in the microfabrication process is certainly plausible.

7.3.3 Coolant Flow Characterization

The cooling passages of a number of the die were characterized by flowing coolant through them and measuring the coolant flow rate and pressure drop. In the initial coolant flow setup using water, the upstream coolant pressure is set, and the downstream metering valves are adjusted to vary the coolant flow rate and pressure drop. The addition of the pressurized coolant outlet tanks now allows for the pressure drop across the chamber to be set directly.

The flow rate as a function of pressure drop is shown in Figure 7-6 for Build 1 die A2, B1, and C4, each of which were run using water as the coolant. For the data from die A2 and C4 at pressure drops below 500 psi, the mass flow split between top and side passages is measured directly by shutting off the flow that is not being measured. For the higher pressure drop data from die C4, the split is estimated by ensuring that the slope of the

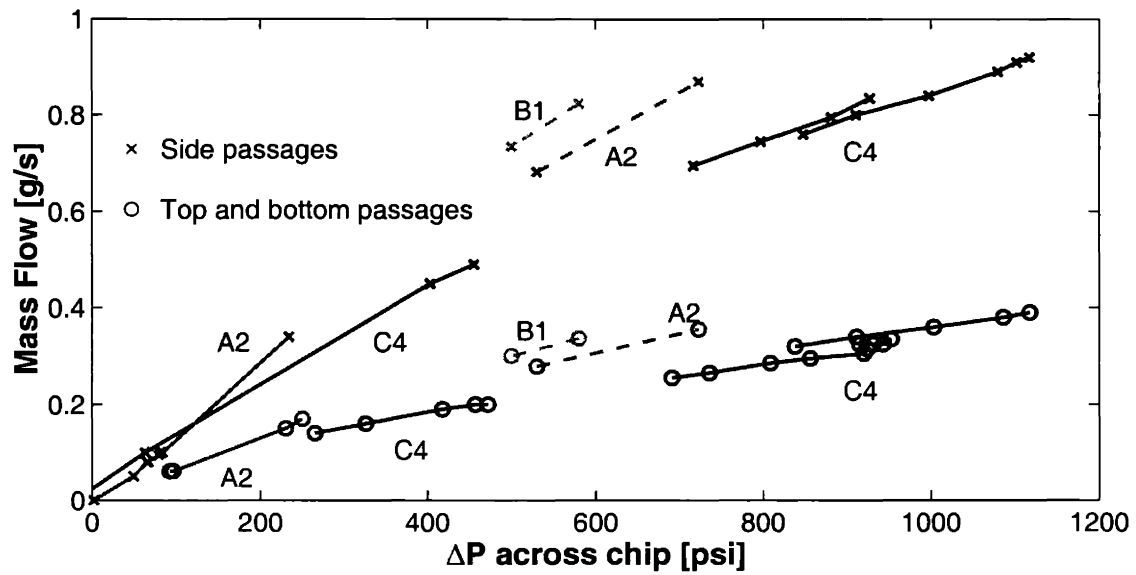


Figure 7-6: Coolant flow characterization

calculated C_v value[†] of the valve remains constant with number of turns open. The dashed lines are flow data taken from just prior to hot fire test runs, where the flow split is assumed to be the same as for die C4, namely 29% of the flow passes through the top and bottom passages.

The flow rate for the top and bottom passages is much lower than desired in the design, which calls for the top-side coolant flow rate to be 25% larger than the side coolant flow. As can be seen in the figure, the top flow is in fact less than half of the side flow. This is likely due to a large pressure drop associated with the pins placed above and below the throat in the passages to enhance heat transfer to the coolant. In addition to the difference in relative flow rates from the design goals, the magnitude of the side flow rate at the highest pressure drops shown in the figure is approximately half of that desired for operation at the design chamber pressure of 125 bar.

The more critical of these two issues appears to be the fact that the top and bottom cooling flow rate is low relative to the side cooling flow. To counteract this, the pins were removed from builds 2 and 3 of the thrust chamber.

[†]The C_v characterizes the flow of a valve and is defined as $Q\sqrt{G/\Delta P}$, where Q is the volumetric flow rate in gallons per minute, G is the specific gravity of the fluid, and ΔP is the pressure drop across the valve in psi. For the metering valves used, C_v increases linearly with number of turns open.

7.4 Ignition Results

The first two tests performed with die B1 had successful ignitions, but after a section of its nozzle wall delaminated during a low pressure coolant test, the first 6 attempts to run die A2 at the same control settings failed to ignite. After analyzing the data from these tests, it was apparent that the ratio of oxygen to methane injector area of die A2 was different from that of B1. This meant that these tests were operating at a lower O/F ratio during the ignition phase than had the tests of B1. For the seventh attempt, the relative supply pressure of oxygen was increased to bring the propellant mixture closer to stoichiometry. This attempt was also unsuccessful, but the following two attempts using the same ignition conditions were successful.

Figure 7-7 shows the as-measured mixture ratios for these tests, with those that did ignite marked as 'x,' and those that did not marked as 'o.' These mixture ratios are calculated from the supply pressures, assuming choked flow, and using the injector area ratio from the injector area characterization. This method is preferred to using the mass flow measurements directly as the latter typically do not reach steady state during the ignition time. It appears that there is a critical O/F near 2.3 below which ignition does not occur. Another factor to be considered is the timing of ignition. The ignition is initiated manually, at some point after the flow profile begins for the test begin conducted. However, there is a zero-band on the regulators that control the flow test, in that they produce no response until their command signal exceeds approximately 150 mV. Since the flow profiles were typically set to ramp from a control signal of zero to approximately 250 mV at the ignition condition over about 1.5 seconds, this means that for most of the first second of a run, there is no flow, and if the ignition is initiated prior to the end of this time period, it will have no effect. It is likely that the failed ignition for run 71 with an O/F above 2.3 was due to this fact. To alleviate this, for tests after run 110, the control signal profile was modified to step to 125 mV once initiated, and then ramp from there to the ignition value over the ignition ramp time.

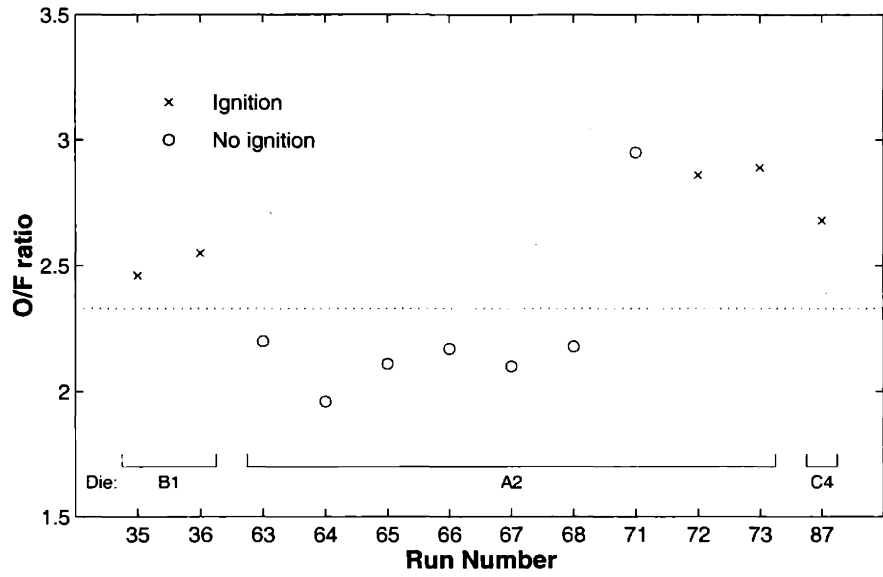


Figure 7-7: Ignition results

7.5 Initial Tests: Low Pressure

The first two tests of a microrocket thrust chamber were of die B1. Both were run at equal control settings for the methane and oxygen. The first test was a four second run at a control setting of 200 mV, which corresponds to a propellant supply pressure of approximately 6.5 bar. The second run was a five second run at a control setting of 250 mV, or approximately 11 bar. Each used water as the coolant, with a coolant supply pressure of approximately 40 bar. Frames from the visual and infrared recordings are shown for each in Figure 7-8.

For the first run, the flow rate was low enough that the ignitor remained in the chamber during the run. Figure 7-9 is a picture of the ignitor after the test, showing its melted insulation.

Figure 7-10(b) shows the coolant flow rate for the first hot fire test, a cold flow test immediately following it, and the second hot fire test. The coolant flow rate appears to increase by approximately 20% during the time combustion is occurring in the nozzle. Lopata[29] and Foust[?] observed a similar phenomenon in their heat transfer experiments in small tubes. Once the power was turned on, and the walls were heated, the pressure drop across the

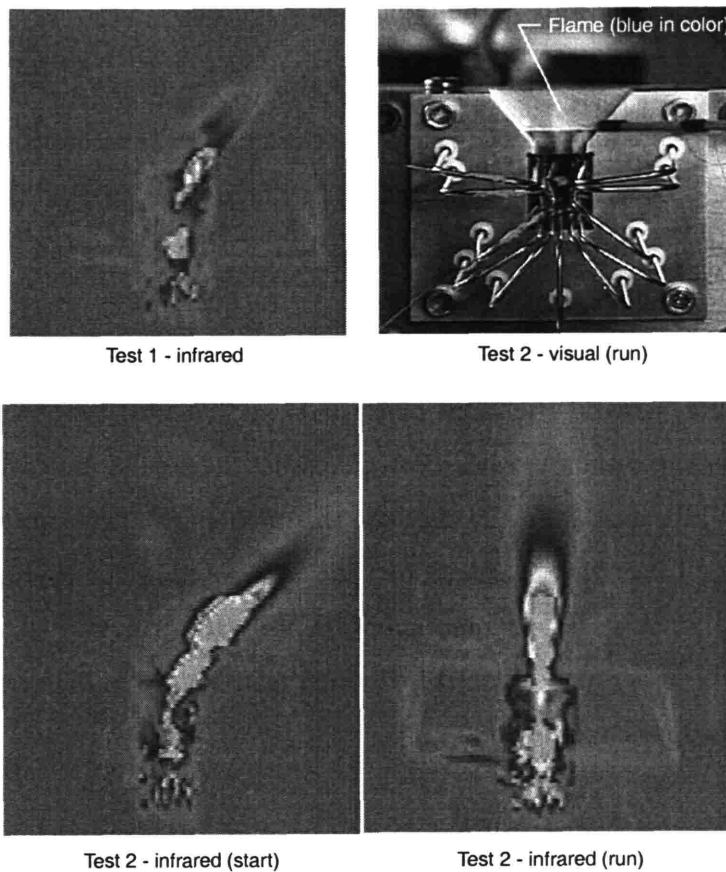


Figure 7-8: Images from tests 1 and 2. In the first test, the chamber pressure was sufficiently low for the flow to remain attached to the side of the nozzle. In the second test, the flow began attached, but then separated.

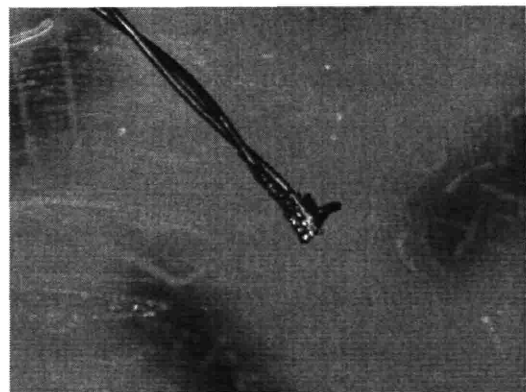


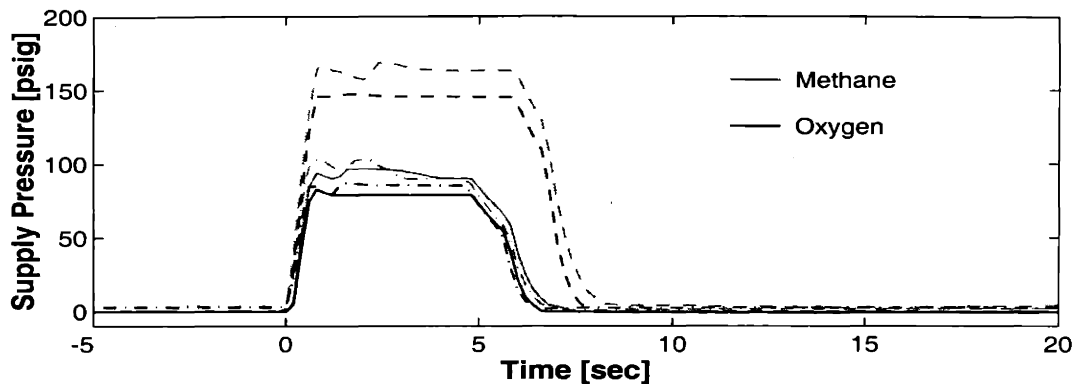
Figure 7-9: Ignitor wires after first test

tube decreased dramatically, leading to higher mass flows. This effect is probably due to a decrease in viscosity at the wall as the temperature increases.

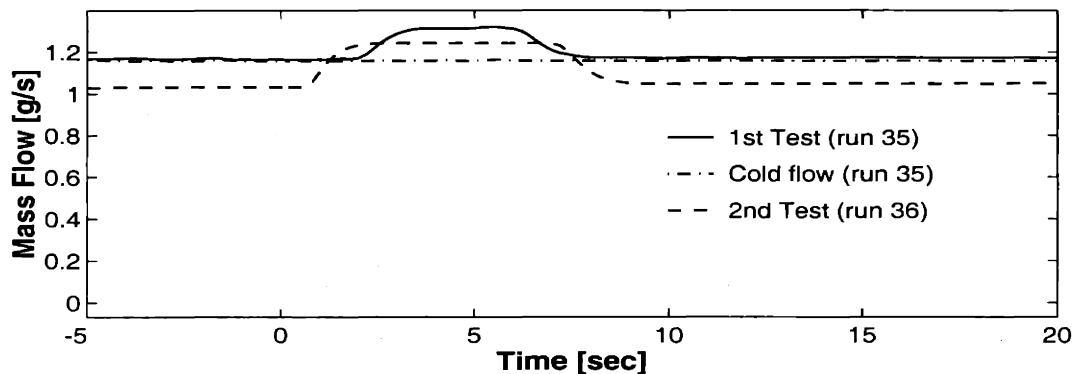
Figure 7-10(c) shows the recorded thrust levels during the tests. It is apparent that the thrust levels recorded are non-physical, as thrust continues to be recorded well after the time where combustion is occurring (as indicated by the increase in coolant flow). Additionally, the 1.5 N of thrust recorded in the second hot test would correspond to an unrealizable I_{sp} of nearly 750 sec. It appears that the force on the load cell being recorded is due to a thermal expansion of the steel coolant outlet tubes that are the two outside tubes of the thrust stand flexure between the large block and the fluid distribution block. This was verified by heating these tubes with a heat gun, with the results indicating a false thrust reading, as shown in Figure 7-11. To alleviate this problem, the coolant outlet tubes were replaced by copper tubes with a single loop in them to allow for thermal expansion, as shown in Figure 7-12. A closer examination of Figure 7-10(c) shows that the actual thrust signal appears to be superimposed on this thermal transient, as is illustrated in the figure. This thrust level is approximately 0.2 N.

7.6 Water-cooled tests

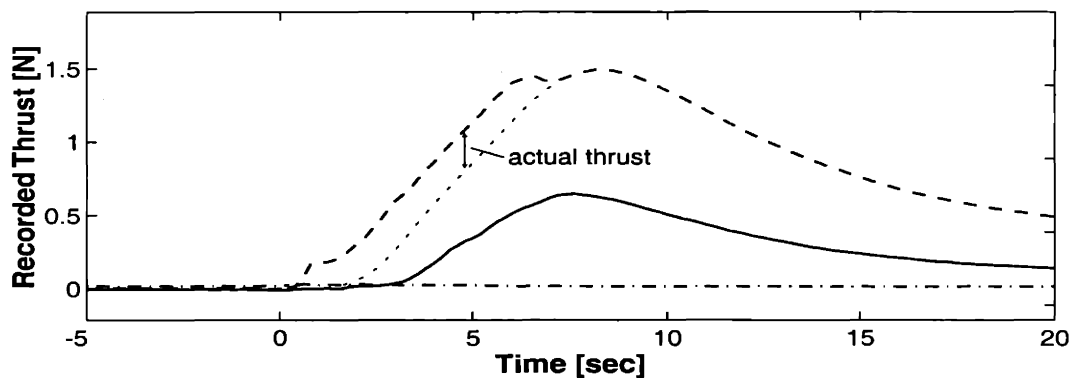
Following the two low pressure tests, three additional tests were performed using water as a coolant. The first two of these tests were performed using die A2, and were two-step runs. This means that the control signal for each propellant was initially ramped to a low pressure for ignition, and then ramped up to a run pressure where they are held for approximately 5 seconds. The first test had a peak chamber pressure of about 7 bar, and produced approximately 0.6 N of thrust. The second test produced 1 N of thrust at a chamber pressure of 12.3 bar, but lead to the failure of the die. The next test was designed to be a three-step run, where the ignition step was followed by two run levels at increasing pressures. Die C4 was used and ran successfully at 7 bar chamber pressure, but then failed near a chamber pressure of 10 bar as it was ramping up to the second operating point at higher pressure. Frames from the visual and infrared recordings of these tests are shown in Figures 7-13 to 7-15. The following sections will discuss some specific aspects of the tests.



(a) Propellant Supply Pressure



(b) Coolant Flow



(c) Recorded Thrust

Figure 7-10: Time traces of propellant supply pressures, coolant flow and recorded thrust during first low chamber pressure tests. The solid lines are the first test, run 35, the dot-dash lines are for a cold flow test at the same conditions immediately following it, and the dashed line is for the second test, run 36.

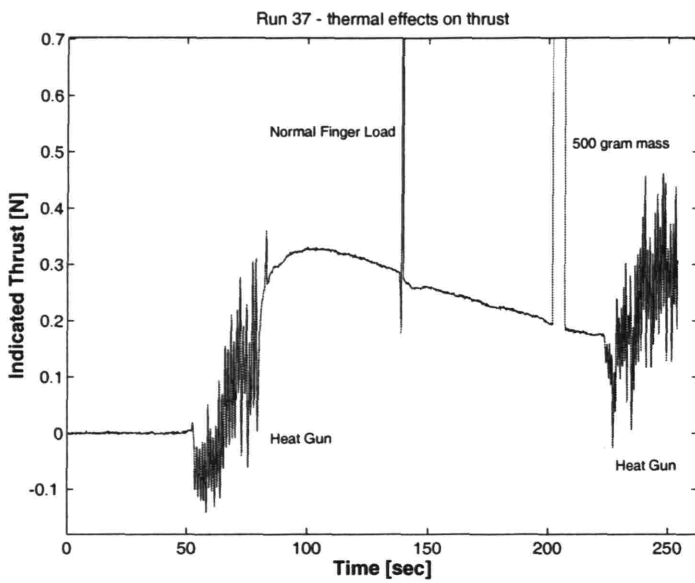


Figure 7-11: Thrust produced by thermal expansion of supply tubes

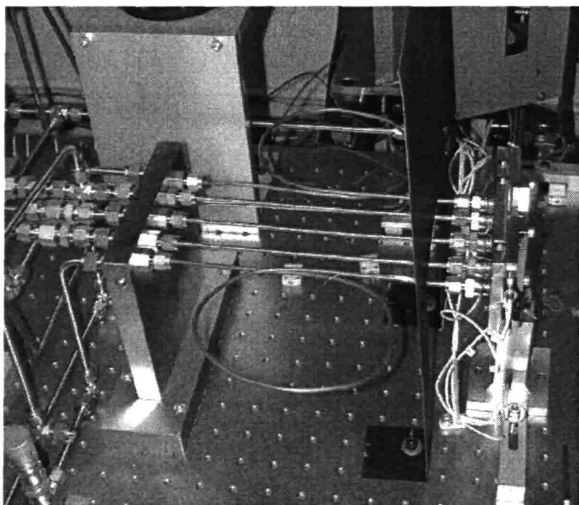


Figure 7-12: Copper loops added to thrust stand to alleviate indicated thrust due to thermal expansion

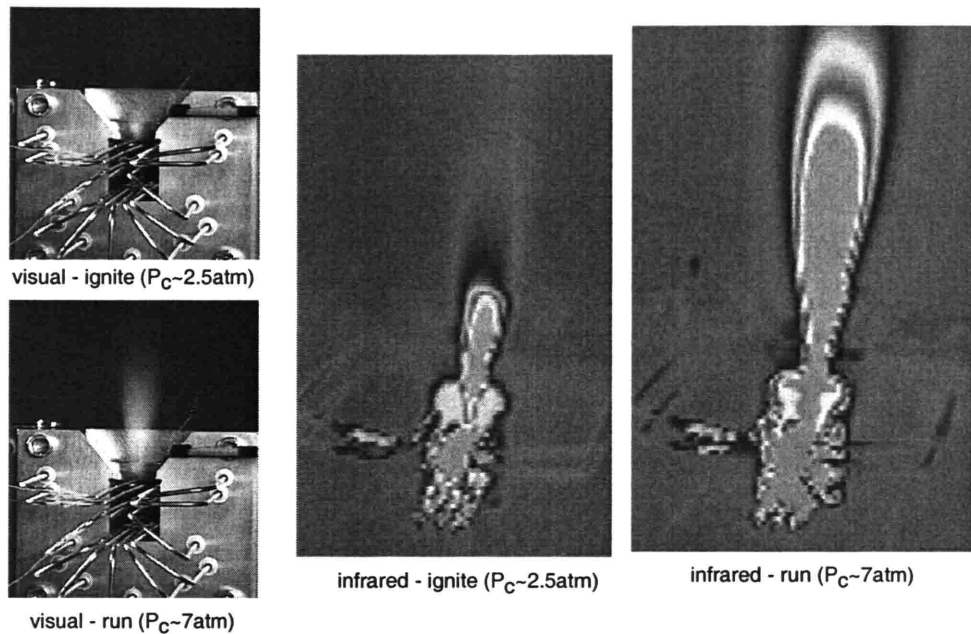


Figure 7-13: Images from third successful water cooled test, run 72. Chamber pressure of 7 bar, thrust of 0.6 N for run condition

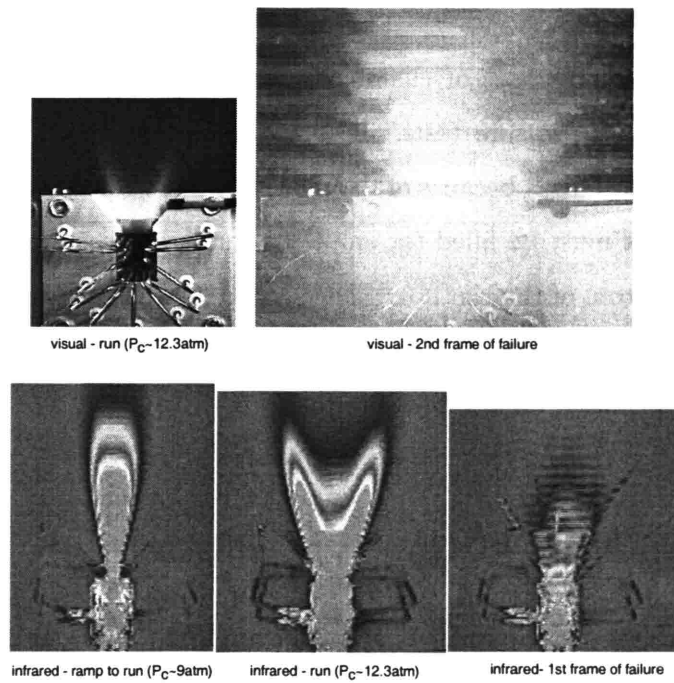


Figure 7-14: Images from fourth successful water cooled test, run 73. Chamber pressure of 12.3 bar, thrust of 1 N for run condition

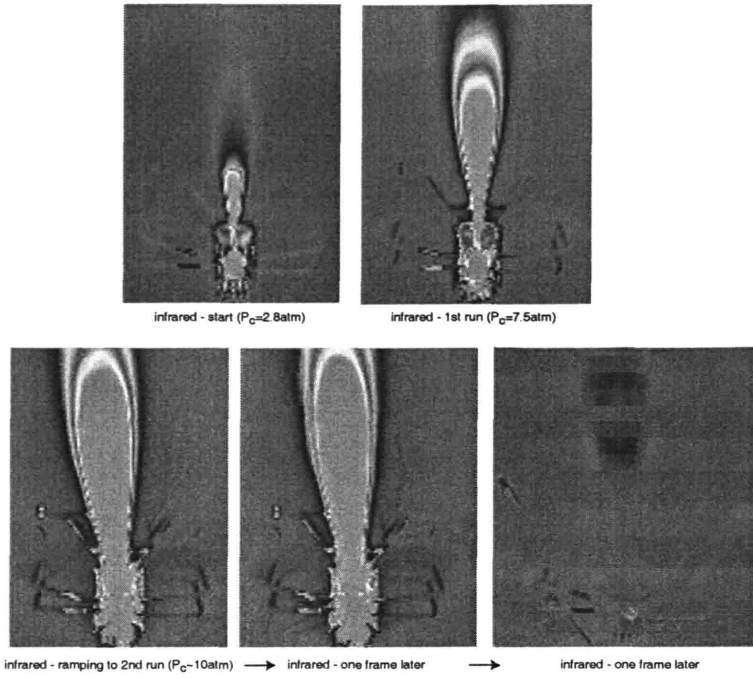


Figure 7-15: Images from fifth successful water cooled test, run 87. Chamber pressure of 7 bar, thrust of 0.7 N for first run condition

7.6.1 Chamber Pressure and Thrust

Figure 7-16 shows the time traces of chamber pressure and thrust for each of the three successful higher chamber pressure tests. It is apparent that there is a time lag in the chamber pressure signal. This is because of the relatively large volume between the chamber and the transducer that must be filled (or emptied) through the 50 μm -diameter pressure taps in the top and bottom of the chamber. The second test has a sudden drop in chamber pressure at the time of failure because the silicon fracture opened a direct path to the inlet port for the tube that is used for the pressure tap.

7.6.2 Propellant Flow Rate

The propellant flow rates are shown in Figure 7-17 for Run 72. In addition, the cold flow tests both prior and after this test are shown, which were run with identical regulator control levels (though the ignition time was 0.5 sec shorter for the run prior). It clearly shows that the flow rates of both the oxygen and methane are lower during the hot runs, even though

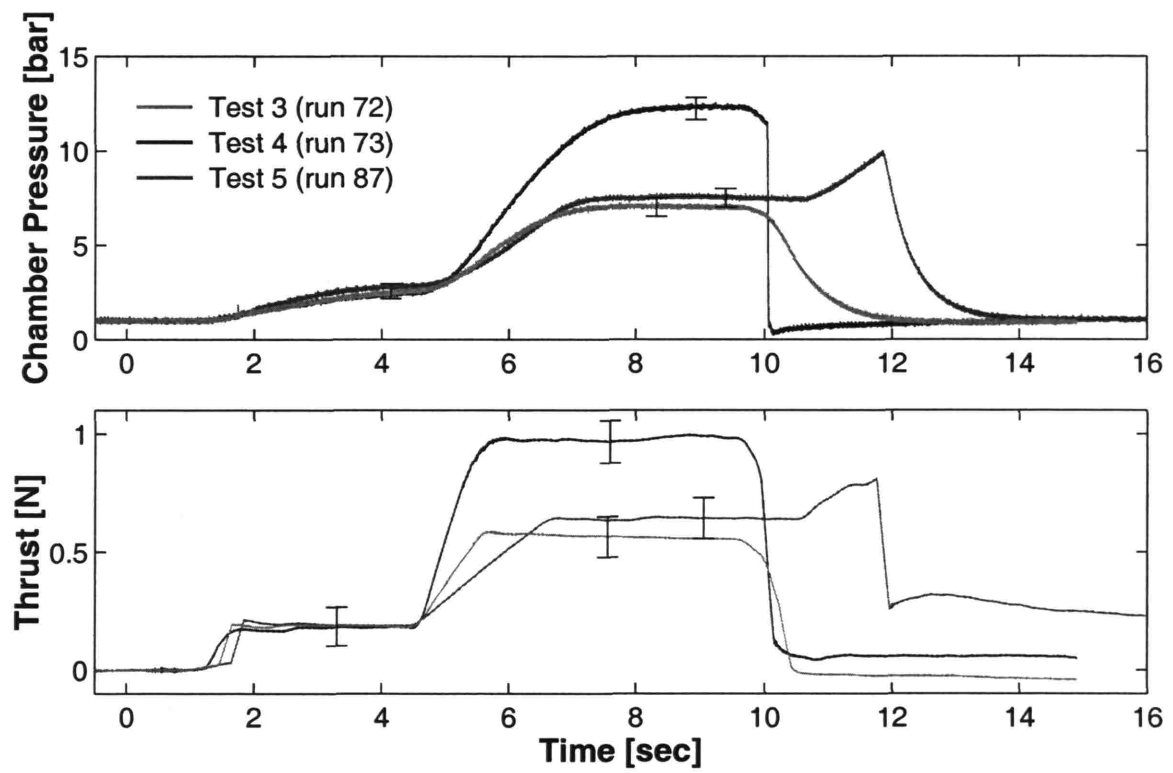


Figure 7-16: Chamber Pressure and Thrust for the water-cooled tests

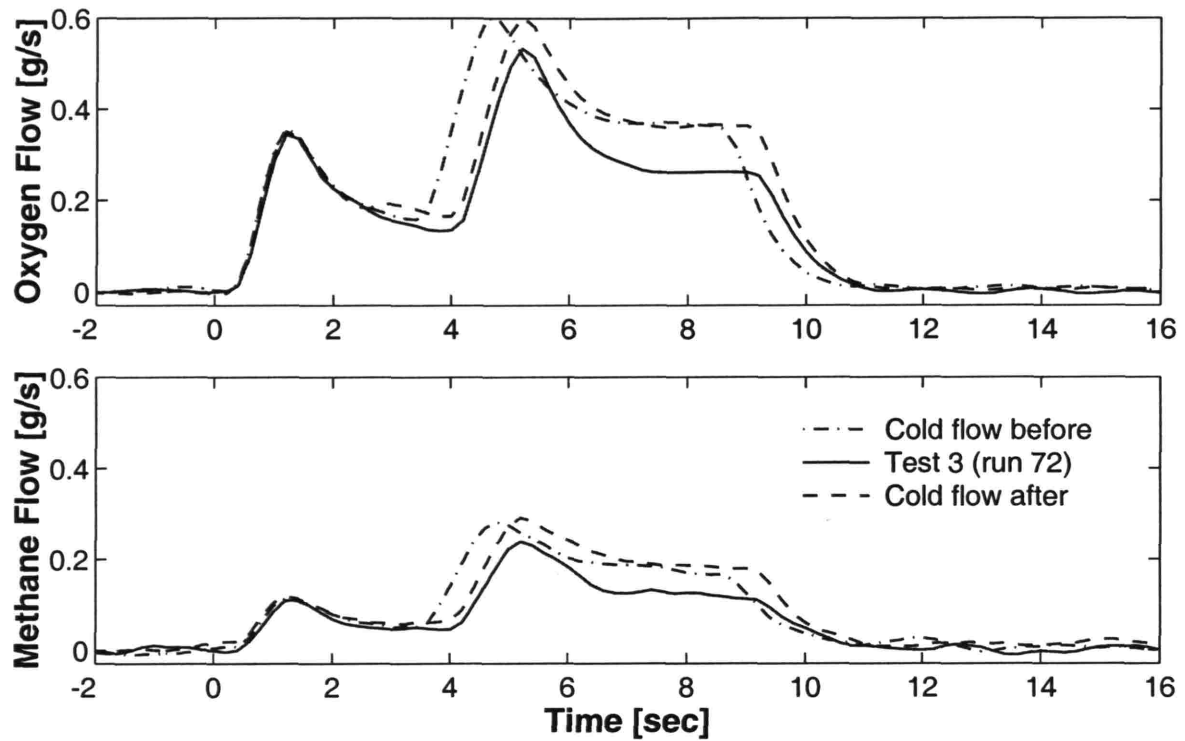


Figure 7-17: Propellant flow rates for the water-cooled tests

the supply pressure is constant. This appears to be due to the fact that the propellants being injected are also serving as coolants for the injection area at the forward end of the chamber and have an increased temperature prior to injection. Equation 7.1 shows that a higher T_t would lead to a lower mass flow for a constant injection area. Since the propellant mass flows during cold flow tests before and after the hot test remain essentially constant, a change in area does not appear to have occurred, leaving the temperature change as the most likely explanation for this effect, which could be used to provide an estimate the chamber heat flux.

7.6.3 Coolant Pressures, Flow Rate, and Temperature

Figure 7-18 and 7-19 show the mass flow, exit pressures, and entrance and exit temperatures of the coolant for Runs 72 and 73, the water-cooled tests of die A2. The vertical dotted line in the second figure is the time when the failure occurred, based on when the chamber pressure suddenly drops.

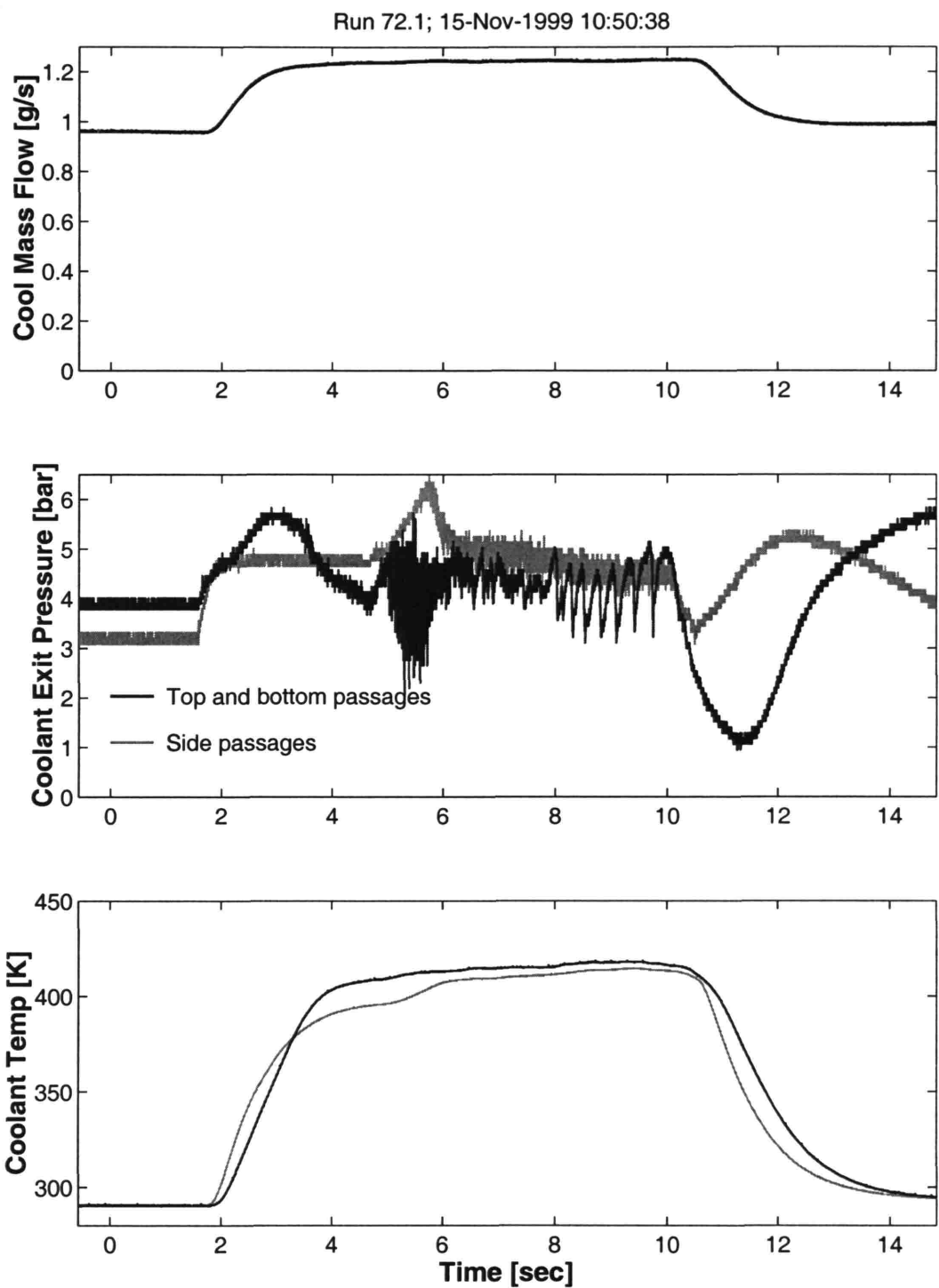


Figure 7-18: Time traces of coolant flow rate, outlet pressures, and outlet temperatures for Run 72.

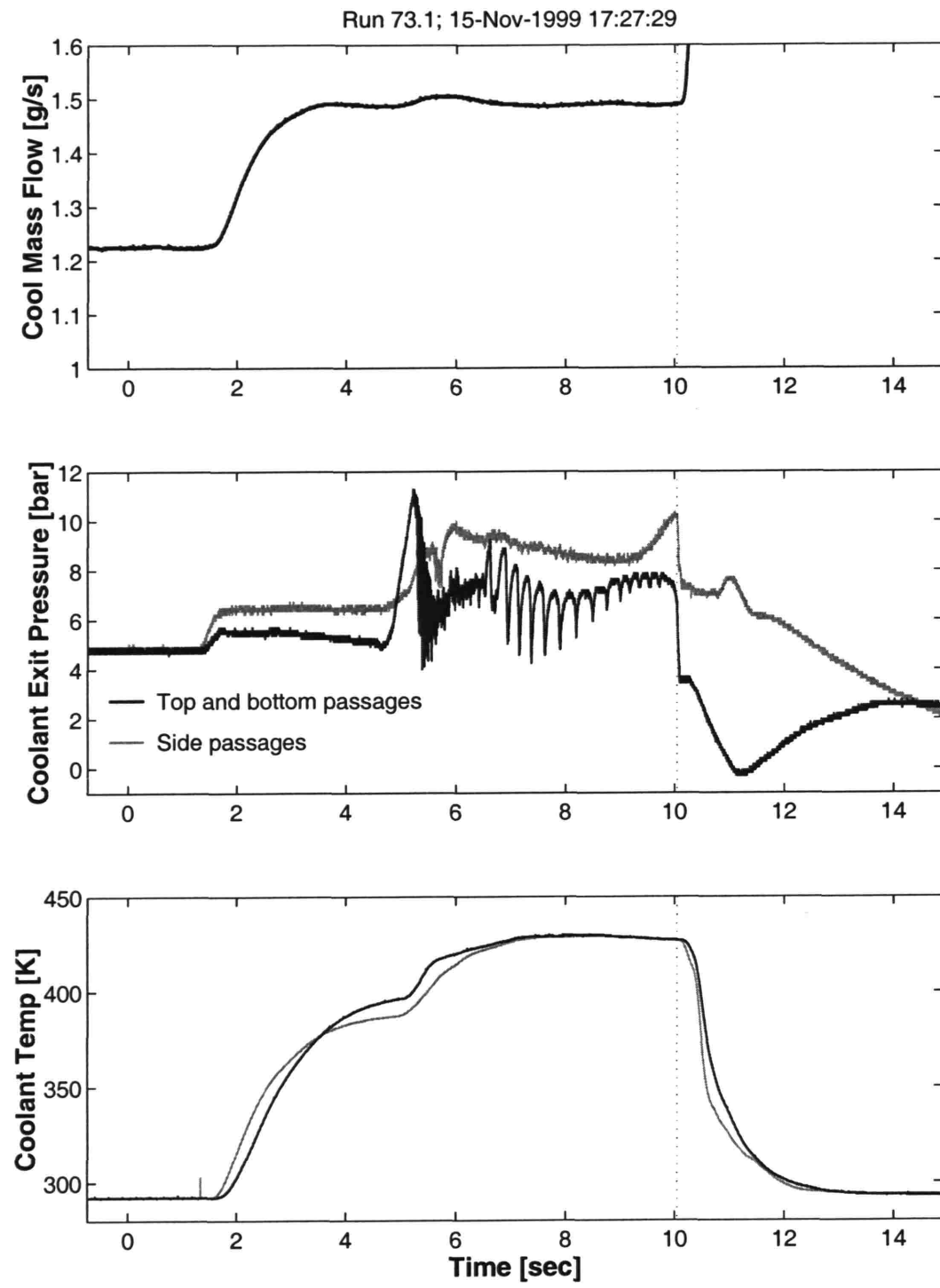


Figure 7-19: Time traces of coolant flow rate, outlet pressures, and outlet temperatures for Run 73.

The coolant mass flow rate increases during the firing by more than 20% in a manner similar to the results at low chamber pressure. However, the more interesting traces are those of the coolant exit pressure. As soon as the ignition occurs, the outlet pressure increases. This can be explained by the fact that since the coolant flow rate has increased, more flow must pass through the same size orifice set by the position of the metering valve downstream. The outlet pressure then rises to the level needed to drive the correct flow through the valve opening.

The oscillations in the top and bottom cooling passage outlet pressure during the second step of the run are a very prominent feature of the time traces. They may be caused by boiling of the coolant. Figure 7-20 is an expanded view of four seconds of Run 72, showing the pressure and temperature of the coolant at the outlet from the top and bottom cooling passages. One can see that the pressure is oscillating around an average pressure of approximately 4 bar, and that the coolant outlet temperature corresponds quite closely to the saturation temperature at this pressure, 417 K. Another example of this is shown in Figure 7-21, which shows the same information for Run 73. Again, the exit pressure oscillates around the pressure (6 bar) that corresponds to a saturation temperature equal to the coolant outlet temperature (430 K).

A qualitative description of the phenomena causing the oscillations could be as follows: the combination of the heat load and smaller than desired coolant flow rate leads to local boiling of the coolant and generates a number of small vapor pockets in the passages. The vapor has a smaller density than the liquid, and therefore needs to expand in volume, "pushing" on the liquid both downstream and upstream. This expansion means that a larger mass flow must go through the metering valve, which leads to a higher pressure at the coolant outlet. But by raising the pressure, the saturation temperature also increases, and the vapor that had formed eventually collapses back to its liquid state, decreasing in volume, and eliminating the need for a higher pressure to push the old pockets' volume of liquid through the metering valve. This leads to a drop in pressure, and the cycle repeats.

These effects are not desired, and they are considered a likely part of the cause of the failures that have been observed. Two measures have been taken to address this. The first is the removal of the pins, which appear to be the cause of the low coolant flow rate in the top and bottom passages, as seen earlier in the discussion of the cold flow characterization of the

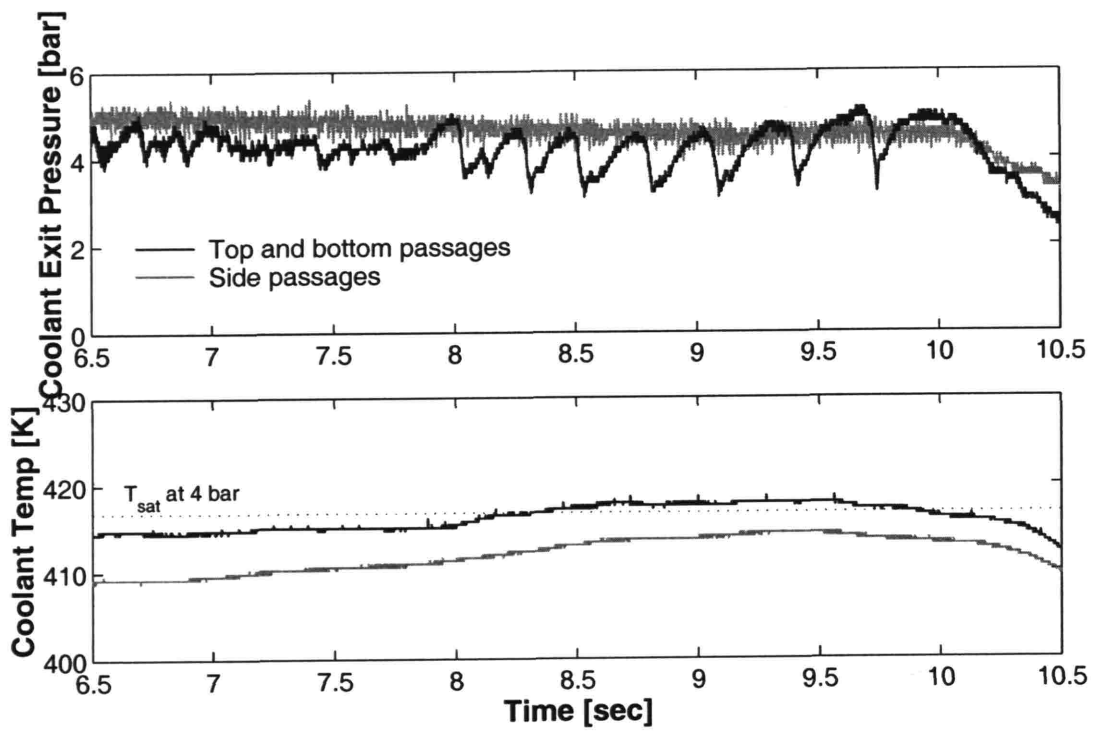


Figure 7-20: Closeup of coolant pressure and temperature, run 72. The outlet pressure is oscillating around a pressure near the saturation pressure for the coolant outlet temperature

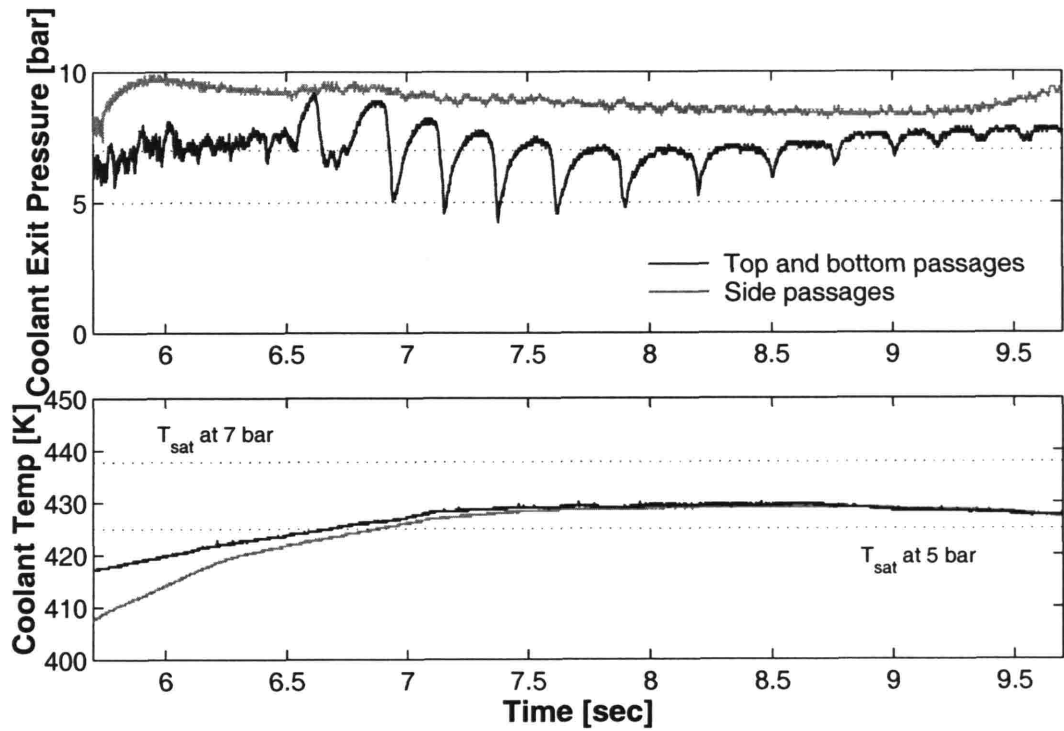


Figure 7-21: Closeup of coolant pressure and temperature, run 73. The outlet pressure is oscillating around a pressure near the saturation pressure for the coolant outlet temperature

coolant passages. For a given total heat load, a low flow rate would lead to a higher increase in enthalpy of the coolant, and would mean a larger fraction of the fluid would be converted to vapor. By increasing the flow rate, the vapor fraction could be decreased. Switching to a constant pressure coolant exit condition is the second change that was implemented, the implementation of which is discussed in the previous chapter. Removing the orifice as the exit condition allows the flow rate and coolant outlet pressure to be decoupled, which should help to prevent the oscillations encountered in these tests. Specifically, when using ethanol as a coolant, it should be possible to set the outlet pressure above the critical pressure of the coolant (63 bar for ethanol, but 220 bar for water), which should eliminate the possibility of boiling in the cooling passages.

7.7 Summary

This chapter has presented the results of the initial tests of a microfabricated rocket engine thrust chamber. Using water as a coolant, these tests were conducted at chamber pressures up to 12 bar. The following chapter will present a more detailed analysis of the results from these tests in an effort to further quantify the performance and potential of micro-rocket engines.

CHAPTER 8

ANALYSIS AND DISCUSSION OF RESULTS

8.1 Introduction

This chapter will present the performance and heat load parameters that can be derived from the experimental measurements. It will focus on the specific impulse of a measure of rocket performance, and will show that after correction for non-adiabatic and nozzle effects, the experimental values of I_{sp} are within 5-15% of the expected ideal values.

8.2 Specific Impulse

The specific impulse, or I_{sp} is the derived quantity easiest to determine, as it is defined as

$$I_{sp} = \frac{F}{\dot{m}g} \quad (8.1)$$

where g is the acceleration of gravity. Since both thrust and mass flow are measured directly, the I_{sp} is easily calculated. For the three higher chamber pressure runs (72, 73, 87) considered here, both the ignition and run conditions are considered, for a total of six cases. In each case, the I_{sp} is calculated at three points once the mass flow transient is complete, and then averaged. It is approximately 150 sec for the run conditions of these tests, and approximately 100 sec for the start phases of these tests. For comparison, the ideal I_{sp} would be about 320 sec at the design condition. This chapter will examine the components that make up the I_{sp} , and after accounting for non-idealities that can be estimated, show that the experimental I_{sp} is within 5-15% of the values that are expected for the conditions of each run.

The I_{sp} , or more specifically the effective exhaust velocity, c ($= I_{sp}g = F/\dot{m}$), can be written as the product of two terms:

$$c = c^* C_F \quad (8.2)$$

where

$$c^* = \frac{P_c A_t}{\dot{m}}, \quad \text{and} \quad C_F = \frac{F}{P_c A_t} \quad (8.3)$$

and A_t is the throat area. The characteristic exhaust velocity, c^* , can be considered a measure of the efficiency of combustion. The non-dimensional thrust coefficient, C_F , is a measure of how effective the nozzle is in expanding the high pressure gasses of the chamber to produce thrust.

The next section will discuss the measured and inferred heat load to the coolant, as this information will be important in estimating the expected value of c^* . The following two sections will then present estimates of c^* and C_F for the rocket tests that have been conducted, and discuss the implications of these results.

8.3 Heat Load

This section will discuss how the experimental results can be used to estimate the integrated internal heat flux of the thrust chamber. Evaluating the heat load is important for two reasons. First, it will quantify the energy loss due to cooling for these tests. In order to compare the results from these tests to ideal adiabatic calculations and to what would be expected from eventual regeneratively cooled microrocket engines, a correction must be made for this energy loss. Second, it will provide preliminary information as to the accuracy and applicability of the various hot-side heat transfer correlations used in the design and modeling phase of this work.

The total heat absorbed is equivalent to the total enthalpy rise of the coolant, which is calculated from measurements of the coolant mass flow and its inlet and outlet temperature. As was discussed in Chapter 6, the experimental setup is such that the total mass flow is

measured at the inlet to the thrust chamber, and then the coolant is split internally into two flows: one cools the side walls and one cools the top and bottom walls. Each of the flows exits the engine independently, and the outlet temperature and pressure of each is measured. An initial estimate of the total heat load to the coolant, as inferred from the average temperature rise and total coolant mass flow is shown in Figure 8-1 for the six test conditions in order of decreasing chamber pressure. Additionally, four values of the overall heat load that would be predicted by the design model for each run condition are shown for each case, two for each of the high and nominal heat flux correlations. The hot-side heat transfer coefficient can be estimated independently of the cold-side cooling properties, but a wall temperature is required to predict a heat flux which is then integrated to yield the total heat load. The two cases considered as bounds are setting the hot-side wall temperature, T_w , to the design point of 900 K, and setting the cold-side wall temperature, T_{wc} , to 450 K. The latter would correspond to having film boiling throughout the entire passages of sufficient effectiveness that the cold-side wall temperature remained at the saturation temperature independent of heat flux. Faust[?] has observed conditions similar to this in experiments with water-cooled heated microtubes.

It appears that the nominal heat load correlation gives the best agreement with the data, and though this encouraging, it is somewhat misleading, as the total heat load is probably higher than has been calculated based simply on the coolant temperature rise. As was discussed in the previous chapter, the exit temperatures and pressures measured during these tests correspond quite closely with the saturation conditions of water. This is illustrated in Figure 8-2, which shows that the difference between the measured coolant outlet temperature and the saturation temperature corresponding to the measured outlet pressure is less than 7 K for the top cooling flow in most of the runs. This implies that some fraction of the top coolant is vapor at its outlet, which in turn implies that additional energy has been deposited in the flow to form vapor which is not accounted for by simply measuring the temperature rise of the propellant. Given the measurements that have been taken, it is nearly impossible to quantify how much vapor has been produced, which therefore makes it difficult to accurately quantify the total heat load.

If one assumes that the side wall coolant has not been heated past its saturation temperature, it is possible to estimate the total heat load to the top and bottom walls if one has an

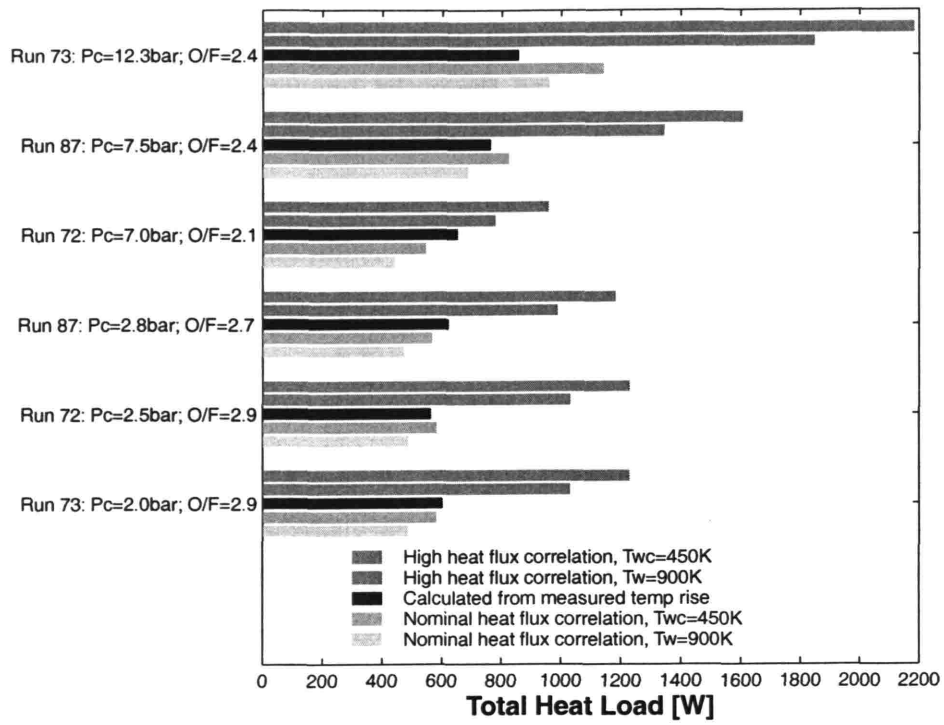


Figure 8-1: The total heat load measured from the coolant temperature rise is compared to the correlations used in design and modelling. Each correlation considers two wall conditions, one with fixed hot-side temperature, $T_w = 900$ K; the other with fixed cold-side temperature, $T_{wc} = 450$ K.

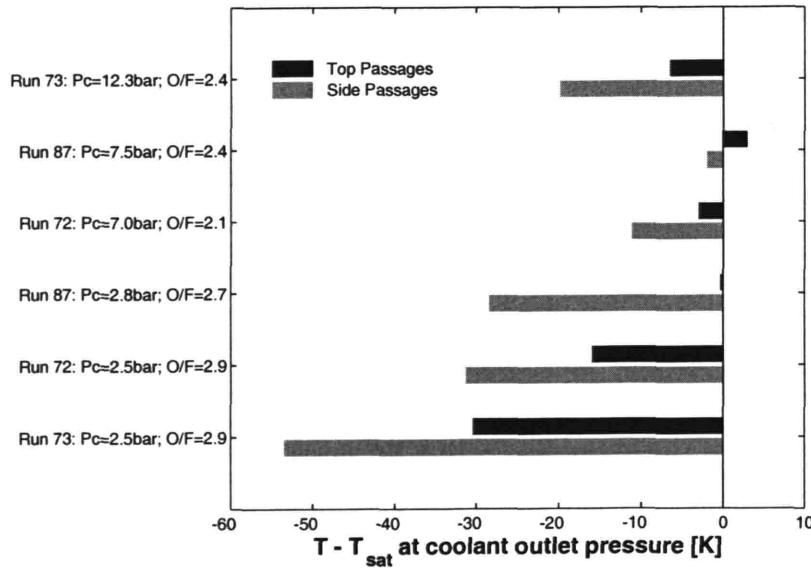


Figure 8-2: The coolant in the top passages appears to be at saturation temperature, as the difference between the measured outlet temperature and the saturation temperature at the measured outlet pressure is small.

estimate of the ratio between top and side cooling heat loads. Given this estimate of the top wall heat load, one can subtract off the energy required to heat the coolant to its saturation temperature, and be left with the quantity of energy that would be used in converting some fraction of the coolant to vapor. The design model suggests that this ratio between top and side-wall heat loads is approximately 1.15 to 1.30, so this ratio will be used to estimate the total top wall heat load given a side wall heat load.

In order to estimate the heat load to the side walls and perform this calculation, the mass flow split between the top and side passages must be known. During the cold flow characterization, it was determined that approximately 30% of the coolant mass flow was through the top passages. Once combustion begins, the coolant flow rate increases by approximately 25%, and it is not known how this additional flow is distributed between the passages. One could assume that the flow distribution remains the same as in cold flow, which would lead to the results shown in Figure 8-3. In this case, the total side wall heat load is better predicted by the high heat flux correlation, though still falls between the predictions of the two correlations, except in the case where the O/F is 2.1 which is under-predicted by the correlations. This could imply that the variation in heat load with mixture ratio is not as severe as that predicted by the correlations.

It is conceivable, though not very likely,* that all of the additional coolant flow ends up going through the top passages. This can be considered an upper bound on the top coolant flow. Adding the 25% increase in overall flow to the top cooling flow would imply that 45% of the coolant flow was through the top passages, and the heat load results given this assumption are shown in Figure 8-4. In this case, the heat loads inferred from the data are between the predictions of the two correlations, but are closer to the nominal correlation.

If one assumes that the mass flow distribution remains approximately that observed in the cold-flow characterization, this implies, as shown in Figure 8-3, that 35-55% of the coolant in the top channels has been vaporized prior to exiting the cooling passages, even at the ignition conditions. However, this is based on the assumption that the ratio of top to side heat load predicted by the model is accurate, which may not be the case as this ratio will

*Using a set of estimated c_v values based on the settings of the metering valves during the runs, the coolant outlet pressures predict a ratio of top to side flow near 0.4, which is consistent with the 30/70 split found in the cold flow characterization.

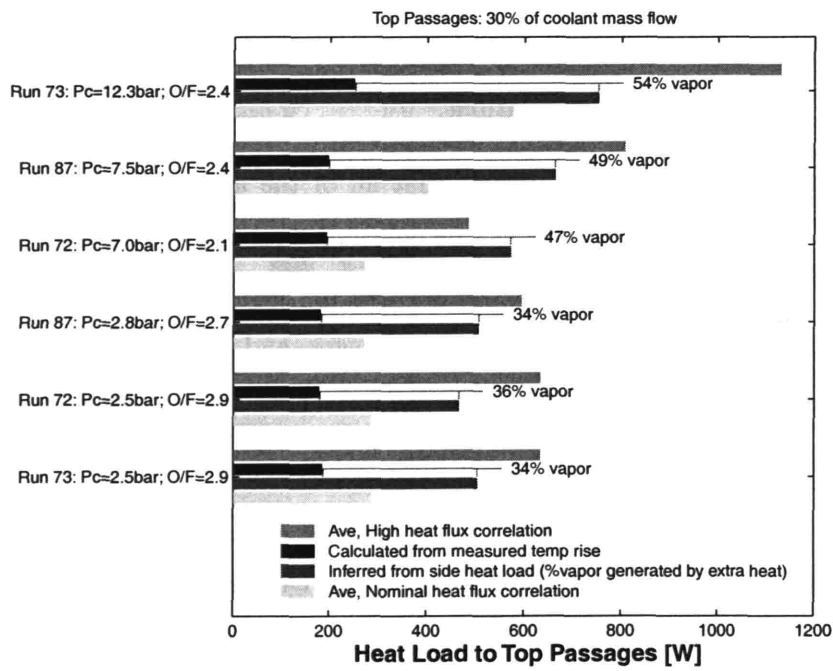
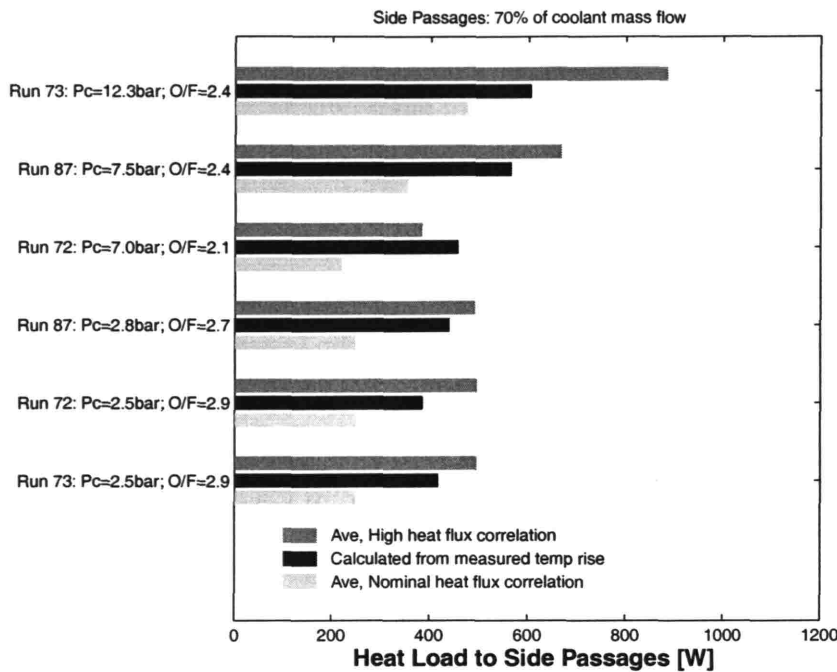


Figure 8-3: The top figure shows the total heat load to the side passages, assuming 70% of the coolant flows through them, and no vaporization occurs. The lower figure shows the heat load that would correspond to the measured temperature rise of the top coolant, as well as that predicted by scaling the side heat load. The difference is assumed to generate vapor in the top passages.

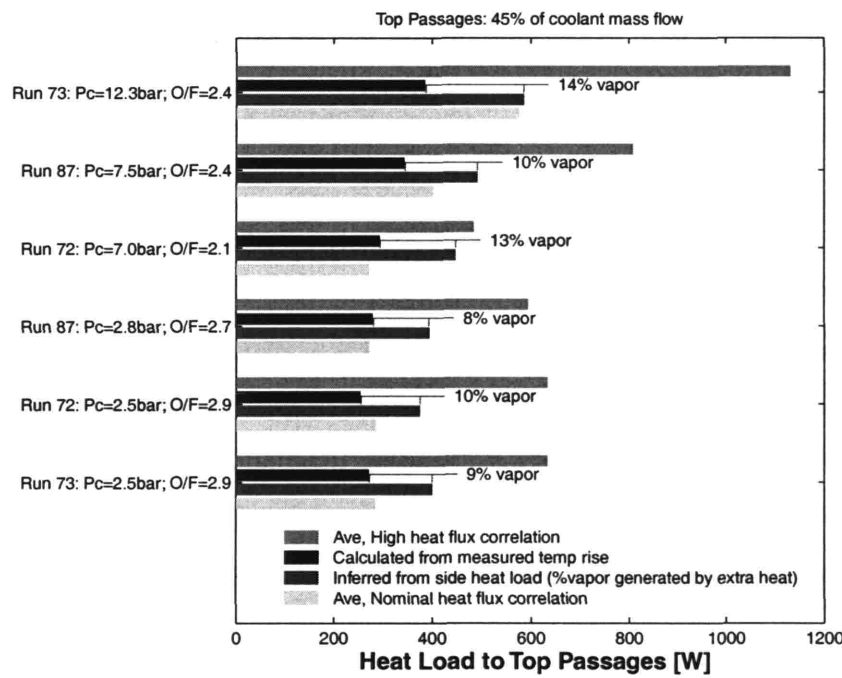
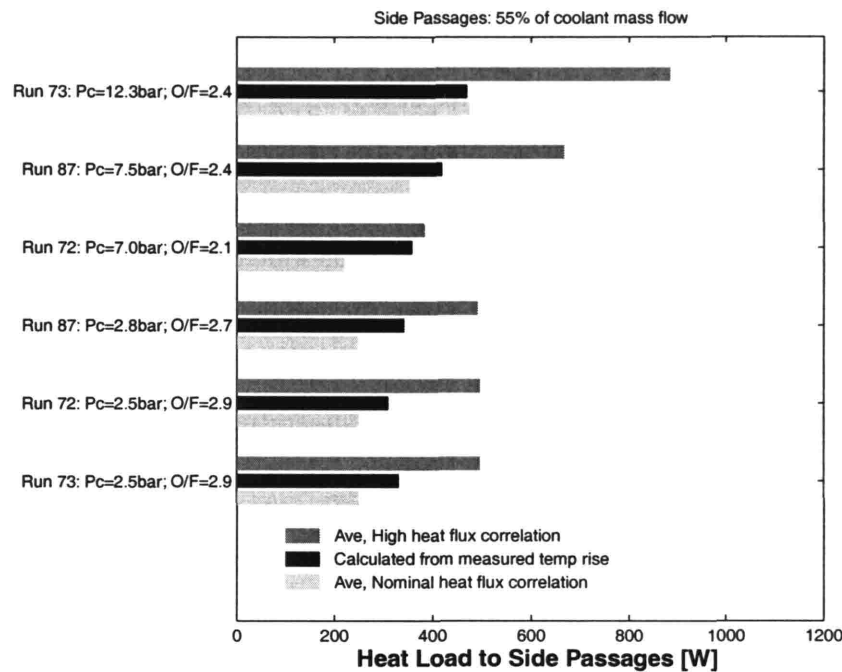


Figure 8-4: The same plots as Figure 8-3, but with 55% of the coolant flowing through the side passages. A lower side coolant mass flow means less heat has been absorbed into the side passages, which when scaled means a lower total heat load to the top walls. Additionally, a larger fraction of this total must be used to heat the top coolant's larger mass flow to saturation temperature, leaving even less for use in generation of vapor.

depend on the heat flux profile through the nozzle. This is because the side walls are more influenced by the throat heat flux than are the top and bottom walls because there is more side wall area than top area near the throat while the opposite is true in the chamber. The model predicts that about 15% of the total heat load to the top passages comes from the area within 1 mm of the throat, while about 40% of the side wall heat load is from this area. The model suggests that the ratio between the peak heat flux at the throat and that in the chamber is approximately 100, but if this value were different, the ratio of top to side heat load would be as well. This would change the predicted top heat load of Figures 8-3 and 8-4, and therefore the estimate of the amount of vapor formed as well. Unfortunately, until more experiments are performed where the temperature of both top and side coolants remains below their saturation temperature, it is not possible to quantify this further.

The conclusion is that the total heat load appears to fall somewhere between the predictions of the nominal and high heat flux correlations, depending on what quantity of coolant is vaporized. The two bounds of zero vaporization (corresponding to a total heat load of about 900 W), and that predicted by a mass flow split equivalent to the cold flow tests (about 1300 W) will be used in the section that follows to correct for non-adiabatic effects in estimating c^* , the characteristic exhaust velocity.

8.4 Characteristic Exhaust Velocity, c^*

Given the effective throat area determined by cold flow characterizations, the characteristic exhaust velocity, c^* , can be calculated, and it is shown as a function of chamber pressure in Figure 8-5. In the same figure, the corresponding ideal adiabatic values are shown, along with two sets of non-adiabatic estimates. These three sets of predicted values are calculated by the CEA code for the mixture ratio and chamber pressure of each case.

As was mentioned previously, c^* can be considered a measure of the combustion effectiveness. For an idealized one-dimensional rocket flow, it can be written as

$$c^* = \sqrt{RT_c} \left(\frac{\gamma + 1}{2\gamma} \right)^{\frac{\gamma+1}{2(\gamma-1)}} \quad (8.4)$$

and thus is a measure of the chamber temperature, or how much thermal energy is de-

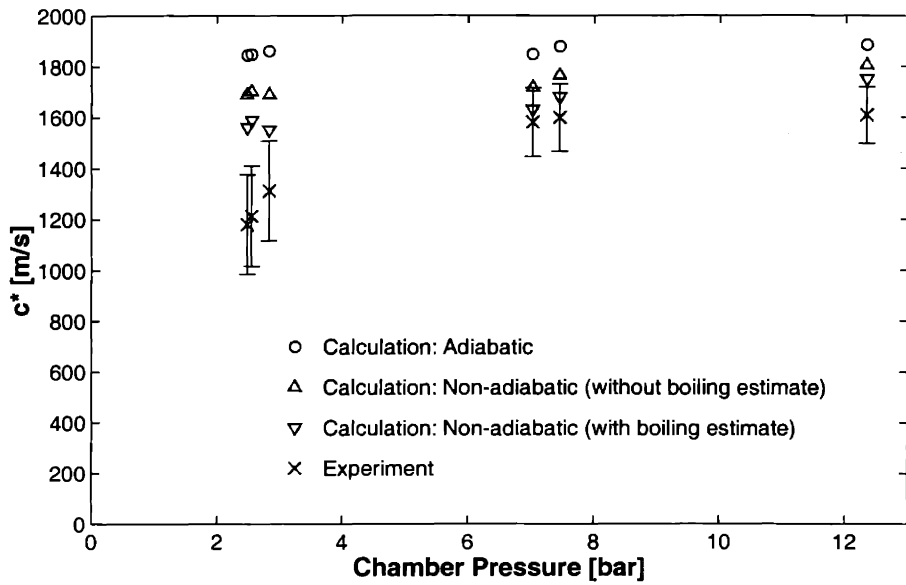


Figure 8-5: The values of c^* inferred from the experimental measurements are compared with three sets of calculated values assuming equilibrium combustion and three different heat loss cases. The fact that c^* appears to be constant with pressures above 7 bar implies that the kinetic reaction rates are not limiting the combustion process. The fact that the non-adiabatic calculations are in reasonable agreement with the experimental values implies that the injection and mixing processes are of the right order for complete combustion.

posited in the combustion products during combustion. As such, the difference between the experimental and ideal values of c^* can be considered a measure of the completeness of combustion. As was mentioned earlier, there are two sets of processes that must be completed during the time the propellants are in the chamber to ensure complete combustion. First, the propellants must be injected and mix sufficiently to allow the chemical reactions to occur. Second, the chemical reactions themselves must be completed. The implications of the experimental values of c^* on each of these steps will be discussed below, in reverse order.

If the combustion processes were limited by the reaction rates, one would expect that c^* would increase significantly with chamber pressure, as the kinetic reaction rates tend to scale as P_c to some power greater than one. Though there is an increase in c^* between a P_c of 2 and 7 bar, it is nearly unchanged between a P_c of 7 and 12.5 bar, where one would expect the kinetic rates to at least double while the residence time remains essentially unchanged. The fact that c^* remains nearly constant as the pressure increases suggests that the kinetics are not limiting the combustion process. Because the kinetics are one of the few aspects

of rocket engine design over which the designer has little engineering control, this is a very important result, as it suggests that the factors limiting rocket engine performance at this scale are mixing and the nozzle expansion, two things that can be improved through engineering and better design.

Since c^* is a measure of the energy deposited in the combustion products, it will be reduced through the loss of some of this energy in heat transfer to the coolant. The non-adiabatic calculations shown in Figure 8-5 attempt to quantify this effect, using the estimates of total heat load to the coolant shown in the previous section. For each case, the design model predicts that a certain fraction of the heat load to the coolant occurs upstream of the throat (usually around 75%). One of the inputs to the CEA calculation is the inlet enthalpy of the propellants, and if this is reduced by the quantity corresponding to this chamber heat load, a non-adiabatic estimate of c^* is produced, as is shown in Figure 8-5. Two cases are considered, with first assuming no coolant vaporization, and the second assuming a total heat load scaled from the side passage heat load, as in Figure 8-3.

The agreement between the experimental and calculated values of c^* begin to suggest that the mixing processes are of the right order to provide complete combustion, though the uncertainties in these results make it difficult to quantify this further. It is likely that the agreement is less good at the highest chamber pressure because the quantity of vapor generation here that is not accounted for in the calculations is larger.

8.5 Thrust Coefficient

Given the effective exhaust velocity, c , and the characteristic exhaust velocity, c^* , the thrust coefficient can be determined. It is shown in Figure 8-6, along with the maximum C_F as a function of chamber pressure for a sea-level ambient condition. The later is a one-dimensional idealized calculation given by

$$C_F = \sqrt{\frac{2\gamma^2}{\gamma-1} \left[1 - (P_e/P_c)^{\frac{\gamma-1}{\gamma}} \right]} \left(\frac{2}{\gamma+1} \right)^{\frac{\gamma+1}{2(\gamma-1)}} + \frac{P_e - P_{atm}}{P_c} \frac{A_e}{A_t} \quad (8.5)$$

This can be considered a function of P_c/P_e and the nozzle area ratio only, as P_e/P_c can

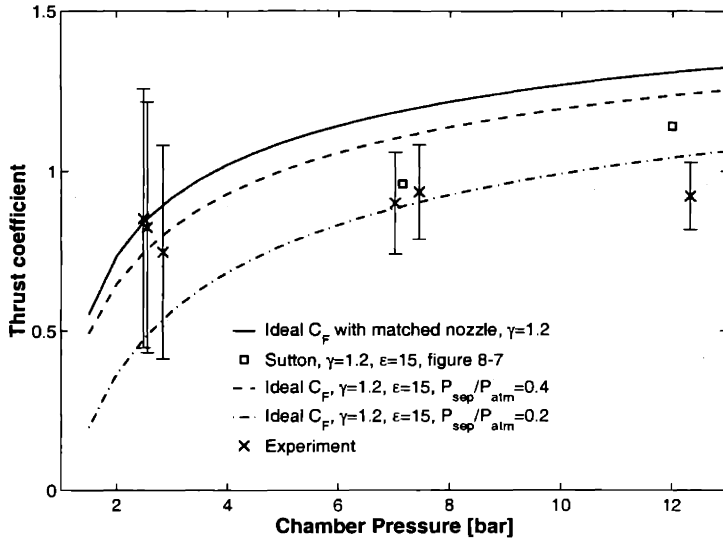


Figure 8-6: Measured thrust coefficient as function of pressure compared to maximum C_F for $\gamma = 1.8$. (This would require the nozzle area ratio to vary in order to match exit and atmospheric pressure.) Also shown are two points taken from Figure 8-7 via Sutton [38], that show the expected value of C_F for a nozzle area ratio of 15, as in the current work, accounting for separation in the nozzle.

be determined by the nozzle area ratio, $\epsilon = A_e/A_t$. For a given chamber pressure, C_F is maximized for the nozzle area ratio that yields $P_e = P_{atm}$, and it is this maximum C_F that is shown as the solid line in Figure 8-6. However, the nozzle area ratio is fixed at 15, and one would expect the flow in the nozzle to separate well upstream of the exit, given the low chamber pressures of these tests. This separation is typically characterized by the pressure ratio between the point of separation and ambient conditions, or P_{sep}/P_{atm} . For axisymmetric nozzles this value is typically about 0.4 [38], but it is not known what this ratio would be for the prismatic geometry of the nozzle considered here. Presumably it would somewhere in the range of 0.2-0.5. The dashed and dot-dashed lines are plots of Equation 8.5 which account for separation by assuming that the nozzle ends when $P_e = P_{sep}$. Sutton [38] has provided a plot of C_F that accounts for the separation effect and additional boundary growth in axisymmetric nozzles, which is reproduced here as Figure 8-7.

A vertical line has been superimposed on this plot to illustrate the area ratio of the current work, and horizontal lines show this idealized C_F , including the effect of separation, for $P_c/P_e = 7$ and 12. These values are also plotted in Figure 8-6 as squares. For the tests with $P_c \sim 7$ bar, the data show fairly good agreement with the prediction of Sutton,

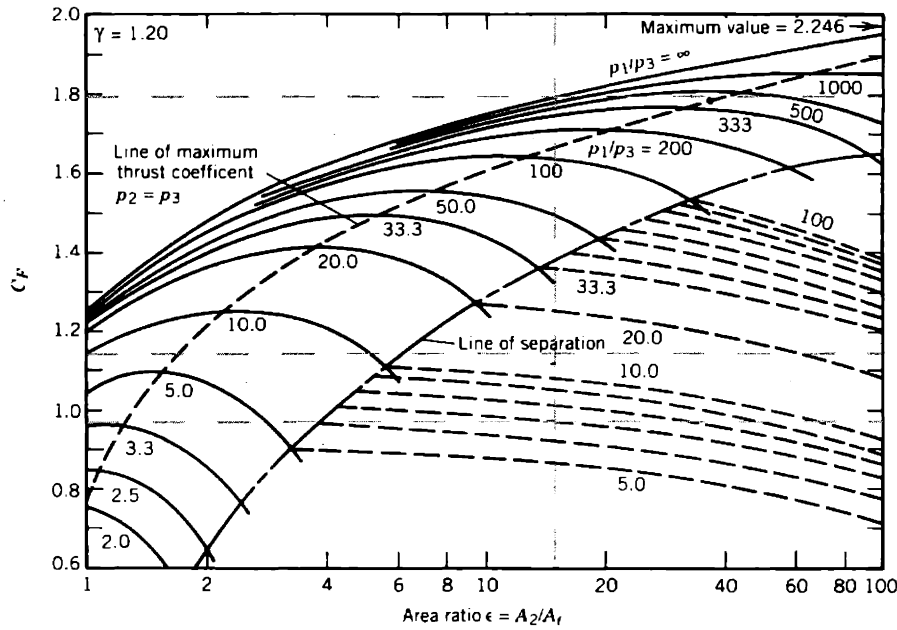


Figure 8-7: Ideal C_F as function of nozzle area ratio and pressure for $\gamma = 1.20$. Reproduced from Sutton [38]. In his nomenclature, p_1 is chamber pressure (P_c), p_2 is exit pressure (P_e), and p_3 is the ambient pressure (P_{atm}). The vertical dashed line corresponds to the thrust chambers expansion ratio of 15, and the horizontal lines show the ideal C_F for the chamber pressures of 7 and 12 bar in the tests considered, as well as the potential C_F if the engine were to be run in vacuum.

but the agreement is less good for the case of $P_c \sim 12$ bar. A partial explanation for this discrepancy is the split plume seen in this test. (See Figure 7-14). The angle from centerline to each side of the plume is approximately 25 degrees, which would correspond to a 10% reduction in thrust and thrust coefficient if all of the fluid's momentum was directed at this angle. One can see that a correction of this magnitude would make the measured C_F more in line with the idealized case of a one-dimensional nozzle flow at this chamber pressure. In any case, the best estimate of the experimental C_F appears to be within 5-15% of the theoretical value expected for one-dimensional flow based on the chamber pressure and nozzle expansion ratio. It must be restated that the geometry of the present nozzle is sufficiently different from conventional rocket engine nozzles to make it difficult to predict the C_F of the separated nozzle flow that has been observed. It does appear to be in the range that would be expected based on experience with large axisymmetric nozzles, which suggests that viscous effects in the nozzle should not significantly limit the performance of micro rocket engines.

8.6 Specific Impulse

The overall performance is quantified by I_{sp} , which is the scaled product of c^* and C_F . The experimental and predicted values of I_{sp} are shown in Figure 8-8. The predictions in the upper plot use the theoretical values of C_F from Figure 8-7,[†] but as it is not known how well these correspond to the actual geometry tested, the predictions in the lower plot use the experimental C_F , and are therefore basically a plot of how close the experimental c^* is to the predicted values, expressed in terms of I_{sp} .

Overall, the experiment and predictions agree to within 10-20%. The agreement is improved when only the combustion processes (meaning c^*) are considered.

As a side note, it is worth considering what would have happened if these tests were to have been run in vacuum. As the C_F approached its limiting value of 1.8 for a nozzle with an area ratio of 15, the measured c^* would imply a vacuum I_{sp} of 290 to 295 sec. If the system was made regeneratively cooled, and c^* approached its adiabatic value, this becomes 310 to 340 sec. However, it is unlikely that C_F would be this large, even in a vacuum ambient, as there would likely be a significant component of non-axial momentum in the exhaust flow.

8.7 Summary

This chapter has discussed the analysis of the experimental results presented in the previous chapter. The primary conclusions are as follows:

1. The characteristic exhaust velocity, or c^* , becomes nearly constant with increasing pressure. This implies that the chemical kinetics are not limiting the combustion process.
2. The experimental values of c^* agree well with non-adiabatic predictions, implying that the mixing and transport processes within the chamber are of the right order to provide for complete combustion.

[†]For run 73, this value is reduced by 10% to account for the split plume

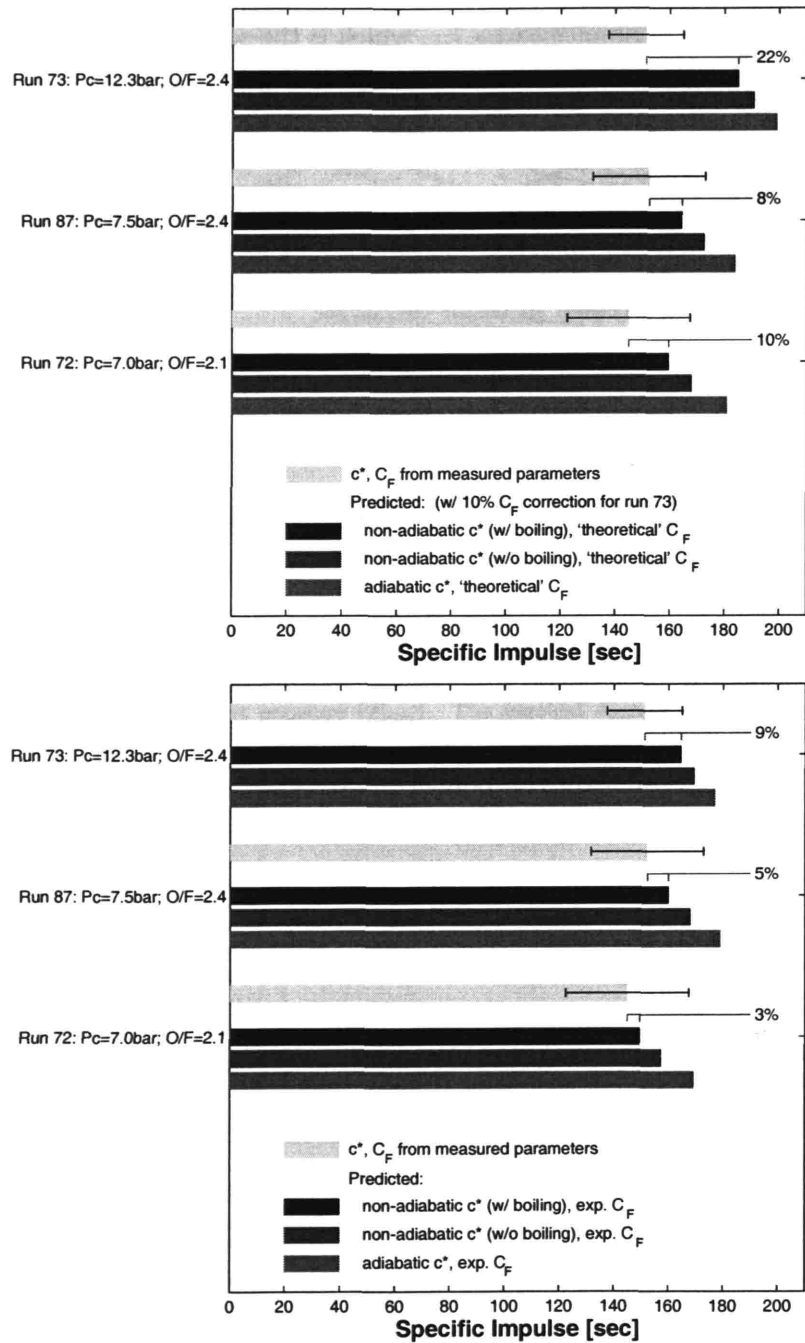


Figure 8-8: Comparison of experimental and predicted I_{sp} . The upper plot uses the theoretical C_F from Figure 8-7, and the lower uses the experimental values, making the latter essentially a comparison of experimental and predicted c^* . The three cases of c^* considered are the same shown in Figure 8-5, namely an adiabatic case, a non-adiabatic case not accounting for vapor generation, and a non-adiabatic case including an estimate of the quantity of vapor generated.

3. The experimental values of the thrust coefficient, or C_F , is in the range that would be expected based on experience with separated nozzle flow in large rocket engines. This implies that the viscous effects in expansion nozzles of the current size should not severely impact the performance of microrocket engines

Taken together, these results suggest that high-performance rocket thrust chambers are realizable.

Finally, the path to improved I_{sp} performance is also clear. The chamber pressure must be increased. As c^* appears to be near its theoretical limit, and does not depend directly on pressure, performance improvements will come through an increased thrust coefficient, which does increase with increased chamber pressure, as can be seen in Figure 8-7. Depending on the performance of the nozzle at higher pressure ratios, enhancements of up to 60% in I_{sp} are possible. Additionally, it is likely that maximizing performance will require an optimized nozzle geometry to provide a more uniformly-directed velocity profile at the exit.

CHAPTER 9

CONCLUSIONS AND RECOMMENDATIONS

This chapter will present a summary of the research discussed in this thesis, describe the specific contributions of this research, and make recommendations for future work in this area.

9.1 Summary

The concept of microfabricated bipropellant liquid rocket engines has been introduced. These devices, made from silicon or other refractory ceramics, will integrate turbopumps, a thrust chamber, valves, and other controls into a single silicon rocket engine “chip,” providing functionality and performance similar to that of large scale rocket engines, but at the millimeter to centimeter scale.

The performance of such devices has been modeled, and using these models, the physical constraints of these systems are identified and used to describe the design space of this technology. This design space is presented in terms of a feasible specific impulse envelope, which describes the maximum feasible I_{sp} as a function of chamber pressure for a given geometry. The I_{sp} is limited at low pressures by the total heat load to the coolant, and at high pressures by the maximum heat flux at the throat that can be successfully transferred to the coolants.

As an initial validation of this concept, a demonstration thrust chamber has been designed, fabricated, packaged, and tested. The device was fabricated sixteen-at-a-time from a set of six silicon wafers, which were individually etched to define the combustion chamber, exit nozzle, propellant injectors, and liquid cooling passages, and then bonded together to form

a monolithic set of devices, which is then cut into individual thrust chamber die.

A packaging technique has been developed that can be used to provide a high pressure and high temperature capable fluid interface to silicon microdevices. This technique is used to make the eleven fluid connections necessary to test the thrust chamber.

A test apparatus has been constructed and used to test a number of the fabricated thrust chambers. To date, six successful ignitions have occurred, using four separate thrust chambers. The maximum recorded thrust was 1 N, at a chamber pressure of 12.3 bar, for a thrust-to-weight ratio of 85:1.

The limitations that have prevented tests at higher chamber pressure appear to be a combination of insufficient cooling flow due to a higher than expected pressure drop through the cooling passages, and insufficient packaging yield in that a single failure out of the eleven high pressure glass seals prevents a test from occurring.

The experimental data collected have been analyzed, and suggest that the small scale of these devices is not significantly limiting the combustion process. The best estimates of specific impulse based on the experimental measurements agree to within 5-20% of the ideal values as calculated for the test conditions, once corrections are made for chamber heat loss and nozzle separation effects.

9.2 Contributions

The contributions of this work may be summarized as follows:

1. The design, fabrication, packaging, and testing of a liquid-cooled bipropellant rocket engine thrust chamber made of silicon with a throat area of less than 1 mm².

Specifically, a cooled-thrust chamber has been designed and constructed from six individually etched silicon wafers bonded together. Additionally, a packaging technique has been developed to allow for high pressure and high temperature fluidic connections to silicon microdevices.

2. An experimental demonstration that the performance of rocket engine combustion systems of the millimeter scale can approach ideal levels.

Continuous combustion of oxygen and methane has been demonstrated at chamber pressures of up to 12 atm. The characteristic exhaust velocity, c^* , a measure of combustion effectiveness, appears to be nearly independent of chamber pressure, indicating that chemical reaction rates are not limiting the combustion. Additionally, once corrected for chamber heat loss, c^* appears to approach its ideal value, indicating that the transport and mixing of propellants in the combustion chamber is of the right order to provide for complete combustion.

3. The development of a methodology for mapping the feasible design space of micro-rocket engines.

The mechanisms that present the primary feasibility limitations of microrocket engine systems have been identified, and models have been developed to describe how these limitations depend on engine size and geometry.

9.3 Recommendations for Future Work

The recommendations for future work in this area are as follows:

Using current gaseous propellant design:

1. The current thrust chamber, now modified to have a higher coolant flow capability, should be able to be run at higher chamber pressures. This will lead to smaller uncertainties in the measurements than has been presented in this thesis, and should lead to a much improved specific impulse as the thrust coefficient increases.
2. Additionally, higher coolant flow rates will allow for a more accurate characterization of the ratio of top to side wall heat loads, which will provide additional information about the relative magnitude of the throat and chamber heat fluxes. This will be important in future redesigns of the cooling system.
3. Improved temperature instrumentation, either using in situ measurement techniques or via a infrared camera, that could provide information about the internal temperatures of the cooling walls would prove valuable in evaluating the effectiveness of the

cold-side heat transfer design. This will be particularly important once a regeneratively cooled system is implemented.

Potential second generation rocket thrust chambers:

1. Liquid Propellants. An eventual microrocket device will run on liquid propellants, and though these will likely be heated to a near gaseous phase at the design condition, they will have to start as liquids. Thus building and testing a liquid fueled-thrust chamber, ideally with the capability to pre-heat the propellants, would prove valuable.
2. Packaging. The symmetric packaging scheme requiring 11 fluid connections should be eliminated in favor of a design that uses 6 connections, with only one connection per fluid port. This will decrease the number of successful joints that needs to be made during packaging, and should improve packaging yield.
3. Consideration should be given to having separate top and side cooling circuits, so that the coolant mass flow of each may be measured independently.
4. Expansion Nozzle. A new design of the expansion nozzle has the potential to improve the performance of the thrust chamber through ensuring that a greater fraction of the exit momentum is directed in the axial direction.

APPENDIX A

UNCERTAINTY ANALYSIS

A.1 Introduction

This appendix presents an analysis of the uncertainty associated with the measurements and derived quantities presented in this thesis. The nomenclature used for representing this uncertainty is the fractional uncertainty, S_x , where

$$S_x = \frac{\text{Uncertainty in value of } x}{\text{Indicated value of } x} \quad (\text{A.1})$$

The uncertainty of the independent measurements is presented first, followed by a discussion of how these uncertainties are propagated to derived quantities.

A.2 Uncertainty of the Independent Measurements

A.2.1 Pressure

The pressure transducers were calibrated using two gauges, each with a stated accuracy of 0.25% full scale. For the high pressure calibrations, the reference gauge was a 0-6000 psi gauge, so the accuracy of the reference pressure was ± 15 psi. For the low pressure calibration, a 300 psi gauge was used, implying an accuracy of approximately ± 1 psi in the reference. The goal of each calibration is to determine a scale factor for the gauges which is multiplied by the difference between the gauge reading and the zero value taken prior to each run to determine the indicated pressure. Figures A-1 to A-3 show the results of the calibrations. For each transducer, the scale factor, sf, is shown as calculated for that

Table A.1: Example uncertainties in pressure measurements

Pressure [bar]	Uncertainty [bar] (%)	Comment
2.5	0.4 (15 %)	Chamber pressure during ignition
7.0	0.5 (6.7%)	Chamber pressure run 71,87
12.5	0.6 (4.6%)	Chamber pressure run 72
100	3.0 (3.0%)	Typical propellant feed pressure

calibration, as well as the percent difference from the scale factor used to reduce the data for the results shown in this thesis. These three calibrations were taken over the period of six months, and the maximum variation in scale factor is 1.6%, which would correspond to a $\pm 1.6\%$ error in any given measurement. To be conservative, it is assumed that the possible error in scale factor from run to run is $\pm 2\%$, leading to a corresponding uncertainty in the pressure measurements. In addition to the error from the drift of the scale factor, one can see that there is an additional uncertainty. For the calibrations at high pressure, the variations in indicated pressure are within ± 15 psi, the accuracy of the reference. For the low pressure calibration, the variations in pressure are within ± 5 psi, except for sensor 4, the side cooling outlet, which has a variation of approximately 7 psi.

Therefore, the estimations of uncertainty for the pressure measurements are as follows:

$$\begin{aligned}
 S_P &= \pm 0.02 \pm \frac{15 \text{ psi}}{P}, \quad \text{for } P > 250 \text{ psig} \\
 &= \pm 0.02 \pm \frac{5 \text{ psi}}{P}, \quad \text{for } P < 250 \text{ psig} \\
 &= \pm 0.02 \pm \frac{10 \text{ psi}}{P}, \quad \text{for } P < 250 \text{ psig, sensor4}
 \end{aligned} \tag{A.2}$$

Table A.1 provides the expected uncertainty in pressure for a number of example cases.

A.2.2 Thrust

The thrust stand was calibrated by adding weights of known mass to the thrust stand and recording the output of the load cell. 500 gram masses were used, which were weighed on a balance accurate to 0.01 g, which verified that they were within 0.05% of their nominal

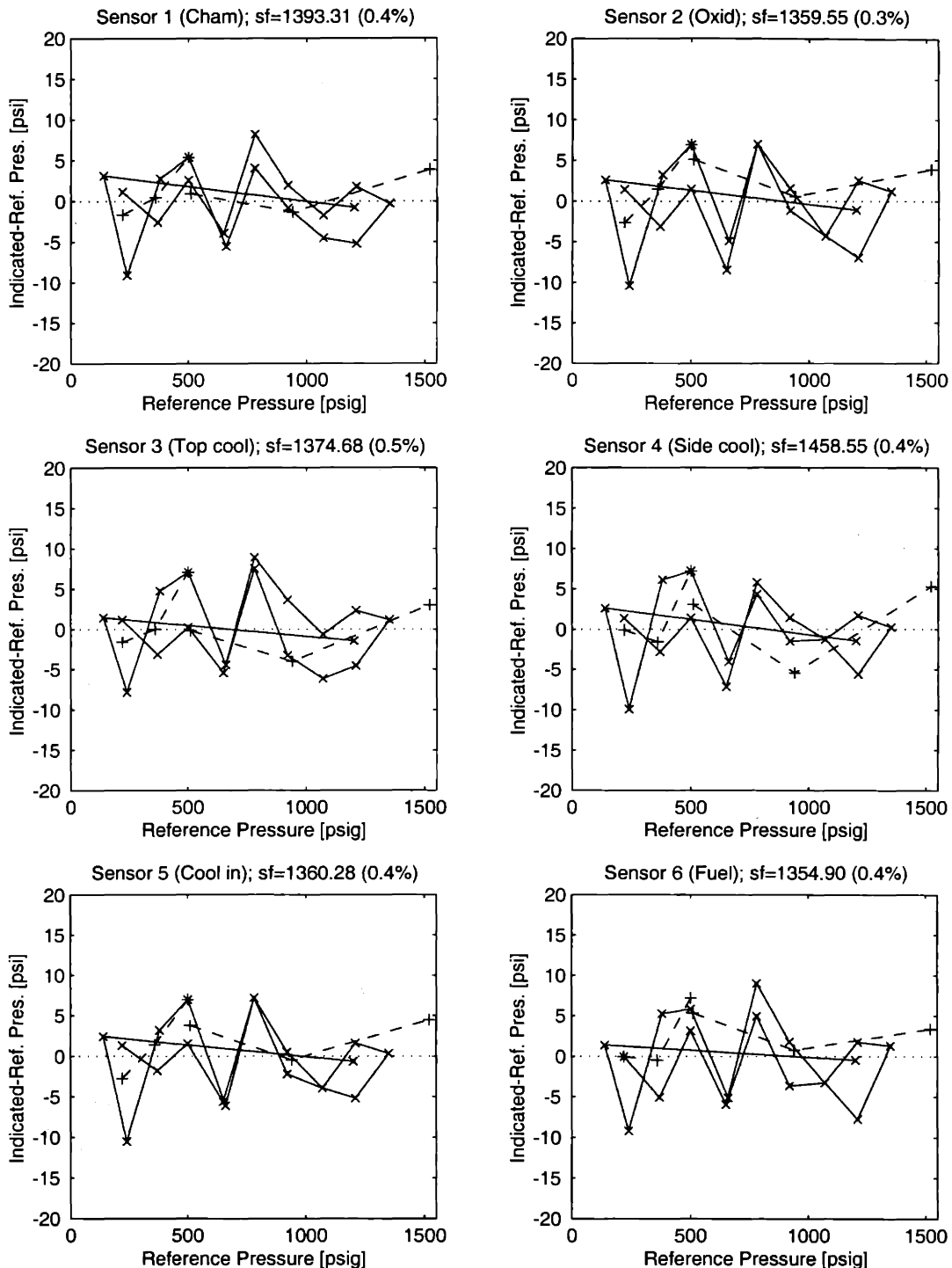


Figure A-1: This figure shows the difference between the indicated and reference pressures for calibrations # 6 and 7, performed in October 1999. The scale factor, sf, is in units of psi/Volt, and the number in parentheses is the percent difference between this scale factor and the one used to reduce the data presented in the thesis. The dashed line is Cal #6, and the solid, Cal #7.

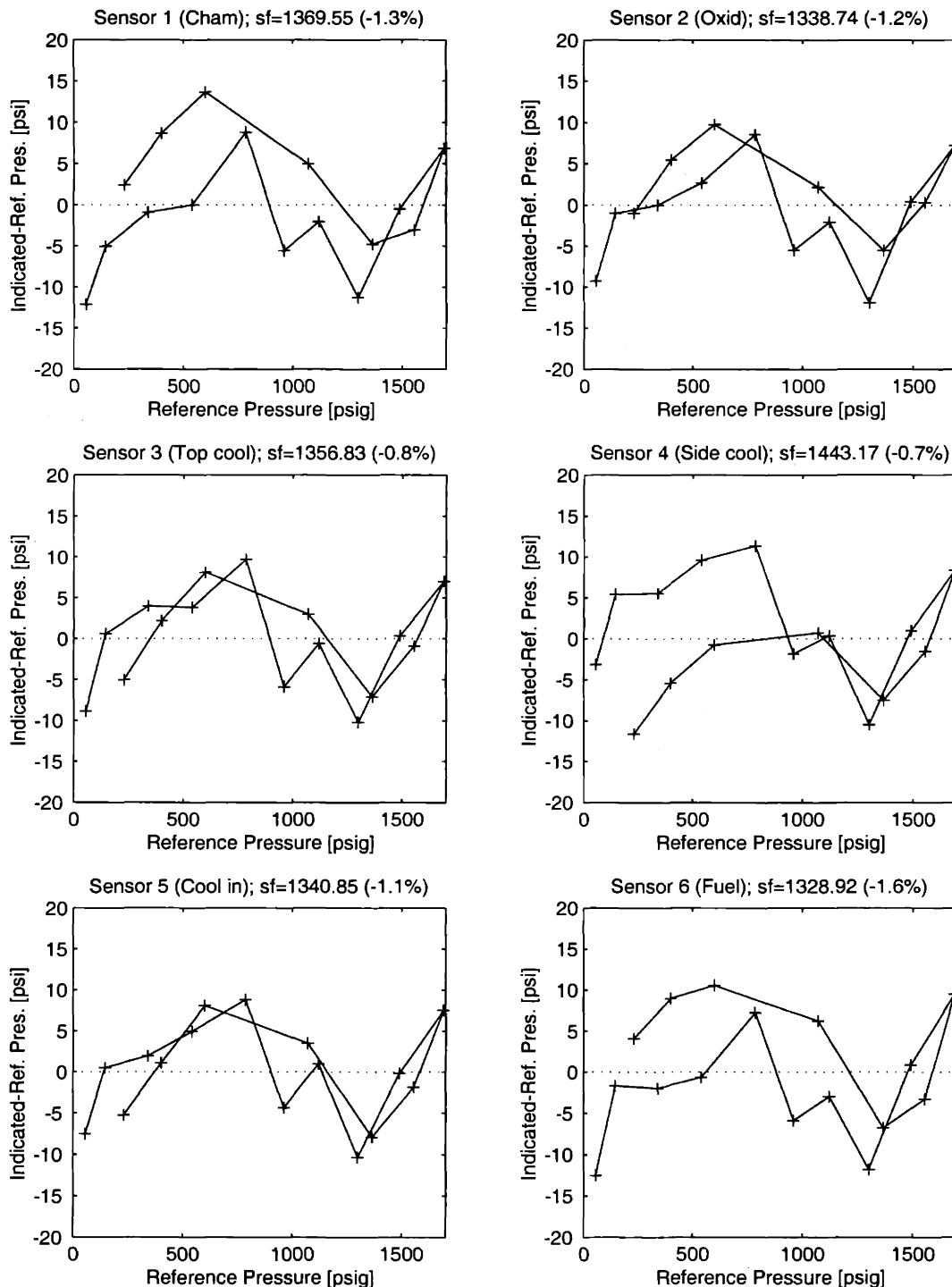


Figure A-2: This figure shows the difference between the indicated and reference pressures for calibration # 51 and 52, performed in January 2000. The scale factor, sf, is in units of psi/Volt, and the number in parentheses is the percent difference between this scale factor and the one used to reduce the data presented in the thesis.

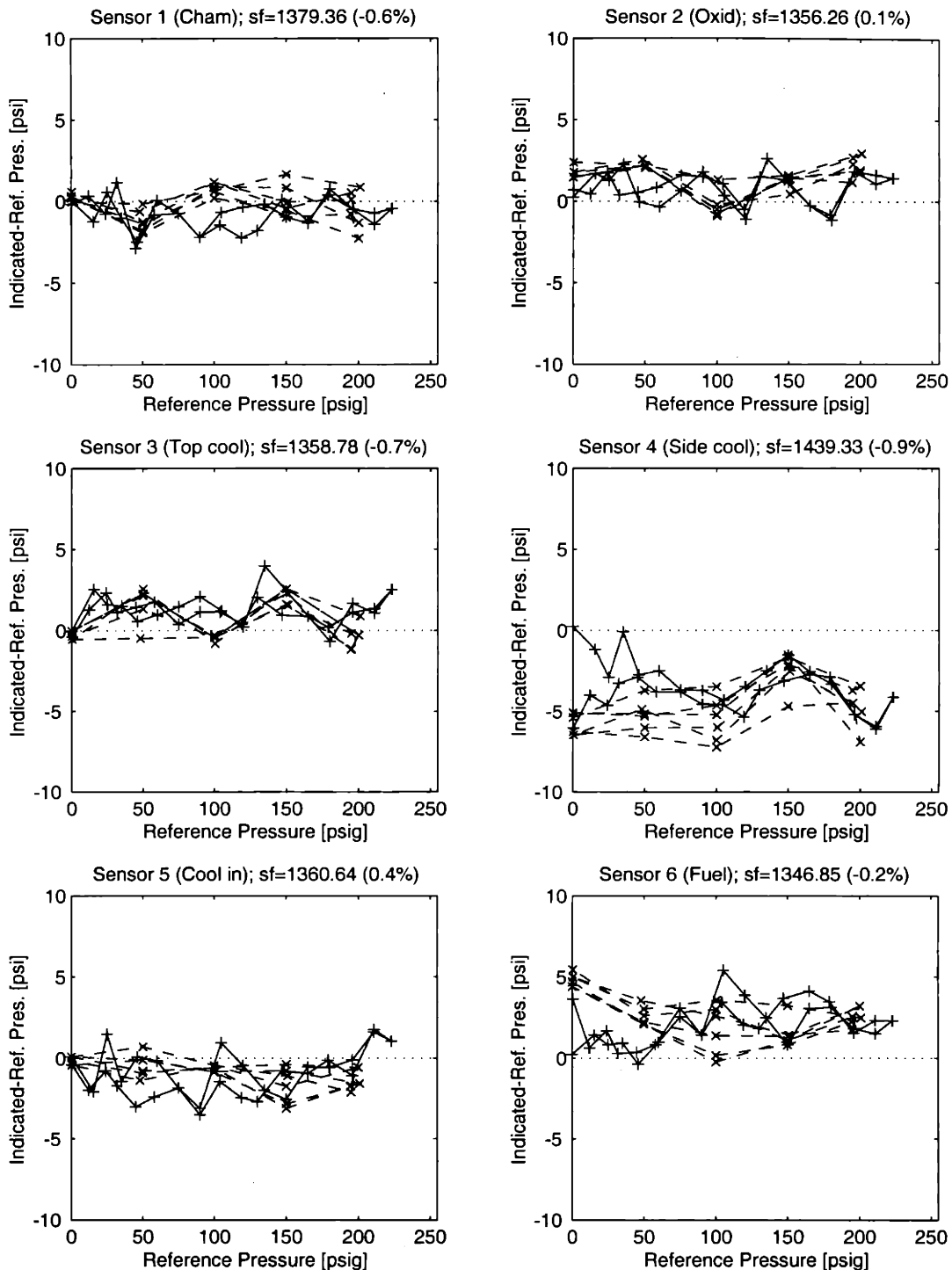


Figure A-3: This figure shows the difference between the indicated and reference pressures for the low pressure calibration (# 5 and 5) performed in March 2000. The scale factor, sf, is in units of psi/Volt, and the number in parentheses is the percent difference between this scale factor and the one used to reduce the data presented in the thesis. The dashed line is Cal #5, and the solid, Cal #5.

mass. The scatter in the calibration can be seen in Figure A-4 to be approximately ± 5 gram, which corresponds to ± 0.05 N. Additionally, the calibration was repeated after 6 months, with a drift in scale factor of approximately 0.8%. This implies that the uncertainty in the thrust measurements are approximately $\pm 1\%$ of indicated thrust ± 0.05 N. However, in looking at the results shown in Chapter 7, it is clear that the modifications to remove the thermal effects on the measured thrust were not entirely successful, as the indicated thrust returns to a non-zero value after the completion of a run. For the runs considered here, the indicated thrust at the completion of a run ranges from 0.058 N to -0.076 N. Therefore, a more conservative estimate of the uncertainty in the thrust measurement is:

$$S_F = \pm 0.01 \pm \frac{0.08 \text{ N}}{F} \quad (\text{A.3})$$

For a thrust of 1 N, this corresponds to an uncertainty of ± 0.09 N, or $S_F = \pm 9\%$. For a thrust of 0.6 N, this corresponds to an uncertainty of ± 0.086 N, or $S_F = \pm 14\%$.

A.2.3 Mass Flow

Each propellant mass flow is measured using a factory-calibrated Micro Motion Elite CMF010 meter, high pressure model. They have a stated accuracy when measuring gases of:

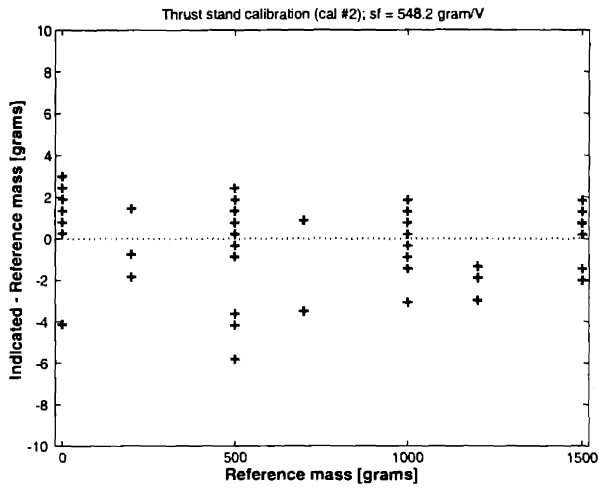
$$S_{\dot{m}} = \pm 0.005 \pm \frac{0.0011 \text{ g/sec}}{\dot{m}} \quad (\text{A.4})$$

The second term is the zero stability of the model. For a typical flow rate of 0.4 g/sec of propellant, this corresponds to an uncertainty of ± 0.003 g/sec, or $S_{\dot{m}} = \pm 0.8\%$.

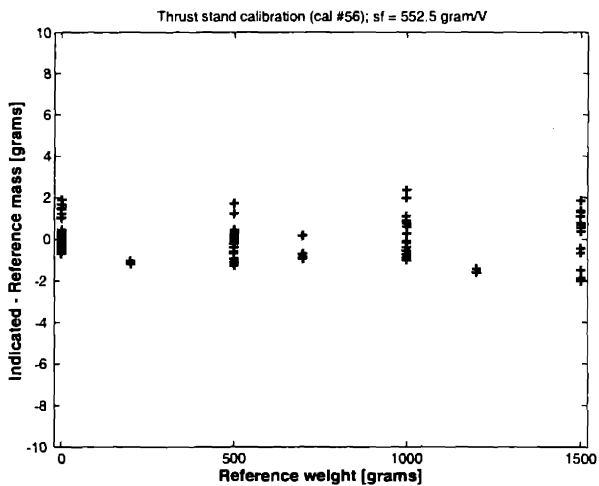
The coolant mass flow is measured using a factory-calibrated Micro Motion D6 meter, high pressure model. It has a stated accuracy for liquid flow of:

$$S_{\dot{m}} = \pm 0.002 \pm \frac{0.0033 \text{ g/sec}}{\dot{m}} \quad (\text{A.5})$$

Again, the later term is the zero stability of the meter. For a typical flow rate of 1 g/sec, this corresponds to an uncertainty of 0.005 g/sec, or $S_{\dot{m}} = \pm 0.5\%$.



(a) October 1999



(b) March 2000

Figure A-4: This figure shows the difference between the indicated and reference masses used for calibration of the thrust stand. One gram is approximately equivalent to 0.01 N.

A.2.4 Temperature

The coolant outlet temperature is measured using 0.010 inch thermocouples affixed to the coolant outlet tubes. Mehra [31] suggests that the accuracy of these devices is ± 12 K. Because the heat transfer coefficient of the liquid coolant inside the tube is sufficiently large,* there is no appreciable difference between the coolant temperature and the wall temperature. Therefore the fractional uncertainty in the temperature measurements is taken as:

$$S_T = \pm \frac{12 \text{ K}}{T} \quad (\text{A.6})$$

which corresponds to $S_T = 2.7\%$ for $T = 450$ K.

A.3 Uncertainty of the Derived Quantities

The uncertainty of each of the derived quantities is propagated from the uncertainty in the independent measurements as follows. If y is the quantity in question, it is written as a function of the independent measurements x_1, x_2, \dots, x_n :

$$y = f(x_1, x_2, \dots, x_n) \quad (\text{A.7})$$

A set of influence coefficients, C_{x_i} , are defined, which are essentially non-dimensionalized partial derivatives of y with respect to each variable:

$$C_{x_i} = \left| \frac{\partial f}{\partial x_i} \Big|_o \left(\frac{x_i}{y} \right)_o \right| \quad (\text{A.8})$$

where the subscript o refers to the indicated and calculated values at the point of interest. The value of C_{x_i} represents the percentage change in y that would result from a one percent

*For 0.3 gram/sec of water flow at 450 K, the calculated internal heat transfer coefficient is 12,000 W/m²K. This is three orders of magnitude larger than the typical values for free convection (~ 10 W/m²K), which implies a thermal response time of the tube of 90 msec. If the heat transfer coefficient for free convection to the room is taken as 30 W/m²K, this implies a difference between the temperature of the coolant and the outer wall of about 0.5 K. The total integrated heat loss through the tube of about 2.5 W would reduce the coolant bulk temperature by less than 0.1 K

change in the input x_i . The overall fractional uncertainty S_y is then:

$$S_y = \sqrt{\sum_{i=1}^n (C_{x_i} S_{x_i})^2} \quad (\text{A.9})$$

For the cases below when $C \neq 1$, the actual calculation of the influence coefficients is done numerically, by varying each input slightly and observing the change in output.

A.3.1 Specific Impulse

The specific impulse is simply a ratio of thrust to mass flow, so

$$C_F = C_{\dot{m}} = 1 \quad (\text{A.10})$$

and

$$S_{I_{sp}} = \sqrt{S_F^2 + S_{\dot{m}}^2} \quad (\text{A.11})$$

For Run 73, $S_{I_{sp}} = 9.1\%$, which corresponds to an overall uncertainty of ± 14 sec.

A.3.2 Injector Diameter

The injector diameters are determined via the choked flow equation, which means that C will not be one in this case.

$$\frac{\dot{m}}{A_{eff}} = \frac{P}{\sqrt{RT_t}} \left(\frac{2}{\gamma + 1} \right)^{\frac{\gamma+1}{2(\gamma-1)}} \quad (\text{A.12})$$

Table A.2 shows an example case for the calculation of the injector diameters. The propagated $S_{D_j} = \pm 2\%$.

A.3.3 Throat Area

The throat area calculation is similar to the Injector diameter calculation. Table A.3 shows an example case for the uncertainty parameters used for this quantity. The propagated

Table A.2: Example uncertainties in injector diameters

x_i	C_{x_i}	S_{x_i}
\dot{m}	0.50	1%
P	0.50	3%
γ	0.18	5% [†]
R	0.25	0%
T	0.25	3% [†]

[†] Estimate

Table A.3: Example uncertainties in throat area

x_i	C_{x_i}	S_{x_i}
\dot{m}_o	0.65	0.6%
\dot{m}_f	0.35	0.7%
P_c	1.00	4.5%
γ_o	0.21	5% [†]
γ_f	0.14	5% [†]
R_o	0.21	0%
R_f	0.29	0%
T	0.50	3.5% [†]

[†] Estimate

$$S_{A_t} = \pm 5.05\%.$$

A.3.4 Characteristic Exhaust Velocity, c^*

The characteristic exhaust velocity, is also simply a ratio $c^* = P_c A_t / \dot{m}$, so

$$C_{P_c} = C_{A_t} = C_{\dot{m}} = 1 \quad (\text{A.13})$$

and

$$S_{c^*} = \sqrt{S_{P_c}^2 + S_{A_t}^2 + S_{\dot{m}}^2} \quad (\text{A.14})$$

For run 73, $S_{c^*} = 6.9\%$, which corresponds to an overall uncertainty in c^* of 81 m/sec.

A.3.5 Thrust Coefficient

Similarly to I_{sp} and c^* , the thrust coefficient is also a ratio $c_F = F/P_c A_t$, so

$$C_F = C_{P_c} = C_{A_t} = 1 \quad (\text{A.15})$$

and

$$S_{c_F} = \sqrt{S_F^2 + S_{P_c}^2 + S_{A_t}^2} \quad (\text{A.16})$$

For run 73, $S_{c_F} = 11.4\%$, which corresponds to an overall uncertainty in c_F of 0.094.

A.3.6 Heat Load

The total heat load to the propellants can not be determined exactly, as there is most likely some quantity of coolant that has been vaporized. However, the uncertainty in the total enthalpy flux, which is taken as a lower bound on the heat load, is a simple product, $Q = \dot{m}\Delta h = \dot{m}c_p\Delta T$.[†] Therefore,

$$C_{\dot{m}} = C_T = 1 \quad (\text{A.17})$$

and

$$S_Q = \sqrt{S_{\dot{m}}^2 + S_T^2} \quad (\text{A.18})$$

For a typical case with $\dot{m} = 1.25$ gram/sec and $\Delta T = 150$ K ($Q \sim 800$ W), this corresponds to a $S_Q = \pm 2.75\%$, or an uncertainty in total heat load of 22 W.

[†] c_p varies with temperature, but it is considered well known relative to the other quantities.

APPENDIX B

FABRICATION DETAILS

The first section of this appendix presents a table of the process steps used in constructing the microrocket thrust chamber, and the second provides a description of the various recipes used in the primary etching tool.

B.1 Process Steps

Table B.1 shows the process steps for microfabricating the thrust chamber.

B.2 Recipes used in the STS Etcher

For reference, Tables B.2 to B.8 present the recipes used in the STS etcher for the deep etches in this work. With the exception of recipe TM-02, developed by Nagle [34], and RKT-04, developed as part of this work, the recipes were all developed and characterized by Ayon and colleagues. [3, 4, 5].

Table B.1: Process steps for fabricating thrust chamber

Process Step	Facility	Machine	Comments
Align Mark Process - All Wafers			
Thin coat resist side 1	TRL	coater	1 um thick
photo side 1 (Mask 0)	TRL	<td></td>	
Etch side 1	ICL	etcher1	recipe 19 - 1.5um deep
Thin coat resist side 2	TRL	coater	1 um thick
photo side 2 (Mask 0 - IR)	TRL	<td>done via IR alignment</td>	done via IR alignment
Etch side 2	ICL	etcher1	recipe 19 - 1.5um deep
Oxide Deposit - All wafers			
premetal clean	ICL	premetal	
deposit 2um oxide	ICL	novellus	both sides
densify oxide	ICL	tubeB6	1100C for 1 hr
Oxide Pattern - All wafers			
Thin coat resist side 1	TRL	coater	2 um thick
photo side 1 (Mask 2,6,8,9)	TRL	<td>mask varies with wafer</td>	mask varies with wafer
Etch side 1	ICL	AME	often protect opposite side with resist
Thin coat resist side 2	TRL	coater	2 um thick
photo side 2 (Mask 4,6)	TRL	<td>mask varies with wafer</td>	mask varies with wafer
Etch side 2	ICL	AME	often protect opposite side with resist
Cap Plate - front side			
thick coat resist	TRL	coater	10 um thick
photo (Mask 1,9)	TRL	<td></td>	
STS 350um	TRL	STS	recipe MIT 59 + 30sec SF6_4 to smooth
Cap Plate - back side			
thick coat resist	TRL	coater	
photo (Mask 3)	TRL	<td>also attach handle wafer</td>	also attach handle wafer
STS 180um	TRL	STS	recipe TM02
strip resist	TRL	acid hood	pirhanna
STS 20um	TRL	STS	recipe MIT 56
Wall Plate - back side			
STS 250um	TRL	STS	recipe RKT 04
Wall Plate - front side			
thick coat resist	TRL	coater	10-12 um thick
photo (Mask 5)	TRL	<td>also attach handle wafer</td>	also attach handle wafer
STS 130um	TRL	STS	recipe TM 02
strip resist	TRL	acid hood	pirhanna
STS 30um	TRL	STS	recipe MIT 56 + 30sec SF6_4 to smooth
Nozzle Plate - front side			
thick coat resist	TRL	coater	8-10 um
photo (Mask 7)	TRL	<td></td>	
STS 175um	TRL	STS	recipe MIT 51
strip resist	TRL	acid hood	pirhanna
STS 200um	TRL	STS	recipe RKT 04
Nozzle Plate - back side			
attach handle wafer	TRL		
STS 200um	TRL	STS	recipe RKT 04
Clean and Bond			
strip resist	TRL	acid hood	pirhanna
BOE oxide masks	TRL	acid hood	BOE
RCA clean bonding wafers	TRL	RCA	
align and bond	TRL	evbond	
Anneal	TRL	tubeB3	1100C for 1 hr
Note: HMDS, prebake and postbake steps are not shown.			
Each resist coat step is preceded by a coating of HMDS in the HMDS oven to improve adhesion, and is followed by a prebake of approximately 30-60 min at 90C.			
Each photo step is followed by a postbake of approximately 30-60 min at 90-120C.			

Table B.2: Recipe RKT-04

Parameter	Passivation Cycle Value	Etch Cycle Value	Unit
Platen power	0	120	Watt
Coil Power	600	600	Watt
Cycle time	9.5	15	sec
over-run	0	0.5	sec
SF6 flow	0	140	sccm
C4F8 flow	95	0	sccm
APC angle	62.5	62.5	degree

Table B.3: Recipe MIT-37

Parameter	Passivation Cycle Value	Etch Cycle Value	Unit
Platen power	0	120	Watt
Coil Power	600	600	Watt
Cycle time	11	15	sec
over-run	0	0.5	sec
SF6 flow	0	140	sccm
C4F8 flow	95	0	sccm
APC angle	65	65	degree

Table B.4: Recipe MIT-59

Parameter	Passivation Cycle Value	Etch Cycle Value	Unit
Platen power	60	120	Watt
Coil Power	600	750	Watt
Cycle time	11	15	sec
over-run	0	0.5	sec
SF6 flow	0	105	sccm
C4F8 flow	40	0	sccm
APC angle	65	65	degree

Table B.5: Recipe TM-02. This recipe was developed by Nagle[34].

Parameter	Passivation Cycle Value	Etch Cycle Value	Unit
Platen power	60	120	Watt
Coil Power	600	750	Watt
Cycle time	11	15	sec
over-run	0	0.5	sec
SF6 flow	0	105	sccm
C4F8 flow	60	0	sccm
APC angle	65	65	degree

Table B.6: Recipe MIT-56

Parameter	Passivation Cycle Value	Etch Cycle Value	Unit
Platen power	60	120	Watt
Coil Power	600	800	Watt
Cycle time	11	15	sec
over-run	0	0.5	sec
SF6 flow	0	105	sccm
C4F8 flow	40	0	sccm
APC angle	65	65	degree

Table B.7: Recipe MIT-51

Parameter	Passivation Cycle Value	Etch Cycle Value	Unit
Platen power	20	120	Watt
Coil Power	600	600	Watt
Cycle time	7	14.8	sec
over-run	0	0.7	sec
SF6 flow	0	136	sccm
C4F8 flow	90	0	sccm
APC angle	65	65	degree

Table B.8: Recipe SF6-4

Parameter	Etch Cycle Value	Unit
Platen power	120	Watt
Coil Power	950	Watt
SF6 flow	30	sccm
APC angle	75	degree

APPENDIX C

EXAMPLE CEA INPUT AND OUTPUT FILES

C.1 LOX/Ethanol Combustion

The following CEA input and output files are for LOX/Ethanol combustion at $P_c = 120$ bar and O/F=1.3.

C.1.1 Input File

```
# CEA input file p120r13.inp generated: 29-Dec-1999 16:10:03

#
# Subsonic in chem equilibrium to throat:
#
    problem rocket fac ac=16 equilibrium o/f=1.3
case=1 p,atm=120 subar=13,10,5,2
    reactants
fuel = C2H5OH(L) , wt% 100. t(k) 288.
oxid = O2(L) , wt% 100. t(k) 90.
    only CO CO2 H H2 OH H2O O O2
    output siunits short transport
end

#
# Supersonic chem frozen after throat:
#
    problem rocket fac ac=16 nfz=3 o/f=1.3
case=2 p,atm=120 supar=2,3,4,6,8,10,12,15
    reactants
fuel = C2H5OH(L) , wt% 100. t(k) 288.
oxid = O2(L) , wt% 100. t(k) 90.
    only CO CO2 H H2 OH H2O O O2
    output siunits short transport
end
```

C.1.2 Output File

NASA-LEWIS CHEMICAL EQUILIBRIUM PROGRAM CEA, AUGUST 1995
 BY BONNIE MCBRIDE AND SANFORD GORDON
 REFS: NASA RP-1311, OCTOBER 1994 AND NASA RP-

```
# CEA input file p120r13.inp generated: 29-Dec-1999 16:10:03

#
# Subsonic in chem equilibrium to throat:
#
 problem rocket fac ac=16 equilibrium o/f=1.3
case=1 p,atm=120 subar=13,10,5,2
 reactants
fuel = C2H5OH(L) , wt% 100. t(k) 288.
oxid = O2(L) , wt% 100. t(k) 90.
only CO CO2 H H2 OH H2O O O2
output siunits short transport
end

END OF CHAMBER ITERATIONS
```

THEORETICAL ROCKET PERFORMANCE ASSUMING EQUILIBRIUM

COMPOSITION DURING EXPANSION FROM FINITE AREA COMBUSTOR

```
Pinj = 1763.5 PSIA
Ac/At = 16.0000      Pinj/Pinf = 1.000814
CASE = 1
```

	REACTANT	WT FRACTION (SEE NOTE)	ENERGY KJ/KG-MOL	TEMP K
FUEL	C2H5OH(L)	1.0000000	-278629.883	288.000
OXIDANT	O2(L)	1.0000000	-12979.000	90.000
O/F =	1.30000 %FUEL = 43.478262 R,EQ.RATIO= 1.475781 PHI,EQ.RATIO= 1.602885			
	INJECTOR COMB END THROAT EXIT EXIT EXIT EXIT			
Pinj/P	1.0000 1.0016 1.7672 1.0021 1.0029 1.0093 1.0603			
P, BAR	121.59 121.39 68.805 121.34 121.24 120.47 114.68			
T, K	3059.52 3059.13 2809.05 3058.94 3058.56 3055.72 3033.80			
RHO, KG/CU M	1.0058 1 1.0043 1 6.2199 0 1.0040 1 1.0032 1 9.9785 0 9.5708 0			
H, KJ/KG	-2858.86 -2859.85 -3516.76 -2860.36 -2861.39 -2869.09 -2928.33			
U, KJ/KG	-4067.70 -4068.53 -4622.98 -4068.96 -4069.84 -4076.36 -4126.52			
G, KJ/KG	-38598.2 -38595.6 -36331.2 -38594.0 -38590.5 -38565.1 -38368.3			
S, KJ/(KG)(K)	11.6814 11.6817 11.6817 11.6817 11.6817 11.6817 11.6817			
M, (1/n)	21.044 21.044 21.113 21.044 21.044 21.045 21.052			
(dLV/dLP)t	-1.00366 -1.00366 -1.00190 -1.00365 -1.00365 -1.00363 -1.00344			
(dLV/dLT)p	1.0744 1.0744 1.0415 1.0744 1.0743 1.0739 1.0705			
Cp, KJ/(KG)(K)	2.9148 2.9146 2.6499 2.9144 2.9139 2.9106 2.8850			
GAMMAS	1.1804 1.1804 1.1895 1.1804 1.1804 1.1805 1.1813			
SON VEL,M/SEC	1194.5 1194.5 1147.1 1194.4 1194.3 1193.8 1189.7			
MACH NUMBER	.000 .037 1.000 .046 .060 .120 .313			

TRANSPORT PROPERTIES (GASES ONLY)
CONDUCTIVITY IN UNITS OF MILLIWATTS/(CM)(K)

VISC, MILLIPOISE	.96930	.96922	.91198	.96917	.96909	.96845	.96348
------------------	--------	--------	--------	--------	--------	--------	--------

WITH EQUILIBRIUM REACTIONS

Cp, KJ/(KG)(K)	2.9148	2.9146	2.6499	2.9144	2.9139	2.9106	2.8850
CONDUCTIVITY	5.2585	5.2576	4.3063	5.2568	5.2552	5.2435	5.1535
PRANDTL NUMBER	.5373	.5373	.5612	.5373	.5373	.5376	.5394

WITH FROZEN REACTIONS

Cp, KJ/(KG)(K)	2.2958	2.2957	2.2701	2.2957	2.2957	2.2954	2.2933
CONDUCTIVITY	3.4031	3.4027	3.1546	3.4025	3.4022	3.3994	3.3776
PRANDTL NUMBER	.6539	.6539	.6563	.6539	.6539	.6539	.6542

PERFORMANCE PARAMETERS

Ae/At	16.001	1.0000	13.000	10.000	5.0000	2.0000
CSTAR, M/SEC	1702.8	1702.8	1702.8	1702.8	1702.8	1702.8
CF	.0261	.6736	.0321	.0418	.0840	.2189
Ivac, M/SEC	27269.6	2111.5	22165.8	17063.8	8585.4	3587.4
Isp, M/SEC	44.4	1147.1	54.7	71.1	143.0	372.7

MOLE FRACTIONS

*CO	.29107	.29107	.28792	.29106	.29106	.29103	.29078
*CO2	.10613	.10614	.11060	.10614	.10615	.10620	.10658
*H	.00681	.00681	.00410	.00681	.00680	.00677	.00650
*H2	.15749	.15749	.16141	.15750	.15750	.15754	.15784
H2O	.43168	.43168	.43276	.43168	.43169	.43172	.43193
*O	.00017	.00017	.00005	.00017	.00017	.00017	.00015
*OH	.00647	.00646	.00310	.00646	.00645	.00640	.00605
*O2	.00018	.00018	.00005	.00018	.00018	.00018	.00016

* THERMODYNAMIC PROPERTIES FITTED TO 20000.K

NOTE. WEIGHT FRACTION OF FUEL IN TOTAL FUELS AND OF OXIDANT IN TOTAL OXIDANTS

```

#
# Supersonic chem frozen after throat:
#
 problem rocket fac ac=16 nfz=3 o/f=1.3
 case=2 p,atm=120 supar=2,3,4,6,8,10,12,15
 reactants
 fuel = C2H5OH(L) , wt% 100. t(k) 288.
 oxid = O2(L) , wt% 100. t(k) 90.
 only CO CO2 H H2 OH H2O O O2
 output siunits short transport
 end

```

END OF CHAMBER ITERATIONS

THEORETICAL ROCKET PERFORMANCE ASSUMING EQUILIBRIUM

COMPOSITION DURING EXPANSION FROM FINITE AREA COMBUSTOR

Pinj = 1763.5 PSIA
 Ac/At = 16.0000 Pinj/Pinf = 1.000814
 CASE = 2

	REACTANT	WT FRACTION		ENERGY		TEMP	
		(SEE NOTE)		KJ/KG-MOL	K		
FUEL	C2H5OH(L)	1.0000000	-278629.883	288.000			
OXIDANT	O2(L)	1.0000000	-12979.000	90.000			
O/F=	1.30000	%FUEL=	43.478262	R,EQ.RATIO=	1.475781	PHI,EQ.RATIO=	1.602885
	INJECTOR	CDMB	END	THROAT	EXIT	EXIT	EXIT
Pinj/P	1.0000	1.0016	1.7672	8.3219	15.438	23.416	41.349
P, BAR	121.59	121.39	68.805	14.611	7.8759	5.1927	2.9406
T, K	3059.52	3059.13	2809.05	2174.25	1950.47	1810.68	1634.28
RHO, KG/CU M	1.0058	1 1.0043	1 6.2199	0 1.7121	0 1.0291	0 7.3091-1	4.5860-1
H, KJ/KG	-2858.86	-2859.85	-3516.76	-5029.45	-5529.18	-5836.44	-6220.43
U, KJ/KG	-4067.70	-4068.53	-4622.98	-5882.81	-6294.53	-6546.88	-6861.65
G, KJ/KG	-38598.2	-38595.6	-36331.2	-30428.3	-28314.0	-26988.2	-25311.6
S, KJ/(KG)(K)	11.6814	11.6817	11.6817	11.6817	11.6817	11.6817	11.6817
M, (1/n)	21.044	21.044	21.113	21.184	21.190	21.191	21.192
(dLV/dLP)t	-1.00366	-1.00366	-1.00190	-1.00018	-1.00005	-1.00002	-1.00001
(dLV/dLT)p	1.0744	1.0744	1.0415	1.0047	1.0015	1.0007	1.0002
Cp, KJ/(KG)(K)	2.9148	2.9146	2.6499	2.2708	2.2130	2.1887	2.1689
GAMMAS	1.1804	1.1804	1.1895	1.2111	1.2163	1.2187	1.2209
SON VEL, M/SEC	1194.5	1194.5	1147.1	1016.6	964.8	930.5	884.8
MACH NUMBER	.000	.037	1.000	2.050	2.395	2.623	2.930

TRANSPORT PROPERTIES (GASES ONLY)

CONDUCTIVITY IN UNITS OF MILLIWATTS/(CM)(K)

VISC, MILLIPOISE	.96930	.96922	.91198	.75972	.70324	.66705	.62027	.58964	.56720	.54967	.52916
------------------	--------	--------	--------	--------	--------	--------	--------	--------	--------	--------	--------

WITH EQUILIBRIUM REACTIONS

Cp, KJ/(KG)(K)	2.9148	2.9146	2.6499	2.2708	2.2130	2.1887	2.1689	2.1630	2.1630	2.1660	2.1737
CONDUCTIVITY	5.2585	5.2576	4.3063	2.7308	2.4125	2.2518	2.0778	1.9797	1.9149	1.8682	1.8183
PRANDTL NUMBER	.5373	.5373	.5612	.6318	.6451	.6484	.6474	.6442	.6407	.6373	.6326

WITH FROZEN REACTIONS

Cp, KJ/(KG)(K)	2.2958	2.2957	2.2701	2.1809	2.1385	2.1084	2.0662	2.0368	2.0144	1.9966	1.9755
CONDUCTIVITY	3.4031	3.4027	3.1546	2.5187	2.2928	2.1519	1.9754	1.8642	1.7853	1.7255	1.6577
PRANDTL NUMBER	.6539	.6539	.6563	.6578	.6559	.6536	.6488	.6442	.6400	.6360	.6306

PERFORMANCE PARAMETERS

Ae/At	16.001	1.0000	2.0000	3.0000	4.0000	6.0000	8.0000	10.000	12.000	15.000
CSTAR, M/SEC	1702.8	1702.8	1702.8	1702.8	1702.8	1702.8	1702.8	1702.8	1702.8	1702.8
CF	.0261	.6736	1.2236	1.3571	1.4331	1.5227	1.5770	1.6148	1.6434	1.6758
Ivac, M/SEC	27269.6	2111.5	2493.1	2642.2	2731.4	2840.2	2907.6	2955.3	2991.7	3033.3
Isp, M/SEC	44.4	1147.1	2083.5	2311.0	2440.3	2592.9	2685.3	2749.8	2798.5	2853.6

MOLE FRACTIONS

*CO	.29107	.29107	.28792	.27393	.26541	.25850	.24733	.23829	.23059	.22384	.21499
*CO2	.10613	.10614	.11060	.12592	.13455	.14149	.15266	.16170	.16941	.17616	.18501
*H	.00681	.00681	.00410	.00054	.00018	.00008	.00002	.00001	.00000	.00000	.00000
*H2	.15749	.15749	.16141	.17707	.18582	.19280	.20400	.21305	.22075	.22751	.23636
H2O	.43168	.43168	.43276	.42236	.41401	.40713	.39598	.38694	.37924	.37249	.36364
*O	.00017	.00017	.00005	.00000	.00000	.00000	.00000	.00000	.00000	.00000	.00000
*OH	.00647	.00646	.00310	.00017	.00004	.00001	.00000	.00000	.00000	.00000	.00000
*O2	.00018	.00018	.00005	.00000	.00000	.00000	.00000	.00000	.00000	.00000	.00000

* THERMODYNAMIC PROPERTIES FITTED TO 20000.K

NOTE. WEIGHT FRACTION OF FUEL IN TOTAL FUELS AND OF OXIDANT IN TOTAL OXIDANTS

WARNING!! FOR FROZEN PERFORMANCE, SUBSONIC AREA
RATIOS WERE OMITTED SINCE n_{fz} IS GREATER THAN 1 (ROCKET)

THEORETICAL ROCKET PERFORMANCE ASSUMING FROZEN COMPOSITION
AFTER POINT 3

$P_{inj} = 1763.5 \text{ PSIA}$
 $Ac/At = 16.0000 \quad P_{inj}/P_{inf} = 1.000814$
CASE = 2

	REACTANT	WT FRACTION (SEE NOTE)	ENERGY KJ/KG-MOL	TEMP K
FUEL	C ₂ H ₅ OH(L)	1.0000000	-278629.883	288.000
OXIDANT	O ₂ (L)	1.0000000	-12979.000	90.000

O/F = 1.30000 %FUEL= 43.478262 R,EQ.RATIO= 1.475781 PHI,EQ.RATIO= 1.602885

	INJECTOR	COMB END	THROAT	EXIT	EXIT	EXIT	EXIT	EXIT	EXIT	EXIT	EXIT
P_{inj}/P	1.0000	1.0016	1.7672	8.4877	15.803	24.050	42.745	63.788	86.754	111.37	150.99
P, BAR	121.59	121.39	68.805	14.325	7.6941	5.0556	2.8445	1.9062	1.4016	1.0918	.80527
T, K	3059.52	3059.13	2809.05	2126.78	1897.33	1753.80	1571.15	1452.93	1366.82	1299.76	1221.44
RHO, KG/CU M	1.0058	1.0043	1.6.2199	0 1.7104	0 1.0297	0 7.3201-1	4.5974-1	3.3314-1	2.6039-1	2.1329-1	1.6741-1
H, KJ/KG	-2858.86	-2859.85	-3516.76	-5033.72	-5525.81	-5827.59	-6203.81	-6442.08	-6612.78	-6743.91	-6894.97
U, KJ/KG	-4067.70	-4068.53	-4622.98	-5871.25	-6272.99	-6518.25	-6822.54	-7014.25	-7151.04	-7255.77	-7375.98
G, KJ/KG	-38598.2	-38595.6	-36331.2	-29878.1	-27689.8	-26314.9	-24557.5	-23414.8	-22579.6	-21927.3	-21163.5
S, KJ/(KG)(K)	11.6814	11.6817	11.6817	11.6817	11.6817	11.6817	11.6817	11.6817	11.6817	11.6817	11.6817
M, (1/n)	21.044	21.044	21.113	21.113	21.113	21.113	21.113	21.113	21.113	21.113	21.113
Cp, KJ/(KG)(K)	2.9148	2.9146	2.6499	2.1681	2.1197	2.0847	2.0338	1.9967	1.9675	1.9434	1.9138
GAMMAS	1.1804	1.1804	1.1895	1.2220	1.2282	1.2329	1.2401	1.2457	1.2502	1.2541	1.2591
SON VEL,M/SEC	1194.5	1194.5	1147.1	1011.6	957.9	922.8	876.0	844.2	820.3	801.2	778.2
MACH NUMBER	.000	.037	1.000	2.062	2.411	2.641	2.953	3.171	3.340	3.479	3.651

TRANSPORT PROPERTIES (GASES ONLY)

CONDUCTIVITY IN UNITS OF MILLIWATTS/(CM)(K)

VISC,MILLIPOISE	.96930	.96922	.91198	.74470	.68476	.64605	.59519	.56114	.53570	.51547	.49132
-----------------	--------	--------	--------	--------	--------	--------	--------	--------	--------	--------	--------

WITH FROZEN REACTIONS

Cp, KJ/(KG)(K)	2.2958	2.2957	2.2701	2.1681	2.1197	2.0847	2.0338	1.9967	1.9675	1.9434	1.9138
CONDUCTIVITY	3.4031	3.4027	3.1546	2.4289	2.1743	2.0122	1.8033	1.6665	1.5664	1.4881	1.3965
PRANDTL NUMBER	.6539	.6539	.6563	.6647	.6676	.6693	.6713	.6723	.6729	.6732	.6733

PERFORMANCE PARAMETERS

Ae/At	16.001	1.0000	2.0000	3.0000	4.0000	6.0000	8.0000	10.000	12.000	15.000
CSTAR, M/SEC	1702.8	1702.8	1702.8	1702.8	1702.8	1702.8	1702.8	1702.8	1702.8	1702.8
CF	.0261	.6736	1.2248	1.3563	1.4310	1.5189	1.5721	1.6091	1.6370	1.6685
Ivac, M/SEC	27269.6	2111.5	2487.2	2633.0	2720.1	2825.7	2890.8	2936.5	2971.1	3010.5
Isp, M/SEC	44.4	1147.1	2085.6	2309.5	2436.7	2586.5	2677.0	2740.0	2787.5	2841.2

MOLE FRACTIONS

*CO	.28792	*CO2	.11060	*H	.00410
*H2	.16141	H2O	.43276	*O	.00005
*OH	.00310	*O2	.00005		

* THERMODYNAMIC PROPERTIES FITTED TO 20000.K

NOTE. WEIGHT FRACTION OF FUEL IN TOTAL FUELS AND OF OXIDANT IN TOTAL OXIDANTS

C.2 Oxygen/Methane Combustion

The following CEA input and output files are for gaseous Oxygen and Methane combustion at $P_c = 120$ atm and O/F=2.3.

C.2.1 Input File

```
# CEA input file p120r23.inp generated: 14-Jul-1999 23:18:03

#
# Subsonic in chem equilibrium to throat:
#
    problem rocket fac ac=16 equilibrium o/f=2.3
case=1 p,atm=120 subar=13,10,5,2
    reactants
fuel = CH4 , wt% 100. t(k) 300.
oxid = O2 , wt% 100. t(k) 300.
    only CO CO2 H H2 OH H2O O O2
    output siunits short transport
end

#
# Supersonic chem frozen after throat:
#
    problem rocket fac ac=16 nfz=3 o/f=2.3
case=2 p,atm=120 supar=2,3,4,6,8,10,12,15
    reactants
fuel = CH4 , wt% 100. t(k) 300.
oxid = O2 , wt% 100. t(k) 300.
    only CO CO2 H H2 OH H2O O O2
    output siunits short transport
end
```

C.2.2 Output File

```
*****
```

NASA-LEWIS CHEMICAL EQUILIBRIUM PROGRAM CEA, AUGUST 1995
 BY BONNIE MCBRIDE AND SANFORD GORDON
 REFS: NASA RP-1311, OCTOBER 1994 AND NASA RP-

```
*****
```

CEA input file p120r23.inp generated: 14-Jul-1999 23:18:03

```
#
# Subsonic in chem equilibrium to throat:
#
 problem rocket fac ac=16 equilibrium o/f=2.3
case=1 p,atm=120 subar=13,10,5,2
 reactants
fuel = CH4 , wt% 100. t(k) 300.
oxid = O2 , wt% 100. t(k) 300.
only CO CO2 H H2 OH H2O O 02
output siunits short transport
end
```

END OF CHAMBER ITERATIONS

THEORETICAL ROCKET PERFORMANCE ASSUMING EQUILIBRIUM

COMPOSITION DURING EXPANSION FROM FINITE AREA COMBUSTOR

Pinj = 1763.5 PSIA
 Ac/At = 16.0000 Pinj/Pinf = 1.000819
 CASE = 1

	REACTANT	WT FRACTION (SEE NOTE)	ENERGY KJ/KG-MOL	TEMP K
FUEL	CH4	1.0000000	-74533.907	300.000
OXIDANT	O2	1.0000000	54.358	300.000
O/F=	2.30000 %FUEL= 30.303031 R,EQ.RATIO= 1.734430 PHI,EQ.RATIO= 1.734430			
	INJECTOR COMB END THROAT EXIT EXIT EXIT EXIT			
Pinj/P	1.0000 1.0016 1.7730 1.0021 1.0029 1.0094 1.0606			
P, BAR	121.59 121.39 68.579 121.34 121.24 120.46 114.64			
T, K	3143.68 3143.26 2876.36 3143.06 3142.66 3139.62 3116.20			
RHO, KG/CU M	8.1365 0 8.1243 0 5.0359 0 8.1214 0 8.1155 0 8.0719 0 7.7428 0			
H, KJ/KG	-1406.68 -1407.91 -2223.00 -1408.54 -1409.82 -1419.39 -1493.01			
U, KJ/KG	-2901.06 -2902.08 -3584.81 -2902.61 -2903.69 -2911.73 -2973.61			
G, KJ/KG	-43438.9 -43435.8 -40682.2 -43433.7 -43429.6 -43398.6 -43159.0			
S, KJ/(KG)(K)	13.3704 13.3708 13.3708 13.3708 13.3708 13.3708 13.3708			
M, (1/n)	17.491 17.491 17.562 17.491 17.491 17.492 17.499			
(dLV/dLP)t	-1.00452 -1.00452 -1.00245 -1.00452 -1.00451 -1.00448 -1.00427			
(dLV/dLT)p	1.0864 1.0863 1.0505 1.0863 1.0862 1.0858 1.0822			
Cp, KJ/(KG)(K)	3.4271 3.4269 3.1039 3.4266 3.4261 3.4221 3.3917			
GAMMAS	1.1893 1.1893 1.1989 1.1893 1.1893 1.1894 1.1902			
SON VEL,M/SEC	1333.1 1333.1 1277.7 1333.0 1332.9 1332.3 1327.5			
MACH NUMBER	.000 .037 1.000 .046 .059 .120 .313			

TRANSPORT PROPERTIES (GASES ONLY)

CONDUCTIVITY IN UNITS OF MILLIWATTS/(CM)(K)

VISC, MILLIPOISE	.95778	.95769	.89833	.95764	.95755	.95689	.95172
------------------	--------	--------	--------	--------	--------	--------	--------

WITH EQUILIBRIUM REACTIONS

Cp, KJ/(KG)(K)	3.4271	3.4269	3.1039	3.4266	3.4261	3.4221	3.3917
CONDUCTIVITY	6.9505	6.9493	5.5967	6.9482	6.9460	6.9296	6.8035
PRANDTL NUMBER	.4723	.4723	.4982	.4723	.4723	.4725	.4745

WITH FROZEN REACTIONS

Cp, KJ/(KG)(K)	2.6234	2.6234	2.5912	2.6233	2.6233	2.6230	2.6203
CONDUCTIVITY	4.1417	4.1412	3.8206	4.1410	4.1405	4.1368	4.1086
PRANDTL NUMBER	.6067	.6067	.6093	.6067	.6067	.6067	.6070

PERFORMANCE PARAMETERS

Ae/At	16.001	1.0000	13.000	10.000	5.0000	2.0000
CSTAR, M/SEC	1888.1	1888.1	1888.1	1888.1	1888.1	1888.1
CF	.0262	.6767	.0323	.0420	.0844	.2201
Ivac, M/SEC	30236.5	2343.5	24577.4	18920.4	9519.8	3978.8
Isp, M/SEC	49.5	1277.7	60.9	79.3	159.4	415.5

MOLE FRACTIONS

*CO	.28068	.28068	.27908	.28068	.28068	.28066	.28056
*CO2	.04971	.04971	.05264	.04971	.04972	.04975	.04999
*H	.01149	.01149	.00681	.01148	.01147	.01142	.01096
*H2	.27634	.27635	.28083	.27635	.27636	.27641	.27678
H2O	.37581	.37581	.37783	.37581	.37582	.37586	.37614
*O	.00014	.00014	.00004	.00014	.00014	.00014	.00013
*OH	.00575	.00575	.00275	.00574	.00574	.00570	.00538
*O2	.00008	.00008	.00002	.00008	.00008	.00008	.00007

* THERMODYNAMIC PROPERTIES FITTED TO 20000.K

NOTE. WEIGHT FRACTION OF FUEL IN TOTAL FUELS AND OF OXIDANT IN TOTAL OXIDANTS

```

#
# Supersonic chem frozen after throat:
#
 problem rocket fac ac=16 nfz=3 o/f=2.3
 case=2 p,atm=120 supar=2,3,4,6,8,10,12,15
 reactants
 fuel = CH4 , wt% 100. t(k) 300.
 oxid = O2 , wt% 100. t(k) 300.
 only CO CO2 H H2 OH H2O O O2
 output siunits short transport
 end

```

END OF CHAMBER ITERATIONS

THEORETICAL ROCKET PERFORMANCE ASSUMING EQUILIBRIUM

COMPOSITION DURING EXPANSION FROM FINITE AREA COMBUSTOR

Pinj = 1763.5 PSIA

Ac/At = 16.0000 Pinj/Pinf = 1.000819

CASE = 2

	REACTANT		WT FRACTION (SEE NOTE)		ENERGY KJ/KG-MOL		TEMP K					
FUEL	CH4		1.0000000		-74533.907		300.000					
OXIDANT	O2		1.0000000		54.358		300.000					
O/F =	2.30000	%FUEL = 30.303031	R, EQ. RATIO = 1.734430	PHI, EQ. RATIO = 1.734430								
	INJECTOR	COMB END	THROAT	EXIT	EXIT	EXIT	EXIT	EXIT	EXIT	EXIT	EXIT	EXIT
Pinj/P	1.0000	1.0016	1.7730	8.4522	15.784	24.056	42.774	63.751	86.515	110.77	149.48	
P, BAR	121.59	121.39	68.579	14.386	7.7036	5.0546	2.8426	1.9073	1.4054	1.0977	.81340	
T, K	3143.68	3143.26	2876.36	2196.54	1955.69	1805.44	1616.55	1496.56	1410.69	1344.91	1269.47	
RHO, KG/CU M	8.1365	8.1243	0	5.0359	0	1.3894	0	8.3593-1	5.9417-1	3.7321-1	2.7049-1	2.1145-1
H, KJ/KG	-1406.68	-1407.91	-2223.00	-4087.77	-4698.33	-5071.57	-5535.16	-5827.67	-6036.73	-6197.10	-6381.67	
U, KJ/KG	-2901.06	-2902.08	-3584.81	-5123.17	-5619.89	-5922.26	-6296.81	-6532.78	-6701.38	-6830.77	-6979.79	
G, KJ/KG	-43438.9	-43435.8	-40682.2	-33457.3	-30847.5	-29211.8	-27149.7	-25837.8	-24898.8	-24179.6	-23355.5	
S, KJ/(KG)(K)	13.3704	13.3708	13.3708	13.3708	13.3708	13.3708	13.3708	13.3708	13.3708	13.3708	13.3708	
M, (1/n)	17.491	17.491	17.562	17.639	17.645	17.646	17.647	17.647	17.647	17.647	17.647	
(dLV/dLP)t	-1.00452	-1.00452	-1.00245	-1.00023	-1.00007	-1.00002	-1.00001	-1.00000	-1.00000	-1.00000	-1.00000	
(dLV/dLT)p	1.0864	1.0863	1.0505	1.0060	1.0019	1.0008	1.0002	1.0001	1.0000	1.0000	1.0000	
Cp, KJ/(KG)(K)	3.4271	3.4269	3.1039	2.5894	2.5056	2.4708	2.4427	2.4349	2.4357	2.4411	2.4538	
GAMMAS	1.1893	1.1893	1.1989	1.2255	1.2326	1.2360	1.2391	1.2400	1.2398	1.2392	1.2376	
SON VEL,M/SEC	1333.1	1333.1	1277.7	1126.4	1065.8	1025.4	971.5	935.1	907.8	886.1	860.4	
MACH NUMBER	.000	.037	1.000	2.056	2.407	2.640	2.958	3.180	3.352	3.493	3.666	
TRANSPORT PROPERTIES (GASES ONLY)												
CONDUCTIVITY IN UNITS OF MILLIWATTS/(CM)(K)												
VISC, MILLIPOISE	.95778	.95769	.89833	.74059	.68188	.64433	.59597	.56449	.54154	.52370	.50294	
WITH EQUILIBRIUM REACTIONS												
Cp, KJ/(KG)(K)	3.4271	3.4269	3.1039	2.5894	2.5056	2.4708	2.4427	2.4349	2.4357	2.4411	2.4538	
CONDUCTIVITY	6.9505	6.9493	5.5967	3.2942	2.8503	2.6347	2.4071	2.2810	2.1986	2.1400	2.0783	
PRANDTL NUMBER	.4723	.4723	.4982	.5821	.5994	.6042	.6048	.6026	.5999	.5974	.5938	
WITH FROZEN REACTIONS												
Cp, KJ/(KG)(K)	2.6234	2.6234	2.5912	2.4798	2.4265	2.3886	2.3357	2.2990	2.2715	2.2497	2.2243	
CONDUCTIVITY	4.1417	4.1412	3.8206	3.0076	2.7199	2.5411	2.3183	2.1791	2.0811	2.0074	1.9246	
PRANDTL NUMBER	.6067	.6067	.6093	.6106	.6083	.6057	.6004	.5956	.5911	.5869	.5813	
PERFORMANCE PARAMETERS												
Ae/At	16.001	1.0000	2.0000	3.0000	4.0000	6.0000	8.0000	10.000	12.000	15.000		
CSTAR, M/SEC	1888.1	1888.1	1888.1	1888.1	1888.1	1888.1	1888.1	1888.1	1888.1	1888.1	1888.1	
CF	.0262	.6767	1.2265	1.3589	1.4339	1.5219	1.5749	1.6117	1.6394	1.6707		
Ivac, M/SEC	30236.5	2343.5	2762.8	2925.0	3021.6	3138.6	3210.7	3261.5	3300.0	3344.0		
Isp, M/SEC	49.5	1277.7	2315.6	2565.8	2707.4	2873.5	2973.5	3043.0	3095.3	3154.4		
MOLE FRACTIONS												
*CO	.28068	.28068	.27908	.26895	.26191	.25594	.24591	.23748	.23012	.22354	.21478	
*CO2	.04971	.04971	.05264	.06423	.07138	.07738	.08742	.09585	.10322	.10980	.11855	
*H	.01149	.01149	.00681	.00079	.00024	.00009	.00002	.00001	.00000	.00000	.00000	
*H2	.27634	.27635	.28083	.29505	.30250	.30858	.31867	.32711	.33447	.34105	.34981	
H2O	.37581	.37581	.37783	.37084	.36395	.35800	.34798	.33955	.33219	.32561	.31686	
*O	.00014	.00014	.00004	.00000	.00000	.00000	.00000	.00000	.00000	.00000	.00000	
*OH	.00575	.00575	.00275	.00014	.00003	.00001	.00000	.00000	.00000	.00000	.00000	
*O2	.00008	.00008	.00002	.00000	.00000	.00000	.00000	.00000	.00000	.00000	.00000	

* THERMODYNAMIC PROPERTIES FITTED TO 20000.K

NOTE. WEIGHT FRACTION OF FUEL IN TOTAL FUELS AND OF OXIDANT IN TOTAL OXIDANTS

WARNING!! FOR FROZEN PERFORMANCE, SUBSONIC AREA
RATIOS WERE OMITTED SINCE n_{fz} IS GREATER THAN 1 (ROCKET)

THEORETICAL ROCKET PERFORMANCE ASSUMING FROZEN COMPOSITION
AFTER POINT 3

$P_{inj} = 1763.5 \text{ PSIA}$
 $A_e/A_t = 16.0000 \quad P_{inj}/P_{inf} = 1.000819$
CASE = 2

	REACTANT	WT FRACTION (SEE NOTE)		ENERGY KJ/KG-MOL		TEMP K					
FUEL	CH ₄		1.0000000	-74533.907		300.000					
OXIDANT	O ₂		1.0000000	54.358		300.000					
$O/F = 2.30000 \quad \%FUEL = 30.303031 \quad R, EQ. RATIO = 1.734430 \quad PHI, EQ. RATIO = 1.734430$											
Pinj/P	1.0000	1.0016	1.7730	8.6556	16.223	24.807	44.402	66.612	90.982	117.22	159.65
P, BAR	121.59	121.39	68.579	14.048	7.4950	4.9014	2.7384	1.8254	1.3364	1.0373	.76159
T, K	3143.68	3143.26	2876.36	2137.90	1892.04	1738.92	1544.90	1419.89	1329.15	1258.70	1176.70
RHO, KG/CU M	8.1365	8.1243	0.50355	0.13878	0.83670-1	5.9534-1	3.7438-1	2.7153-1	2.1237-1	1.7406-1	1.3671-1
H, KJ/KG	-1406.68	-1407.91	-2223.00	-4093.66	-4692.37	-5057.27	-5509.40	-5793.93	-5996.77	-6151.98	-6330.03
U, KJ/KG	-2901.06	-2902.08	-3584.81	-5105.85	-5588.15	-5880.56	-6240.83	-6466.18	-6626.05	-6747.91	-6887.14
G, KJ/KG	-43438.9	-43435.8	-40682.2	-32679.0	-29990.4	-28307.9	-26165.9	-24778.9	-23768.5	-22981.8	-22063.4
S, KJ/(KG)(K)	13.3704	13.3708	13.3708	13.3708	13.3708	13.3708	13.3708	13.3708	13.3708	13.3708	13.3708
M, (1/n)	17.491	17.491	17.562	17.562	17.562	17.562	17.562	17.562	17.562	17.562	17.562
Cp, KJ/(KG)(K)	3.4271	3.4269	3.1039	2.4642	2.4043	2.3609	2.2983	2.2530	2.2176	2.1887	2.1536
GAMMAS	1.1893	1.1893	1.1989	1.2378	1.2452	1.2508	1.2594	1.2660	1.2714	1.2760	1.2818
SON VEL, M/SEC	1333.1	1333.1	1277.7	1119.3	1056.1	1014.8	959.8	922.5	894.5	872.0	845.0
MACH NUMBER	.000	.037	1.000	2.071	2.427	2.663	2.985	3.211	3.387	3.533	3.713
TRANSPORT PROPERTIES (GASES ONLY)											
CONDUCTIVITY IN UNITS OF MILLIWATTS/(CM)(K)											
VISC, MILLIPOISE	.95778	.95769	.89833	.72361	.66158	.62166	.56938	.53448	.50846	.48779	.46315
WITH FROZEN REACTIONS											
Cp, KJ/(KG)(K)	2.6234	2.6234	2.5912	2.4642	2.4043	2.3609	2.2983	2.2530	2.2176	2.1887	2.1536
CONDUCTIVITY	4.1417	4.1412	3.8206	2.9040	2.5877	2.3879	2.1322	1.9661	1.8451	1.7511	1.6417
PRANDTL NUMBER	.6067	.6067	.6093	.6140	.6147	.6146	.6137	.6125	.6111	.6097	.6076
PERFORMANCE PARAMETERS											
Ae/At	16.001	1.0000	2.0000	3.0000	4.0000	6.0000	8.0000	10.000	12.000	15.000	
CSTAR, M/SEC	1888.1	1888.1	1888.1	1888.1	1888.1	1888.1	1888.1	1888.1	1888.1	1888.1	1888.1
CF	.0262	.6767	1.2278	1.3577	1.4311	1.5172	1.5689	1.6047	1.6316	1.6620	
Ivac, M/SEC	30236.5	2343.5	2754.8	2912.9	3006.8	3119.9	3189.1	3237.6	3274.1	3315.5	
Isp, M/SEC	49.5	1277.7	2318.2	2563.5	2702.1	2864.5	2962.2	3029.9	3080.7	3137.9	
MOLE FRACTIONS											
*CO	.27908	*CO2		.05264	*H		.00681				
*H2	.28083	H2O		.37783	*O		.00004				
*OH	.00275	*O2		.00002							

* THERMODYNAMIC PROPERTIES FITTED TO 20000.K

NOTE. WEIGHT FRACTION OF FUEL IN TOTAL FUELS AND OF OXIDANT IN TOTAL OXIDANTS

APPENDIX D

COLD-SIDE HEAT TRANSFER CORRELATIONS

This appendix presents the cold-side heat transfer correlations considered in the design of the cooling passages that are compared to the results of Lopata and Faust [29, 13] in Figure 4-4.

D.1 Nomenclature

There are a number of symbols that are used here but not in the rest of the thesis:

f	friction factor
P_{crit}	Critical pressure
T_{pc}	Pseudo-critical Temperature, the temperature at which c_p peaks.
\bar{c}_p	Effective wall c_p , $= (h_w - h_b)/(T_w - T_b)$ (where h is specific enthalpy.)
b	as a subscript, signifies bulk fluid conditions
w	as a subscript, signifies wall conditions (equivalent to wc in rest of thesis)

D.2 Correlations

Unless otherwise noted (ie with no subscript), the properties are evaluated at the bulk temperature, T_b .

Propane

This correlation is from the work of Michel[33], and was developed for supercritical propane cooling of rocket thrust chambers.

$$\text{Nu} = 0.00568 \text{Re}^{0.876} \text{Pr}^{0.4} \left(\frac{\rho}{\rho_w} \right)^{0.12} \left(\frac{\mu}{\mu_w} \right)^{-0.142} \left(\frac{\kappa}{\kappa_w} \right)^{0.828} \left(\frac{c_p}{\bar{c}_p} \right)^{-0.368} \left(\frac{P}{P_{crit}} \right)^{0.254} \quad (\text{D.1})$$

Hines

The Hines correlations, also suggested by Michel[33] is:

$$\text{Nu} = 0.005 \text{Re}^{0.95} \text{Pr}^{0.4} \quad (\text{D.2})$$

Hendricks

This correlation is due to Hendricks [19]:

$$\text{Nu} = 0.021 \text{Re}^{0.8} \text{Pr}^{0.4} \quad (\text{D.3})$$

Nominal and Nominal, film

This correlation is based on those suggested by Ghajar and Asadi [15], and was found to best match the data of Lopata and Faust. [13]

$$\text{Nu} = 0.025 \text{Re}^{0.8} \text{Pr}^{0.4} \quad (\text{D.4})$$

For the film case, the properties are evaluated at the film temperature, $T_f = (T_b + T_w)/2$.

K-P 2

This correlation is suggested by Kakaç [24] as in the best agreement with supercritical data. It is based on a friction factor, f :

$$f = \frac{1}{(3.64 \log \text{Re} - 3.28)^2} \quad (\text{D.5})$$

which is then used to determine the Nu for constant temperature properties:

$$\text{Nu}_{\text{cp}} = \frac{(f/2)\text{Re Pr}}{12.7 \sqrt{f/2} \left(\text{Pr}^{2/3} - 1 \right) + 1.07} \quad (\text{D.6})$$

This is then modified by the following factors to determine the Nu for the variable temperature, supercritical flow.

$$\text{Nu} = \text{Nu}_{\text{cp}} \left(\frac{\rho_w}{\rho} \right)^{0.3} \left(\frac{\bar{c}_p}{c_p} \right)^n; \quad (\text{D.7})$$

where n depends on the bulk temperature:

$$\begin{aligned} n &= 0.4; \quad T < T_w < T_{pc} \quad 1.2T_{pc} < T < T_w \\ &= 0.4 + 0.2(T_w/T_{pc} - 1); \quad T < T_{pc} < T_w \\ &= 0.4 + 0.2(T_w/T_{pc} - 1)(1 - 5(T/T_{pc} - 1)); \quad T_{pc} < T < 1.2T_{pc}, T < T_w \end{aligned} \quad (\text{D.8})$$

APPENDIX E

EXPERIMENTAL CHECKLISTS

This appendix shows copies of the three checklists used in running the microrocket engines. The first is used in filling the thrust chamber with coolant and preparing the test cell, shown in Table E.1. Table E.2 shows the steps for pressurizing the gases, and Table E.3 shows the steps for completing a hot or cold flow test.

Table E.1: Test Cell Preparation Checklist

MicroRocket Prepare Test Cell Checklist
Last Update: 22-Nov-99

Date: _____
Time: _____
Who: _____

Action	Notes:
Video	
<input type="checkbox"/> Turn on IR camera; allow to cool	
<input type="checkbox"/> Power to 3 video cameras and DV	
<input type="checkbox"/> IR camera to first zoom, first range, auto range	
<input type="checkbox"/> Adjust video stand and mirror so IR view through feed tubes	
<input type="checkbox"/> Focus all cameras	
<input type="checkbox"/> IR camera to second range, full scale	
<input type="checkbox"/> Begin DV record	
<input type="checkbox"/> Take remote out of test cell	
Coolant Fill	
<input type="checkbox"/> Close He valve	
<input type="checkbox"/> Open Coolant tank vent	
<input type="checkbox"/> Open Coolant fill isolation valve	
<input type="checkbox"/> Fill with coolant	
<input type="checkbox"/> Allow to settle; record level:	coolant: _____
<input type="checkbox"/> Close Coolant fill isolation valve	level: _____
<input type="checkbox"/> Close Coolant tank vent	
<input type="checkbox"/> Open He valve	
Set Coolant throttle valves	
<input type="checkbox"/> Top coolant flow setting	top: _____
<input type="checkbox"/> Side coolant flow setting	side: _____
Initial Coolant Fill of Rocket Die	
<input type="checkbox"/> Close coolant throttle valves	die id: _____
<input type="checkbox"/> Attach vacuum pump	
<input type="checkbox"/> Run vacuum pump until evacuated	
<input type="checkbox"/> Close vacuum/coolant isolation valve	pressure: _____
<input type="checkbox"/> Open coolant tank vent & fill isolation valves	
<input type="checkbox"/> Manually open coolant flow valve and hold to fill	
Ignitor Installation	
<input type="checkbox"/> Bend ignitor to desired shape	
<input type="checkbox"/> Set stop level with ignitor outside of device	
<input type="checkbox"/> Attach coax cable	
<input type="checkbox"/> Insert ignitor into device to vertical stop	
Miscellaneous	
<input type="checkbox"/> Fan on	
<input type="checkbox"/> Lights out	

Table E.2: Gas Pressurization Checklist

MicroRocket Gas Pressurization Checklist		Date: _____
Last Update: 22-Nov-99		Time: _____
		Who: _____
Action	Notes:	
System Prep		
<input type="checkbox"/>	Verify Oil-free Air at pressure	pressure: _____
<input type="checkbox"/>	Open control air valve in control room.	
<input type="checkbox"/>	Prepare Test Cell for run: coolant/video/etc.	
<input type="checkbox"/>	Run "Relays Only" control in Labview.	
Charge Oxygen cylinder		
<input type="checkbox"/>	Open O2 isolation valve	gas: O2 / N2 /
<input type="checkbox"/>	Fill system w/ low pressure oxygen ~150psi	pressure: _____
<input type="checkbox"/>	Close O2 pump solenoid valve	
<input type="checkbox"/>	Open O2 pump man valve	
<input type="checkbox"/>	Set air regulator to desired pressure	pressure: _____
<input type="checkbox"/>	Open O2 pump solenoid valve	
<input type="checkbox"/>	Monitor O2 tank pressure	
<input type="checkbox"/>	Close O2 pump valve at desired tank pressure	pressure: _____
<input type="checkbox"/>	Close O2 bottle	
Vent O2 pump drive air		
<input type="checkbox"/>	Back off drive air regulator	
<input type="checkbox"/>	Open drive air vent	
<input type="checkbox"/>	Wait for vent to complete	
<input type="checkbox"/>	Open O2 pump solenoid valve	
<input type="checkbox"/>	Close drive air vent	
<input type="checkbox"/>	Close O2 pump man valve	
Bring methane up to pressure.		
<input type="checkbox"/>	Open Methane Bottle	gas: CH4 / He /
<input type="checkbox"/>	Bring regulator up to desired pressure	pressure: _____
Safe System if not testing immediately		
<input type="checkbox"/>	Close Control air valve	
<input type="checkbox"/>	Open Control air vent	
Run Desired tests		
Test(s): _____		
Time: _____		
De-Pressurize System Prep		
<input type="checkbox"/>	Verify Control air vent closed	
<input type="checkbox"/>	Verify Control air valve open	
<input type="checkbox"/>	Verify O2 isolation valve open	
Vent Methane		
<input type="checkbox"/>	Close methane bottle	
<input type="checkbox"/>	Back off methane regulator	
<input type="checkbox"/>	Vent methane through wall	
<input type="checkbox"/>	Set methane regulator to vent regulator and line	
Vent oxygen into room		
<input type="checkbox"/>	Run "Reg Control" in Labview	
<input type="checkbox"/>	Enable oxygen vent	
<input type="checkbox"/>	Open oxygen vent valve	
<input type="checkbox"/>	Ramp up oxygen regulator to vent	
<input type="checkbox"/>	Close oxygen regulator	
<input type="checkbox"/>	Close oxygen vent	
<input type="checkbox"/>	Un-enable oxygen vent	
System Shutdown		
<input type="checkbox"/>	Close O2 isolation valve	
<input type="checkbox"/>	Stop LabView controls, power off	
<input type="checkbox"/>	Close control air valve.	
<input type="checkbox"/>	Open control air vent	
<input type="checkbox"/>	Coolant throttle valves closed	
<input type="checkbox"/>	Fan off	
<input type="checkbox"/>	Shutdown OFA compressor	

Table E.3: Hot or Cold Flow Run Checklist

MicroRocket Hot/Cold Flow Checklist		Date: <input type="text"/>
Last Update: 22-Nov-99		Time: <input type="text"/>
		Who: <input type="text"/>
Action		Notes:
Prep for Run		
<input type="checkbox"/>	Verify Oil-free Air at pressure	pressure: <input type="text"/>
<input type="checkbox"/>	Verify Video System Active	
<input type="checkbox"/>	Verify Coolant throttle settings	
<input type="checkbox"/>	Verify Fan on & lights out	Top: <input type="text"/>
<input type="checkbox"/>	Verify O2 at pressure	Side: <input type="text"/>
<input type="checkbox"/>	Verify methane at pressure	O2 pres: <input type="text"/>
<input type="checkbox"/>	Power on and set ignitor power supply	CH4 pres: <input type="text"/>
<input type="checkbox"/>	Un-safe system, if necessary	volts: <input type="text"/>
<input type="checkbox"/>	Verify relays set correctly: open O2 isolate & all flow	
<input type="checkbox"/>	Close control air vent	
<input type="checkbox"/>	Open control air valve slowly	
Run Data Acquisition		
<input type="checkbox"/>	Set initial coolant level in labview	coolant level: <input type="text"/>
<input type="checkbox"/>	Start labview data acquisition. (yes to replace)	run: <input type="text"/>
<input type="checkbox"/>	Record Control Settings	Ox Start: <input type="text"/>
<input type="checkbox"/>		Fuel Start: <input type="text"/>
<input type="checkbox"/>		Ox Run: <input type="text"/>
<input type="checkbox"/>		Fuel Run: <input type="text"/>
<input type="checkbox"/>		Start time: <input type="text"/>
<input type="checkbox"/>		Run time: <input type="text"/>
<input type="checkbox"/>		Ramps: <input type="text"/>
<input type="checkbox"/>	Zero Values, if desired	
Pressurize Coolant		
<input type="checkbox"/>	Verify coolant flow valve open	
<input type="checkbox"/>	Bring Coolant to desired pressure	pres. / mdot: <input type="text"/>
Prepare to Fire		
<input type="checkbox"/>	Verify propellant flow valves open	
<input type="checkbox"/>	Verify all VCRs recording	
<input type="checkbox"/>	Arm Ignitor Box	
<input type="checkbox"/>	Enable Firing	
<input type="checkbox"/>	FIRE	Time: <input type="text"/>
Post Firing		
<input type="checkbox"/>	Verify Buffer saved	remaining: <input type="text"/>
<input type="checkbox"/>	Note counter/time on VCRs	IR: <input type="text"/>
<input type="checkbox"/>	Refire as cold flow; verify buffer saved	Visual: <input type="text"/>
Stop Coolant Flow		DV: <input type="text"/>
<input type="checkbox"/>	Back off He regulator	remaining: <input type="text"/>
<input type="checkbox"/>	Vent He through wall	
<input type="checkbox"/>	Verify all coolant pressures to zero	
<input type="checkbox"/>	Note coolant level	coolant: <input type="text"/>
Safe system if not venting immediately		
<input type="checkbox"/>	Close control air valve	
<input type="checkbox"/>	Open control air vent	
Shutdown		
<input type="checkbox"/>	Close all flow valves	
<input type="checkbox"/>	Stop Labview Data Acquisition	
<input type="checkbox"/>	Stop VCRs	

BIBLIOGRAPHY

- [1] Al-Midani, O. *Preliminary Design of a Liquid Bipropellant Microfabricated Rocket Engine*. M.S. thesis, Massachusetts Institute of Technology, 1998.
- [2] Armstrong, J., and Winstanley, D. "A Review of Staggered Array Pin Fin Heat Transfer for Turbine Cooling Applications." *Journal of Turbomachinery*, Vol. 110 (January 1988), pp. 94–103.
- [3] Ayón, A. A., et al. "Characterization of a Time Multiplexed Inductively Coupled Plasma Etcher." *Journal of the Electrochemical Society*, Vol. 146, No. 1 (January 1999), pp. 339–349.
- [4] Ayón, A. A., et al. "Influence of Coil Power in the Etching Characteristics in a High Density Plasma Etcher." *Journal of the Electrochemical Society*, Vol. 146, No. 7 (July 1999), pp. 2730–2736.
- [5] Ayón, A. A., et al. "Deep Reactive Ion Etching of Silicon." In *Proceedings of the Materials Research Society Fall Meeting, Materials Science of Microelectromechanical Systems (MEMS) Devices* (1999), vol. 546, pp. 51–61.
- [6] Ayón, A. A., et al. "Application of the Footing Effect in the Microfabrication of Self-Aligned, Free-Standing Structures." *Journal of Vacuum Science and Technology*, Volume A17, No. 4, Part II, pp. 2274-2279, July/August 1999.
- [7] Ayón, A. A., Personal Communication, 1996-1999.
- [8] Bayt, R. *Analysis, Fabrication, and Testing of a MEMS-based Micropulsion System*. Ph.D. thesis, Massachusetts Institute of Technology, 1999.
- [9] Bartz, D. R. "An Approximate Form of Compressible Turbulent Boundary Layer Development in Convergent-Divergent Nozzles." *Transactions of the ASME*, Vol. 77 (1955), pp. 1235–1245.
- [10] Chen, K.-S. *Materials Characterization and Structural Design of Ceramic Micro Tubromachinery*. Ph.D. thesis, Massachusetts Institute of Technology, 1999.
- [11] Choi, D. Personal communication re Ph.D. thesis in progress. Massachusetts Institute of Technology, 1999-2000.
- [12] Epstein, A. H., et al. "Micro-Heat Engines, Gas Turbines, and Rocket Engines: The MIT Microengine Project." Presented at the 28th AIAA Fluid Dynamics Conference and the 4th AIAA Shear Flow Control Conference, Snowmass Village, June 1997. AIAA-97-1773.
- [13] Faust, A. *Forced Convective Heat Transfer to Supercritical Water in Micro-Rocket Cooling Passages*. M.S. thesis, Massachusetts Institute of Technology, 2000.

- [14] Francis, R. *A Systems Study of Very Small Launch Vehicles*. M.S. thesis, Massachusetts Institute of Technology, 1999.
- [15] Ghajar, A. J. and Asadi, A. "Improved Forced Convective Heat-Transfer Correlations for Liquids in the Near-Critical Region." *AIAA Journal*, Vol. 24 (December 1986), pp. 2030–2037.
- [16] Gordon, S. and McBride, B. *Computer Program for Calculation of Complex Chemical Equilibrium Compositions and Applications*. NASA Reference Publication 1311, October 1994.
- [17] Han, J. C. "Heat Transfer and Friction Characteristics in Rectangular Channels with Rib Turbulators." *Journal of Heat Transfer*, Vol. 110 (May 1988), pp. 321–328.
- [18] Harrison, T. Personal communication re M.S. thesis in progress, tentatively titled *Packaging of the MIT Microengine*. Massachusetts Institute of Technology, expected 2000.
- [19] Hendricks, R. C. and Simoneau, R.J. "Survey of Heat Transfer to Near-Critical Fluids." NASA TN D-5886, 1970.
- [20] Hill, P. G., and Peterson, C. R. *Mechanics and Thermodynamics of Propulsion*. Addison-Wesley, 1992.
- [21] Holke, A. and Yang, X.-Y. Personal communication re ongoing work on a valve for Microengine Applications. Massachusetts Institute of Technology, 2000.
- [22] Janson, S. W., and Helvajian, H. "Batch Fabricated Microthrusters: Initial Results". In *33rd AIAA/ASME/SAE/ASEE Joint Propulsion Conference and Exhibit*, AIAA-96-2988, 1996.
- [23] Kakaç, S., Shah, R. K., and Aung, W., Eds. *Handbook of Single-Phase Convective Heat Transfer*. John Wiley and Sons, 1985.
- [24] Kakaç, S. "The Effects of Temperature-Dependent Fluid Properties on Convective Heat Transfer." Chapter 18 in *Handbook of Single-Phase Convective Heat Transfer*. John Wiley and Sons, 1985.
- [25] LeFebvre, A. W. *Gas Turbine Propulsion*. New York: McGraw-Hill, 1983. pp. 58–59.
- [26] Lewis, D. H. "Digital Micropropulsion". presented at 12th IEEE International Micro Electro Mechanical Systems Conference (MEMS '99), January 1999.
- [27] Liou, T.-M., and Hwang, J.-J. "Turbulent Heat Transfer Augmentation and Friction in Periodic Fully Developed Channel Flows". *Journal of Heat Transfer*, Vol. 114. (February 1992), pp. 56–64.
- [28] Lohner, K. A. *Microfabricated Refractory Ceramic Structures for Micro Turbomachinery*. M.S. thesis, Massachusetts Institute of Technology, 1999.
- [29] Lopata, J. *Characterization of Heat Transfer Rates in Supercritical Ethanol for Micro-Rocket Engine Regenerative Cooling*. M.S. thesis, Massachusetts Institute of Technology, 1998.
- [30] Madou, M. *Fundamentals of Microfabrication*. CRC Press 1999.

- [31] Mehra, A. *Development of a High Power Density Combustion System for a Silicon Micro Gas Turbine Engine*. P.D. thesis, Massachusetts Institute of Technology, 2000.
- [32] Metzger, D. E., et. al. "Row Resolved Heat Transfer Variations in Pin Fin Arrays Including Effects of Non-uniform Arrays and Flow Convergence." ASME Paper 86-GT-132.
- [33] Michel, R. W. "Combustion Performance and Heat Transfer Characterization of LOX/Hydrocarbon Type Propellants." NASA CR-171713. Aerojet Liquid Rocket Company, 1983.
- [34] Nagle, S. Personal communication re Ph.D. thesis in progress, tentatively titled *Analysis, Design and Fabrication of an Electric Induction Micromotor for a Micro Gas-Turbine Generator*. Massachusetts Institute of Technology, expected 2000.
- [35] Protz, C. S. *Systems Analysis of a Microfabricated Storable Bipropellant Rocket Engine*. M.S. thesis, Massachusetts Institute of Technology, 2000.
- [36] Robert Bosch Gmbh. Method for Anisotropically Etching Silicon. U.S. Patents 4855017 and 4784720. German Patent 4241045C1.
- [37] Schoenman, L. "LOX/Propane and LOX/Ethanol Combustion Chamber Heat Transfer." *Journal of Propulsion*, Vol. 7, No. 4 (August 1991), pp. 538–548.
- [38] Sutton, G. P. *Rocket Propulsion Elements*, 6th Ed. New York: Wiley-Interscience, 1992.
- [39] Sychev, V. V., et. al. *Thermodynamic Properties of Oxygen*, National standard reference data service of the USSR. Washington: Hemisphere Publishing Corporation, 1987.
- [40] Sychev, V. V., et. al. *Thermodynamic Properties of Methane*, National standard reference data service of the USSR. Washington: Hemisphere Publishing Corporation, 1987.
- [41] Tzeng, Y.-S. *An Investigation of Microcombustion Thermal Phenomena*. M.S. thesis, Massachusetts Institute of Technology, 1997.

Additional references for physical property data:

- [42] Vargaftik, N. B. *Tables on the thermophysical properties of liquids and gases*. New York: Hemisphere Publishing Corporation, 1975
- [43] Reid, R. C., et. al. *Properties of Gases and Liquids*, 4th ed. New York: McGraw-Hill, 1987.